Title

Seismic Performance Limitation of Slender Reinforced Concrete Structural Walls

Author

Segura, Christopher

Publication Date

2017

UNIVERSITY OF CALIFORNIA

Los Angeles

Seismic Performance Limitations of Slender Reinforced Concrete Structural Walls

A dissertation submitted in partial satisfaction of the requirements for the degree Doctor of Philosophy in Civil Engineering

by

Christopher Lee Segura

2017

ABSTRACT OF THE DISSERTATION

Seismic Performance Limitations of Slender Reinforced Concrete Structural Walls

by

Christopher Lee Segura
Doctor of Philosophy in Civil Engineering
University of California, Los Angeles, 2017
Professor John Wright Wallace, Chair

Based on a substantial amount of research on the seismic performance of reinforced concrete structural walls (shear walls), modern design provisions for mid-rise and high-rise shear wall buildings have been developed with the goal of achieving significant ductility in the event of strong earthquake ground shaking. Observations following recent earthquakes in Chile (2010) and New Zealand (2011) have demonstrated that shear wall buildings designed according to modern seismic design codes for tension-controlled action may be vulnerable to brittle compression failure. For walls designed to yield in compression, current reinforced concrete design standards in the United States (ACI 318-14) assume that ductility is ensured if code-prescribed confinement provisions are satisfied at wall boundaries; however, recent laboratory tests suggest that thin, code-compliant walls may be susceptible to compression failure prior to achieving the inelastic deformation capacity assumed by current U.S. design codes (i.e., ASCE 7-10, ASCE 41-13).

Seven, approximately one-half scale, ACI 318-14 compliant wall specimens (designated WP1-WP7) were subjected to reversed cyclic lateral loads and constant axial load. The specimens represented approximately the bottom 1.5 stories of an eight story cantilever wall. The first phase of testing (WP1-WP4) was conducted to identify potential deficiencies in current provisions. Test variables for the phase 1 specimens included the configuration of boundary longitudinal reinforcement, quantity and arrangement of boundary transverse reinforcement, and compression depth (influence by axial load, quantity of longitudinal reinforcement, and wall cross-section). For the second phase of testing (WP5-WP7), walls were designed either with thicker cross-sections, improved boundary transverse reinforcement details (i.e., continuous transverse reinforcement detail rather than hoop and cross-tie detail), or both. Phase 2 specimens were constructed with improved web details whereby longitudinal reinforcement was placed inside of transverse reinforcement and, in some cases, cross-ties were used to provide lateral restraint to longitudinal reinforcement.

Abrupt compression failures occurred at plastic rotations as low as 1.1% for the thinnest walls. Plastic rotations greater than 2.5% were observed for walls that were 25% and 50% thicker and/or constructed with more stringent confinement detailing than required by ACI 318-14. Based on experimental results, it is suggested to improve the deformation capacity of thin walls by avoiding the use of cross-tie confinement, and using overlapping hoops or continuous transverse reinforcement instead. Within the web region of walls, it is recommended to provide transverse reinforcement for web longitudinal reinforcement within the plastic hinge region. A lateral drift capacity prediction equation was developed in a displacement-based design format and was shown to agree with experimentally measured drift capacities for a small database of slender wall laboratory tests. It was demonstrated that, in addition to provided boundary transverse reinforcement, drift capacity of slender walls is most impacted by compression depth (c), wall thickness (b), and wall length (l_w). Based on experimental data, drift capacities greater than 2% may be expected for code compliant walls designed such that $c/b<2.5$, while drifts lower than 1% are expected when $c/b>5.0$.

This dissertation of Christopher Lee Segura is approved.

Scott J. Brandenberg

Henry J. Burton

Jack P. Moehle

Thomas A. Sabol

John Wright Wallace, Committee Chair

University of California, Los Angeles

2017

TABLE OF CONTENTS

LIST OF FIGURES

LIST OF TABLES

LIST OF SYMBOLS

A_{ch}	Cross-sectional area measured to outside edges of transverse reinforcement, in.^{2}
A_{cv}	Gross area of concrete section bounded by web thickness and length of section in the direction of shear force considered, in.^{2}
A_g	Gross area of concrete section, in.^{2}
A_{sh}	Total cross-sectional area of transverse reinforcement (including cross-ties) within spacing s and perpendicular to dimension b_c, in.^{2}
$A_{sh,req'd}$	Cross-sectional area of transverse reinforcement required by ACI 318-14, in.^{2}
b	Width of the compression face of member, in.
b_c	Cross-sectional dimension of member core measured to the outside edges of the transverse reinforcement composing area A_{sh}, in.
c	Neutral axis depth, in.
c_c	Clear cover to outside edge of reinforcement, in.
C_d	Deflection amplification factor
d_b	Nominal diameter of reinforcing bar, in.
E_c	Modulus of elasticity of concrete, psi
E_s	Modulus of elasticity of reinforcement, psi
f'_c	Specified compressive strength of concrete, psi
$f'_{c,test}$	Measured compressive strength of concrete cylinder, psi
f_{rup}	Tension rupture strength of reinforcement, psi
f_{peak}	Peak measured strength of reinforcement, psi
f_y	Specified yield strength of reinforcement, psi
$f_{y,test}$	Measured yield strength of reinforcement, psi

f_{yt}	Specified yield strength of transverse reinforcement, psi
h_{eff}	Effective height of wall, in.
h_u	Unsupported story height of wall, in.
h_w	Height of wall from base to top, in.
h_x	Maximum center-to-center horizontal spacing of cross-ties or hoop legs on all faces of column, in.
I_g	Moment of inertia of gross concrete section about centroidal axis, neglecting reinforcement, in.^{4}
l_{be}	Length of confined boundary region measured horizontally from extreme compression fiber, in.
l_d	Development length in tension of deformed reinforcing bar, in.
l_p	Plastic hinge length, in.
l_w	Length of wall in direction of shear force, in.
M_{base}	Moment at base of wall, in.-lb
M_{cr}	Cracking moment, in.-lb
M_n	Nominal flexural strength at section, in.-lb
M_{peak}	Maximum measured moment, in.-lb
M_u	Factored moment at section, in.-lb
M_y	Yield moment, in.-lb
P_n	Nominal axial compressive strength of member, lb
P_u	Factored axial load, lb
R	Seismic response modification coefficient
s	Center-to-center spacing of transverse reinforcement, in.

v_u	Shear stress demand, lb
V_n	Nominal shear strength, lb
V_u	Factored shear force at section, lb
α_c	Coefficient defining the relative contribution of concrete strength to nominal wall shear strength
δ_f	Lateral flexural displacement, in.
$\delta_{f,wall}$	Lateral displacement of wall panel specimen due to flexure, in.
$\delta_{f,base}$	Lateral displacement due to base slip/extension, in.
$\delta_{f,y}$	Lateral displacement at yielding of flexural reinforcement, in.
$\delta_{f,p}$	Inelastic flexural lateral displacement, in.
$\delta_{f,pu}$	Inelastic lateral flexural displacement at 20% reduction in lateral strength, in.
$\delta_{f,u}$	Lateral flexural displacement at 20% reduction in lateral strength, in.
δ_s	Lateral shear displacement, in.
$\delta_{s,slide}$	Shear sliding displacement, in.
δ_{tot}	Total lateral deformation, in.
δ_u	Design lateral displacement, in.
ε_c	Extreme fiber compression strain
$\varepsilon_{c0,test}$	Strain corresponding to measured peak cylinder compressive strength
ε_{cu}	Extreme fiber compression strain at 20% reduction in lateral strength
ε_{rup}	Tension rupture strain of reinforcement
ε_{sh}	Hardening strain of reinforcement
ε_t	Extreme fiber tension strain
ε_{tu}	Extreme fiber tension strain at 20% reduction in lateral strength

ε_{peak}	Strain at peak strength of reinforcement
ε_y	Yield strain of reinforcement
θ_y	Yield rotation, rad.
θ_p	Inelastic rotation, rad.
θ_{peak}	Rotation at peak measured lateral strength, rad.
θ_{pu}	Inelastic rotation at 20% reduction in lateral strength, rad.
θ_u	Ultimate rotation, rad.
λ	Modification factor to reflect the reduced mechanical properties of lightweight concrete relative to normalweight concrete of the same compressive strength
ρ_l	Ratio of distributed longitudinal reinforcement to gross concrete area perpendicular to that reinforcement
ρ_{lb}	Boundary element reinforcing ratio
ρ_t	Ratio of distributed transverse reinforcement to gross concrete area perpendicular to that reinforcement
ϕ	Strength reduction factor
ϕ_{cr}	Curvature at horizontal flexural cracking at wall boundaries, in.$^{-1}$
ϕ_y	Curvature at yielding of flexural reinforcement, in.$^{-1}$
ϕ_p	Inelastic curvature, in.$^{-1}$
ϕ_u	Ultimate curvature, in.$^{-1}$

ACKNOWLEDGEMENTS

I am incredibly grateful for the unconditional love my wife, Jennifer, has provided as I worked to complete my doctoral studies. The support I've received from Jennifer over the past several years has been my greatest motivation, and our occasional adventures together have reenergized me as I worked to finish this work. Thank you, Jennifer, for being so patient and helpful when I was busy and stressed. It is truly a blessing to have you in my life. I would also like to express my sincere gratitude to my father, mother, and step-father for all of their encouragement and support.

When you have the chance to do work that truly interests you, and to work amongst people with whom you enjoy spending your time, hard work does not feel like work at all. My research advisor, John W. Wallace, provided such an environment for me. I want to thank him for giving me the opportunity to work on an exciting project, for continually challenging and supporting me, and for providing unique opportunities for me to work with other experts in the earthquake engineering field. I would also like to express my gratitude to the other members of my doctoral committee, Scott J. Brandenberg, Henry J. Burton, Jack P. Moehle, and Thomas A. Sabol, for their guidance and input on this research.

This research could not have been completed without the tremendous support and guidance of laboratory engineers Steve Keowen, Alberto Salamanca, and Eric Ahlberg, who assisted with test specimen fabrication, test setup, specimen instrumentation, test control, and data acquisition. I am truly grateful to Mr. Keowen, Dr. Salamanca, and Dr. Ahlberg for all of the help they have provided and for their willingness to share the knowledge they have gained. A special thanks is given to colleagues Christopher Motter, Carlos Arteta, Christopher Hilson, Weijing Zhang, Saman Abdullah, Amin Safdari, Ellie Moore, and Negin Aryaee for their assistance with laboratory tests and for valuable feedback on this research. Thank you also to the many undergraduate and high school students who contributed to this project: Anna Flintrop, Marissa Shea, Jose Guitierrez, Sophia Poulos, Andrew Yu, Davis Thomas, Michael Daciolas, Rouzbeh Mahmoudzadeh, Alicia Pedneault, Andrew Kao, Sergio Herrera, Bernardo Neves, Alexander Arroyo, Ramin Mousacohen, Josue Perez, and Wendy Torres.

I would like to express my gratitude for funding provided by the National Science Foundation (NSF) through the Network for Earthquake Engineering Simulation Program Grant No. CMMI-1208192, which provided financial support for this research. The laboratory experiments reported herein were conducted in a laboratory renovated with funds provided by the NSF under Grant No. 0963183. This financial support is gratefully acknowledged. Any opinions, findings, and conclusions or recommendations expressed in this report are those of the author and do not necessarily reflect the views of others mentioned here.

VITA

2009	B.S., Civil Engineering University of Colorado, Boulder
2011	M.S., Civil Engineering University of Colorado, Boulder
2010-2011	Graduate Student Researcher Department of Civil, Environmental and Architectural Engineering University of Colorado, Boulder
2011-2017	Graduate Student Researcher Department of Civil and Environmental Engineering University of California, Los Angeles
2013-2017	Teaching Assistant Department of Civil and Environmental Engineering University of California, Los Angeles
2013-2014	Graduate Student Mentor NEES Research Experience for Undergraduates (NEES REU) Program ULCA High School Summer Research Program (HSSRP)

Chapter 1 Introduction

1.1 Overview

In areas impacted by large magnitude earthquakes, reinforced concrete structural walls (shear walls) are commonly used as the primary lateral seismic force-resisting system for mid-rise and high-rise construction. Because of the rarity of large magnitude earthquakes at a particular building site, modern seismic design codes (i.e., ASCE 7-10, ACI 318-14) allow for inelastic response of the seismic force-resisting system. For mid-rise and high-rise shear wall (slender wall) buildings, flexural yielding, usually at a single critical region near the base of the wall, is the desired mechanism to achieve a ductile response. Research has demonstrated that slender walls can achieve large lateral drift ratios when compression zones in yielding regions are adequately detailed to remain stable (Oesterle, et al., 1976; Paulay, et al., 1985; Thomsen, et al., 2004; Brueggen, 2009); thus, ACI 318-14 design provisions for slender walls are intended to prevent premature compression failure. It is assumed that code-compliant walls can achieve the lateral drift limits imposed by buildings codes (i.e., ASCE 7-10, ASCE 41-13) by means of a tension-controlled failure mechanism. However, field observations of slender walls following the 2010 Maule earthquake in Chile and the 2011 Christchurch earthquake in New Zealand, both in locations where seismic design codes similar to those used in the U.S. have been adopted, demonstrated the potential for code-compliant walls to experience brittle compression failure. Damage was generally concentrated near the base of walls and included wall boundary and web crushing, buckling of longitudinal reinforcement, and out-of-plane instability of wall boundary regions (Massone, et al., 2012; Wallace, et al., 2012).

Studies conducted following the earthquake in Chile revealed that damage occurred primarily in newer buildings which were likely to contain walls that were taller, thinner, and designed for larger axial stress demands than typical designs of previous decades (Massone, et al., 2012). It is anticipated that a similar trend toward less conservative designs has occurred in the U.S. over the past few decades as engineers have sought to produce more economical designs, spurred by advances in structural modeling capabilities, less conservative design approaches/provisions, and other factors (e.g., use of higher strength concrete). Of particular importance is the fact that it is now standard practice in many parts of the world, including the U.S., to construct rectangular walls and walls comprised of rectangular sections (i.e., T-shape, I-shape, C-shape, etc.), although recent laboratory tests on ACI 318 compliant rectangular walls (Nagae, et al., 2012; Lowes, et al., 2012) and rectangular boundary element specimens (Arteta, 2015; Welt, 2015) have demonstrated the inability of relatively thin rectangular sections to remain stable when subjected to compression yielding. The laboratory tests presented in this report were conducted to address issues that led to observed poor wall performance, to identify potential deficiencies in current ACI 318 design provisions, and to evaluate the performance of walls designed with details exceeding the requirements of ACI 318-14.

1.2 Research Significance

The objective of the research reported in this paper is to characterize critical performance limitations of slender walls. For walls designed to yield in compression, ACI 318 assumes that ductility is ensured if code-prescribed confinement provisions are satisfied at wall boundaries; however, recent laboratory tests suggest that code-compliant walls may be susceptible to premature compression failure. Furthermore, the role of wall thickness and confinement detailing on slender wall performance have not been fully addressed in ACI 318-14. Because of the widespread use of slender walls in areas impacted by strong earthquake ground shaking, it is critical to understand the design conditions (e.g., wall thickness, compression depth) for which walls designed to current ACI provisions do not provide sufficient deformation capacity to satisfy code-allowable drift limits. It is equally important to identify the conditions for which current code requirements provide adequate deformation capacity, so that all walls are not required to be designed and detailed for the worst-case scenario.

Numerous tests have been conducted on isolated walls in the past several decades. Due to laboratory constraints, however, a large majority of these tests were conducted at small scale, and very few test specimens had geometry and reinforcement arrangement representative of modern walls. Many experiments have been conducted with little or no axial load and applied lateral loading that might not represent the demands on high-rise buildings. Very little experimental data, therefore, exists on modern wall designs that satisfy current code provisions.

1.3 Organization of the Document

This document presents details of an experimental program intended to address potential issues identified in recent earthquakes and laboratory tests. It is organized into six chapters. Chapter 1 provides an introduction and research motivation. Chapter 2 provides a review of relevant scientific literature related to modern slender wall design and construction. Current U.S. building code requirements for structural walls are discussed in Chapter 2, followed by observations reported following the 2010 earthquake in Chile and the 2011 earthquake in New Zealand. Previous research on slender walls is discussed with an overview of several experimental programs. Chapter 2 ends with a summary of the literature review and research objectives and goals. The design of the test specimens is discussed in Chapter 3, and details of the experimental program are provided in Chapter 4. An overview of the experimental results and a detailed description of observed behavior for each of the test specimens is presented in Chapter 5. A detailed analysis of experimental results is provided in Chapter 6. In Chapter 7, a lateral drift capacity limit formulation is presented and compared to experimental results for the seven tests reported herein, as well as laboratory tests from eight other experimental programs. Chapter 8 provides a summary and conclusions of the research.

Chapter 2 Literature Review

In this chapter, current provisions for the design of slender walls are discussed, followed by a review of observations to shear wall buildings following the 2010 earthquake in Chile and the 2011 earthquake in New Zealand. Following that, previous experimental work conducted on slender walls is discussed. A summary and research objectives are included at the end of the chapter.

2.1 Current Provisions for Shear Wall Buildings: ASCE 7-10 and ACI 318-14

ASCE/SEI 7-10 Minimum Design Loads for Buildings and Other Structures, herein referred to as ASCE 7-10, provides provisions for the design and analysis of new buildings. For typical structures without irregularities, either a linear or nonlinear analysis may be used to determine the response of the structure to Design Earthquake (DE) level demands (ASCE/SEI, 2010). Linear analyses are based on the Equivalent Lateral Force (ELF) Procedure of ASCE 7-10 Section 12.8 – a static analysis in which lateral seismic story forces are distributed vertically up the height of the structure based on the design seismic base shear (ASCE/SEI, 2010). The seismic base shear is determined from the code-prescribed pseudo-spectral acceleration at the building site (related to location and soil conditions) for the building's fundamental period. A linear modal response spectrum analysis (ASCE 7-10 Section 12.9) or response history analysis (ASCE7-10 Chapter 16) may also be used. In both cases, an adequate number of modes must be considered such that the modal mass participation for all modes considered is at least 90%.

For a linear analysis, ASCE 7-10 Table 12.2-1 prescribes the seismic force reduction factor (R) and displacement amplification factor (C_d) for each LFRS. For a Special Reinforced Concrete Shear Wall building (ASCE7-10 designation) R=5 and C_d= 5. Analysis response parameters (i.e., forces and displacements) resulting from the analysis are reduced by R, and displacements are amplified by C_d. The reduced forces are used to design individual components of the LFRS, and the amplified displacements are compared to code-allowable interstory drift limits given in Table 12.12-1 (Figure 2-1). For typical shear wall buildings (i.e., classified as Risk Category I or II according to ASCE 7-10), allowable interstory drift limits are 2.5% of the story height for structures that are four stories or less, and 2% of the story height for taller structures. Only the structural components designated as part of the lateral seismic force-resisting system (LFRS) are used to determine the effective stiffness of the structure.

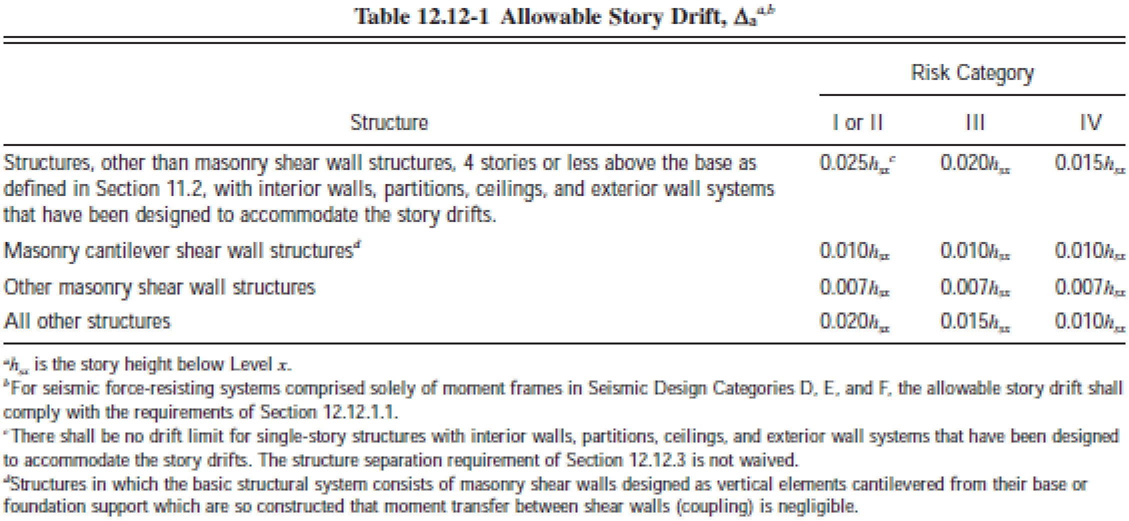

Table 12.12-1 Allowable Story Drift, Δ_a[a,b]

Structure	Risk Category I or II	III	IV
Structures, other than masonry shear wall structures, 4 stories or less above the base as defined in Section 11.2, with interior walls, partitions, ceilings, and exterior wall systems that have been designed to accommodate the story drifts.	$0.025h_{sx}$[c]	$0.020h_{sx}$	$0.015h_{sx}$
Masonry cantilever shear wall structures[d]	$0.010h_{sx}$	$0.010h_{sx}$	$0.010h_{sx}$
Other masonry shear wall structures	$0.007h_{sx}$	$0.007h_{sx}$	$0.007h_{sx}$
All other structures	$0.020h_{sx}$	$0.015h_{sx}$	$0.010h_{sx}$

[a] h_{sx} is the story height below Level x.

[b] For seismic force-resisting systems comprised solely of moment frames in Seismic Design Categories D, E, and F, the allowable story drift shall comply with the requirements of Section 12.12.1.1.

[c] There shall be no drift limit for single-story structures with interior walls, partitions, ceilings, and exterior wall systems that have been designed to accommodate the story drifts. The structure separation requirement of Section 12.12.3 is not waived.

[d] Structures in which the basic structural system consists of masonry shear walls designed as vertical elements cantilevered from their base or foundation support which are so constructed that moment transfer between shear walls (coupling) is negligible.

Figure 2-1: ASCE 7-10 Table 12.12-1 Allowable Drift Limits

The American Concrete Institute (ACI) Building Code Requirements for Structural Concrete (ACI 318-14) and Commentary provides minimum requirements for design and construction of structural concrete members in a building (ACI Committee 318, 2014). ACI 318-14 S4.4.6.1 dictates the selection of the Seismic Design Category (SDC) in accordance with ASCE 7-10. SDCs are determined based on an importance factor assigned to the structure and the anticipated earthquake ground motion intensity at the building site (ASCE/SEI, 2010). For structures assigned to SDC D, E, and F, provisions of ACI 318-14 Chapter 18 apply to structural systems designated as part of the seismic force-resisting system, as well as structural members not designated as part of the seismic force-resisting system but required to support other loads while undergoing deformations associated with earthquake effects. For structures assigned to SDC B and C, Chapter 18 applies only to structural systems designated as part of the seismic force-resisting system (ACI Committee 318, 2014).

The provisions of Chapter 18 are considered the minimum requirements for a cast-in-place or precast concrete structure to sustain a series of oscillations into the inelastic range without critical deterioration in strength (i.e., a low probability of collapse). The ability of the structure to maintain its strength in the inelastic range is critical because the Design Earthquake forces defined in ASCE 7-10 are considered less than those corresponding to linear response at the anticipated earthquake intensity (i.e., R>1). Except for structures assigned to SDC A, for which Chapter 18 does not apply, Special Structural Walls (ACI 318 designation) are required to satisfy dimensioning and detailing requirements of S18.10 (ACI Committee 318, 2014). Requirements of S18.10 are summarized in the following sections.

2.1.1 Design Forces, Design Strength, and Wall Web Detailing

Special Structural Walls (ACI 318 designation) are required to resist the shear force, axial force, and overturning moment demands imposed by gravity loads in combination with earthquake inertial forces. Design forces (P_u, V_u, and M_u) are determined according to the analysis methods of ASCE 7-10 Chapter 12 (ELF procedure or response spectrum analysis) or Chapter 16 (response history analysis) with load combinations that include gravity loads simultaneously with the effects of vertical and horizontal earthquake ground motions. Design wall strength is taken as the nominal strength reduced by a strength reduction factor (ϕ).

Axial and flexural capacity (P_n, M_n) are determined by a section analysis, assuming a linear strain profile (i.e., plane sections remain plane assumption) and accounting for all concrete and developed reinforcement within wall boundary elements, the wall web, and effective flange widths. An elastic perfectly plastic stress-strain model is used to represent longitudinal reinforcement in tension and compression. The contribution of concrete in tension is neglected, and a maximum extreme compression fiber strain (ε_c) of 0.003 is assumed for concrete in compression. The concrete compressive stress-strain behavior may be idealized using an equivalent rectangular stress block or any other shape that is in good agreement with comprehensive material testing (ACI Committee 318, 2014). To determine the nominal (design) strength ($\phi P_n, \phi M_n$), ϕ is taken as 0.90 for tension-controlled sections and 0.65 for compression-controlled sections. Sections are considered tension-controlled if the extreme tension fiber strain (ε_t) is greater than or equal to 0.005 when ε_c=0.003. Compression-controlled sections are defined as sections in which ε_t is less than or equal to the reinforcing bar yield strain ($\varepsilon_y = f_y/E_s$) when ε_c=0.003. Linear interpolation is used to determine ϕ for sections falling into the transition region between tension-controlled and compression-controlled sections.

The nominal wall shear strength is determined by Eqn. 2.1

$$\phi V_n = \phi A_{cv}\left(\alpha_c \lambda \sqrt{f'_c} + \rho_t f_y\right) \qquad 2.1$$

where ϕ=0.60 when V_n is less than the shear demand required to develop the nominal flexural strength (i.e., $V_n/V_u@M_n<1.0$), and ϕ=0.75 when V_n is sufficient to develop M_n (ACI 318-14 Table S21.2.1). For an individual wall, ACI 318-14 limits V_n to $10A_{cv}\sqrt{f'_c}$. For all vertical walls sharing a common lateral force, V_n is limited to $8A_{cv}\sqrt{f'_c}$. The upper limit of strength to be assigned to any one member is imposed to limit the degree of redistribution of shear force (ACI Committee 318, 2014).

2.1.2 Boundary Element and Web Detailing

ACI 318-14 boundary element detailing requirements are described in detail in this section. Some changes have been incorporated into ACI 318-14 to address issues identified for slender walls in recent earthquakes and laboratory tests. A comparison of ACI 318-11 and ACI 318-14 provisions is made at the end of the section (Table 2-1) to summarize detailing requirements and to outline the changes incorporated in ACI 318-14.

Two design approaches for evaluating detailing requirements at wall boundaries are included in ACI 318-14 S18.10.6: (1) a displacement-based approach (S18.10.6.2) by which detailing requirements are determined directly based on expected lateral displacements of the wall, and (2) a stress-based approach (S18.10.6.3) by which detailing requirements are determined based on the extreme fiber compression stress. The displacement-based approach is based on the assumption that inelastic response of the wall is dominated by flexural action (i.e., slender wall) at a critical, yielding section (ACI Committee 318, 2014).

For walls that are effectively continuous from the base of the structure to the top of the wall and designed to have a single critical section for flexure and axial loads, the need for Special Boundary Element (SBE) detailing may be determined using either the displacement-based approach or the stress-based approach. By the displacement-based approach, compression zones are required to be reinforced with SBEs when the largest neutral axis depth (c) calculated for the factored axial load and nominal moment strength consistent with the design displacement (δ_u) exceeds a critical value given by Eqn. 2.2.

$$c \geq \frac{l_w}{600(1.5\delta_u / h_w)} \tag{2.2}$$

A minimum value for the design roof drift ratio (δ_u/h_w) in Eqn. 2.2 of 0.005 is imposed. Eqn. 2.2 was derived using the plastic hinge formulation, summarized in Figure 2-2, to relate the roof lateral drift demand (δ_u/h_w) to the strain demand at the extreme compressive fiber within the plastic hinge region of the wall. The lateral displacement at the top of a cantilever wall is comprised of the flexural and shear responses (i.e., $\delta_u=\delta_f+\delta_s$). Slender walls are designed to yield in flexure prior to reaching the nominal shear strength of the wall; thus, the inelastic response is dominated by flexural behavior. Figure 2-2(a) presents the plastic hinge model formulation used to express the lateral flexural displacement (δ_f) at the top of a cantilever wall in terms of elastic drift ($\delta_{f,y}$) and inelastic drift ($\delta_{f,p}$). For a cantilever wall that is effectively continuous from the base of the structure to the top of the wall, flexural yielding occurs at the bottom of the wall where the overturning moment is largest. Elastic drift can be estimated as $\delta_{f,y} = \gamma\phi_y h_w^{\;2}$, where ϕ_y is the curvature at flexural yielding and h_w is the height of the wall if it is assumed that the wall cross-section is uniform up its full height and if the increased stiffness of the uncracked section, in the upper stories, is neglected. The value of γ depends on the applied loading pattern: γ=11/40 for an inverted triangular loading pattern (as shown in Figure 2-2), and γ=1/3 for a lateral point load applied at the top of the wall, which is a common laboratory testing configuration to simulate lateral earthquake inertial forces. According to the plastic hinge model, inelastic drift is assumed to occur as plastic rotation (θ_p) centered about the centroid of the plastic curvature profile ($\bar{x}$ in Figure 2-2). For a known plastic curvature profile, denoted $\phi_p(x)$ in Figure 2-2(a), θ_p can be determined by integrating over the height of the plastic curvature profile (denoted H_p in Figure 2-2): $\theta_p = \int_0^{H_p} \phi_p(\mathrm{x})dx$. As illustrated in Figure 2-2(b), it is common to idealize plastic curvature as constant over an assumed plastic hinge length (l_p), in which case δ_u may be approximated by Eqn. 2.3, which neglects shear deformations:

$$\delta_u \approx \delta_f = \delta_{f,y} + \delta_{f,p} = \gamma\phi_y h_w^{\,2} + \theta_p (h_w - \bar{x}) = \gamma\phi_y h_w^{\,2} + \left(\phi_u - \phi_y\right) l_p (h_w - l_p/2) \tag{2.3}$$

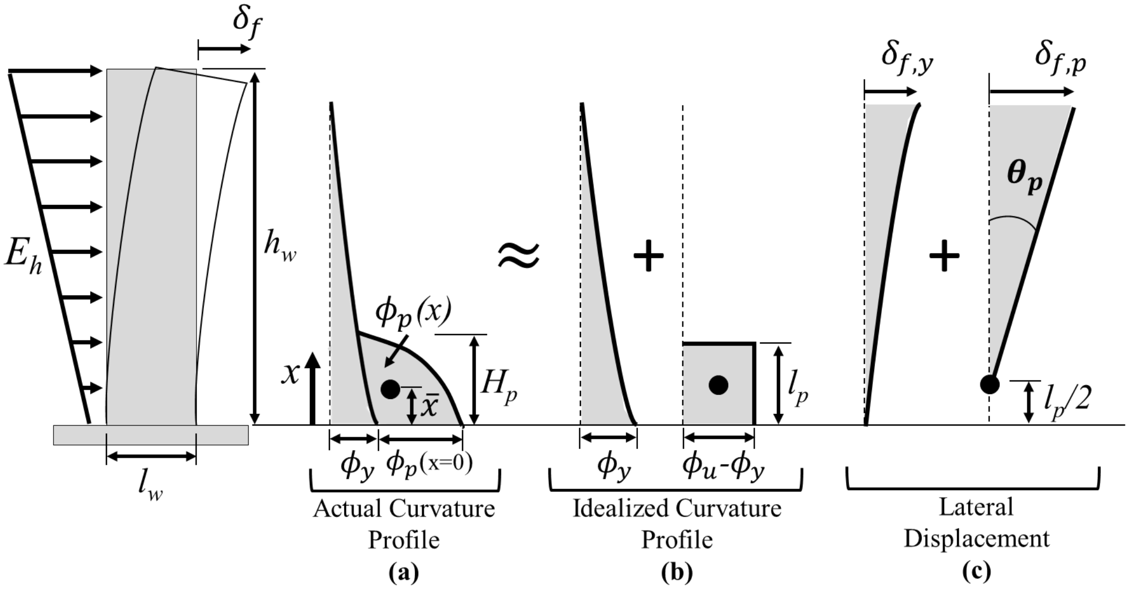

Actual Curvature Profile
(a)

Idealized Curvature Profile
(b)

Lateral Displacement
(c)

Figure 2-2: Plastic hinge model for cantilever walls - (a) Actual curvature profile; (b) Idealized curvature profile; and (c) Lateral displacements for idealized curvature profile

Assuming plane sections remain plane, ϕ_u in Eqn. 2.3 can be defined as the extreme fiber compression strain (ε_c) divided by the compression depth (c), leading to the definition of θ_p and $\delta_{f,p}$ in Eqns. 2.4 and 2.5, respectively. At large ductility demands, Eqn. 2.5 can be simplified (Eqn. 2.6) by recognizing that θ_p is nearly equal to $\delta_{f,p}/h_w$ (i.e., $h_w \approx h_w - l_p/2$); hence, plastic drift ($\delta_{f,p}/h_w$) can be directly related to extreme fiber compression strain for an assumed plastic hinge length and a given compression depth, typically assumed to be relatively constant for $\varepsilon_c \geq 0.003$.

$$\theta_p = \left(\frac{\varepsilon_c}{c} - \phi_y\right) l_p \tag{2.4}$$

$$\frac{\delta_{f,p}}{h_w} = \frac{1}{h_w}\left(\frac{\varepsilon_c}{c} - \phi_y\right) l_p (h_w - l_p/2) \qquad 2.5$$

$$\frac{\delta_{f,p}}{h_w} \approx \theta_p \approx \frac{\varepsilon_c}{c} l_p \qquad 2.6$$

Eqn. 2.2 is based on the simplified formulation of Eqn. 2.6, where inelastic rotation is assumed to occur at the base of the wall. In Eqn. 2.2, elastic deformations are neglected such that $\delta_u \approx \delta_{f,p}$. A plastic hinge length equal to one-half the length of the wall ($l_p = l_w/2$) is assumed and SBE detailing is required when the extreme fiber compressive strain exceeds 0.003 (Wallace, et al., 2002), in which case Eqn. 2.6 can be rearranged and expressed as Eqn. 2.7.

$$\varepsilon_c = \frac{\delta_u}{h_w}\frac{c}{l_p} \le 0.003 \quad \rightarrow \quad c \le \frac{0.003 l_p}{\delta_u/h_w} = \frac{0.003 l_w}{2(\delta_u/h_w)} \approx \frac{l_w}{600(\delta_u/h_w)} \qquad 2.7$$

In the 2014 version of ACI 318, a 1.5 multiplier on δ_u/h_w was added to Eqn. 2.7, which results in Eqn. 2.2, to produce detailing requirements more consistent with the building code performance intent of a low probability of collapse in Maximum Considered Earthquake (MCE) level shaking (ACI Committee 318, 2014).

Figure 2-3 demonstrates the impact of neutral axis depth on the need for SBE detailing for design roof drift ratio demands up to 0.02. For typical design roof drift ratios (δ_u/h_w=0.01-0.02), SBEs are required when the neutral axis depth exceeds approximately 10% of the wall length. For a neutral axis depth greater than $0.22l_w$, SBEs are always required.

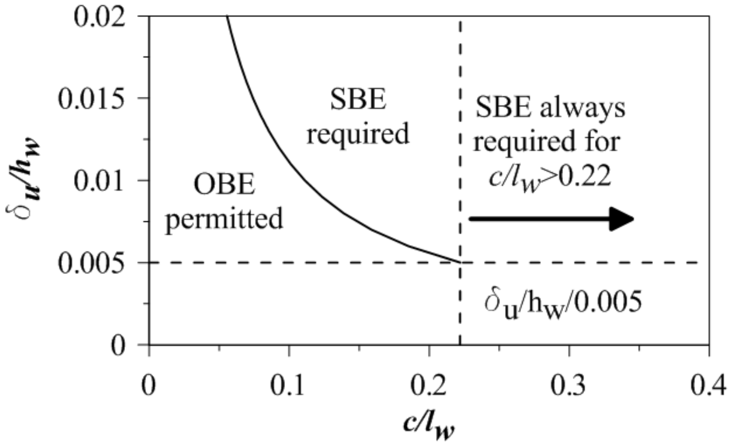

Figure 2-3: Impact of neutral axis depth (c/l_w) and design roof drift ratio (δ_u/h_w) on the need for SBEs

Where SBEs are required by the displacement-based approach, they must extend vertically above and below the critical section at least the greater of l_w and $M_u/4V_u$. Where the critical section occurs at the wall base, the boundary transverse reinforcement is required to be extended into the support a length equal to or greater than the development length of the largest longitudinal bar.

By the stress-based approach of S18.10.6.3, SBEs are required at wall boundaries and edges around openings of structural walls where the maximum extreme fiber compressive stress, corresponding to load combinations including earthquake effects, exceeds $0.2f'_c$. The extreme fiber compressive stress is determined for the factored axial load and overturning moment using a linear elastic model of the gross section properties. Where SBEs are required by the stress-based approach, they are permitted to be discontinued where the calculated extreme fiber compressive stress is less than $0.15f'_c$. The stress-based approach is typically considered to be overly conservative for most slender walls, requiring confinement when extreme fiber compression strains may be reasonably low (i.e., $\varepsilon_c<0.003$) for the expected lateral drift demands (Wallace, et al., 1992; Wallace, et al., 2002).

Where SBEs are required by either the displacement-based approach or the stress-based approach, S18.10.6.4 provides dimensioning and detailing requirements. A minimum confined length (l_{be}), measured horizontally from the extreme compression fiber (Figure 2-4), is required to satisfy Eqn. 2.8. The first term, c-0.1l_w, was derived to limit the compressive strain at the inner edge of hoop reinforcement to 0.003 at the design roof drift ratio. The value of $c/2$ provides a minimum length of the SBE.

$$l_{be} \geq \begin{cases} c - 0.1l_w \\ c/2 \end{cases} \tag{2.8}$$

The width of the flexural compression zone, b (Figure 2-4), over the length determined by l_{be} in Eqn. 2.8 must be at least $h_u/16$, where h_u is the clear story height of the wall. This slenderness limit was introduced in the 2014 edition of ACI 318 based on lateral instability failures of slender walls observed in recent earthquakes and laboratory tests (ACI Committee 318, 2014). A minimum compression zone thickness of 12 in. (305 mm) is enforced for walls where $c/l_w \geq 3/8$. A value of $c/l_w \geq 3/8$ indicates a section that is not tension-controlled, and the minimum thickness has been imposed to reduce the likelihood of lateral instability of the compression zone after spalling of cover concrete (ACI Committee 318, 2014).

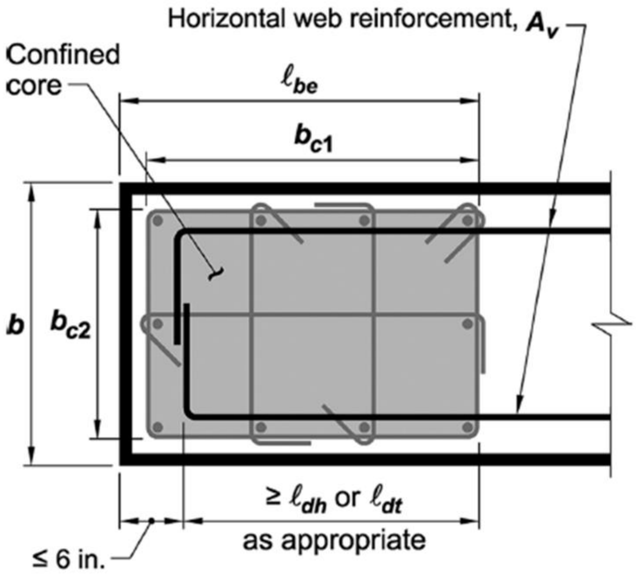

Figure 2-4: SBE detailing (ACI Committee 318, 2014)

SBE transverse reinforcement is required to be comprised of single or overlapping spirals, circular hoops, or rectilinear hoops with or without cross-ties. Where rectilinear cross-ties are used, they are required to provide lateral support to longitudinal reinforcement with alternating 90°-135° seismic hooks engaging peripheral longitudinal reinforcing bars (Figure 2-5). Horizontal spacing of transverse reinforcement (h_x) is required to satisfy Eqn. 2.9. The value used for h_x in Eqn. 2.9 is taken as the largest value of x_i in Figure 2-5. The term 2/3b in Eqn. 2.9 was introduced in the 2014 version of ACI 318 and is intended to provide more uniform spacing of hoops and cross-ties for thin walls (ACI Committee 318, 2014).

$$h_x \leq \begin{cases} 14\ in. \\ \dfrac{2}{3}b \end{cases} \tag{2.9}$$

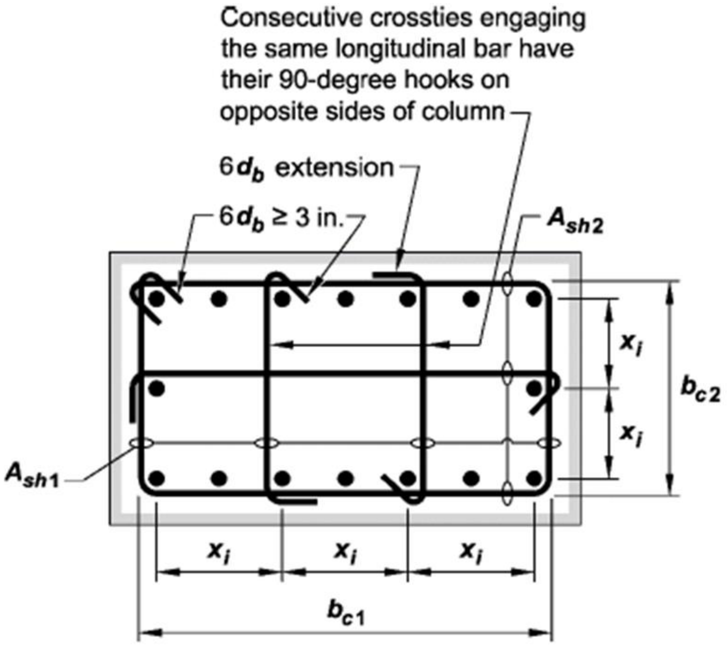

Figure 2-5: SBE transverse reinforcement (ACI Committee 318, 2014)

Vertical spacing of transverse reinforcement (s) is required to satisfy Eqn. 2.10 which is based on ACI 318 provisions for Special Moment Frame columns. The spacing requirements are intended to provide adequate confinement for concrete in compression and to restrain longitudinal reinforcement buckling following spalling of concrete cover.

$$s \leq \begin{cases} b/3 & (a) \\ 6d_b & (b) \\ 4" \leq 4" + \left(\dfrac{14" - h_x}{3}\right) \leq 6" & \text{(c)} \end{cases} \qquad 2.10$$

The quantity of transverse reinforcement provided in SBEs (A_{sh}), using rectilinear hoops and cross-ties, is required to satisfy Eqn. 2.11(a) and Eqn. 2.11(b). Eqn. 2.11(a) was applied to wall SBEs prior to the 1999 version of ACI 318. It has been reinstated in the 2014 edition due to concerns that Eqn. 2.11(b) by itself does not provide adequate transverse reinforcement for thin walls where concrete cover accounts for a significant portion of the wall thickness. For SBEs with rectangular cross-sections, A_g and A_{ch} in Eqn. 2.11(b) are defined as $A_g=l_{be}b$ and $A_{ch}=b_{c1}b_{c2}$ based on the dimensions shown in Figure 2-4 and Figure 2-5. Comparison of Eqns. 2.11(a) and (b) indicates that Eqn. 2.11(a) will govern for cases where A_g/A_{ch} >1.3.

$$\frac{A_{sh}}{sb_c} \geq \begin{cases} 0.3\left(\frac{A_g}{A_{ch}}-1\right)\frac{f'_c}{f_{yt}} & (a) \\ 0.09\frac{f'_c}{f_{yt}} & (b) \end{cases} \qquad 2.11$$

Where SBEs are not required, ordinary boundary element (OBE) detailing is required if the longitudinal reinforcement ratio at the wall boundary exceeds $400/f_y$. For OBEs, vertical spacing of transverse reinforcement (s) is limited to the smaller of 8 in. (203 mm) and $8d_b$ of the smallest primary flexural reinforcing bars. Within a distance equal to the greater of l_w and $M_u/4V_u$ above and below sections at which yielding is expected, vertical spacing is limited to the smaller 6 in. (152 mm) and $6d_b$. The vertical spacing requirements are intended to inhibit buckling of longitudinal reinforcement that may occur as the result of cyclic load reversals. Horizontal spacing of transverse reinforcement (h_x) is limited to 14 in. (356 mm) if the boundary longitudinal reinforcement ratio exceeds $400/f_y$. Where rectilinear cross-ties are used, they are required to provide lateral support to longitudinal reinforcement with alternating 90°-135° seismic hooks engaging peripheral longitudinal reinforcing bars (Figure 2-5). Table 2-1 compares the SBE and OBE requirements of ACI 318-11 and ACI 318-14.

Wall web reinforcement ratios, ρ_l and ρ_t, are generally required to be greater than or equal to 0.0025 and comprised of two curtains of web reinforcement. The maximum allowable spacing of web longitudinal and transverse reinforcement is 18 in. (457 mm). Where SBEs are required, horizontal web reinforcement is required to be anchored in the confined core of the boundary element using standard hooks or heads, and web bars must extend to within 6 in. (152 mm) of the end of the wall (Figure 2-4).

Table 2-1: Boundary transverse reinforcement detailing – ACI 318-11 & ACI 318-14

Variable		**ACI 318-11**	**ACI 318-14**
Displacement-based design approach, SBE required if:		$c \ge \frac{l_w}{600(\delta_u / h_w)}$ where $\delta_u / h_w \ge 0.007$	$c \ge \frac{l_w}{600(1.5\delta_u / h_w)}$ where $\delta_u / h_w \ge 0.005$
l_{be}	SBE	$l_{be} \ge \begin{cases} c - 0.1l_w \\ c/2 \end{cases}$	$l_{be} \ge \begin{cases} c - 0.1l_w \\ c/2 \end{cases}$
	OBE		
b (provisions for SBEs only)	SBE	No requirement	$b \ge \frac{h_u}{16}$ $b \ge 12\ in.$ if $c / l_w \ge 3/8$
h_x	SBE	$h_x \le 14\ in.$	$h_x \le \begin{cases} 14\ in. \\ \frac{2}{3}b \end{cases}$
	OBE		$h_x \le 14\ in.$
s	SBE	$s \le \begin{cases} b/3 \\ 6d_b \\ 4" \le 4" + \left(\frac{14" - h_x}{3}\right) \le 6" \end{cases}$	$s \le \begin{cases} b/3 \\ 6d_b \\ 4" \le 4" + \left(\frac{14" - h_x}{3}\right) \le 6" \end{cases}$
	OBE	$s \le 8\ in.$	$s \le \begin{cases} 8\ in. \\ 8d_b \end{cases}$ $s \le \begin{cases} 6\ in. \\ 6d_b \end{cases}$ in yielding region
A_{sh} (provisions for SBEs only)	SBE	$\frac{A_{sh}}{sb_c} \ge 0.09 \frac{f'_c}{f_{yt}}$	$\frac{A_{sh}}{sb_c} \ge \begin{cases} 0.3\left(\frac{A_g}{A_{ch}} - 1\right)\frac{f'_c}{f_{yt}} \\ 0.09 \frac{f'_c}{f_{yt}} \end{cases}$

2.2 Research Leading up to Current U.S. Code Provisions

Design provisions for Special Structural Walls (ACI 318 designation) were first introduced into the 1971 version of ACI 318, and code changes ensued in ACI 318-77 and ACI 318-83 based primarily on research conducted at the Portland Cement Association (PCA) on isolated walls with various cross-sectional geometries and with boundaries designed with and without confinement (Cardenas, et al., 1973; Cardenas, et al., 1973; Oesterle, et al., 1976; Barda, et al., 1977; Oesterle, et al., 1979; Cardenas, et al., 1980; Corley, et al., 1981; Shiu, et al., 1981; Oesterle, et al., 1984). The stress-based approach for special boundary detailing of wall boundaries was introduced into ACI 318-83 (SA.5.3.1) based on this research (ACI Committee 318, 1983), and remains in ACI 318-14. ACI 318-83 requirements for determining the geometry of the confined boundary region were more stringent than those of ACI 318-14, requiring that the boundary element be designed to resist all factored overturning and axial load demands (i.e., $\phi P_n \geq P_u$); thus, the contribution of the web in resisting compression was neglected. The minimum quantity of transverse reinforcement (A_{sh}) and maximum hoop spacing (s) allowed by ACI 318-83 were based on provisions for columns of Special Moment Frames, and were also more stringent than ACI 318-14 requirements:

$$\frac{A_{sh}}{sb_c} \geq \begin{cases} 0.3\left(\dfrac{A_g}{A_{ch}} - 1\right)\dfrac{f'_c}{f_{yt}} \\ 0.12\dfrac{f'_c}{f_{yt}} \end{cases} \tag{2.12}$$

$$s \leq \begin{cases} b/4 \\ 4" \end{cases} \tag{2.13}$$

Requirements for the horizontal distribution of boundary transverse reinforcement were similar to the 2011 version of the code. The provisions of ACI 318-83 often resulted in barbell shape walls with boundary “columns”. This was considered economical because the boundary “columns” were required to resist all compression demands due to axial load and overturning, and a thinner web could be used to resist shear demands.

The 1985 earthquake in Chile (EERI, 1986) presented a good opportunity to assess design and construction practice for modern shear wall buildings. Research following the earthquake (Wood, et al., 1987; Wallace, et al., 1992) indicated that approximately 400 modern reinforced concrete buildings were subjected to strong ground shaking with little or no apparent damage. The buildings ranged between 5 and 23 stories in height and most of them contained structural walls. It was reported that the Chilean code-prescribed lateral seismic forces were similar to those used in the highest seismic risk regions in the United States; however, the Chilean code did not require confinement at wall boundaries and construction inspection was less stringent than U.S. standards. Good performance of the shear wall buildings was attributed to the large stiffness of the buildings due to the large ratio of wall area to floor plan area (A_w/A_f). Wallace and Moehle (1992) pointed out that U.S. seismic design codes in place at the time (e.g., the Uniform Building Code) would have classified the predominant form of concrete construction in the affected region as bearing wall construction and that bearing wall buildings could rarely be constructed economically in the U.S. because U.S. design codes prescribed larger design lateral seismic forces for bearing wall systems than for ductile moment-resisting frames and dual systems. The 1985 earthquake demonstrated that the type of bearing wall construction used in Chile could be an economical choice. Wallace and Moehle demonstrated that U.S. code requirements were overly conservative for the design of slender walls in the majority of structural wall buildings, and that more economical designs could be achieved using a displacement-based approach (Wallace, et al., 1992; Wallace, 1994). The displacement-based approach was introduced into the 1999 version of ACI

318 (Wallace, et al., 2002) with validating support from a number of tests on isolated walls (Thomsen, et al., 1995; Thomsen, et al., 2004; Paulay, et al., 1985; Wood, et al., 1996).

2.3 Observed Damage to Shear Walls in Recent Earthquakes

The February 27, 2010 earthquake in Chile (EERI, 2010) affected the most densely populated region in the country and caused damage to a large number of mid-rise and high-rise buildings. Massone et al. (2012) reported that 1,939 construction permits were issued between 1985 and 2009 for reinforced concrete buildings with nine or more stories, most of which were shear wall buildings. Damage occurred primarily in these newer buildings, of which approximately 40 were severely damaged requiring repair or, in rare cases, demolition. A comparison of typical construction practice in the region prior to and following the 1985 earthquake (Massone, et al., 2012; Wallace, et al., 2012) revealed that shear wall buildings constructed after 1985 tend to be taller with thinner walls. Whereas pre-1985 buildings are typically less than 15 stories with 20-30 cm (8-12 in.) thick walls, buildings constructed after 1985 are typically 15 to 20 stories with 15-20 cm (6-8 in.) thick walls. While the ratio of wall area to floor plan area (A_w/A_f), for which good performance of shear wall buildings was attributed in the 1985 earthquake, has remained relatively consistent, the ratio of wall area to seismic weight (A_w/W) for newer buildings is smaller because of the increase in typical building height. Furthermore, walls in modern buildings in Chile are often adjoined in transverse directions along a central corridor of the building, resulting in complex shapes (e.g., T-shape, L-shape) for which large tensile and compression strain demands may occur. The combination of these factors indicates that modern buildings are likely to be designed for larger drift demands, and larger axial stress and strain demands than typical designs of previous decades. It is likely that a good number of these buildings were designed according to NCh433.Of96 (Instituto Nacional de Normalización (INN), 1996), which was adopted in 1996.

The analysis approaches allowed by NCh433.Of96 are similar to those of ASCE 7-10, including an equivalent static procedure (similar to ASCE 7-10 ELF procedure) and modal response spectrum analysis. NCh433.Of96 references ACI 318-95 provisions for the design of shear walls; however, based on the good performance of shear wall buildings in the 1985 earthquake, the requirement for confinement at wall boundaries was excluded.

Observed damage to shear walls in Santiago, Viña del Mar, and Concepción (Figure 2-6) following the 2010 earthquake (Figure 2-6) generally included crushing and spalling of concrete, buckling of vertical reinforcement, and lateral (out-of-plane) buckling of wall compression zones (Wallace, et al., 2012). Damage typically occurred near the base of walls over a very short height, often extending along the full length of the wall. Large spacing of transverse reinforcement and opening of 90^{o} hooks was observed at the boundaries of damaged walls. Wallace et al. (2012) pointed out that prior to the 2010 earthquake, lateral instability failures had primarily been observed only in laboratory tests. Also, the damage patterns observed in the field suggested that lateral instabilities were not likely driven by prior tensile yielding of reinforcement as studied by previous research (Paulay, et al., 1993; Chai, et al., 1999); rather, the instabilities appeared to occur following, or as the result of, crushing of the thin compression zone.

To address issues with compression failure and high axial load ratio in thin walls, a compression strain limit of 0.008, with a corresponding gage length equal to one-half the length of the wall (i.e., $l_p=l_w/2$), has been enforced in the Chilean reinforced concrete standard, DS No. 60 (MINVU, 2011). The strain limit has been implemented in a displacement-based design format, similar to Eqns. 2.4 and 2.6. DS No. 60 estimates roof drift as plastic rotation about the base of the wall (i.e., $\delta_u/h_w \approx \theta_p$), and elastic curvature may either be included (DS No. 60 Eqn. 21-7b), in keeping with Eqn. 2.4, or neglected (DS No. 60 Eqn. 21-7a), as is the case for Eqn. 2.6.

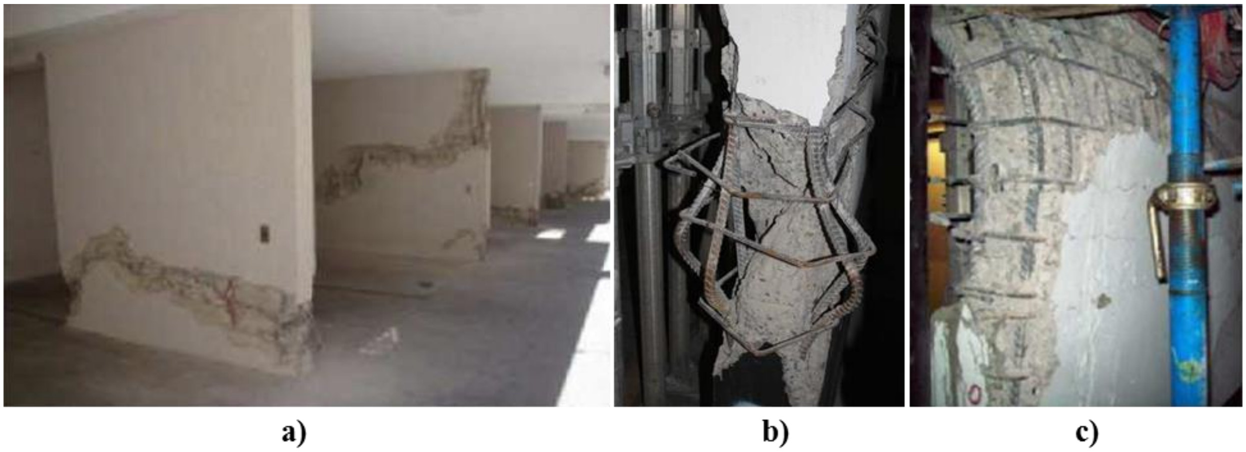

Figure 2-6: Observed damage to shear walls in Chile: a) Concrete crushing, b) Rebar buckling, and c) Lateral (out-of-plane) instability, Images: Wallace et al. (2012)

The February 22, 2011 earthquake in New Zealand (EERI, 2011) was centered just outside of Christchurch, the second largest city in the nation, causing strong ground shaking in Christchurch's Central Business District (CBD). Kam et al. (2011) presented metrics of the building stock in the CBD, indicating that 175 buildings between 5 and 22 stories in height were in place at the time of the earthquake. Of these, 25% were shear wall buildings. While reinforced concrete buildings were generally considered to have performed well, significant damage to many modern shear wall buildings suggested issues related to complex wall shapes, lack of confinement in wall webs outside of confined boundary regions, low vertical reinforcement ratios, and splices in plastic hinge regions. General observations indicated that modern walls tend to be thin, designed with low vertical (axial) reinforcement ratios, and likely designed for larger axial stress demands than older walls. Damage to modern shear walls included crushing and spalling of concrete, lateral (out-of-plane) buckling of wall webs, and buckling and fracture of vertical reinforcement (Kam, et al., 2011; Elwood, 2013).

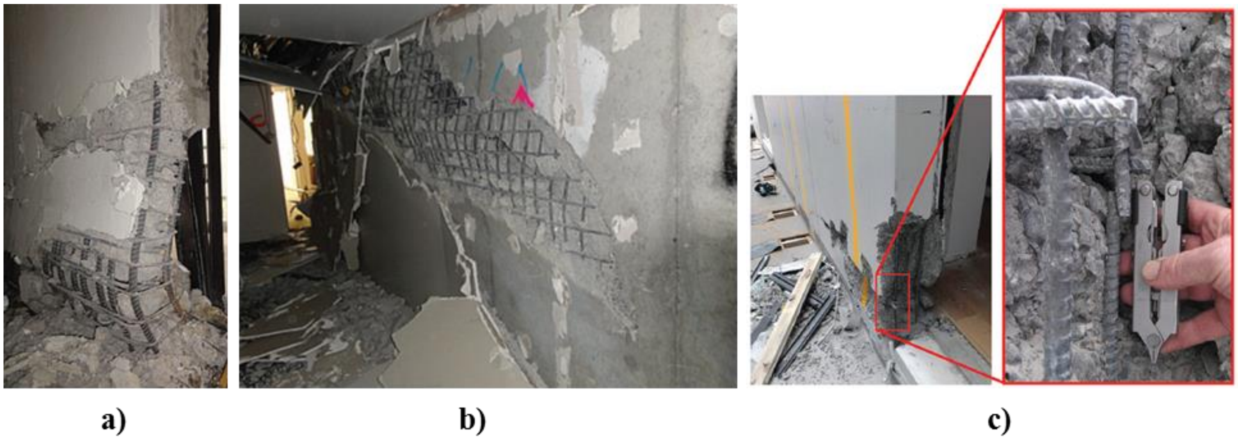

Figure 2-7: Observed damage to shear walls in Christchurch: a) Lateral (out-of-plane) instability, b) Web crushing, and c) Reinforcement fracture, Images: Elwood et al. (2013)

2.4 Tests on Well-Detailed Slender Walls

Numerous tests conducted on isolated walls are available in scientific literature; however, due to laboratory constraints, a large majority of these tests were conducted at relatively small scale (e.g., 1/4 to 1/3), and very few test specimens have geometry, reinforcement arrangement, and applied loading representative of modern design and construction practice for slender walls. A good number of experiments were conducted on walls with barbell-shape cross-sections, and many of the tests have been conducted with little or no axial load, relatively low vertical boundary reinforcing ratios, and boundary detailing that either does not represent typical design and construction practice (e.g., boundaries with a square hoop enclosing only four primary vertical reinforcing bars) or does not satisfy current ACI 318 confinement provisions. As a result, the demands at boundaries of these walls may not be representative of modern, ductile walls. A select number of tests are presented here with a focus primarily on walls with rectangular or T-shape cross-sections.

2.4.1 PCA: Oesterle et al. (1976 and 1979) and Shiu et al. (1981)

Oesterle et al. (1976; 1979) summarized the results of 16 tests on isolated walls with various cross-sectional shapes (rectangular, barbell, and flanged) and varying boundary detailing. All test specimens were 75 in. (1905 mm) long and 15 ft. (4572 mm) tall with a 4 in. (102 mm) thick web (Figure 2-8). Design steel reinforcement yield strength (f_y) was 60 ksi (414 MPa) for all specimens, and design nominal concrete compressive strength (f'_c) was 6 ksi (41.4 MPa) for all but one of wall.

The experimental test setup for the first phase of testing is shown in Figure 2-9. Lateral load was applied at the top of the specimens. For the two rectangular shaped specimens, designated R1 and R2, no axial load was applied. The boundary regions of R1 and R2 extended 10% of the length of the wall ($0.10l_w$) from wall edges. For specimen R1, the quantity of boundary vertical and transverse reinforcement was relatively low (Figure 2-8b), consisting of four No. 3 vertical reinforcing bars and a 0.20 in (5 mm) diameter hoop spaced at 4 in. (102 mm, s/d_b=10.7) up the height of the wall. For specimen R2 (Figure 2-8c), boundary reinforcement consisted of six No. 4 vertical bars up the height of the wall. Boundary transverse reinforcement consisted of a 6 mm (0.24 in) diameter hoop and cross-tie spaced at 1.33 in. (33.9 mm, s/d_b=2.7) in the lower 6 ft. (1829 mm) of the wall (i.e., plastic hinge region) and a 0.20 in (5 mm) diameter hoop spaced at 4 in. (102 mm, s/d_b=10.7) in the top 9 ft. (2743 mm) of the wall. For design material properties, the compression depth for specimens R1 and R2, for an extreme fiber compression strain of 0.003, is $0.05l_w$ and $0.10l_w$, respectively. As such, special boundary transverse detailing would be required by the displacement-based approach of ACI 318-14 for a design roof drift ratio of 2.4% for specimen R1 and 1.8% for specimen R2. Specimen R2 contained approximately 94% of the boundary transverse reinforcement that would be required by ACI 318-14 for a special boundary element, and satisfied ACI 318-14 hoop spacing requirements. Specimen R1, on the other hand, had large hoop spacing (s/d_b=10.7) that would not satisfy ACI 318-14 provisions for an ordinary boundary element.

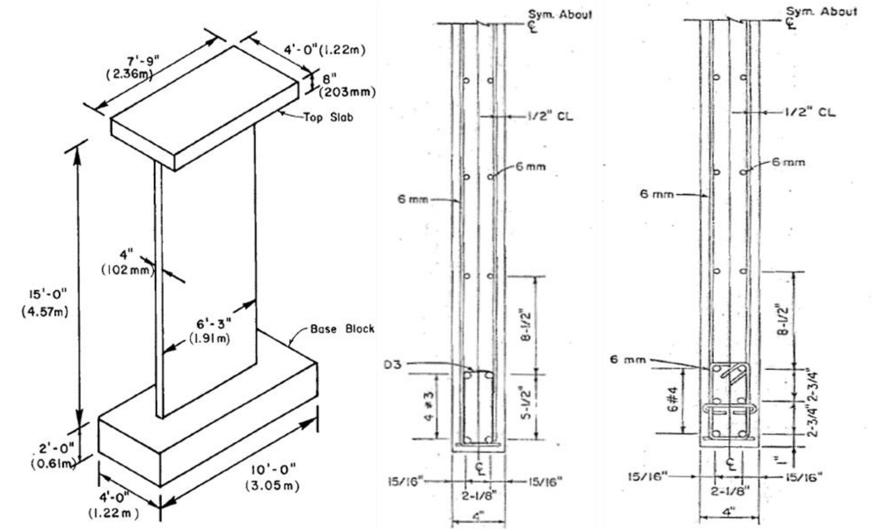

a) b) c)

Figure 2-8: Oesterle et al. (1976) rectangular walls – a) Specimens dimensions, b) Specimen R1 cross-section, and c) Specimen R2 cross-section

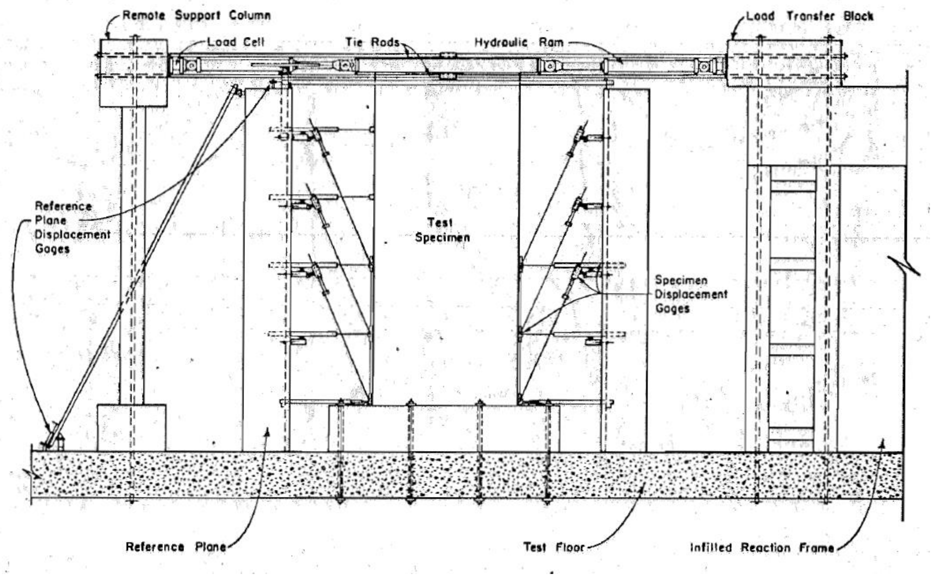

Figure 2-9: Oesterle et al. (1976) experimental test setup

The experimentally measured applied lateral load vs. lateral drift at the top of the walls (i.e., at a height of 15 ft. [4572 mm] above the base of the wall) are presented in Figure 2-10 and Figure 2-11. For specimen R1, initial strength loss occurred at approximately 1.67% drift due to buckling of vertical reinforcement at the wall edge. Reversal of the load resulted in tension fracture of the previously buckled bars at approximately 2.22% drift. It was reported that the wall was able to carry 80% of its peak capacity for 3 consecutive cycles up to 1.67% drift levels. For specimen R2, a small out-of-plane instability of the compression zone was first observed while loading to 1.67% rotation. During cycles to drift levels of 2.22%, a 3 in. (76.2 mm) out-of-plane displacement was measured approximately 42 in. (1067 mm) above the base of the wall. Supplemental lateral bracing was applied to simulate the presence of a floor slab; however, fracture of vertical reinforcement, additional lateral deformations, and crushing of concrete resulted in strength loss in the following cycles. It was reported that the wall was able to carry 80% of its peak capacity for 3 consecutive cycles up to 2.22% drift levels.

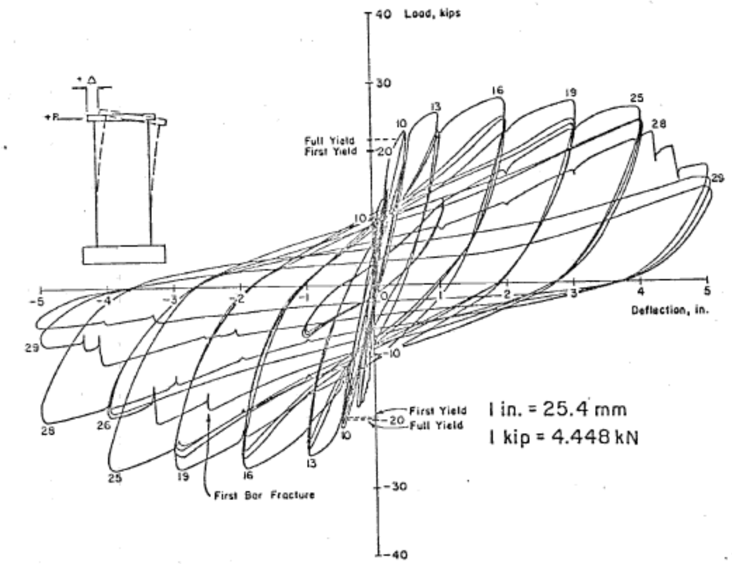

Figure 2-10: Specimen R1 lateral load vs. drift at top of wall

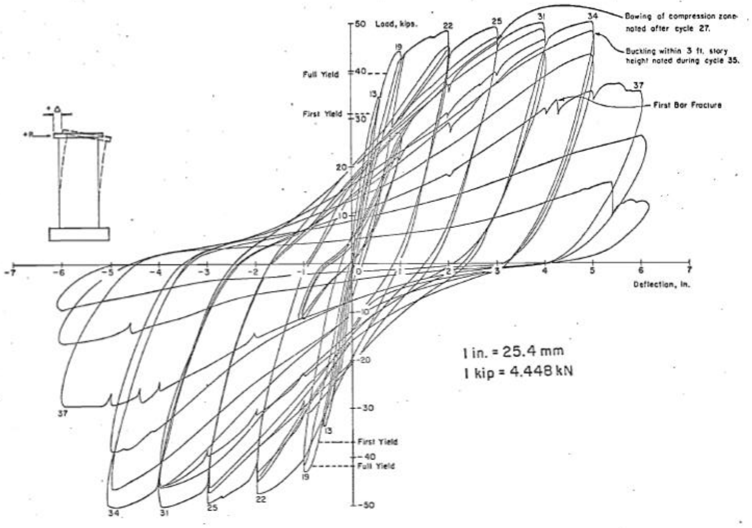

Figure 2-11: Specimen R2 lateral load vs. drift at top of wall

Shiu et al. (1981) conducted two tests to explore the impact of openings in structural walls. One wall, designated, CI-1, did not contain any openings while the other wall, designated PW-1, contained openings with coupling beams at each story height. The cross-sectional dimensions of specimen CI-1 (Figure 2-12b) were the same as specimens those of Oesterle et al. (1976) R1 and R2; however, the wall was 18 ft. (5486 mm) in height and included 2.5 in. (63.5 mm) thick slabs at each story (Figure 2-12a). Design material properties were f_y=60 ksi (414 MPa) and f'_c=3 ksi (20.7 MPa).

Similar to specimens R1 and R2, lateral loads were applied at the top of the specimens and no axial load was applied. Boundary regions extended $0.17l_w$ from each end of the walls. Boundary reinforcement for specimen CI-1 (Figure 2-12b) consisted of twelve No. 4 vertical bars enclosed by a 0.20 in (5 mm) diameter hoop. Hoops were spaced at 1.33 in. (33.9 mm, s/d_b=2.7) in the lower 6 ft. (1829 mm) of the wall and at 4 in. (102 mm, s/d_b=10.7) in the top 12 ft. (3657 mm) of the wall. For design material properties, the compression depth for an extreme fiber compression strain of 0.003, is 10.1 in. ($0.14l_w$ [258 mm]). For this compression depth, special boundary transverse detailing would be required by ACI 318-14 displacement-based approach for a design roof drift ratio of 0.8%. Specimen CI-1 contained approximately 85% of the boundary transverse reinforcement that would be required by ACI 318-14 for a special boundary element and satisfied ACI 318-14 hoop spacing requirements; although, ACI 318-14 would require supplemental cross-ties to support every other vertical bar.

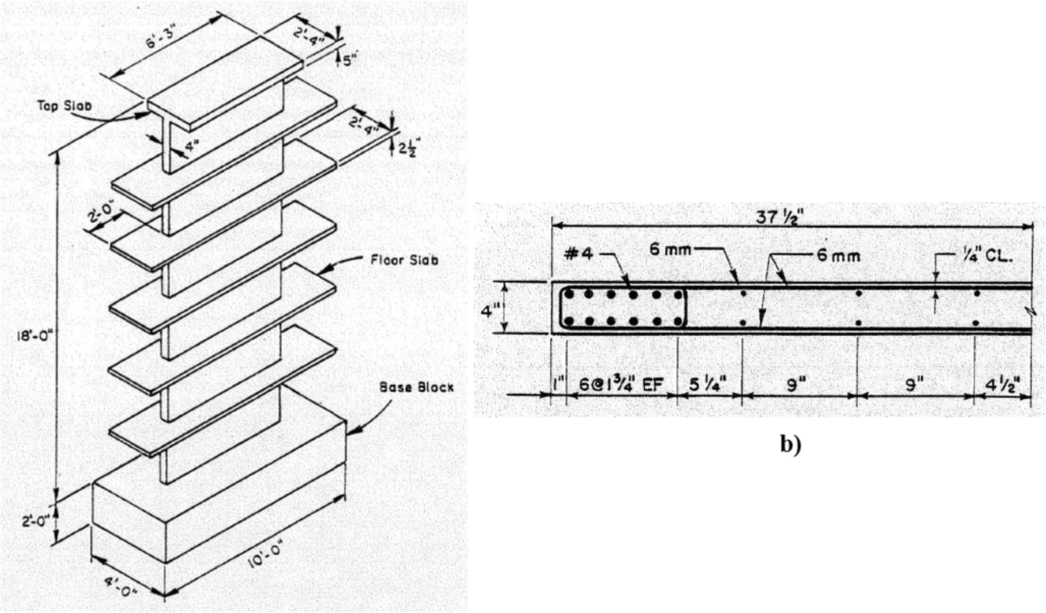

b)

a)

Figure 2-12: Shiu et al. (1981) specimen CI-1 – a) Overall geometry, and b) Cross-section

The experimentally measured applied lateral load vs. lateral drift at the top of the wall (i.e., at a height of 18 ft. [5486 mm] above the base of the wall) is presented in Figure 2-13. Strength loss for specimen CI-1 occurred due to degradation of the shear resisting mechanism during cycles to 2.78% drift ratio. The failure mechanism was reported as shear sliding along a wide horizontal crack that formed at mid-height of the first story. As sliding occurred, shear resistance was provided primarily by dowel action of boundary vertical reinforcement.

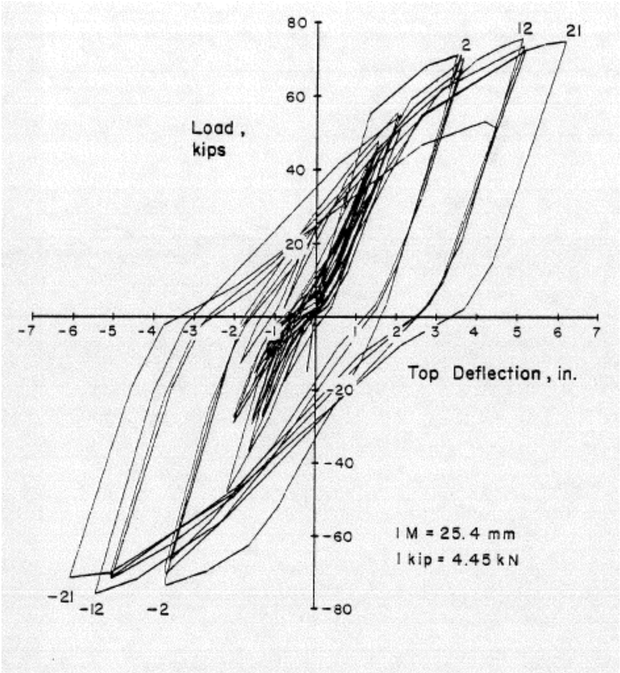

Figure 2-13: Specimen CI-1 lateral load vs. drift at top of wall

2.4.2 Paulay and Goodsir (1985)

Paulay and Goodsir (Paulay, et al., 1985; Goodsir, 1985) conducted tests on four walls, three of which had a rectangular cross-section and one that had a T-shape cross-section. The experimental test setup is shown in Figure 2-14a. The primary objectives of the tests were to examine New Zealand seismic design code provisions for wall slenderness and confinement. Axial load for all four tests was applied eccentrically, resulting in strong axis (in-plane) bending due to the applied axial load. The resulting distribution of moment up the height of the wall, due to the applied lateral and axial loading, was, therefore, dependent on the direction of loading as shown in Figure 2-14b. The applied axial load was also direction dependent. For negative loading, a small axial load, approximately equal to $0.05A_{cv}f'_c$, was applied. In the negative loading direction, an axial load between approximately $0.15A_{cv}f'_c$ and $0.30A_{cv}f'_c$ was applied. This scheme of applied axial load and moment was chosen to impose large cyclic tension/compression strain reversals at the east boundaries of the walls such that failure modes due to out-of-plane instability and boundary/web crushing could be studied. Design material properties were f_y=55.1 ksi (380 MPa) and f'_c=3.6 ksi (25 MPa).

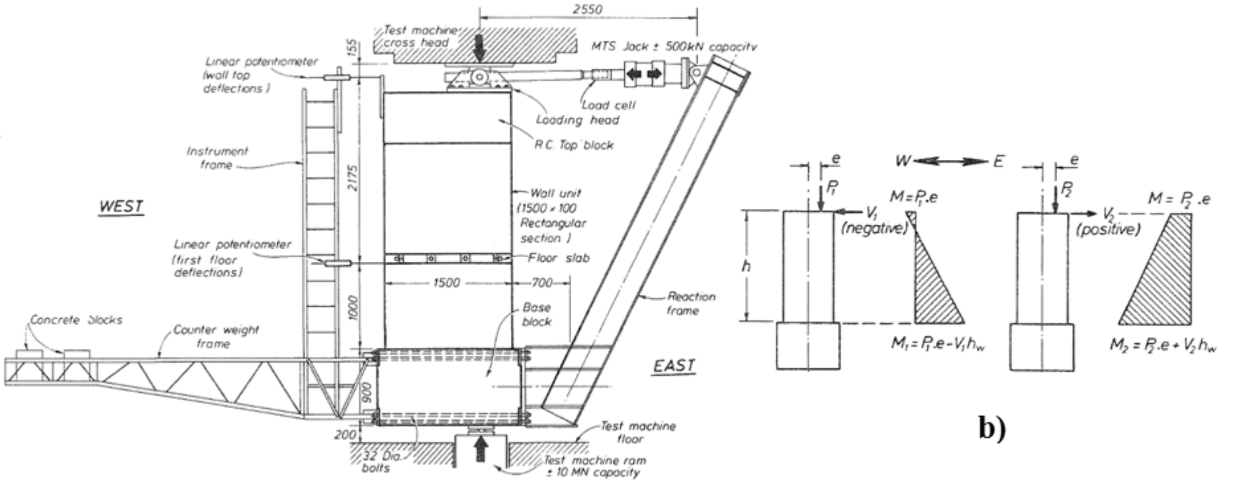

a) b)

Figure 2-14: Paulay and Goodsir (1985) – a) Experimental test setup, and b) Loading pattern

An elevation view of a typical rectangular specimen (Wall 1) is show in Figure 2-15a, and cross-sectional dimensions and reinforcement details for Wall 1 and Wall 3 (T-shape) are shown in Figure 2-15b and Figure 2-15c, respectively. All four walls were 94.5 in. (2400 mm) in height with a 3.9 in. (100 mm) thick web. The three rectangular walls (designated Wall 1, Wall 2, and Wall 4) were 59.1 in. (1500 mm) long, and the T-shape wall was 51.2 long with a 27.6 in (700 mm) wide flange. A 3.9 in. (100 mm) thick slab was constructed at the second story of each specimen. Wall 1, Wall 2, and Wall 3 each had a first story unsupported height of 39.4 in. (1000 mm; h_w/b=10), and Wall 4 had a shorter unsupported height (31.5 in. [800 mm]; h_w/b=8).

For Wall 1 and Wall 4, the confined boundary regions extended $0.22l_w$ from the east edge of the wall and $0.16l_w$ from the west edge of the wall. For Wall 2, the east and west boundaries were both the same as the west boundary of Wall 1. Design axial load for Wall 1 was $0.30A_{cv}f'_c$ and $0.05A_{cv}f'_c$

for loading in the positive and negative loading directions, respectively. Based on observations of Wall 1, the target axial load for the other walls was reduced to $0.15A_{cv}f'_c$ in the positive loading direction. For nominal material properties under the design axial load, the compression depth for loading causing compression at the east boundary (i.e., positive loading) is $0.39l_w$ for Wall 1, $0.24l_w$ for Wall 2 and Wall 4, and $0.30l_w$ for Wall 3. According to the displacement-based approach of ACI 318-14, this range of compression depths would dictate the need for special boundary detailing. In general, the four walls either satisfied or nearly satisfied ACI 318-14 requirements for the quantity (i.e., cross-sectional area) of boundary transverse reinforcement, confined length, and vertical and horizontal spacing of boundary transverse reinforcement (s, s/d_b and h_x). It is worth mentioning that the transverse reinforcement detail used at the boundaries of the walls, shown in Figure 2-16, utilizes overlapping hoops supporting all vertical bars at hoop corners. ACI 318-14 allows details utilizing an outer hoop with 90°-135° cross-tie hooks laterally supporting every other vertical bar. Previous research (Moehle, et al., 1985; Mander, et al., 1988) suggests that hoop and cross-ties configurations provide confinement and bar buckling inhibiting capabilities nearly as effective hoop configurations, although these tests were either conducted on square columns (Moehle, et al., 1985) or included cross-ties with 180° hooks engaging every vertical bar (Mander, et al., 1988).

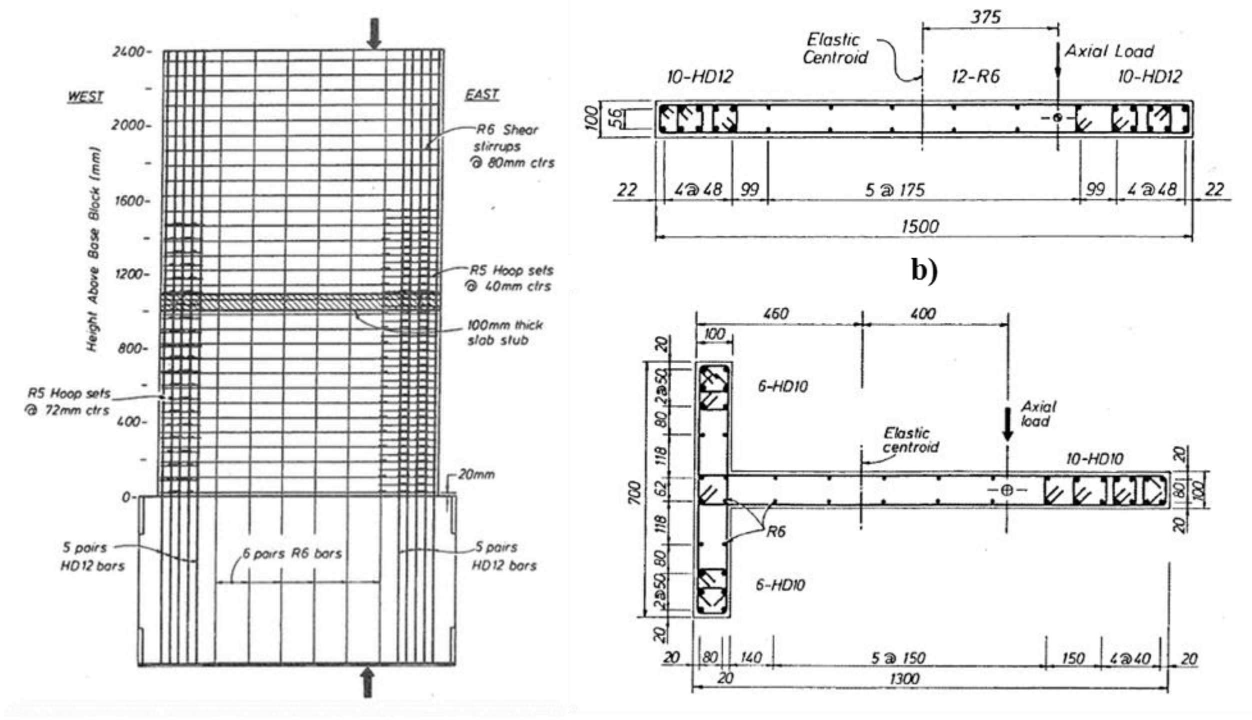

a)

c)

Figure 2-15: Paulay & Goodsir (1985) specimen dimensions and reinforcement – a) Elevation view, b) Rectangular walls, and c) T-shape Wall (Wall 3)

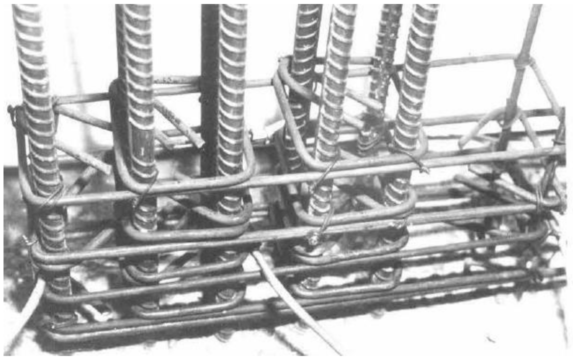

Figure 2-16: Paulay & Goodsir (1985) overlapping hoop detail

For Wall 1, strength loss occurred due to crushing of the compression region. It was reported that the failure appeared to initiate in the unconfined web portion of the wall. Axial compression strains of 0.011 were measured in this region in the previous cycle. The failure occurred following one successful excursion to approximately 2% lateral drift ratio. Photos of the wall at the end of the test are provided in Figure 2-18. The damaged region extended well into the web, causing crushing over approximately 75% of the length of the wall (Figure 2-18b). Of particular interest is the height over which damage appears to have spread at the confined edge of the wall. At the east edge, crushing and spalling of concrete extends vertically approximately half the height of the first story, which is significantly higher than field observations in Chile.

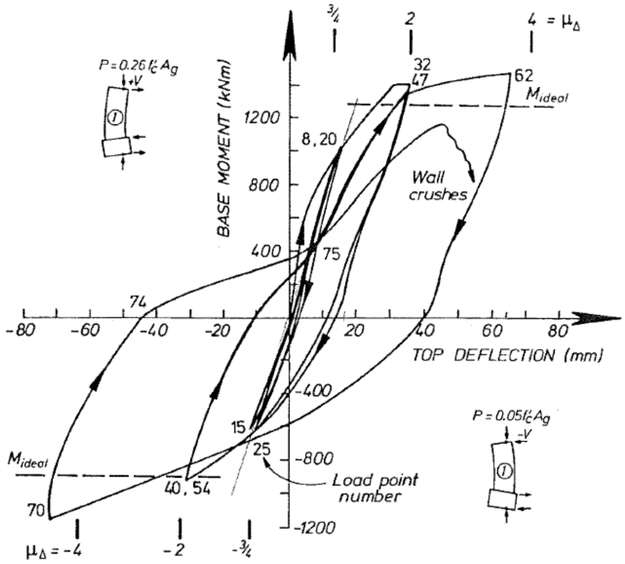

Figure 2-17: Wall 1 base moment vs. drift at top of wall

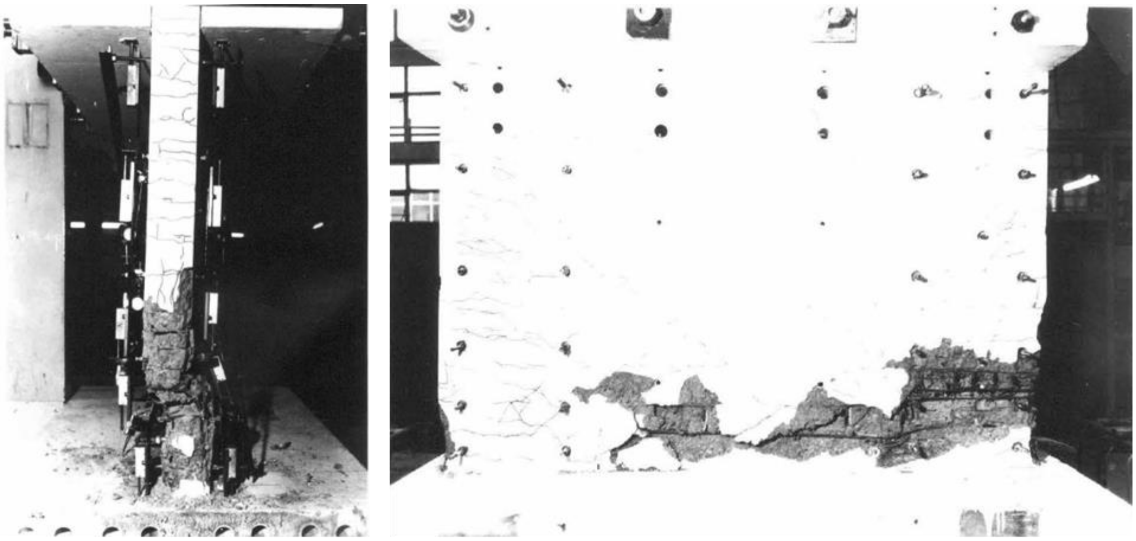

a) **b)**

Figure 2-18: Wall 1 damage at end of test – a) East boundary and b) South face

Strength loss for Wall 2 occurred following two complete cycles to approximately 2.4% drift ratio (Figure 2-19a). Failure occurred at a small positive load due to lateral (out-of-plane) buckling of the east edge of the wall (Figure 2-19b).

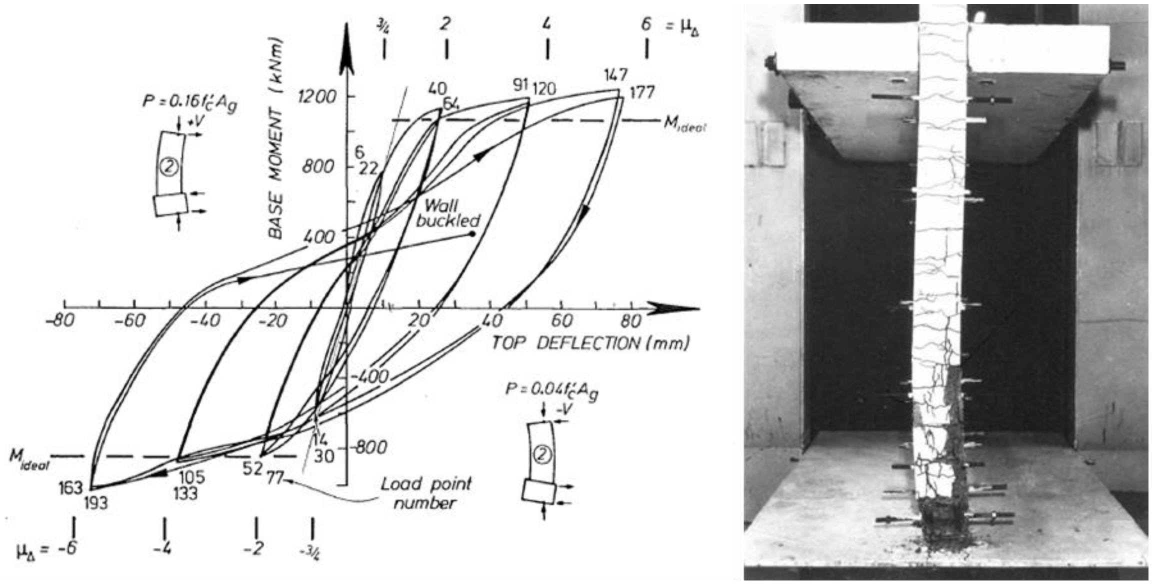

a) **b)**

Figure 2-19: Wall 2 – a) Base moment vs. drift at top of wall, and b) Buckling of wall

A similar failure mode was observed for Wall 3 and Wall 4, combining aspects of the failures observed in Wall 1 and Wall 2. For Wall 3, while attempting a second loading cycle to a target drift ratio of approximately 3.3% (Figure 2-20), the east boundary began to displace out-of-plane; however, lateral displacements appeared to decrease after which a brittle crushing failure was observed (Figure 2-21). Similar to Wall 1, it was reported that crushing likely initiated in the unconfined web region of the wall where a compression strain of 0.024 was recorded prior to the failure. Failure occurred for Wall 4 following one successful cycle to approximately 3% lateral drift ratio. Just before the failure occurred, axial compression strains of 0.026 and 0.036 were measured in the unconfined web and confined boundary, respectively.

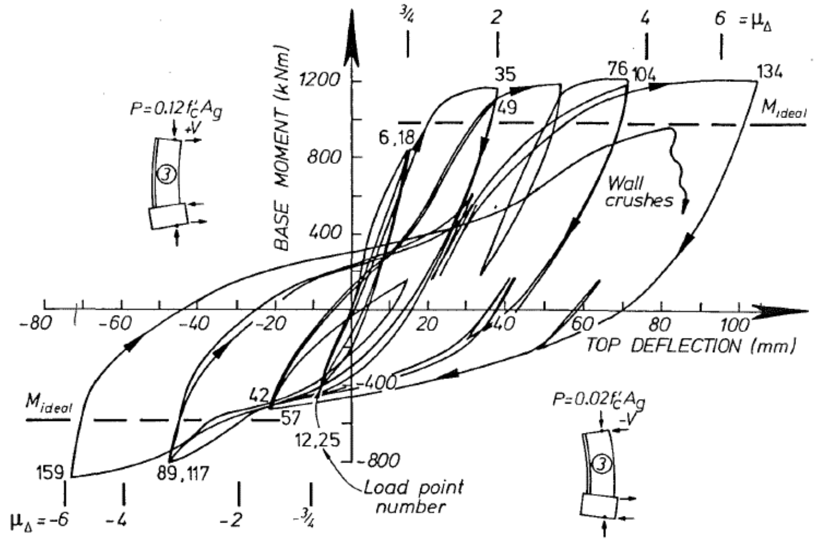

Figure 2-20: Wall 3 base moment vs. drift at top of wall

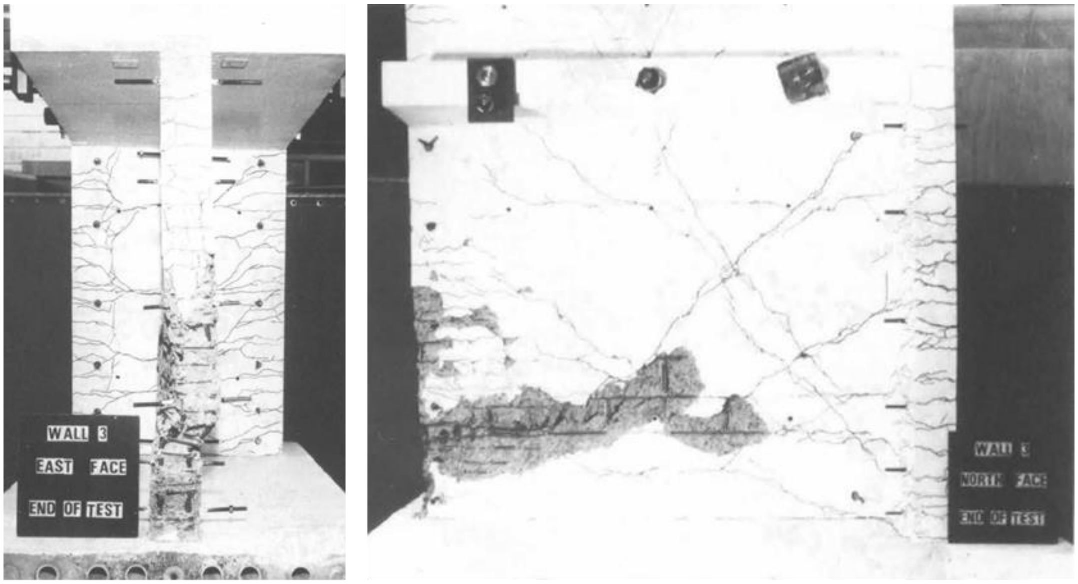

a) **b)**

Figure 2-21: Wall 3 damage – a) Out-of-plane deformation at east boundary, and b) Web crushing

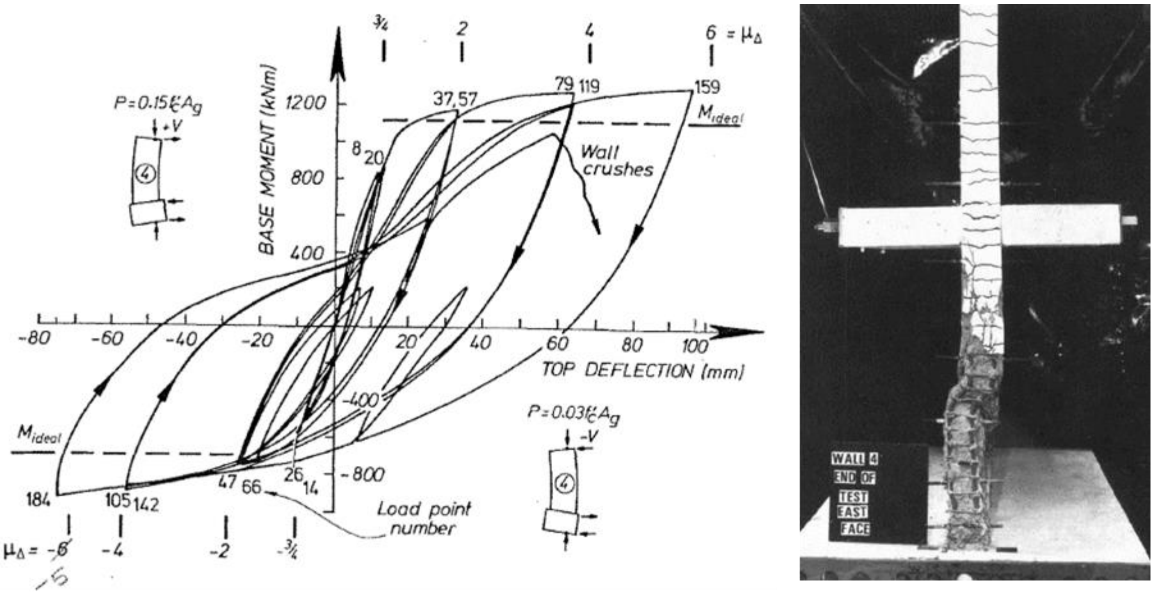

a) b)

Figure 2-22: Wall 4 – a) Base moment vs. drift at top of wall, and b) Damage at east boundary

2.4.3 Thomsen and Wallace (1995, 2004)

Thomsen and Wallace (1995; 2004) conducted tests on two rectangular walls and two T-shape walls, primarily as validation for displacement-based design methodologies. The overall geometry of the walls and experimental test setup are shown in Figure 2-23. All four walls were 12 ft. (3658 mm) tall and 4 ft. (1219 mm) long with a 4 in. (102 mm) thick web. The T-shape walls included a 4 ft. (1219 mm) long and 4 in. (102 mm) thick flange. Lateral loads were applied at the top of the walls by a single actuator, and hydraulic jacks mounted above the walls applied axial load. Design material properties were f_y=60 ksi (414 MPa) and f'_c=4 ksi (27.4 MPa). For all tests, an axial load equal to $0.10A_{cv}f'_c$ was applied.

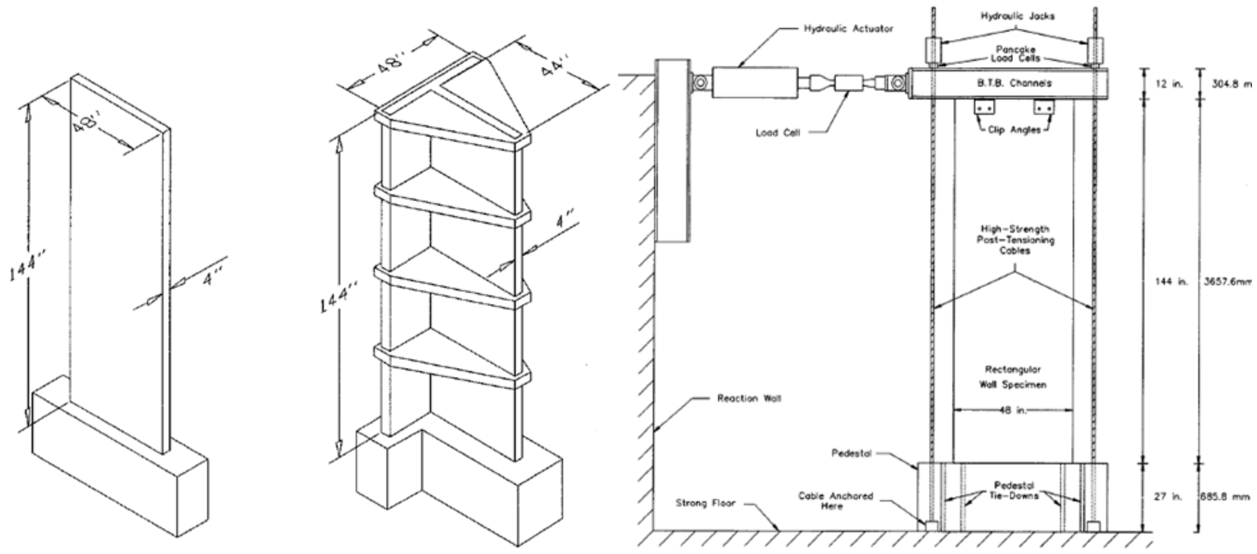

a) **b)**

Figure 2-23: Thomsen and Wallace (1995) – a) Overall geometry, and b) Test setup

Cross-sectional dimensions and reinforcement details for the test specimens are shown in Figure 2-24 and Figure 2-25. Confinement details for specimens RW1, RW2, and TW1 consisted of outer hoops either with or without supplemental cross-ties. For specimen TW2, transverse reinforcement at the web boundary consisted of overlapping hoops and one cross-tie. The confined boundaries at the edges of the rectangular walls and at the web boundary of TW1 extended $0.16l_w$ from wall edges. The confined region at the web boundary of specimen TW2 was longer, extending $0.36l_w$ from the edge of the wall. For nominal material properties under the design axial load, the compression depth is $0.20l_w$ for the rectangular walls and $0.45l_w$ for loading causing compression at the web boundary of the T-shape walls. According to the displacement-based approach of ACI 318-14, special boundary detailing would always be required for the T-walls and would be required for the rectangular walls for a design roof drift ratio greater than or equal to 0.54%.

In general, boundary transverse reinforcement details for the four walls did not satisfy ACI 318-14 provisions. Specimen TW2 contained approximately 92% of the boundary transverse reinforcement required by ACI 318-14, and vertical spacing of boundary transverse reinforcement

($s/d_b=4.0$) was code-compliant. Specimens RW1 and TW1 contained approximately 74% of the confinement area required by ACI 318-14; however, spacing of hoops exceeded code requirements ($s/d_b=8.0>6.0$) and the length of the confined region at the web boundary of TW1 was intentionally designed shorter than required by code. Specimen RW2 satisfied vertical spacing requirements, but horizontal spacing requirements were not satisfied ($h_x=1.5b>2/3b$) and the requirement for cross-ties on every other vertical bar was not met.

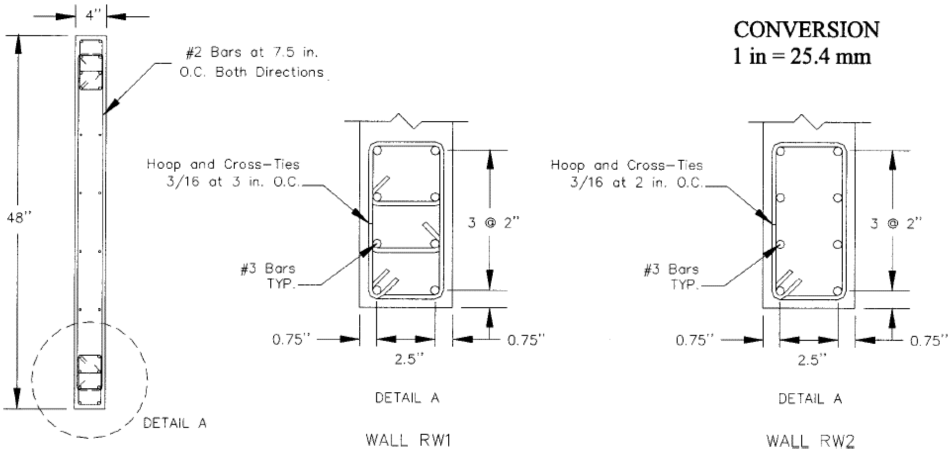

Figure 2-24: Cross-section details of rectangular walls (RW1 and RW2)

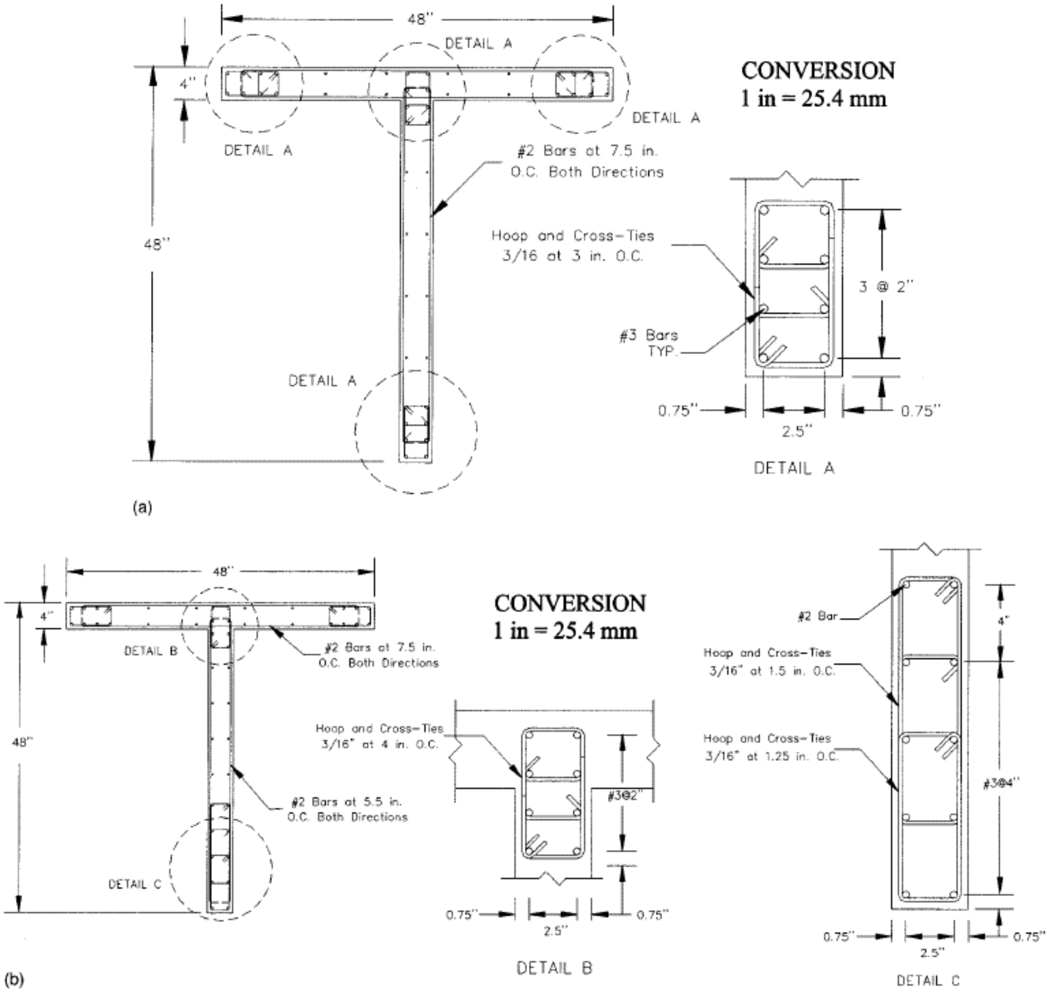

Figure 2-25: Cross-section details of T-shape walls (TW1 and TW2)

Experimentally measured lateral load vs. lateral drift results are presented in Figure 2-26. For specimen RW1, buckling of the outermost boundary vertical bars at each end of the wall occurred during the first cycle to 2% drift ratio. Strength loss occurred due to buckling of vertical reinforcement at approximately 2.5% drift (Figure 2-26a) while attempting to load to 3% drift the first time. For specimen RW2, buckling of vertical reinforcement at the walls edges was observed during the first cycle to 2.5% drift. During the second cycle to 2.5% drift, minor crushing of the boundary occurred with a small drop in strength. The test was terminated after the second 2.5% drift cycle (Figure 2-26b) because of excessive damage to the boundary (Figure 2-27a).

For specimen TW1, strength loss occurred suddenly due to crushing of the boundary and web at approximately 1.25% drift ratio (Figure 2-26c). For specimen TW2, crushing and spalling of cover concrete on the front and rear faces of the wall, at the web boundary, occurred during cycles to 1.5% and 2% drift with little visible distress to the confined region. Minor strength loss occurred due to minor crushing of the confined web boundary during both cycles to 2.5%. During the first 3% drift cycle, failure occurred due to lateral (out-of-plane) instability of the web boundary (Figure 2-27b).

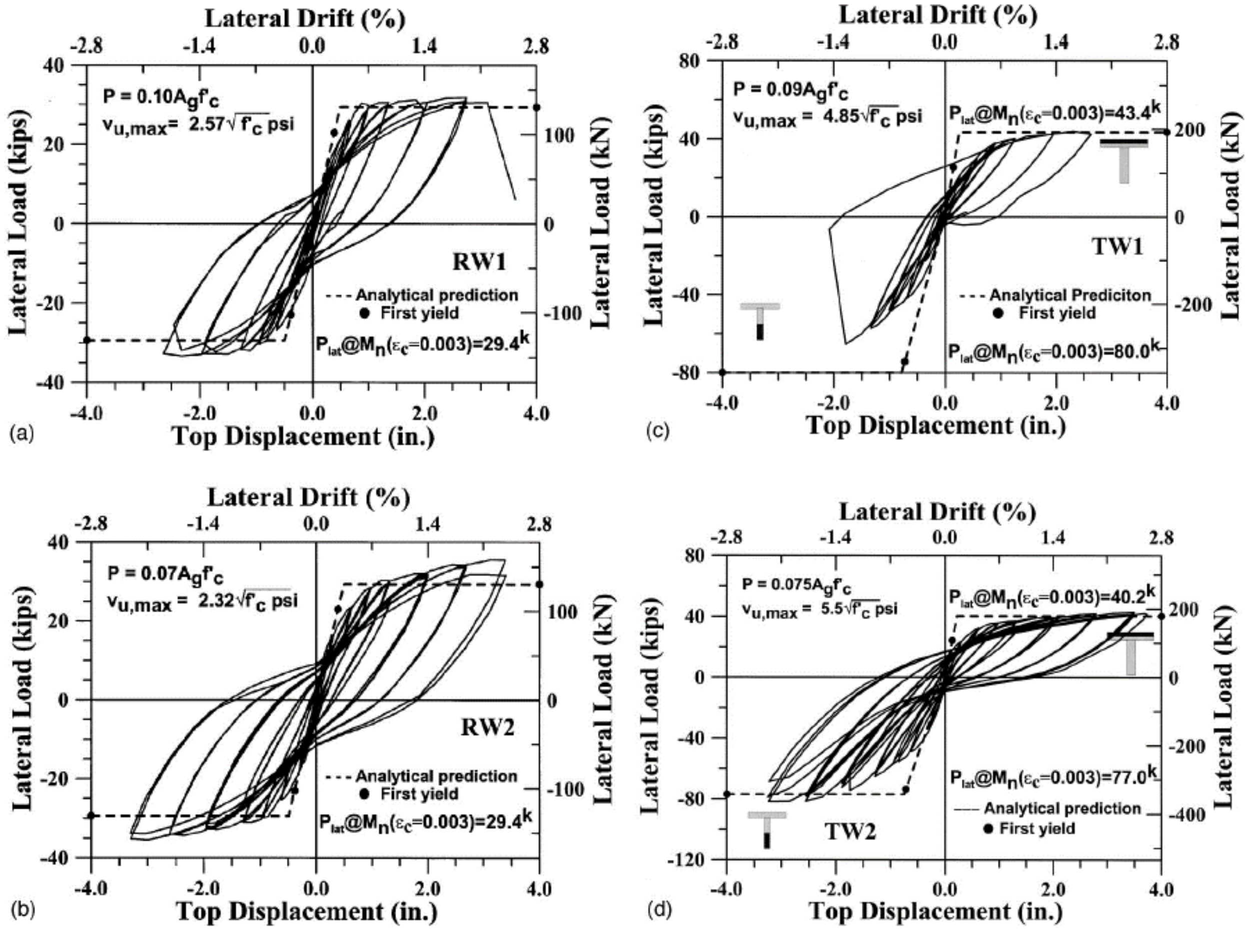

Figure 2-26: Lateral load vs. drift – a) RW1, b) RW2, c) TW1, and d) TW2

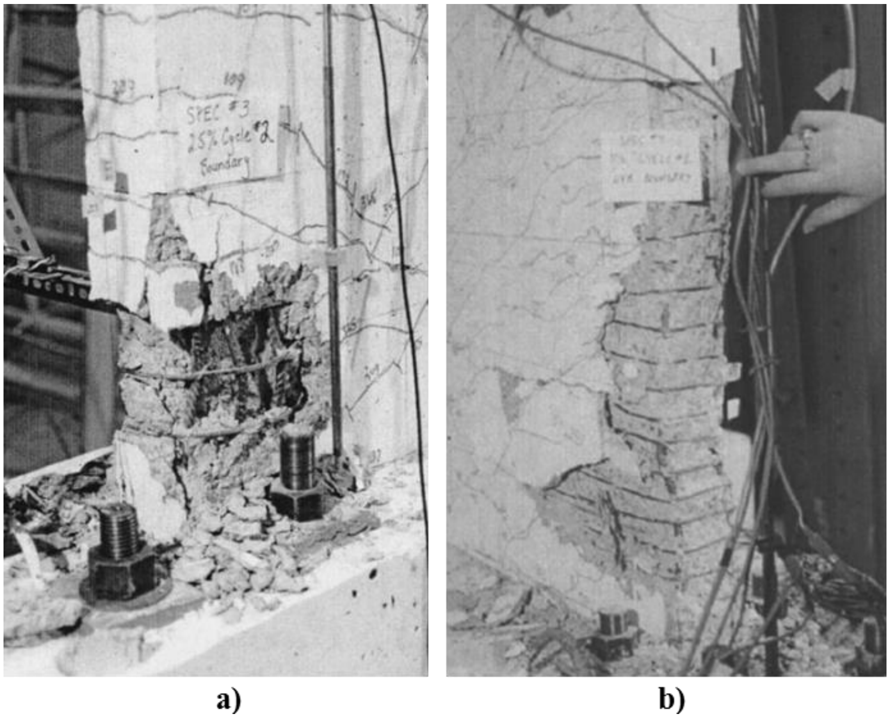

Figure 2-27: Thomsen and Wallace (1995) observations – a) Boundary crushing (RW2), and b) Lateral (out-of-plane) instability (TW2)

2.4.4 Johnson (2007), Aaleti et al. (2013)

Researchers at the University of Minnesota and Iowa State University (Johnson, 2007; Aaleti, et al., 2013) investigated the performance of walls with and without longitudinal reinforcement splices in the plastic hinge region of the wall. Three rectangular walls, with different splice details and with identical geometry and reinforcement, were tested. One of the walls had continuous longitudinal reinforcement with no splice (designated RWN), one wall used mechanical couplers to splice longitudinal bars (RWC), and the other wall had lap splices (RWS). Axial load was not applied for any of the tests. Design material properties were f_y=60 ksi (414 MPa) and f'_c=5 ksi (27.4 MPa).

Specimen geometry and reinforcement details are shown in Figure 2-28. All three walls were 90 in. (2286 mm) long, 6 in. (152 mm) thick, and 21 ft. (6401 mm) in height. Lateral loads were applied at the top of the walls. Out-of-plane movement was prevented at the top of the walls using an out-of-plane restraint system. Intermediate out-of-plane support was not provided. Longitudinal reinforcement was different at the two ends of the wall. At one end, a large quantity of reinforcement was used to simulate the large quantity of reinforcement present in the flange of a T-shape wall. The other boundary represented the web region of a T-shape wall. Confinement at this boundary extended $0.09l_w$ from the edge of the wall and consisted of a hoop and one cross-tie spaced at four times the diameter of the smallest longitudinal reinforcing bar (s/d_b=4.0). The asymmetric boundaries made it possible to impose a short compression depth for the case with the "flange" boundary in compression and a longer compression depth for the case with the "flange" in tension. For nominal material properties, the compression depth was $0.19l_w$ for loading causing compression at the "web" boundary.

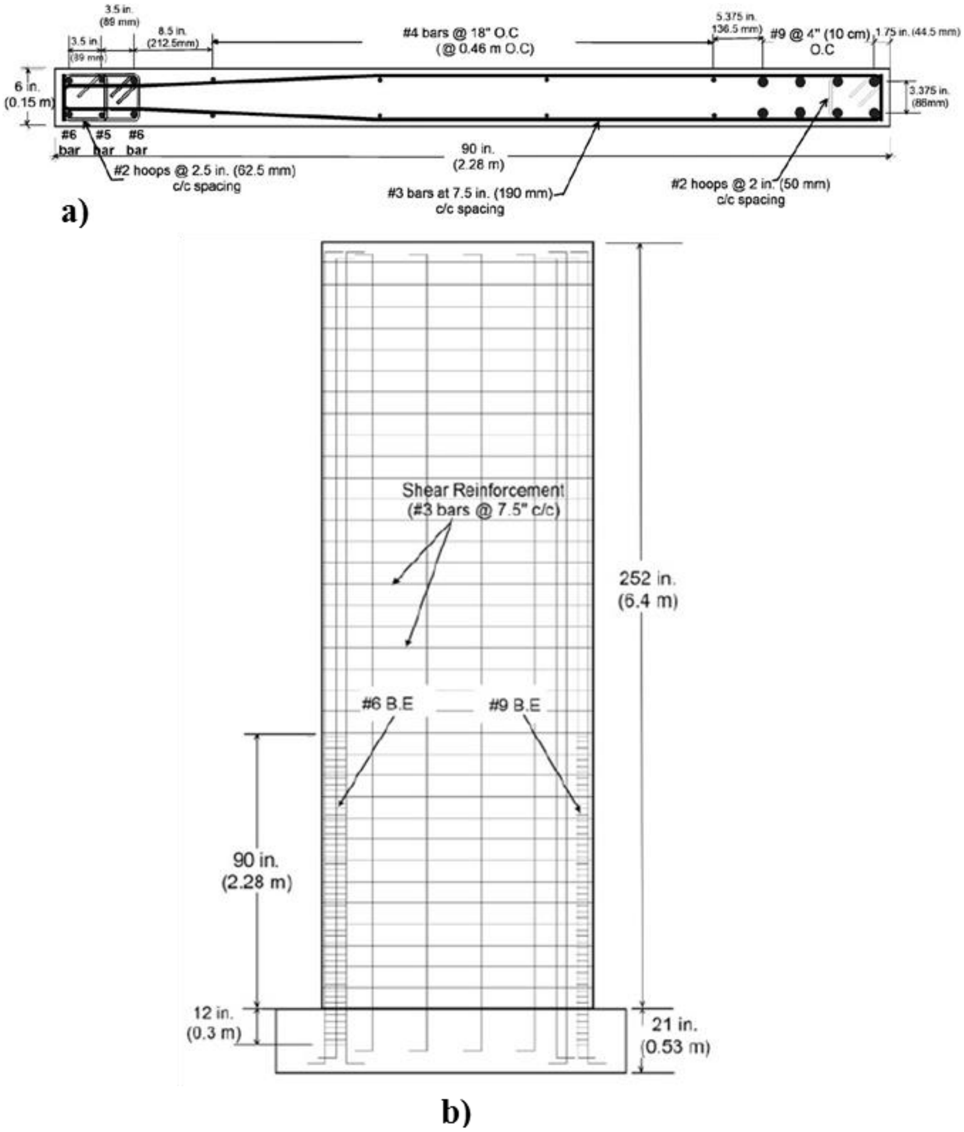

Figure 2-28: Aaleti et al. (2013) – a) Specimen cross-section, and b) Elevation view

The experimentally measured lateral load vs. drift is shown in Figure 2-29 and photos of the typical failure modes are shown in Figure 2-30. As is apparent from the figure, the applied loading pattern was asymmetric, resulting in larger cyclic tension strains at the "web" boundary. Specimens RWN and RWC each experienced out-of-plane instability (Figure 2-30a) at the "web" boundary at approximately -2% drift following an excursion to +2.5% drift. For both walls, compression loading at the "web" boundary was terminated following the occurrence of out-of-plane buckling.

For specimen RWS, strength loss was observed while loading to -1% drift following an excursion to +2% drift. The loss of strength was attributed to failure of the lap splice. Slippage of the spliced bars (Figure 2-30b) occurred immediately outside of the spliced region, reducing the load resisted by the bars.

The researchers concluded that lap splices should be avoided in the plastic hinge region of structural walls because their presence have the potential to reduce the drift capacity and energy dissipating capabilities of a wall.

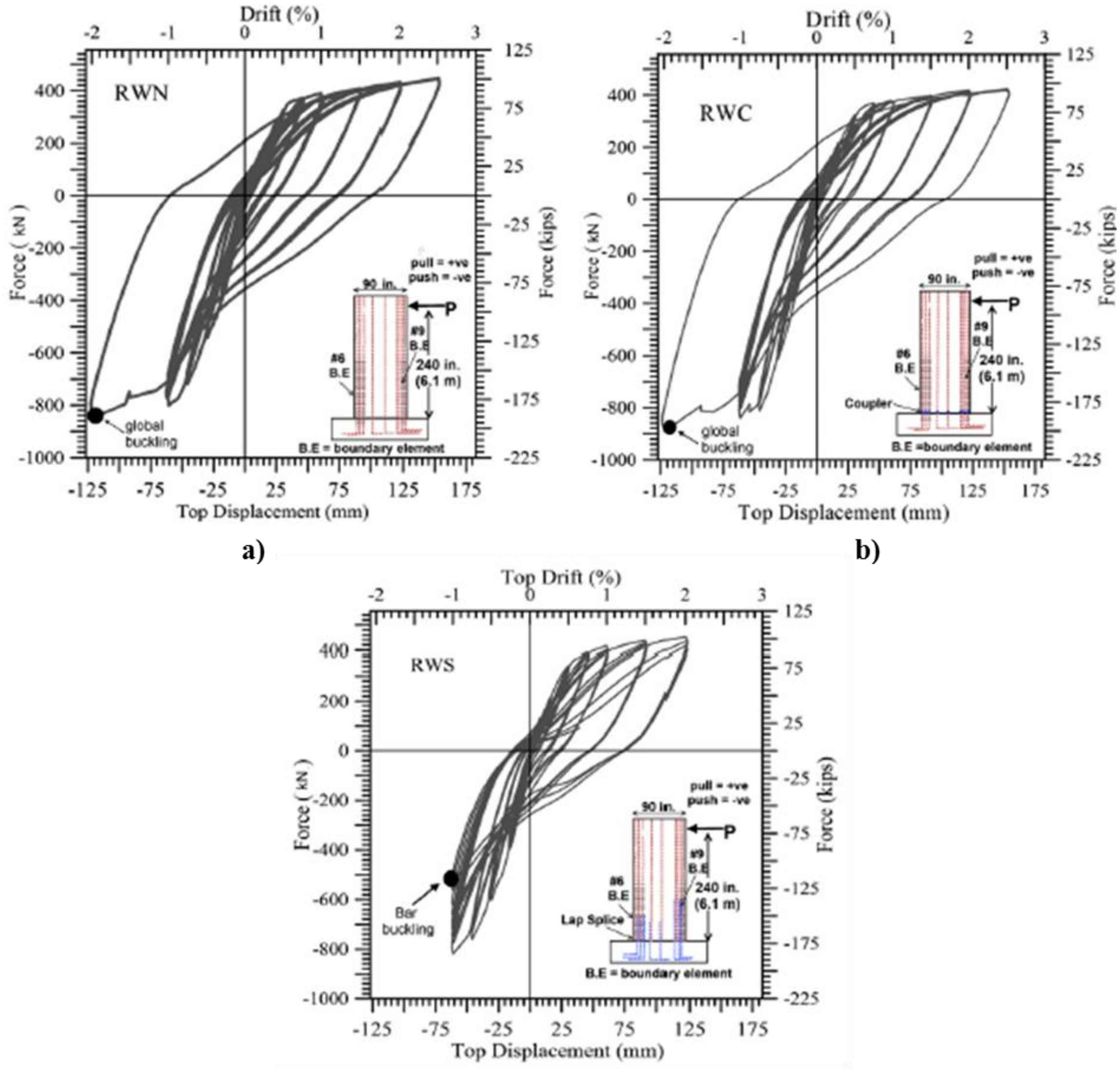

a)

b)

c)

Figure 2-29: Aaleti et al. (2013) lateral load vs. drift – a) RWN, b) RWC, and c) RWS

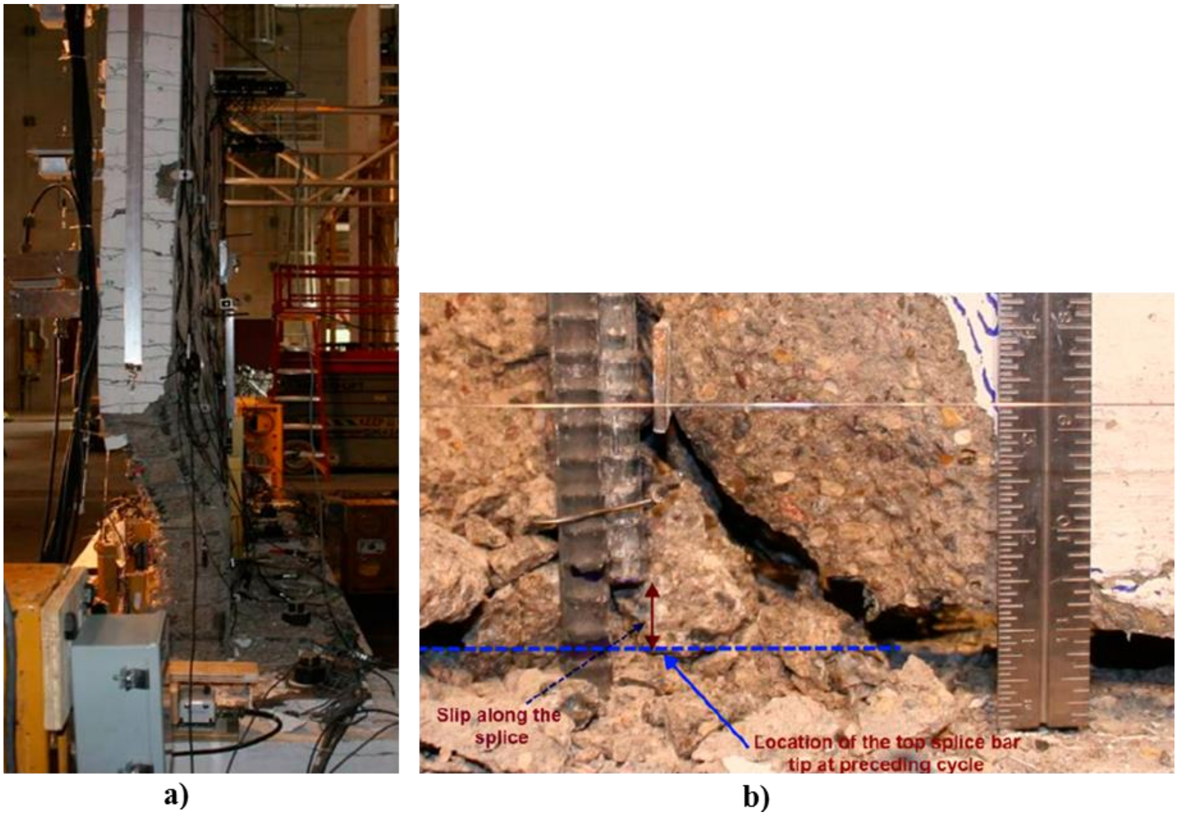

Figure 2-30: Aaleti et al. (2013) observed damage – a) Specimen RWC out-of-plane buckling, and b) Specimen RWS lap slice failure

2.4.5 Dazio et al. (2009)

Dazio et al. (2009) conducted tests on six wall panels designed for moderate seismic risk and representing typical design and construction practice in Central Europe. All six specimens had rectangular cross-sections and relatively low boundary vertical reinforcing ratios. The walls represented the lower portion of a six story wall. The primary objectives of the tests were to investigate the effect of steel reinforcement ductility properties and vertical reinforcing ratios. Axial load demands for the walls ranged between $0.05A_{cv}f'_c$ and $0.13A_{cv}f'_c$. The overall geometry of the walls and experimental test setup are shown in Figure 2-31. All six walls were 78.7 in (2000 mm) long, 5.9 in. (150 mm) thick, and 159 in. (4030 mm) in height.

Lateral loads were applied at the top of the walls by two actuators mounted in series, and axial load was applied at the center of the walls using post-tensioning rods. Average test day steel reinforcement yield strength (f_y) varied between 70 ksi (485 MPa) and 95 ksi (656 MPa), and average test day concrete compressive strength ranged between 5.6 ksi (38.3 MPa) and 6.6 ksi (45.6 MPa). In general, the steel reinforcement used in the tests did not meet ductility and strength requirements of U.S. standards for seismic design applications (i.e., ASCE A615/A706).

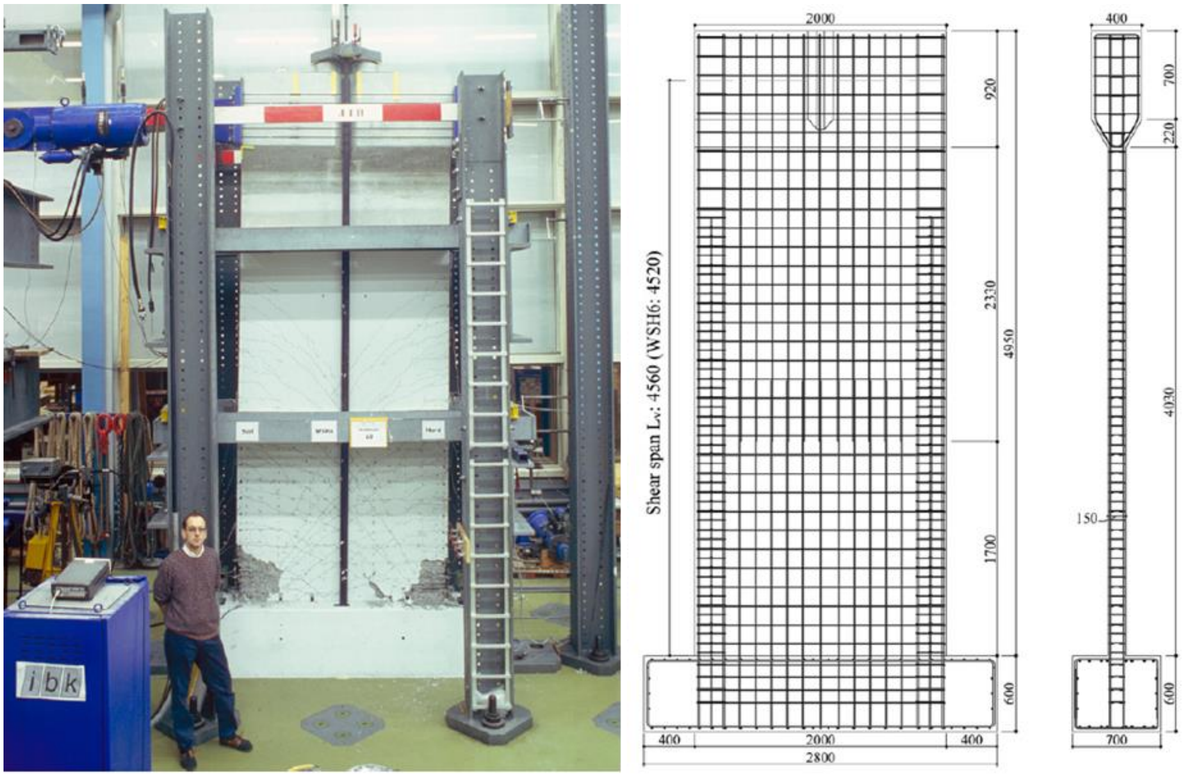

a)

b)

Figure 2-31: Dazio et al. (2009) – a) Test setup, and b) Overall dimensions

Cross-sectional geometries and reinforcement details of the test specimens are shown in Figure 2-32. The confined boundaries of walls WSH1 and WSH2 extended $0.10l_w$ from the edges of walls. Boundaries of WSH3 and WSH5 extended $0.13l_w$ from wall edges, and the boundary of WSH6 extended $0.19l_w$ from the edges of the wall. For test day material properties, compression depth for an extreme fiber compression strain of 0.003 and the applied axial load ranged between $0.10l_w$

(WSH1) and 0.20l_w (WSH5). For these values, special boundary detailing would be required by the ACI 318-14 displacement based procedure for design drift ratios between 0.6% and 1.1%. Boundary transverse reinforcement details consisted of either an outer hoop with a single cross-tie (specimens WSH1, WSH2, WSH3), U-bars with no supplemental cross-ties (WSH4), or overlapping hoops (WSH5 and WSH6). Transverse reinforcement was spaced at 12.5d_b for the specimen with U-bars. Spacing ranged between 6.3d_b and 7.5d_b for walls with hoop and cross-tie configurations, and between 4.2d_b and 6.3d_b for walls with overlapping hoops. In general, boundary transverse reinforcement details for the six walls did not satisfy ACI 318-14 provisions. For test day material properties, the test specimens contained between approximately 50% and 90% of the transverse reinforcement required by ACI 318-14.

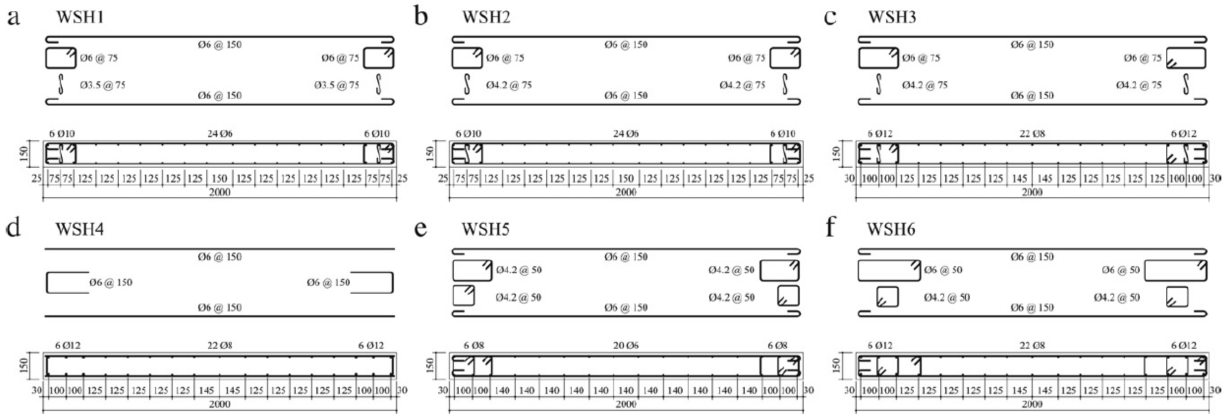

Figure 2-32: Dazio et al. (2009) specimen cross-section dimensions and reinforcement details

Experimentally measured lateral load vs. lateral drift results are presented in Figure 2-33 and photos of specimens following failure are shown in Figure 2-34. Strength loss for specimen WSH1, which contained the reinforcement with the poorest ductility properties, occurred due to fracture of web vertical reinforcement. The first fracture of web reinforcement occurred at approximately 0.68%, and fracture of boundary vertical bars occurred at approximately 1.1%. The load-carrying capacity of WSH1 dropped below 80% of the peak capacity prior to 1% drift. WSH2 was constructed with reinforcement similar to that of WSH1, although the ductility properties were slightly improved. At approximately 1.16% drift, first fracture of web vertical reinforcement occurred. In the following cycles at 1.5% drift levels, fracture of several web bars occurred along a large crack in the web (Figure 2-34b). Spalled cover concrete at the wall edges revealed buckled bars at the boundary. Upon load reversal, the previously buckled bars fractured.

Specimen WSH3 contained reinforcement with better ductility properties that WSH1 and WSH2, and the quantity of vertical reinforcement at the boundaries was larger. At approximately 1.7% drift, spalling of concrete revealed first signs of buckling of vertical reinforcing bars at the edge of the wall. Subsequent cycles resulted in further buckling of vertical bars followed by fracture of previously buckled reinforcement at 1.79%. Vertical reinforcement for specimen WSH4 had similar ductility properties and the same arrangement as WSH3, but no confinement was provided at the boundaries of the wall. Spalling of concrete and buckling of boundary reinforcement occurred nearly simultaneously at 1.02% drift. At 1.63% drift, a sudden drop in load-carrying capacity occurred due to crushing of the compression zone.

Specimen WSH5 had a higher axial load and lower reinforcement ratio than WSH3 and WSH4, but the flexural strength was similar. At 1.01% drift, first fracture of web vertical bars was detected and first signs of buckling of boundary vertical bars was observed. Significant strength loss occurred at approximately 1.35% due to fracture of web and boundary vertical bars. WSH6 was subjected to the same axial load as WSH5, but the vertical reinforcement ratio was the same as WSH3 and WSH4. The onset of bar buckling in the well-confined boundary region was detected at 1.7% drift. At 1.87% drift, strength loss initiated and strength dropped to approximately 80% of peak capacity by 2.11% drift. The actuators ran out of stroke capacity at 2.11%, although it was reported that the boundary was critically damaged and additional loading would have likely resulted in compression failure. Loading in the opposite direction resulted in abrupt crushing at the other boundary at 1.93% drift.

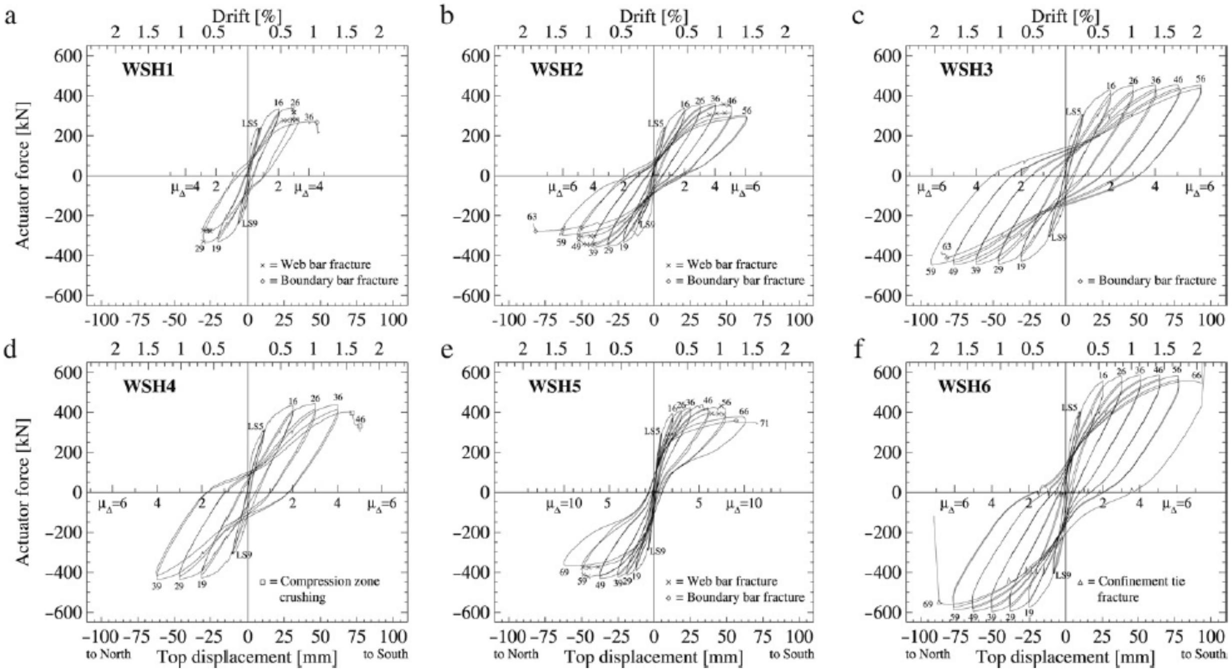

Figure 2-33: Dazio et al. (2009) lateral load vs. drift – a) WSH1, b) WSH2, c) WSH3, d) WSH4, e) WSH5, and f) WSH6

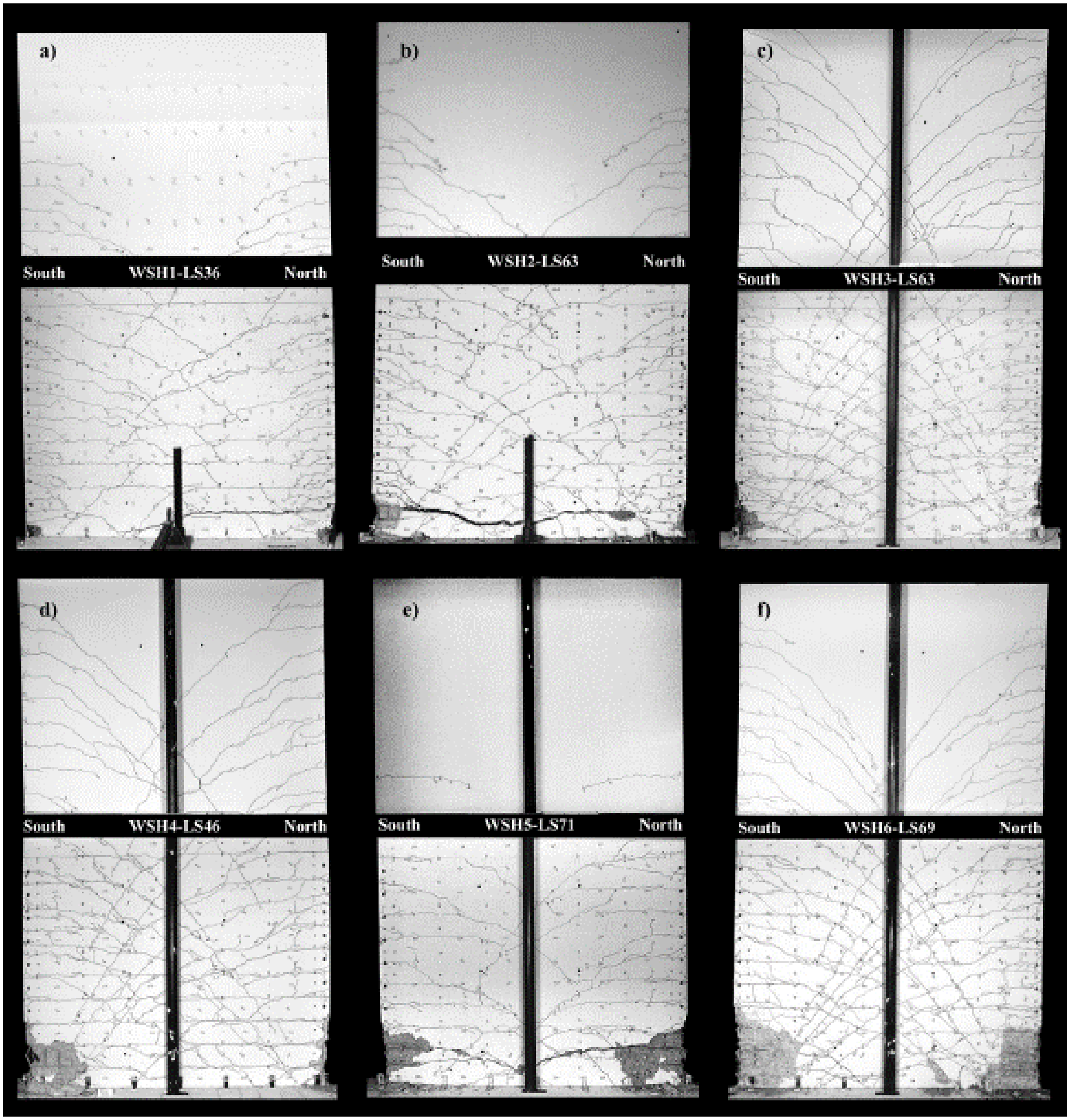

Figure 2-34: Dazio et al. (2009) test specimen photos after failure – a) WSH1, b) WSH2, c) WSH3, d) WSH4, e) WSH5, and f) WSH6

2.4.6 Brueggen (2009)

Brueggen (2009) conducted bidirectional loading tests on two T-shape walls designed according to ACI 318-02. Both walls included a 3.5 in. (89 mm) thick slab at each story. One specimen, designated NTW1, was four stories in height and the other, designated NTW2, was two stories in height. Loading was applied to represent the loads expected in the bottom two or four stories of a six story wall. Lateral drifts and forces were applied in a complex sequence to investigate the effects of multidirectional loading. The applied axial load was approximately $0.07A_{cv}f'_c$. For specimen NTW2, however, the applied axial load was increased by approximately 10% to account for the weight of the two additional stories in NTW1.

Cross-sectional geometries and elevation views of the two specimens are shown in Figure 2-35 and Figure 2-36. Reinforcement was relatively similar between the two specimens with a few exceptions: 1) Longitudinal reinforcement for NTW1 was continuous from the base to the top while specimen NTW2 included a splice at the bottom of the second story, 2) the flange of NTW1 had heavily reinforced boundary elements while longitudinal reinforcement in the flange of NTW2 was distributed, 3) the confined length at the web boundary of NTW2 was longer than that of NTW1, and 4) shear reinforcement in the flange of NTW2 was spaced closer than that of NTW1. Design material properties were f_y=60 ksi (414 MPa) and f'_c=5 ksi (27.4 MPa).

Confinement details at the web boundary of specimen NTW1 consisted of three overlapping hoops and a single cross-tie. Confinement extended $0.25l_w$ from the edge of the wall. Confinement at the web boundary of specimen NTW2 extended $0.29l_w$ from the edge of the wall and consisted of a long, rectangular outer hoop with three square, inner hoops. For nominal material properties under the design axial load, the compression depth was $0.32l_w$ for loading causing compression at the web boundary of the T-shape walls.

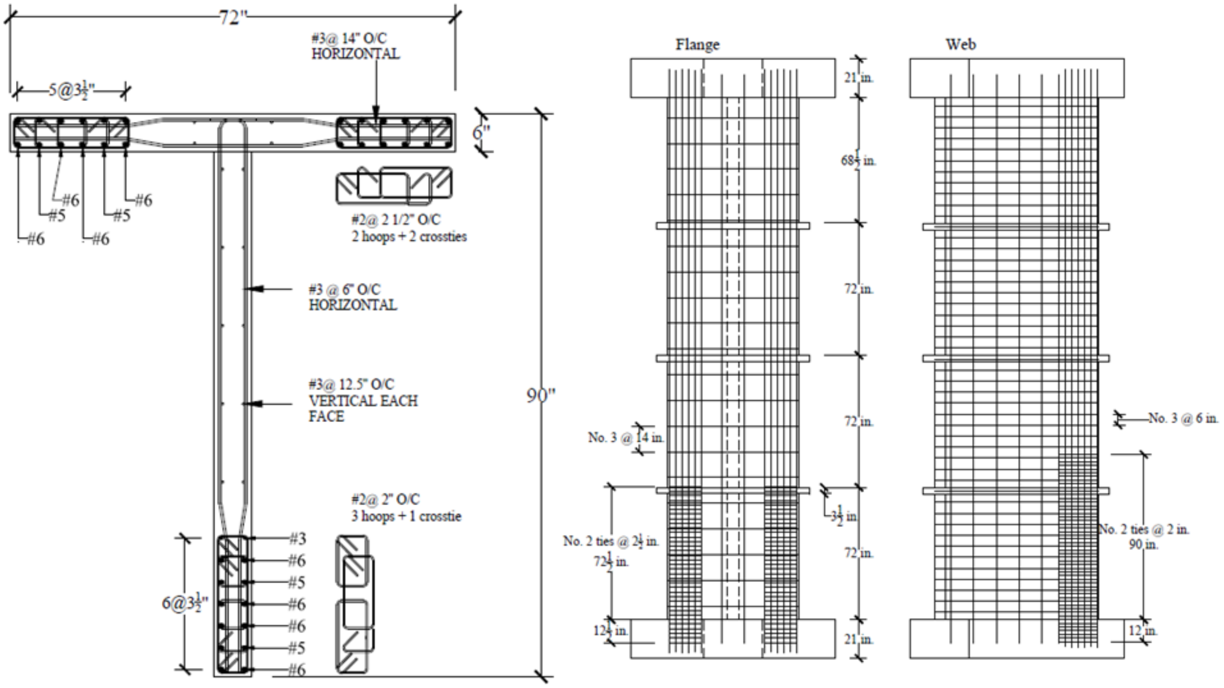

a) b)

Figure 2-35: Brueggen (2009) specimen NTW1

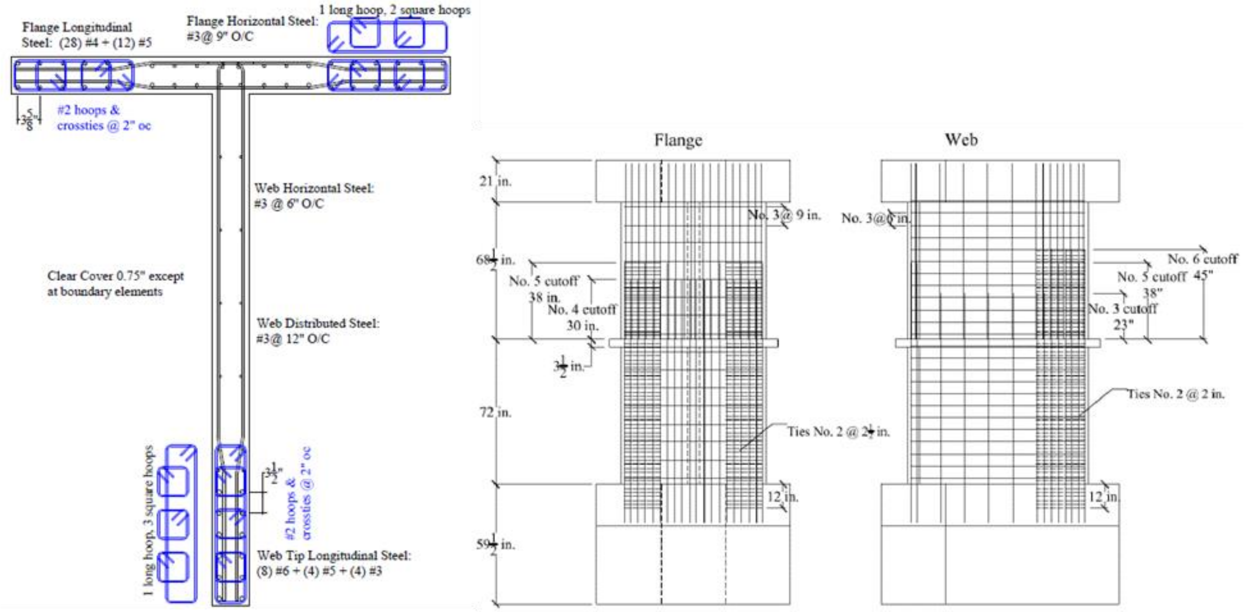

a) b)

Figure 2-36: Brueggen (2009) specimen NTW2

Experimentally measured lateral load vs. drift are shown in Figure 2-37 and observed damage following failures is shown in Figure 2-38. The load-deformation plots in Figure 2-37 ae for loading in the web direction. Strength loss occurred due to crushing of the confined boundary region at 2% drift for NTW1 and at 2.5% drift for NTW2.

The study concluded that bidirectional loading is unlikely to cause significantly larger compression strains at the web boundary or in the unconfined web of the wall. It was recommended to base confined depths on the compression depths determined by sectional analyses in orthogonal directions.

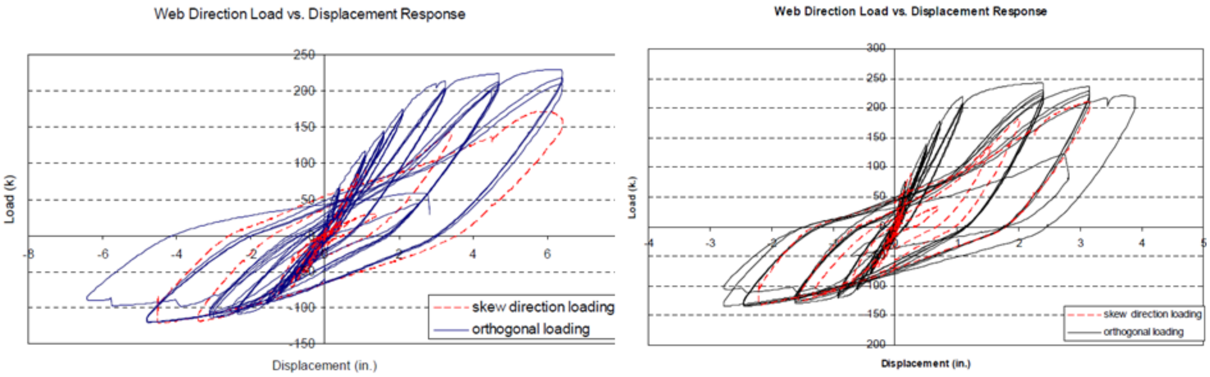

a) **b)**

Figure 2-37: Brueggen (2009) lateral load vs. drift – a) NTW1, and b) NTW2

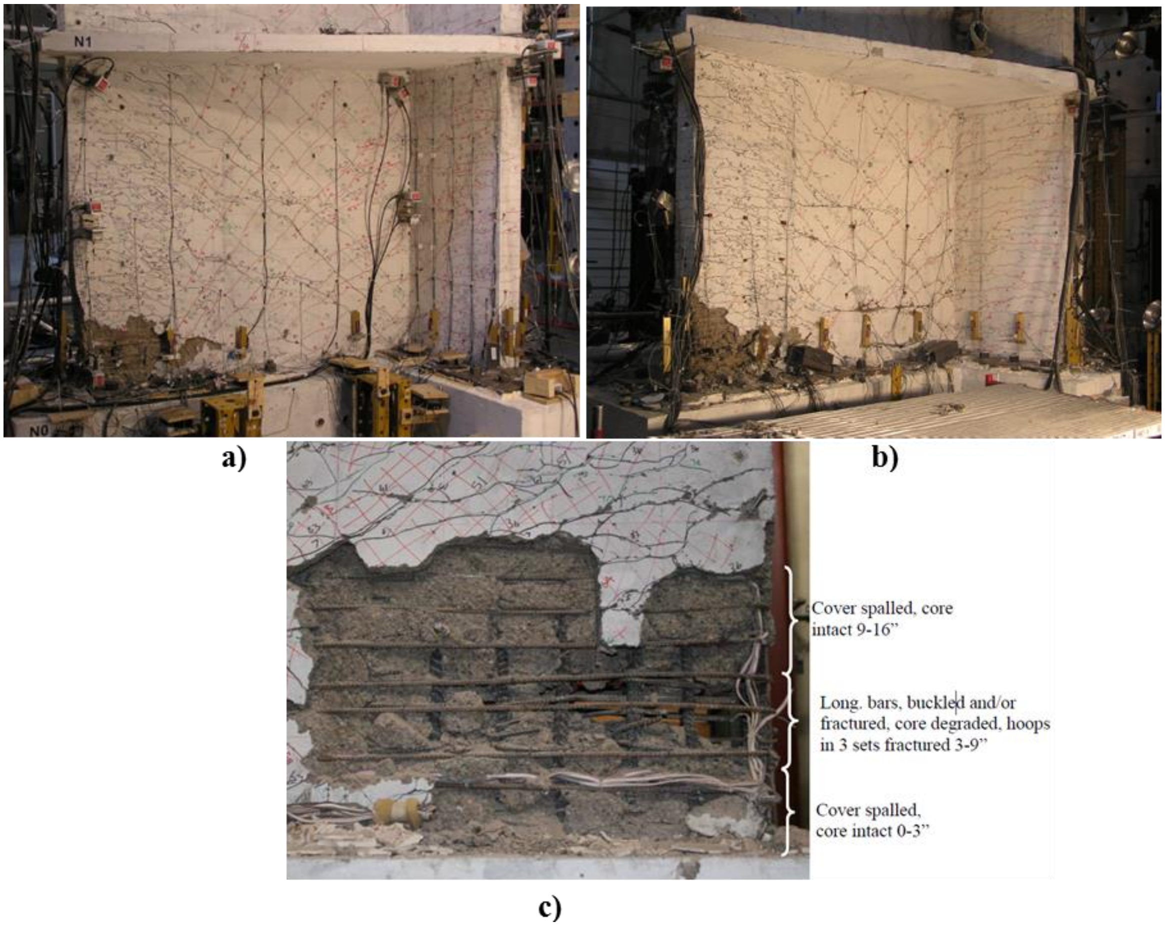

Figure 2-38: Brueggen (2009) observed damage – a) NTW1 web crushing, b) NTW2 web crushing, and c) NTW2 web after failure

2.4.7 Birely (2011), Lowes et al. (2012)

Researchers at the University of Washington and at the University of Illinois Urbana-Champaign (Birely, 2011; Lowes, et al., 2012) conducted tests on four rectangular wall panels that represented the bottom three stories of a ten story wall. The objective of the tests was to study the seismic performance of characteristic rectangular walls found in modern buildings. Based on a survey of mid-rise buildings constructed on the West Coast of North America, aspects of modern wall designs were characterized and used to design the test specimens. Test variables, chosen based on gaps identified between the survey and previous research on slender walls, included shear demand, arrangement of vertical reinforcement, and continuity of vertical reinforcement (i.e., 3 vertical reinforcement was spliced in three walls). The test setup and overall geometry of the walls are shown in Figure 2-39a, and cross-section dimensions and reinforcement are shown in Figure 2-39b and Figure 2-39c for the two configurations of vertical reinforcement tested. All four walls were 10 ft. (3048 mm) long, 6 in. (152 mm) thick, and 12 ft. (3657 mm) in height. Lateral loads were applied at the first and second story, 4 ft. (102 mm) and 8 ft. (203 mm) above the base of the wall. Axial load, overturning moment, and additional lateral load were applied at the top of the wall. Axial load applied to the walls ranged between $0.095A_{cv}f'_c$ and $0.13A_{cv}f'_c$.

Specimens PW1, PW2, and PW3 each included a splice in the plastic hinge region at the base of the wall. For specimen PW1, loading represented the triangular load distribution of the ASCE 7-10 Equivalent Lateral Force Procedure; whereas, the loading scheme for the other three walls represented a uniform distribution of lateral story forces. Specimen PW3 was constructed with uniformly distributed vertical reinforcement. The other walls were constructed with heavily reinforced boundaries.

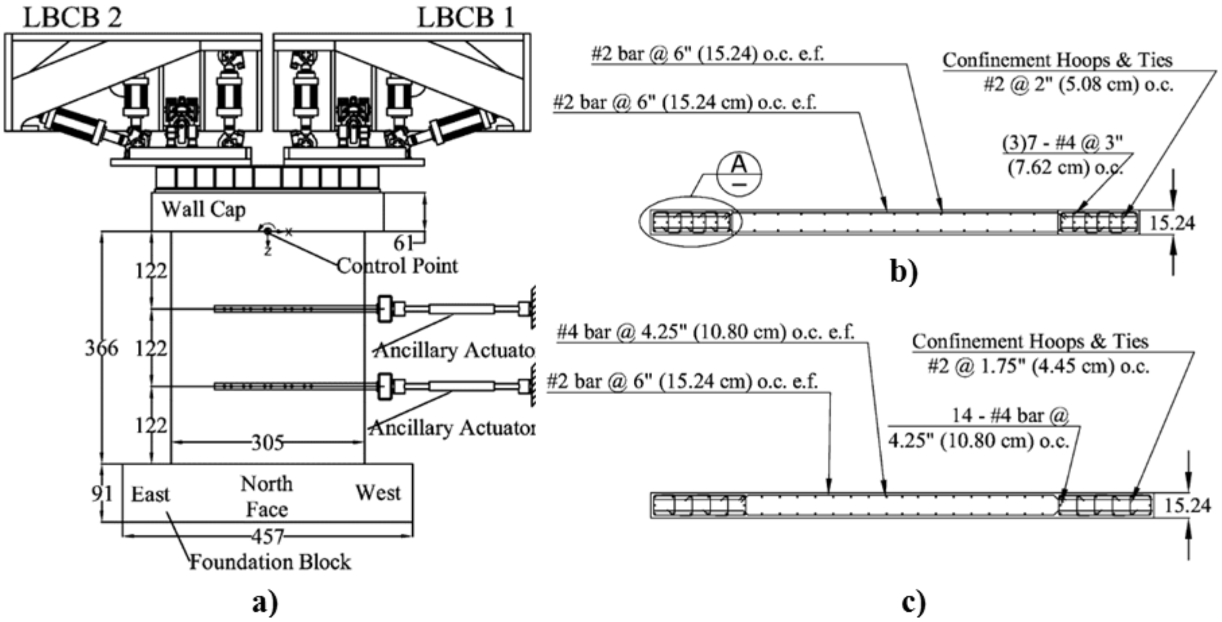

Figure 2-39: UW/UIUC planar walls – a) Test setup and overall geometry; b) Cross-section for specimens PW1, PW2 & PW4; and c) Cross-section for specimen PW3

The confined boundaries of the walls extended $0.10l_w$ from the edges of walls. For all four walls boundary transverse reinforcement consisted of an outer hoop and 5 supplemental cross-ties with 90°-135° hooks spaced at $4.0d_b$. All boundary vertical bars were supported laterally by a hoop corner or cross-tie. For test day material properties, compression depth for an extreme fiber compression strain of 0.003 and the applied axial load ranged between $0.22l_w$ and $0.25l_w$. For these values, special boundary detailing would be required by the ACI 318-14.

Experimentally measured base moment vs. drift results are presented in Figure 2-41 and photos of specimen PW2 (spliced) and PW4 (no splice) are shown in Figure 2-40. For specimen PW1, bar buckling and damage to the confined boundary regions were observed at the height of the splice during the 1% and 1.5% drift cycles. Strength loss occurred during the second 1.5% drift cycle due to fracture of vertical reinforcement. Specimen PW2, which was subjected to a larger shear demand than specimen PW1, failed due to boundary/web crushing and vertical bar buckling in the region of the splice at 1.05% drift (Figure 2-40a). For specimen PW3, which was constructed with uniformly distributed longitudinal reinforcement, buckling of vertical bars minor crushing of the confined boundary were observed during 1% drift cycles. Strength loss occurred suddenly at 1.28% rotation due to boundary/web crushing. Specimen PW4, which did not contain a splice at the base of the wall, experienced strength loss due to boundary and web crushing during the second cycle loading to 1% drift (Figure 2-40b). Damage concentrated at the base of the wall, unlike the other walls where damage concentrated within the splice region.

It was pointed out that failures in the walls with a higher shear demand occurred due to crushing, while strength loss for the wall with a lower shear demand occurred due to fracture of vertical reinforcement. Of particular interest is the low drift capacity, ranging between 1% and 1.5% at the top of the specimens, for code-compliant walls, and the fact that the unspliced wall demonstrated the lowest drift capacity.

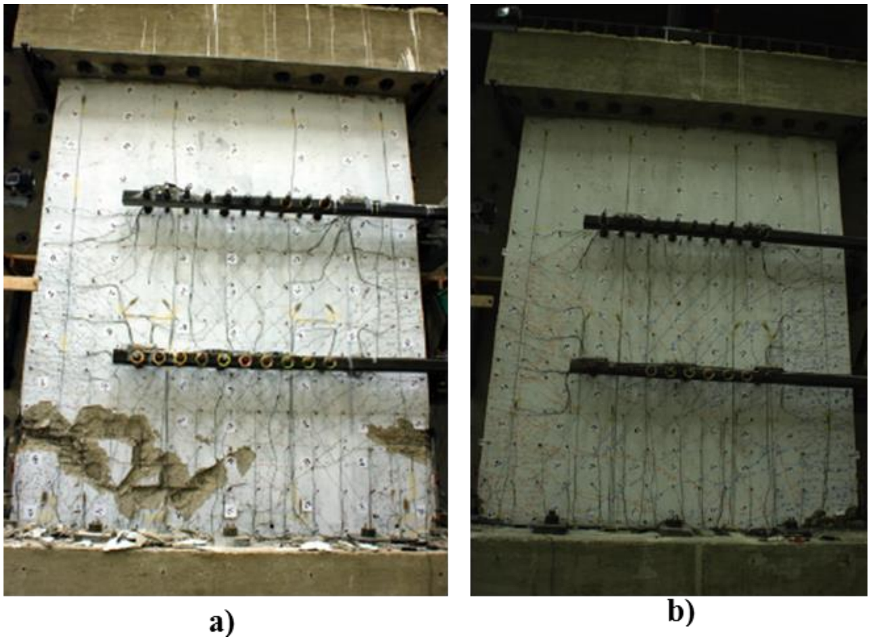
a)

b)

Figure 2-40: Photos after test - a) PW2 (spliced), and b) PW4 (no splice)

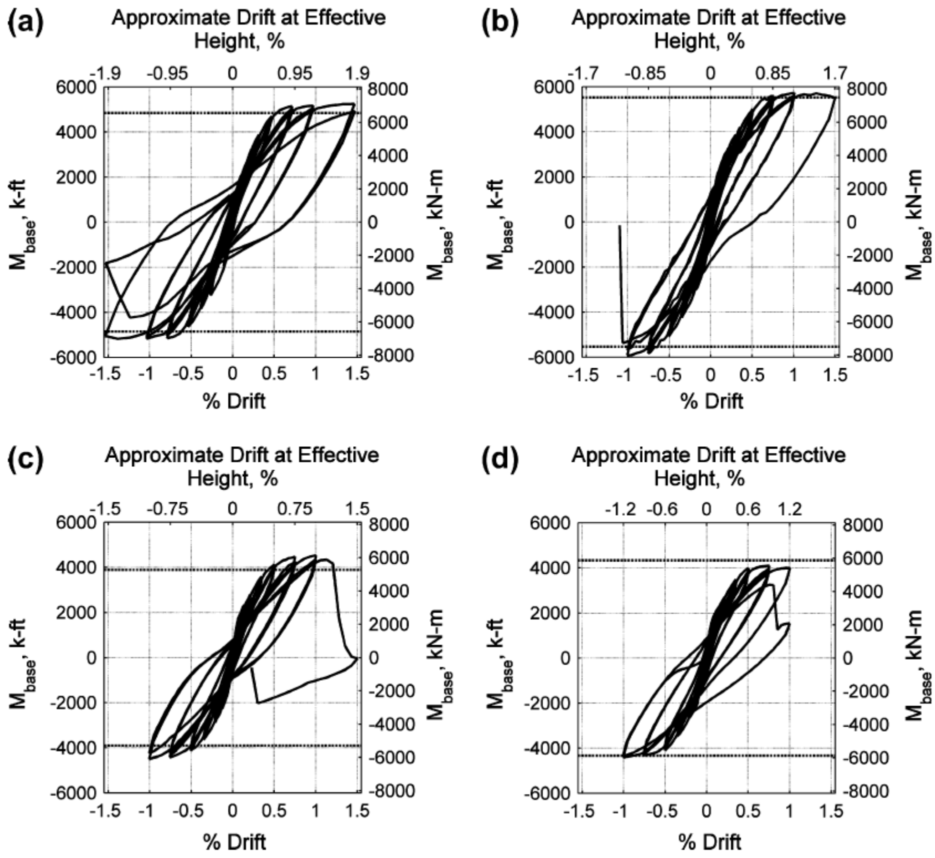

Figure 2-41: UW/UIUC planar walls base moment vs. drift – a) PW1, b)PW2, c) PW3, and d) PW4

2.4.8 Tran (2012), Tran and Wallace (2015)

A study was conducted at the University of California, Los Angeles to assess the seismic performance of moderate aspect ratio walls designed according to ACI 318 (Tran, 2012; Tran, et al., 2015). Two of the walls, designated RW-A20-P10-S38 and RW-A20-P10-S63, had an aspect ratio of h_w/l_w=2.0 which is the minimum allowed for walls designed according to the displacement-based design approach in ACI 318-14 (i.e., slender wall). The two walls differed primarily by the shear stress demand: specimen RW-A20-P10-S38 was designed to resist a shear stress demand less than $4\sqrt{f'_c\,\text{(psi)}}$ $\left(0.33\sqrt{f'_c\,\text{(MPa)}}\right)$ whereas specimen RW-A20-P10-S63 was designed to resist a shear stress demand greater than $6\sqrt{f'_c\,\text{(psi)}}$ $\left(0.5\sqrt{f'_c\,\text{(MPa)}}\right)$. Geometry and reinforcement details for the two walls are shown in Figure 2-42. Both walls were 4 ft. (1219 mm) long, 6 in. (152 mm) thick, and 12 ft. (3657 mm) in height. The axial load and lateral load were applied at the top of the wall at a height of 8 ft. (203 mm) above the footing of the walls. The applied axial load was equal to $0.073A_{cv}f'_c$.

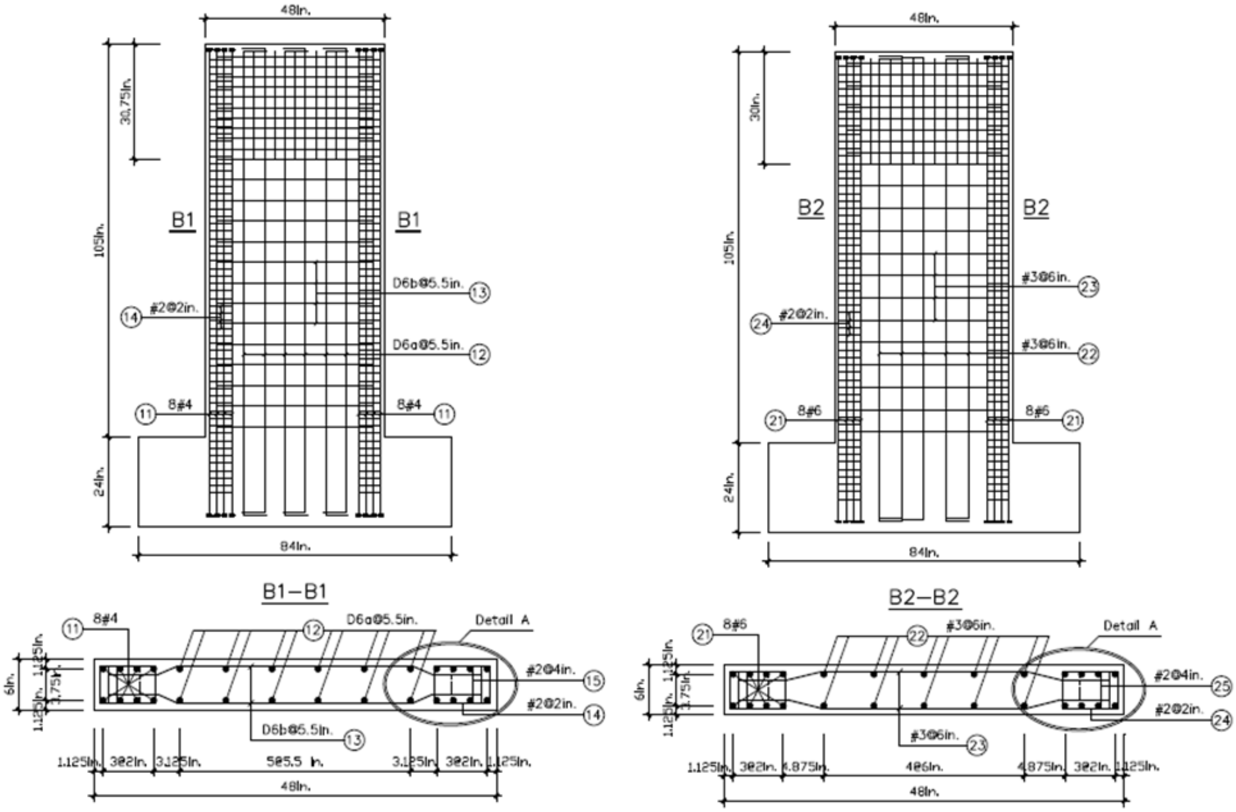

a) b)

Figure 2-42: Tran (2012) wall geometry and reinforcement details; b) Specimen RW-A20-P10-S38; and c) Specimen RW-A20-P10-S63

Experimentally measured lateral load vs. lateral drift results are presented Figure 2-43 for the two walls which were both able to reach 3% lateral drift prior to strength loss. The researchers found that the contribution of nonlinear shear deformations was significantly larger for the wall with larger applied shear stress, with shear contributing to 15% and 35% of the total top displacement for specimens RW-A20-P10-S38 and RW-A20-P10-S63, respectively.

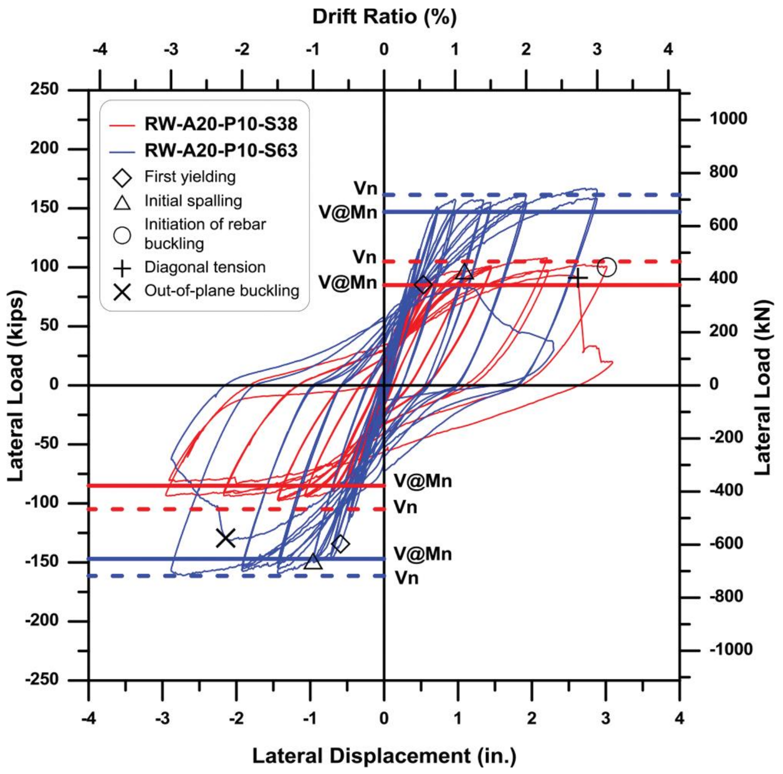

Figure 2-43: Tran (2012) lateral load vs. drift

2.4.9 Matsubara et al. (2013)

Matsubara et al. (2013) conducted five experimental tests on wall specimens representing the plastic hinge region of a wall designed to yield in flexure. Four of the five specimens did not satisfy ACI 318 SBE detailing because confinement in the boundary regions was provided only by cross-ties with no closed hoops. Furthermore, the loading pattern applied to those four walls (M/Vl_w=1.5) was more representative of a low-rise wall than a slender wall. However, one specimen, designated N(M/Qd3.1), was constructed with a single outer hoop and cross-ties and designed for a shear span-to-depth ratio (M/Vl_w) of 3.1. The cross-sectional geometry and an elevation view showing the typical reinforcement layout for the specimens are shown in Figure 2-44. The specimen was constructed with a thickened boundary on one end of the wall to impose large compression demands at the thin boundary of the wall. The quantity and spacing of transverse reinforcement at the thin boundary region satisfied ACI 318-14 SBE requirements.

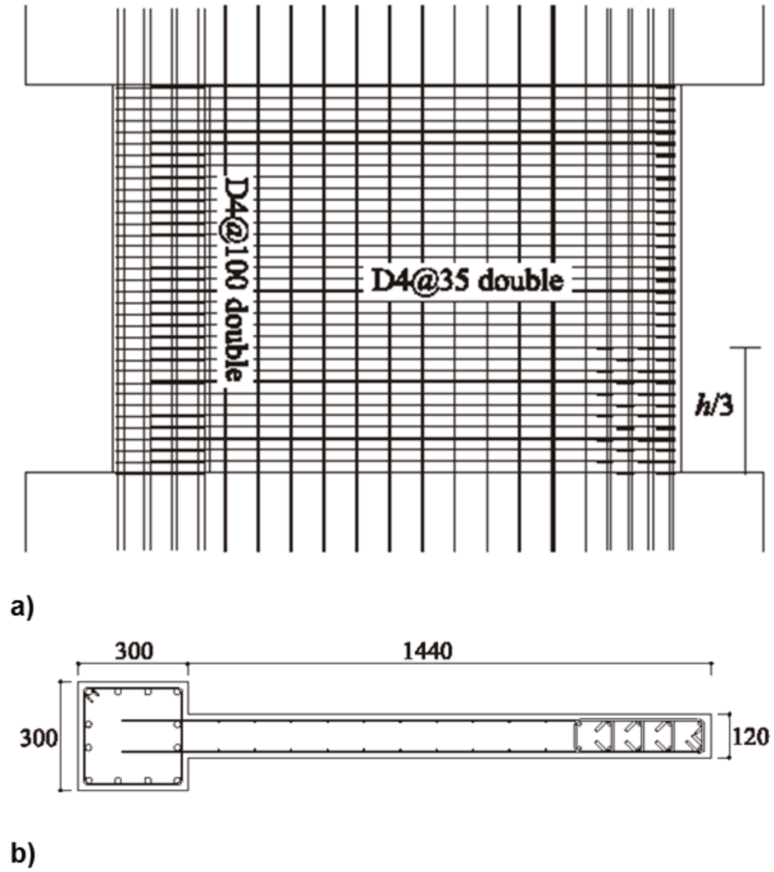

Figure 2-44: Matsubara et al. (2013) specimen N(M/Qd3.1) – a) Wall elevation and reinforcement details; and b) Cross-sectional geometry and reinforcement

Cyclic lateral loading was applied 214 in. (5446 mm) above the wall footing. The applied axial load was approximately $0.07A_{cv}f'_c$. For test day material properties, compression depth for an extreme fiber compression strain of 0.003 and the applied axial load is approximately 25% of the length of the wall ($c=0.25l_w$). The measured lateral load vs drift ratio is shown in Figure 2-45(a). Strength loss occurred at 2.5% drift due to a flexural-compression failure mode (concrete crushing and reinforcement buckling). The flexural contribution to the lateral deformation is shown in Figure 2-45(b). At failure, flexural drift was just under 2%, comprising 80% of the total response.

A schematic of damage to the specimen following the compression failure is shown in Figure 2-45(c). Damage in the compression region concentrated over a 300 mm (11.8 in.) height and extended more than half the length of the wall from the boundary. The researchers found that the detailing used for the specimen improved the ductility in comparison to the other walls without a closed hoop and generally constructed with less boundary transverse reinforcement.

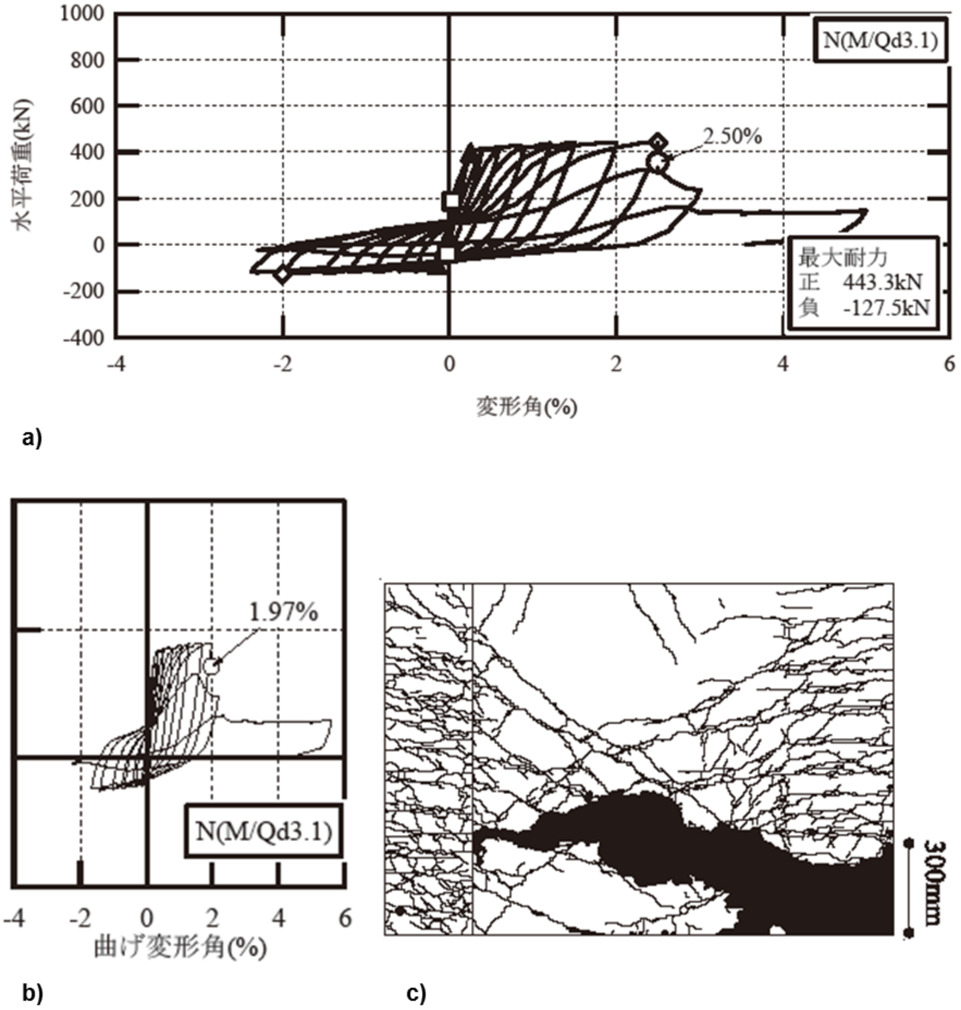

Figure 2-45: Matsubara et al. (2013) specimen N(M/Qd3.1) – a) Lateral load vs. drift ratio; b) Flexural drift vs. lateral load; and c) Observed damage

2.5 Summary and Research Objectives

Based on a substantial amount of research on the seismic performance of reinforced concrete structural walls (shear walls), modern design provisions for mid-rise and high-rise shear wall buildings have been developed with the goal of achieving significant ductility in the event of strong earthquake ground shaking. Observations following recent earthquakes in Chile (2010) and New Zealand (2011) have demonstrated the potential for shear wall buildings designed according to modern seismic design codes to experience brittle failures. Considering the similarities in design and construction practice in the U.S., Chile, and New Zealand, observations from these earthquakes have important implications for U.S. design codes. Based on the extent of damage observed in Chile and New Zealand, it is likely that performance limitations for slender walls have been reached by current design and construction practice. It is important to understand the performance limitations of walls designed for large ductility demands. Some potential issues that must be addressed include:

1. Due to a number of factors, including advances in structural modeling capabilities and less conservative design codes, modern walls are likely to be constructed with thinner compression regions and designed for larger demands (i.e., lateral drift, axial load) than walls in previous decades. Research on construction practice trends in Chile (Massone, et al., 2012) identified an important trend for mid-rise and high-rise shear wall buildings: while average building heights have increased over the past few decades, the ratio of wall area to floor plan area has remained relatively constant, cross-sections have become thinner, and axial stress ratios have increased. Furthermore, complex wall configurations consisting of orthogonal walls framing together are likely to result in deep neutral axis depths on thin compression zones. Given the extent of damage observed in Chile and New

Zealand and in recent laboratory tests, it is vital to understand the performance limitations of thin, code-compliant walls. Also, it is important to understand the design limitations necessary to achieve code-allowable drift demands. This may include limits related to axial load, wall geometry (i.e., thickness), compression depth, and extreme fiber compression strain.

2. Brittle failures modes have been observed in code-compliant walls at drift demands less than those allowed by building codes (Lowes, et al., 2012). Recent tests on well-detailed boundary element specimens (Arteta, 2015; Welt, 2015) suggest that confinement details utilizing an outer hoop and 90^o-135^o cross-ties, a detail allowed to meet ACI 318 requirements, may not provide ductile resistance to the compression strain demands likely to be imposed on thin wall sections. These research programs have focused on characterizing the strain capacity of thin sections with various confinement details, but the research has been conducted on isolated boundary element specimens subjected to uniform stress and strain. It is important to characterize the strain capacity of the boundary element of a wall which is subjected to a strain gradient and shear stress and strain. Similar wall specimens and boundary element specimen designs may make it possible to extrapolate uniform stress/strain tests to behavior in a wall.
3. Field observations in Chile reported little or no flexural cracking at buckled compression zones, in some cases, suggesting that instability may have resulted from damage in compression rather than as the result of inelastic strain reversals. Buckling was observed for a wall in Christchurch with a slenderness ratio of 8.9, which is much less than the value of 16 instated in ACI 318-14 and previously used in UBC-97 (ICBO 1997). Previous research has explored the subject of global buckling following large tensile strains

excursions (Paulay, et al., 1993; Chai, et al., 1999), but the absence of flexural cracks in Chile indicates that thin walls may experience instability due to damage in compression. Because a ductile yielding response is dependent upon stability of the compression zone, it is important to understand the mechanics that may lead to lateral instability and to explore the geometric constrains necessary to maintain stability.

4. Web crushing and buckling of vertical reinforcement over a significant length of the wall were observed in Chile and New Zealand. In such a damaged state, it is possible that residual strength and axial load-carrying capacity are greatly reduced. Building collapse risk, therefore, may be higher in the main event and in the event of a significant aftershock. Few experimental tests have assessed residual strength and axial load-carrying capacity, although this information is critical to characterize collapse risk.

The objective of this research is to conduct experiments to address the issues summarized above. Seven reinforced concrete wall panel specimens, with reinforcement representative of modern design and construction practice, were designed in accordance with ACI 318-14. The tests were designed to: 1) assess performance limitations of thin, code-compliant walls and understand the design limits necessary to achieve code-allowable drift limits for thin walls; 2) assess the strain capacity of thin wall compression zones with various reinforcement arrangements; 3) study the mechanisms leading to lateral instability of wall compression zones; 4) and assess residual strength and axial load-carrying capacity of thin walls following damage at wall boundaries.

Chapter 3 Specimen Design

This chapter summarizes the design of seven, approximately one-half scale, wall panel specimens tested in the Structural/Earthquake Engineering Research Laboratory at UCLA. The test matrix was developed to address the research objectives identified in Chapter 2. Details of the geometry and reinforcement for the seven specimens are provided following the test matrix.

3.1 Test Matrix

Seven, approximately one-half scale, reinforced concrete structural wall panel specimens (designated WP1-WP7) were designed according to ACI 318-14 provisions for Special Structural Walls. The wall panels represented approximately the lower 1.5 stories of an eight story cantilever wall. The tests were conducted in two phases. The first phase of testing (WP1-WP4) was conducted to identify potential deficiencies in current ACI 318 provisions, and the second phase (WP5-WP7) was conducted to study the role of wall thickness and evaluate the impact of confinement and web detailing on the deformation capacity, failure mode, and residual lateral strength and axial load capacity of walls. Six of the specimens had a rectangular cross-section, and one specimen (WP4) had a T-shaped cross-section with an enlarged boundary region at one end of the wall. All seven specimens were designed for an applied axial load of $0.10A_{cv}f'_c$ and peak shear stress of approximately $2.5\sqrt{f'_c\text{ (psi)}}$ $\left(0.2\sqrt{f'_c\text{ (MPa)}}\right)$ at the nominal flexural capacity (M_n) of the wall. The walls were designed such that the shear demand at nominal flexural capacity ($V_u@M_n$) was much lower than the nominal shear capacity (V_n) to enable the study of flexural behavior. All seven wall panel specimens were 90 in. (2286 mm) in length and 84 in. (2134 mm) in height (Figure 3-3). Design concrete compressive strength (f'_c) and steel reinforcement yield strength (f_y) were 5 ksi (34.5 MPa) and 60 ksi (414 Mpa), respectively.

Figure 3-1 summarizes four different boundary reinforcement arrangements, all allowed by ACI 318-14, that were used to design the test specimens. Details BE-1, BE-2, and BE-3 each utilize an outer hoop and cross-ties. Cross-ties for BE-1 and BE-2 are designed with 90°-135° hooks. Details BE-1 and BE-2 differ only by the arrangement of longitudinal reinforcement: in boundary regions utilizing detail BE-1, all longitudinal reinforcement is laterally restrained by a hoop corner or cross-tie hook, whereas every other longitudinal bar is laterally restrained in boundary regions utilizing detail BE-2. For detail BE-3, cross-ties are designed with 135°-135° hooks, a detail intended to prevent opening of cross-tie hooks following crushing/spalling of cover concrete. Detail BE-4, referred to herein as continuous transverse reinforcement, is fabricated as a continuous piece of steel to replicate the transverse reinforcement layout of a hoop and cross-tie configuration. The continuous transverse reinforcement detail is expected to provide confinement and buckling inhibiting performance similar to configurations that utilize overlapping hoops.

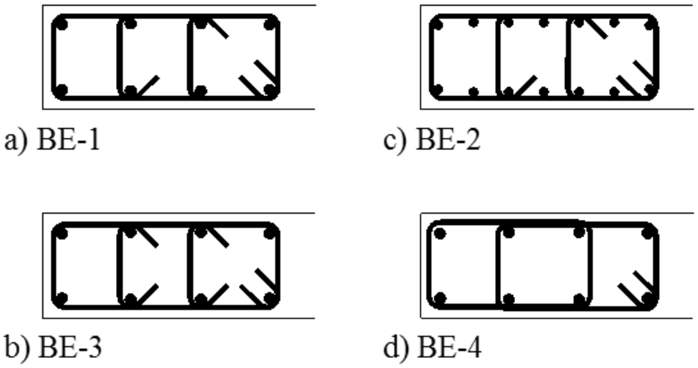

Figure 3-1: Boundary details – a) BE-1; b) BE-2; c) BE-3; and d) BE-4

Three different web reinforcement arrangements, all allowed by ACI 318-14, used to design wall test specimens are shown in Figure 3-2. In detail WEB-1, web longitudinal reinforcement is positioned outside of web transverse reinforcement, which provides no lateral restraint to inhibit buckling of longitudinal bars following concrete crushing/spalling. For details WEB-2 and WEB-

3, web longitudinal bars are placed inside of transverse bars. Cross-ties with 135° hooks at each end are utilized in detail WEB-3.

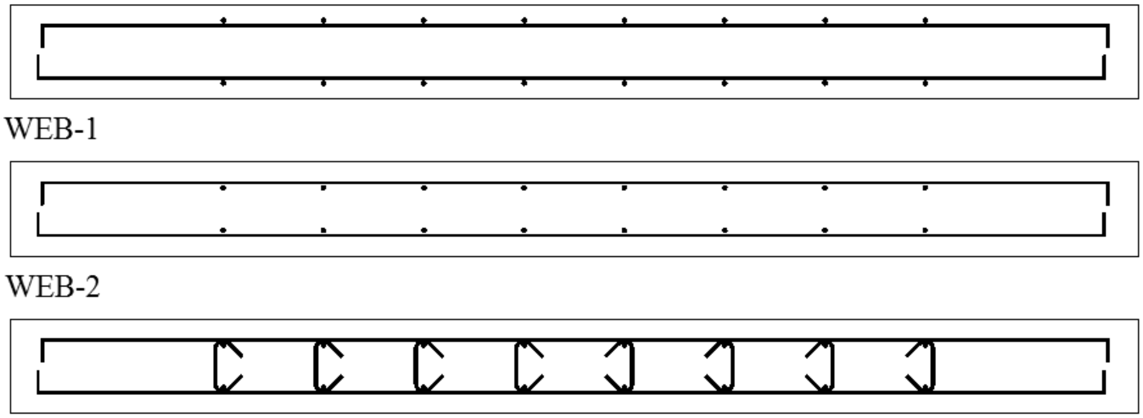

a) WEB-1

b) WEB-2

c) WEB-3

Figure 3-2: Web details – a) WEB-1; b) WEB-2; and c) WEB-3

The testing matrix is provided in Table 3-1, and a detailed description of each specimen is provided in Section 3.2. The primary test variables for each specimen were: WP1) the boundary reinforcement detail used (i.e., Detail BE-1 with all longitudinal reinforcement laterally restrained by a hoop or cross-tie vs. Detail BE-2 with every other longitudinal bar laterally restrained); WP2) the quantity of boundary transverse reinforcement (A_{sh}); WP3) the spacing of boundary transverse reinforcement (s and s/d_b); WP4) the compression depth (c), influence by axial load, quantity of longitudinal reinforcement, and wall cross-section; WP5) the boundary transverse reinforcement detail (i.e., Detail BE-4 consisting of continuous transverse reinforcement rather than detail BE-1 utilizing cross-ties); and WP6 and WP7) the thickness of the compression zone (b).

Wall thickness was 6 in. (152 mm) for specimens WP1-WP4, 7.5 in. (191 mm) for specimen WP6, and 9 in. (229 mm) for specimen WP7. Specimen WP5 was designed with a 6 in. (152 mm) thick web along one-half the length of the wall and a 7.5 in. (191 mm) thick web along the other half of the wall. The six rectangular specimens were designed such that the neutral axis depth, determined using an extreme fiber compression strain of 0.003 (consistent with ACI 318-14 requirements) for an axial load of $0.10A_{cv}f'_c$, was approximately 20% of the length of the wall ($c/l_w=0.20$). The T-shaped specimen (WP4) was designed such that the neutral axis depth was approximately 30% of the length of the wall ($c/l_w=0.30$) for loading causing compression at the web boundary. For loading causing compression at the flange boundary, the neutral axis depth is less than 10% of the length of the wall ($c/l_w<0.10$). SBE detailing was used at the boundaries of all seven walls except for at the flange boundary of specimen WP4, at which compression yielding would not be expected for typical design roof drift values ($\delta_u/h_w=0.01\text{-}0.02$) due to the small compression depth.

For specimens WP1-WP4, the quantity of boundary transverse reinforcement provided was nearly identical to the amount required by ACI 318, and web and boundary detailing consisted of detail WEB-1 and details BE-1 and BE-2. For specimens WP1-WP3, details BE-1 and BE-2 were used at opposite ends of the wall. As such, fewer longitudinal bars were provided at BE-1 boundaries than at BE-2 boundaries. Similar longitudinal reinforcing ratios were desired at wall ends in order to achieve $c/l_w \approx 0.20$ for loading in both directions; hence, larger diameter bars were used at BE-1 boundaries as compared to those at BE-2 boundaries. For specimens WP1 and WP2, the ratio of boundary transverse reinforcement spacing to longitudinal bar diameter (s/d_b) was 3.2 and 4.0 at BE-1 and BE-2 boundaries, respectively. Specimen WP3 was designed with a larger spacing of transverse reinforcement such that s/d_b was 6.0, the largest spacing allowed by ACI 318-14, at each boundary.

Specimen WP5 was designed with continuous transverse reinforcement (detail BE-4) at each end of the wall and the quantity of boundary transverse reinforcement selected was approximately twice the amount required by ACI 318-14. In the web of the wall, longitudinal bars were placed inside of transverse reinforcement and cross-ties were provided to laterally restrain longitudinal reinforcement (web detail WEB-3). Specimens WP6 and WP7 were each designed using web detail WEB-2 over one-half the length of the wall and detail WEB-3 in the other half of the wall. At one end of each wall, boundary detailing was similar to specimens WP1-WP4 except that cross-tie hooks had 135°-135° hooks (boundary detail BE-3). At the other end of the wall, continuous transverse reinforcement (detail BE-4) was used and transverse reinforcement exceeded the quantity required by ACI 318-14 by approximately 60%.

Table 3-1: Test specimen matrix

ID	**Primary Variable(s)**	***b***	**Boundary detail**	**Web detail**	A_{sh}/sb_c	$A_{sh}/A_{sh,req'd}$	s/d_b	c/l_w
		in. (mm)	**(Figure 3-1)**	**(Figure 3-2)**	**%**	**---**	**---**	**---**
WP1	Longitudinal reinforcement arrangement	6.0 (152)	BE-1 BE-2	WEB-1	0.77	1.02	3.2 4.0	0.20
WP2	Quantity of transverse reinforcement (A_{sh})	6.0 (152)	BE-1 BE-2	WEB-1	**1.28**	1.24	3.2 4.0	0.20
WP3	Spacing of transverse reinforcement (*s*)	6.0 (152)	BE-1 BE-2	WEB-1	0.91 0.82	1.09	**6.0**	0.20
WP4	Neutral axis depth (*c*)	6.0 (152)	BE-1	WEB-1	1.21	1.23	3.2	**0.30**
WP5	Boundary & web detailing	6.0 (152) **7.5 (191)**	**BE-4**	**WEB-3**	**1.54**	2.05	3.2	0.20
WP6	1. Wall web thickness (*b*) 2. Boundary & web detailing	**7.5 (191)**	**BE-3** **BE-4**	**WEB-2** **WEB-3**	0.77 1.23	1.02 1.64	3.2	0.20
WP7	1. Wall web thickness (*b*) 2. Boundary & web detailing	**9.0 (229)**	**BE-3** **BE-4**	**WEB-2** **WEB-3**	0.77 1.23	1.02 1.64	3.2	0.20

3.2 Description of Test Specimens

The overall geometry of the wall panel specimens is shown in Figure 3-3. All seven specimens were 90 in. (2286 mm) in length and 84 in. (2134 mm) in height. The test specimens were designed with a footing and a thickened top cap to connect to the laboratory strong floor and to apply actuator loads at the top of the specimens.

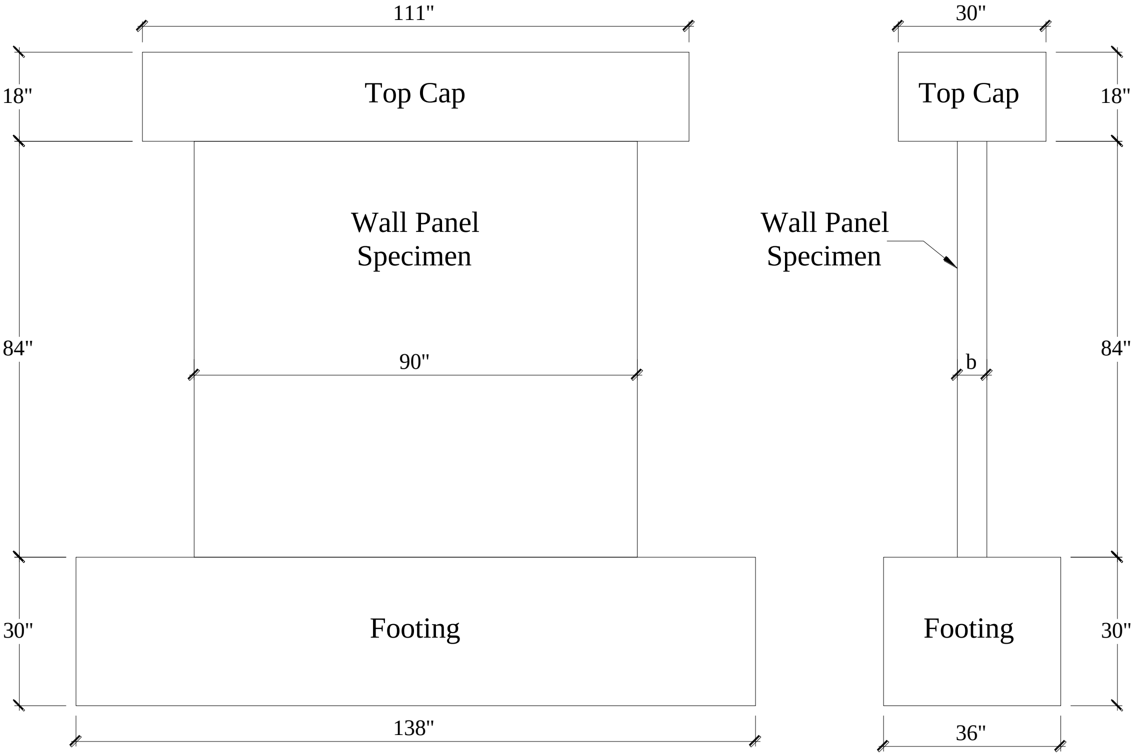

Figure 3-3: Test specimen elevations (Conversion: 1"=25.4mm)

Cross-sectional geometry and reinforcement details of the test specimens are shown in Figure 3-4 through Figure 3-10. Specimens WP1-WP4 had a 6 in. (152 mm) thick web. The web thickness for specimen WP5 was 6 in. (152 mm) over one-half the length of the wall and 7.5 in. (191 mm) over the other half other wall. Specimens WP6 and WP7 had a web thickness of 7.5 in. (191 mm) and 9 in. (229 mm), respectively. Specified concrete compressive strength was 5 ksi (34.5 MPa) for all specimens, and specified steel reinforcement yield strength was 60 ksi (414 MPa) for all reinforcing bars. ASTM A615/A706 Grade 60 (60 ksi [414 MPa] nominal yield strength) deformed bars were used for all No. 3, No. 4, No. 5, and No. 6 reinforcing bars. For specimens WP1-WP4, 1/4" and 5/16” diameter wire (0.252 in. [6.4 mm] and 0.319 in. (8.1 mm) nominal diameter, respectively) was used as boundary transverse reinforcement. At one end of specimen WP3, A615 Grade 60 deformed No. 3 bars were used as boundary transverse reinforcement. Measured yield strengths for the 1/4" and 5/16” diameter wire used for WP1-WP4 were slightly less than the specified value of 60 ksi (414 Mpa). To achieve the desired yield strength, smooth 1/4" and 5/16” diameter wire were used for specimens WP5-WP7. Further details on the materials properties of reinforcing steel used for the tests is summarized in Section 4.1. Mechanical headed anchors were used at the ends of boundary vertical reinforcement to avoid congestion in specimen footings and top caps. Vertical web and boundary reinforcement extended 24 in. (610 mm) into specimen footings and 12 in. (305 mm) into specimen top caps. Web longitudinal and transverse reinforcement for specimens WP1-WP4 (Figure 3-4 through Figure 3-7) consisted of two curtains of No. 3 bars spaced at 8 in. (203 mm) on-center. Web longitudinal reinforcement was placed outside of transverse reinforcement as allowed by ACI 318-14. For specimens WP5-WP7, web reinforcement was similar to specimens WP1-WP4 except that transverse bars were spaced at 6 in. (152 mm) on-center and web longitudinal reinforcement was placed inside of transverse reinforcement (Figure 3-8 through Figure 3-10). Also, cross-ties spaced at 6 in. (152 mm) were used in the web of specimens WP6 and WP7 over one-half the length of the wall (Figure 3-9 and Figure 3-10) and in specimen WP5 over the full length of the wall (Figure 3-8).

Except at the web boundary of specimen WP4, boundary regions extended 14 in. (356 mm) from wall edges. Boundary longitudinal reinforcement for specimens WP1-WP3 consisted of eight No.5 bars at one end (ρ_{lb}=2.92%) and fourteen No. 4 bars at the opposite end (ρ_{lb}=3.27%). Compression depth, determined using an extreme fiber compression strain of 0.003 for an axial load of $0.10A_{cv}f'_c$ (270 kip [1201 kN]), was 19.1 in. ($0.21l_w$; 485 mm) for loading causing compression at the boundary with eight No. 5 bars and 17.9 in. ($0.20l_w$; 455 mm) for loading causing compression at the boundary with fourteen No. 4 bars. Boundary longitudinal reinforcement for specimen WP5 consisted of seven No. 5 bars and five No. 4 bars at the 7.5 in. (191 mm) thick boundary (ρ_{lb}=2.98%) and ten No. 5 bars at the 6 in. (152 mm) thick boundary (ρ_{lb}=3.65%). A different axial load was assumed for loading in opposite directions such that the design axial load was $0.10bl_wf'_c$. For loading causing compression at the thicker boundary (b=7.5 in. [191 mm]), the applied axial load was 337.5 kip (1501 kN), and the applied axial load was 270 kip (1201 kN) for loading causing compression at the 6 in. (152 mm) thick boundary. Compression depth, determined using an extreme fiber compression strain of 0.003 under the applied axial load, was 17.8 in. ($0.20l_w$; 452 mm) for loading causing compression at the thicker boundary, and 18.8 in. ($0.21l_w$; 478 mm) for loading causing compression at the thinner boundary. Specimen WP6 had ten No. 5 boundary longitudinal bars at each end of the wall (ρ_{lb}=2.92%), and specimen WP7 had twelve No. 5 boundary longitudinal bars at each end (ρ_{lb}=2.92%). Compression depth for specimen WP6, determined using an extreme fiber compression strain of 0.003 for the applied axial load (337.5 kip; 1501 kN), was 17.9 in. ($0.20l_w$; 455 mm). For specimen WP7, compression depth at an extreme fiber compression strain of 0.003 for the applied axial load (405 kip; 1802 kN) was 17.5 in. ($0.19l_w$; 445 mm).

For specimen WP4, the web boundary region extended 18 in. from the edge of the wall and the flange boundary region extended 14 in. from the opposite edge of the wall. Boundary longitudinal reinforcement consisted of ten No. 5 bars at the web boundary (ρ_{lb}=2.84%) and fourteen No. 6 bars at the flange boundary (ρ_{lb}=3.44%). Compression depth, determined for an extreme fiber compression strain of 0.003 for the applied axial load (270 kip; 1201 kN), was 26.7 in. ($0.30l_w$; 678 mm) for loading causing compression at the web boundary and 5.6 in. ($0.06l_w$; 142 mm) for loading causing compression at the flange boundary.

Table 3-2 provides details for SBE boundary longitudinal and transverse reinforcement including the longitudinal reinforcement bar size and quantity, transverse reinforcement bar size and spacing (s), the quantity of transverse reinforcement in the direction parallel to the length of the wall (A_{sh1}) and perpendicular to the length of the wall (A_{sh2}), and the ratio of the quantity of transverse reinforcement to the amount required by ACI 318-14 ($A_{sh}/A_{sh,req'd}$).

Table 3-2: Special Boundary Element (SBE) details

ID	**Longitudinal Reinforcement**	**Transverse Reinforcement**				**ACI 318-14 Requirements**		
		Bar Size	s	A_{sh1}/sb_{c1}	A_{sh2}/sb_{c2}	**Eqn. 2.11**		$A_{sh}/A_{sh,req'd}$
						(a)	**(a)**	
	---	---	**in. (mm)**	*%*	*%*	*%*	*%*	---
WP1	**8 No. 5 14 No. 4**	1/4"	2.00 (50.8)	0.77	1.00	0.62	0.75	1.02
WP2	**8 No. 5 14 No. 4**	5/16”	2.00 (50.8)	1.28	1.78	1.03	0.75	1.24
WP3	**8 No. 5 14 No. 4**	No. 3 5/16”	3.75 (95.3) 3.00 (76.2)	0.91 0.82	1.18 1.07	0.62	0.75	1.21 1.09
WP4	**10 No. 5**	5/16”	2.00 (50.8)	1.21	1.78	0.98	0.75	1.23
WP5	**7 No. 5 + 5 No. 4 10 No. 5**	5/16”	2.00 (50.8)	1.54 1.54	1.60 1.84	0.62 0.50	0.75	2.05
WP6	**10 No. 5**	5/16” 1/4"	2.00 (50.8)	0.77 1.23	1.15 1.84	0.50	0.75	1.02 1.64
WP7	**12 No. 5**	5/16” 1/4"	2.00 (50.8)	0.77 1.23	0.94 1.50	0.42	0.75	1.02 1.64

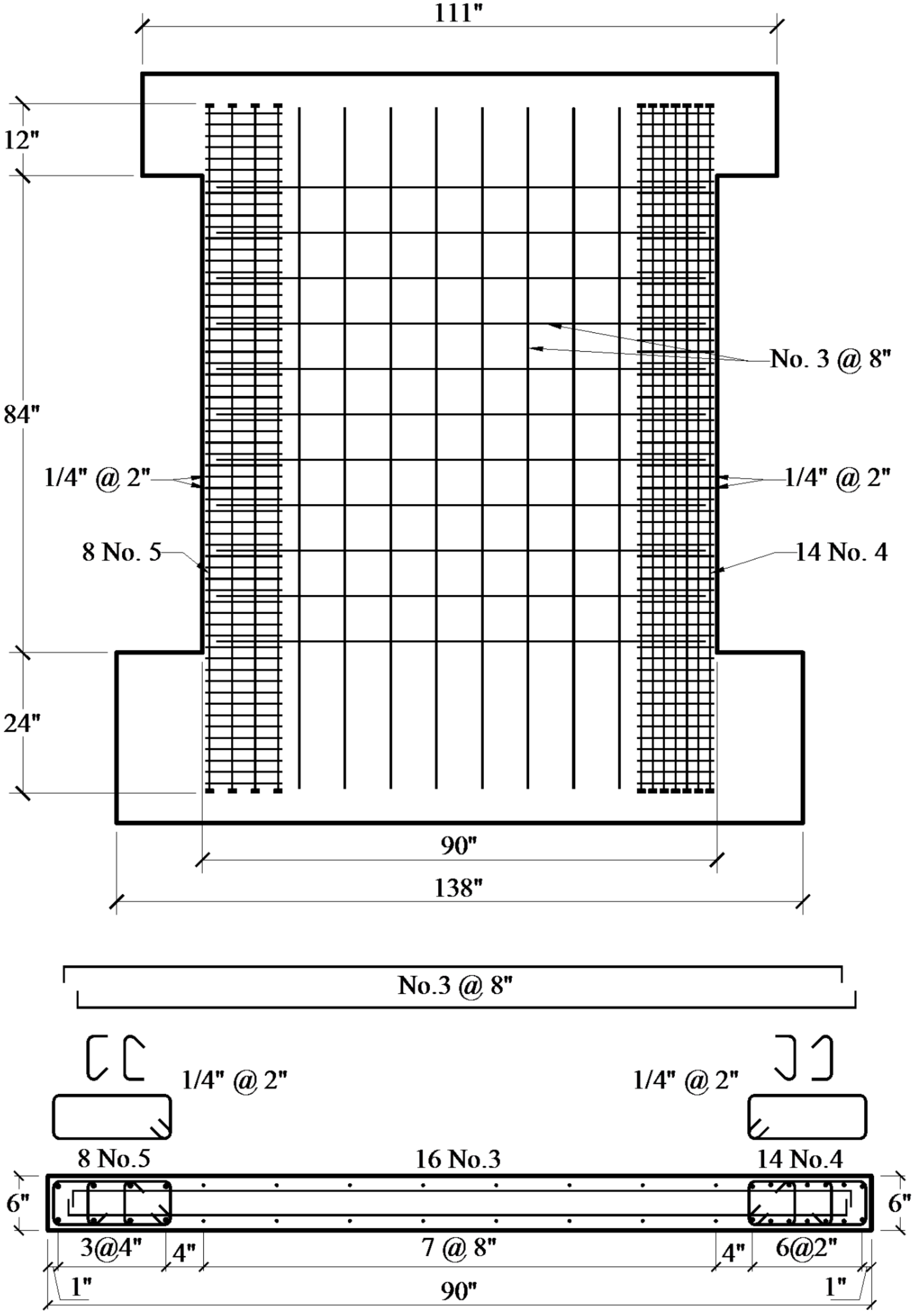

Figure 3-4: Specimen WP1 reinforcement (Conversion: 1”=25.4 mm)

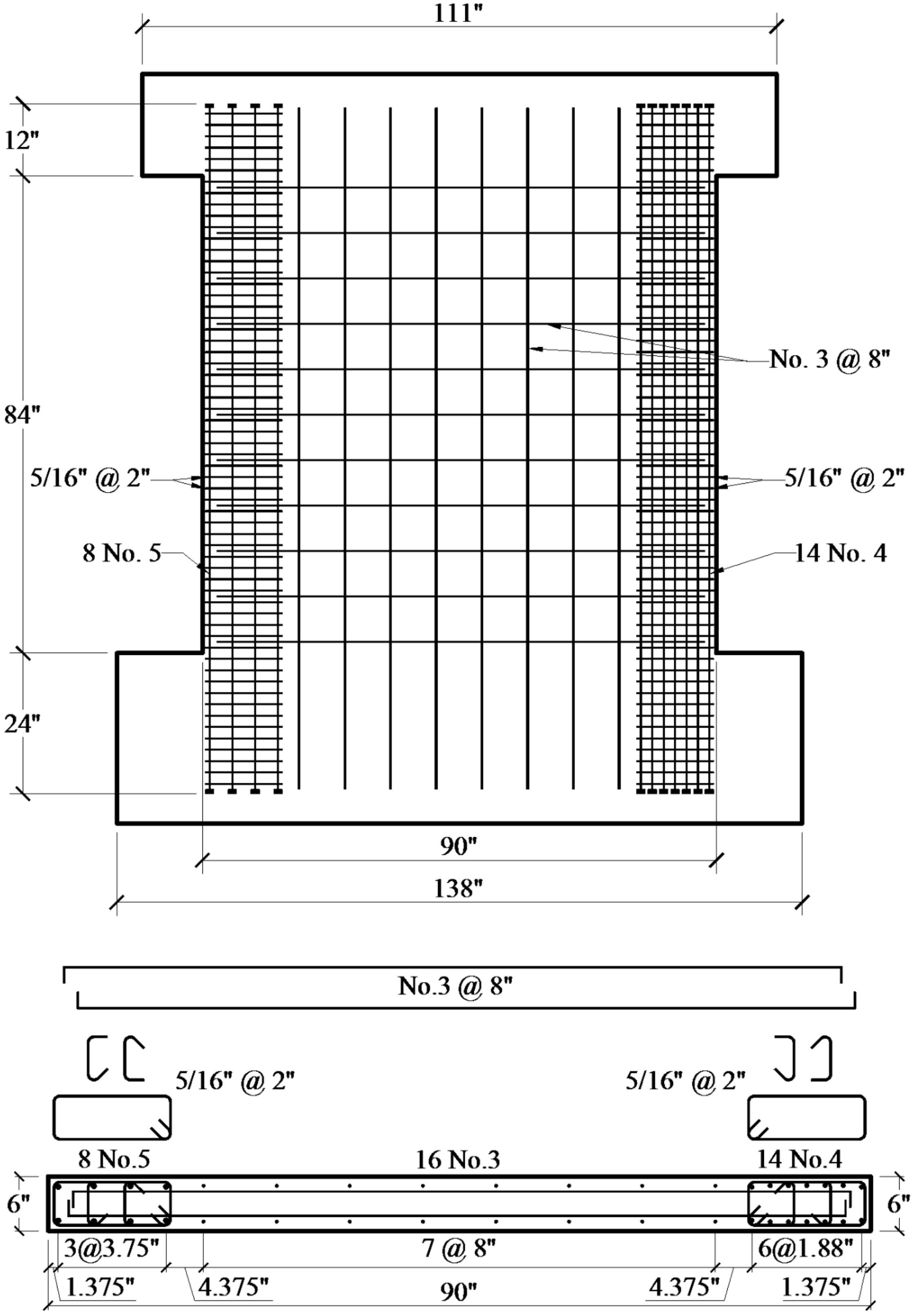

Figure 3-5: Specimen WP2 reinforcement (Conversion: 1"=25.4 mm)

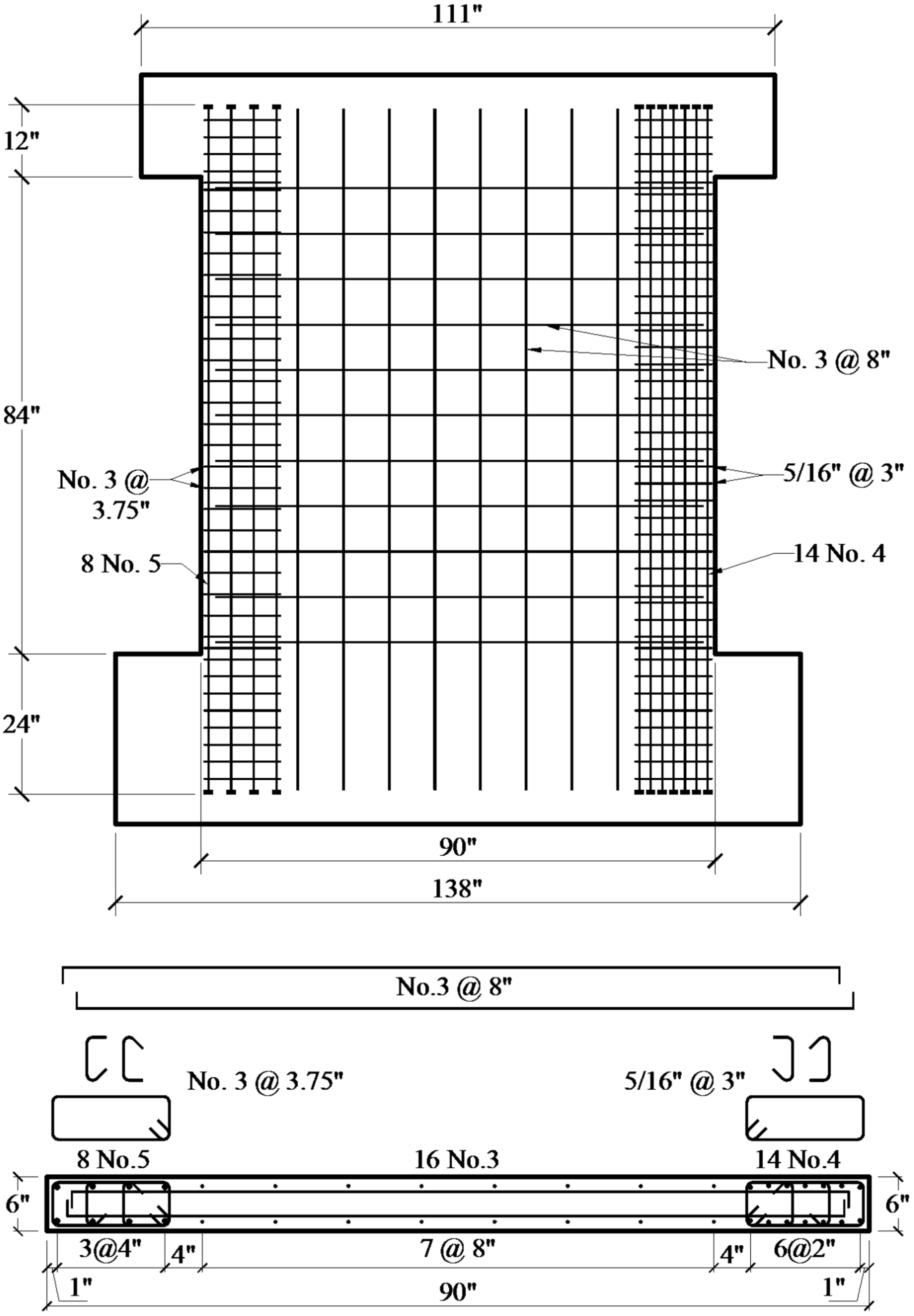

Figure 3-6: Specimen WP3 reinforcement (Conversion: 1”=25.4 mm)

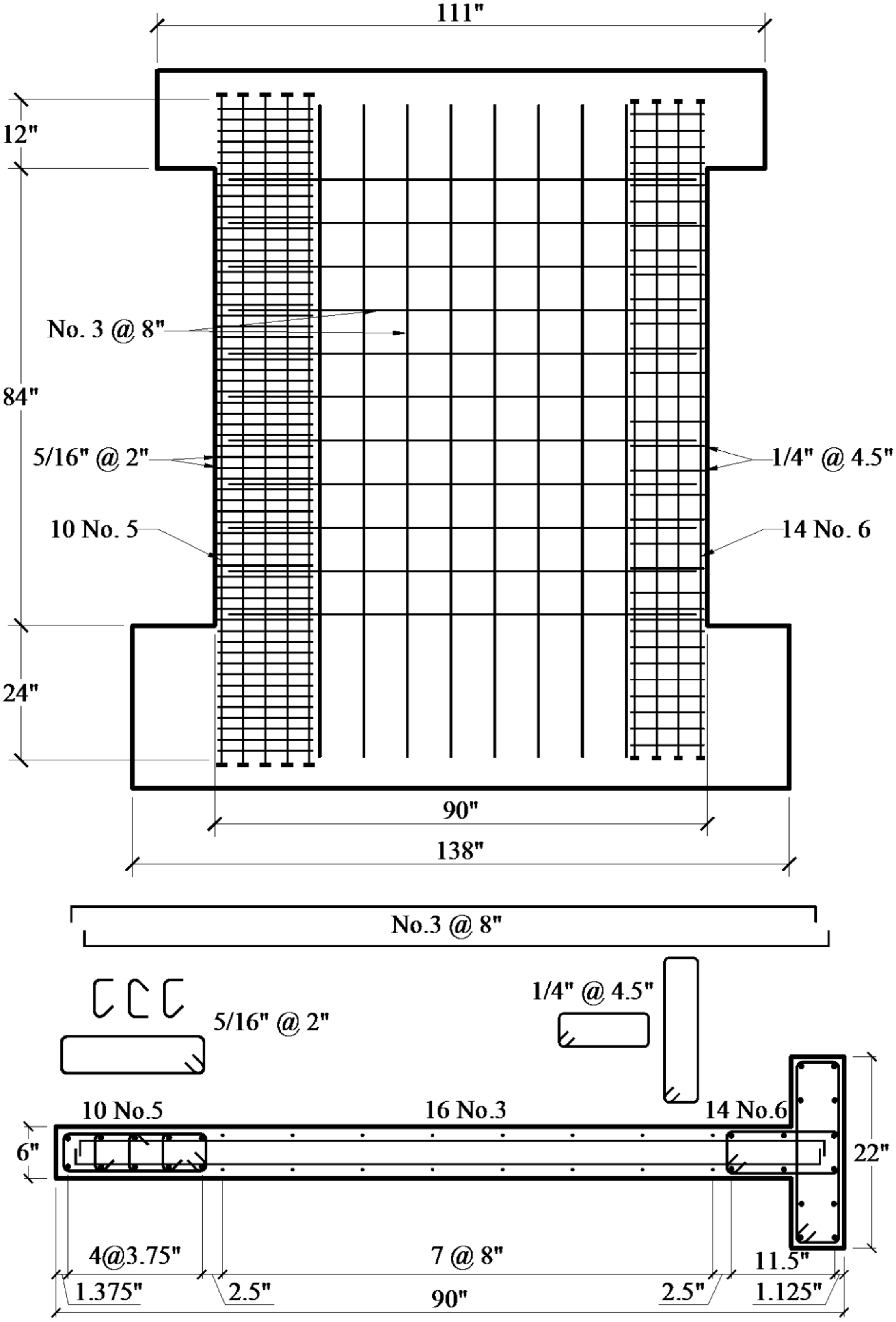

Figure 3-7: Specimen WP4 reinforcement (Conversion: 1”=25.4 mm)

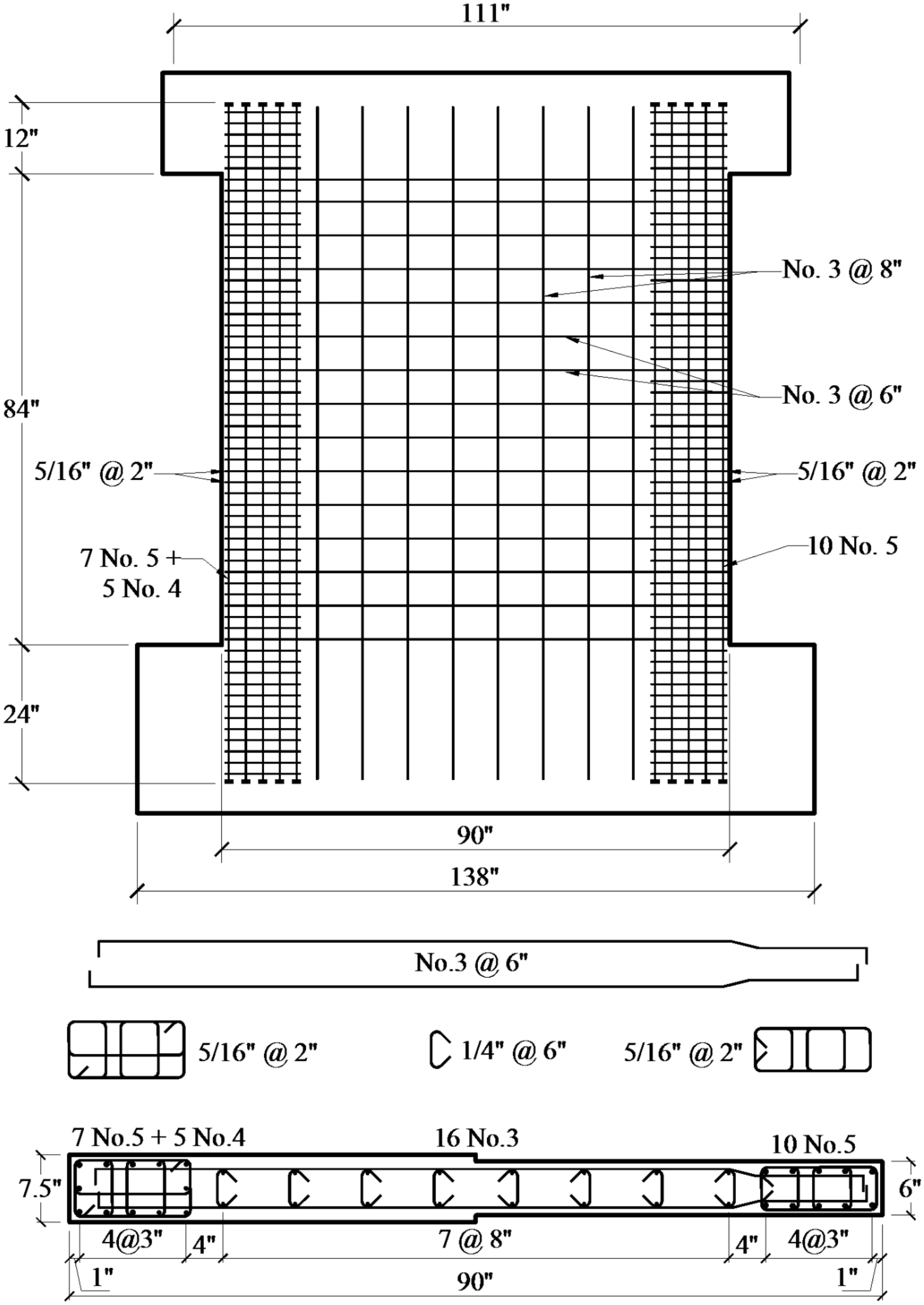

Figure 3-8: Specimen WP5 reinforcement (Conversion: 1”=25.4 mm)

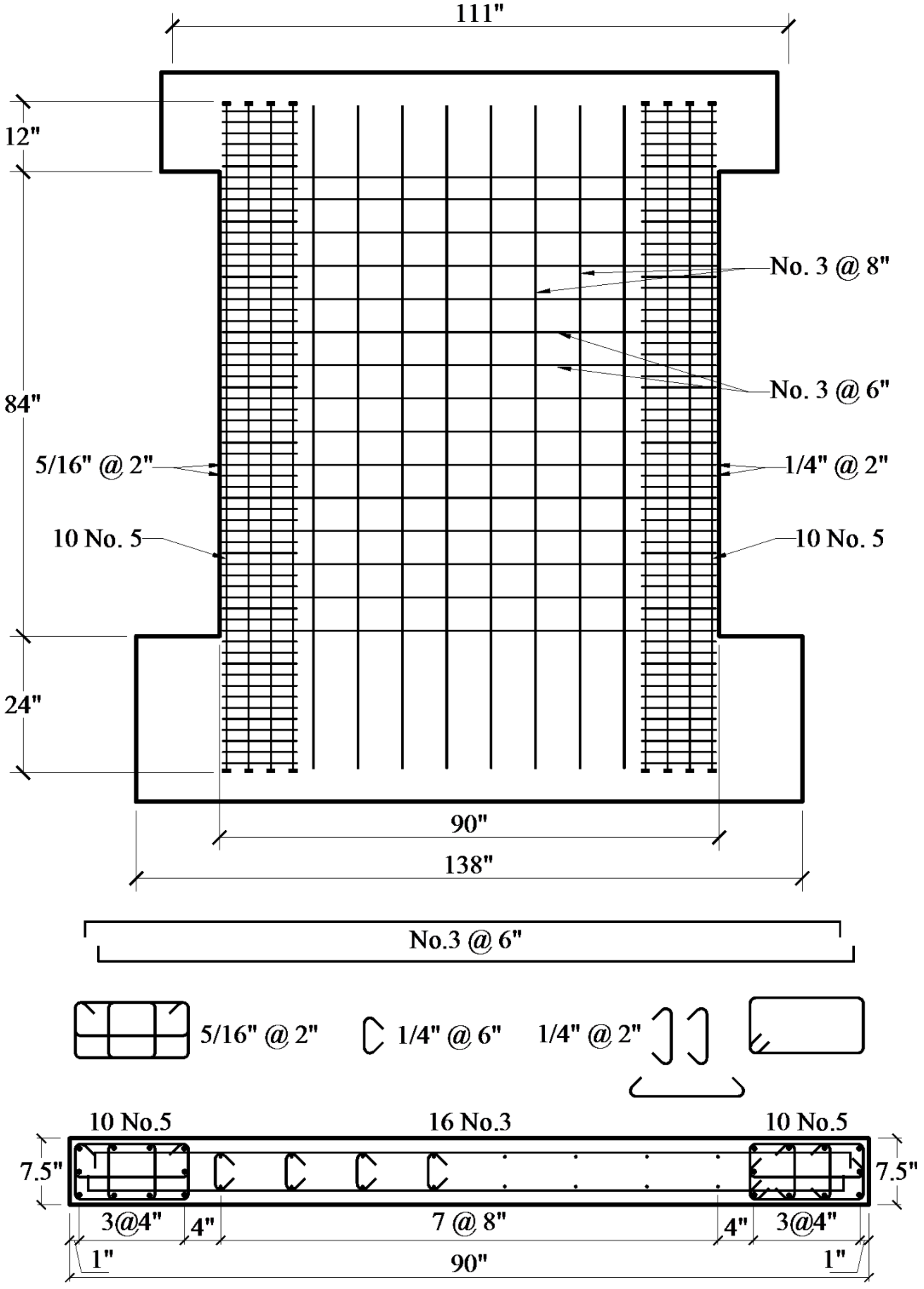

Figure 3-9: Specimen WP6 reinforcement (Conversion: 1”=25.4 mm)

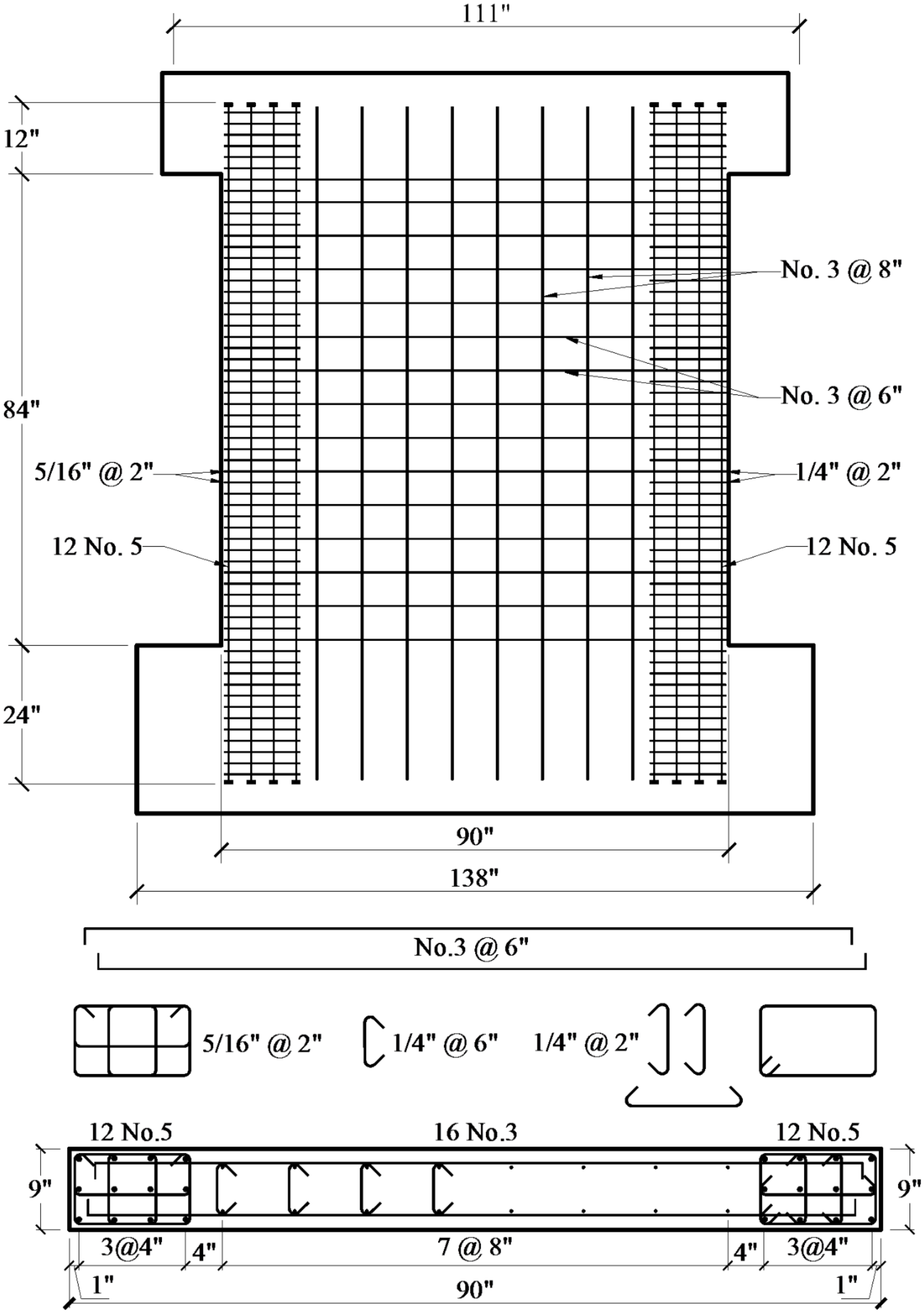

Figure 3-10: Specimen WP7 reinforcement (Conversion: 1"=25.4 mm)

Chapter 4 Experimental Program

This chapter summarizes the details of the experimental program including construction materials, test setup, loading protocol, experimental control, specimen instrumentation, and construction procedures.

4.1 Materials

Information related to the concrete and reinforcing steel used for each of the test specimens is discussed in this section. Test-day material properties are summarized, and individual material test results are provided.

4.1.1 Concrete

Normal-weight concrete with a design twenty-eight day compressive strength (f'_c) of 5 ksi (34.5 MPa) was specified for all test specimens. A 3/8 in. (9.5 mm) maximum aggregate size and 7 in. (178 mm) slump were specified to allow consolidation of concrete around heavily reinforced boundary regions and to accommodate pumping of concrete approximately 200 ft. (61m) from a truck outside of the laboratory.

For each specimen, 6 in. x 12 in. (152 mm x 305 mm) plain concrete cylinders were tested under uniform compression to determine average test-day concrete compressive strength. The tests were conducted at UCLA on a 220 kip (979 kN) capacity universal testing machine. The compressive stress-strain results are shown in Figure 4-2 for each cylinder tested, and measured peak compressive strength ($f'_{c,test}$), and the corresponding strain ($\varepsilon_{co,test}$), are reported in Table 4-1. Average $f'_{c,test}$ and $\varepsilon_{co,test}$ values for a particular wall panel test specimen are summarized in Table 4-2 and indicated in Figure 4-2 for each test specimen. Strain measurements were determined using a single compressometer with a 5 in. (127 mm) gage length (Figure 4-1). Values of $f'_{c,test}$ and $\varepsilon_{co,test}$ are compared in Figure 4-3 for all cylinders tested and grouped according to test specimens.

Figure 4-1: Concrete cylinder test setup

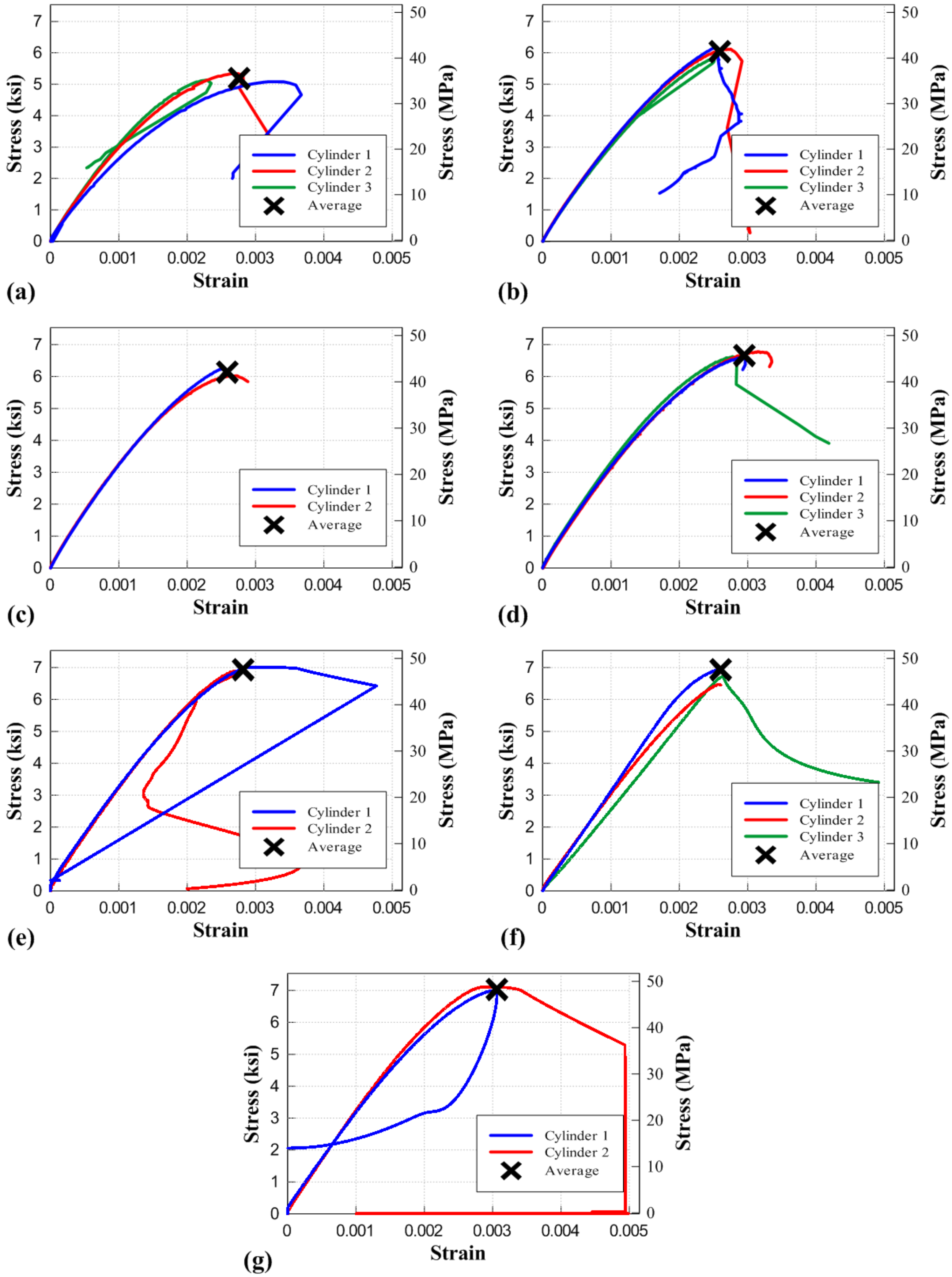

Figure 4-2: Concrete cylinder compressive stress-strain relationship – (a) WP1, (b) WP2, (c) WP3, (d) WP4, (e) WP5, (f), WP6, and (g) WP7

Table 4-1: Measured compressive strength and corresponding strain for concrete cylinders

ID	Wall Test Date	Cylinder Test Date	Cylinder Maturation Days	Cylinder #	$f'_{c,test}$	$\varepsilon_{co,test}$
					psi (Mpa)	---
WP1	8/29/2014	9/1/2014	23	1	5083 (35.0)	0.0033
				2	5339 (36.8)	0.0027
				3	5136 (35.4)	0.0023
WP2	9/16/2014	9/23/2014	45	1	6206 (42.8)	0.0025
				2	6120 (42.2)	0.0027
				3	5809 (40.0)	0.0025
WP3	9/30/2014	10/10/2014	62	1	6260 (43.2)	0.0025
				2	6025 (41.5)	0.0026
WP4	10/22/2014	10/24/2014	76	1	6593 (45.5)	0.0029
				2	6781 (46.8)	0.0032
				3	6624 (45.7)	0.0028
WP5	2/23/2016	2/22/2016	117	1	7008 (48.3)	0.0029
				2	6881 (47.4)	0.0027
WP6	3/14/2016	3/23/2016	147	1	6946 (47.9)	0.0026
				2	6471 (44.6)	0.0026
				3	6712 (46.3)	0.0026
WP7	4/27/2016	5/2/2016	187	1	6985 (48.2)	0.003
				2	7100 (49.0)	0.0031

Table 4-2: Average compressive strength and corresponding strain

ID	Wall Test Date	Cylinder Test Date	Cylinder Maturation Days	# Cylinders Tested	$f'_{c,test}$	$\varepsilon_{co,test}$
					psi (Mpa)	---
WP1	8/29/2014	9/1/2014	23	3	5186 (35.8)	0.0028
WP2	9/16/2014	9/23/2014	45	3	6045 (41.7)	0.0026
WP3	9/30/2014	10/10/2014	62	2	6143 (42.4)	0.0026
WP4	10/22/2014	10/24/2014	76	3	6666 (46.0)	0.0030
WP5	2/23/2016	2/22/2016	117	2	6945 (47.8)	0.0028
WP6	3/14/2016	3/23/2016	147	3	6710 (46.3)	0.0026
WP7	4/27/2016	5/2/2016	187	2	7043 (48.6)	0.0031

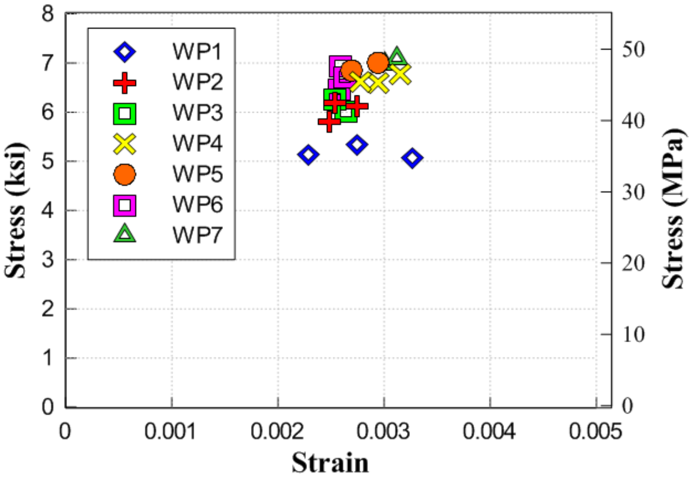

Figure 4-3: Concrete cylinder average compressive strength ($f'_{c,test}$) and peak strain ($\varepsilon_{co,test}$)

4.1.2 Reinforcing Steel

ASTM A615 and A706 (ASTM A615/A615M-16, 2016; ASTM A706/A706M-16, 2016) Grade 60 (60 ksi [414 MPa] nominal yield strength) reinforcement was specified for all test specimens. All No. 3, No. 4, No. 5, and No. 6 reinforcing bars conformed to ASTM A615/A706 Grade 60 standards. Because ASTM A615/A706 Grade 60 reinforcement is not available in the United States in bar sizes smaller than No. 3, 1/4" (actual nominal diameter of 0.252 in. [6.4 mm]) and 5/16” (actual nominal diameter of 0.319 in. [8.1 mm]) wire reinforcement with properties similar to ASTM A615/A706 were used. For specimens WP1-WP4, cold-drawn Grade 80 (80 ksi [552 MPa] nominal yield strength) deformed wire was used. The deformed wire was heat treated to reduce the yield strength and to achieve ductility properties similar to Grade 60 ASTM A615/A706 steel. For specimens WP5-WP7, hot-rolled smooth wire to better match ASTM A615/A706 Grade 60 properties.

For each bar size, 24 in. (610 mm) long sample bars were tested in direct tension to determine as-built steel mechanical properties. The tests were conducted at UCLA on a 220 kip (979 kN) capacity universal testing machine. For specimens WP1-WP4, additional sample bars were tested by Twining prior to the UCLA tests. The tensile stress-strain result for each bar tested at UCLA is shown in Figure 4-7 for specimens WP1-4 and in and Figure 4-8 for specimens WP5-7. The stress-strain curve for 5/16” wire for specimens WP1-WP4 was inferred from Twining strength test results because no additional samples were available for testing at UCLA. Strain measurements were determined using linear variable differential transducers (LVDTs) with an 8 in. (203 mm) gage length (Figure 4-4). The stress-strain at which rupture occurred is indicated by an “x” in Figure 4-7 and Figure 4-8. The reported rupture strain was determined from LVDT results for tests in which rupture occurred within the gage length. For each bar, marks were placed on the bar at 1 in. (25 mm) intervals prior to the test. For tests in which rupture occurred outside of the gage length, reported rupture strain was determined using these marks over an 8 in. (203 mm) length in which rupture occurred (Figure 4-5). For tests in which rupture occurred outside the gage length, a dashed line is shown in Figure 4-7 and Figure 4-8 to indicate the strains measured in the ruptured zone.

Bar cross-sectional dimensions and average measured mechanical properties are provided in Table 4-3. Stress and strain values corresponding to yield ($f_{y,test}$, ε_y), tensile strength (f_{peak}, ε_{peak}), and rupture (f_{rup}, ε_{rup}) are given, along with the strain at which strain-hardening initiated (ε_{sh}). Yield stress was determined using a 0.2% strain offset from the initial elastic branch. Typical stress-strain results are shown in Figure 4-6 for each bar size tested.

Figure 4-4: Steel reinforcement tension test setup

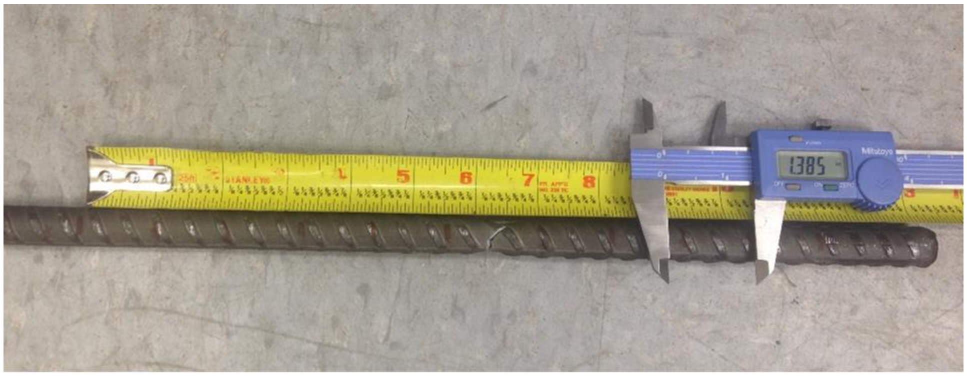

Figure 4-5: Rupture strain measurement outside gage length

Table 4-3: Steel reinforcement tensile stress-strain properties

Test ID	Bar Size	Diameter	Area	$f_{y,test}$	ε_y	ε_{sh}	f_{peak}	ε_{peak}	f_{rup}	ε_{rup}
		in. (mm)	in.^{2} (mm^2)	ksi (Mpa)	---	---	ksi (Mpa)	---	ksi (Mpa)	---
WP1 WP2 WP3 WP4	1/4"	0.252 (6.4)	0.05 (32.2)	48.9 (337)	0.0017	0.005	58.5 (403)	0.059	31.0 (214)	0.075
	5/16”	0.319 (8.1)	0.08 (51.6)	58.9 (406)	0.0020	0.004	69.8 (481)	0.057	---	---
	No. 3	0.375 (9.5)	0.11 (71.3)	83.9 (578)	0.0029	0.008	105.3 (726)	0.103	85.8 (592)	0.134
	No. 4	0.500 (12.7)	0.20 (127)	73.4 (506)	0.0025	0.013	107.8 (743)	0.111	102.5 (707)	0.142
	No. 5	0.625 (15.9)	0.31 (198)	77.0 (531)	0.0027	0.011	107.6 (742)	0.111	78.6 (542)	0.154
	No. 6	0.750 (19.1)	0.44 (285)	76.9 (530)	0.0027	0.014	104.8 (723)	0.138	81.2 (560)	0.186
WP5 WP6 WP7	1/4"	0.252 (6.4)	0.05 (32.2)	70.6 (487)	0.0024	0.012	86.8 (598)	0.092	52.1 (359)	0.096
	5/16”	0.319 (8.1)	0.08 (51.6)	63.7 (439)	0.0022	0.016	77.1 (531)	0.071	34.5 (238)	0.103
	No. 3	0.375 (9.5)	0.11 (71.3)	65.8 (454)	0.0023	0.012	102.4 (706)	0.124	85.3 (588)	0.167
	No. 4	0.500 (12.7)	0.20 (127)	74.1 (511)	0.0026	0.004	105.5 (728)	0.138	77.4 (534)	0.163
	No. 5	0.625 (15.9)	0.31 (198)	70.9 (489)	0.0024	0.012	97.1 (669)	0.143	64.9 (447)	0.169

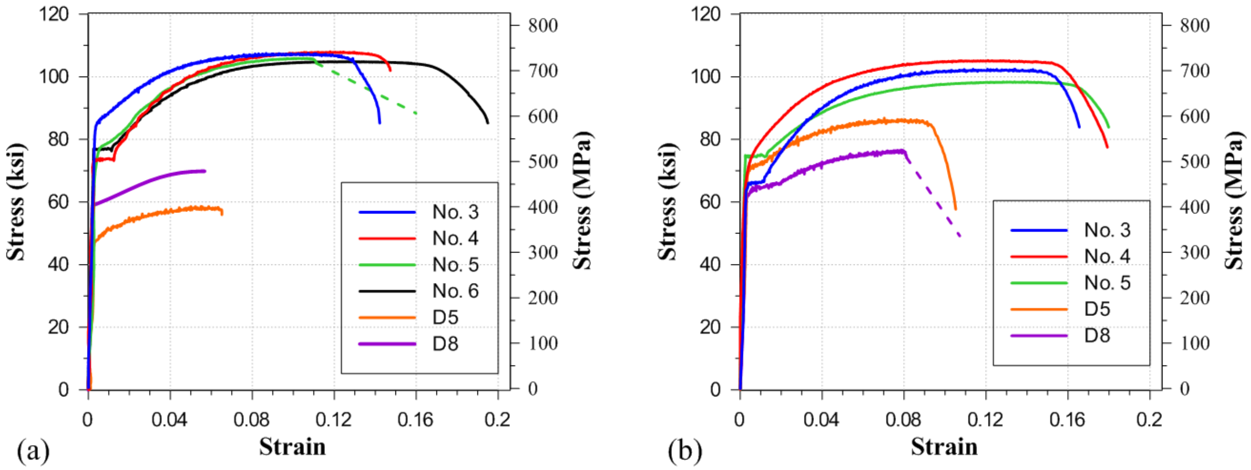

Figure 4-6: Steel reinforcement tensile stress-strain relationship – (a) Specimens WP1-WP4 and (b) Specimens WP5-WP7

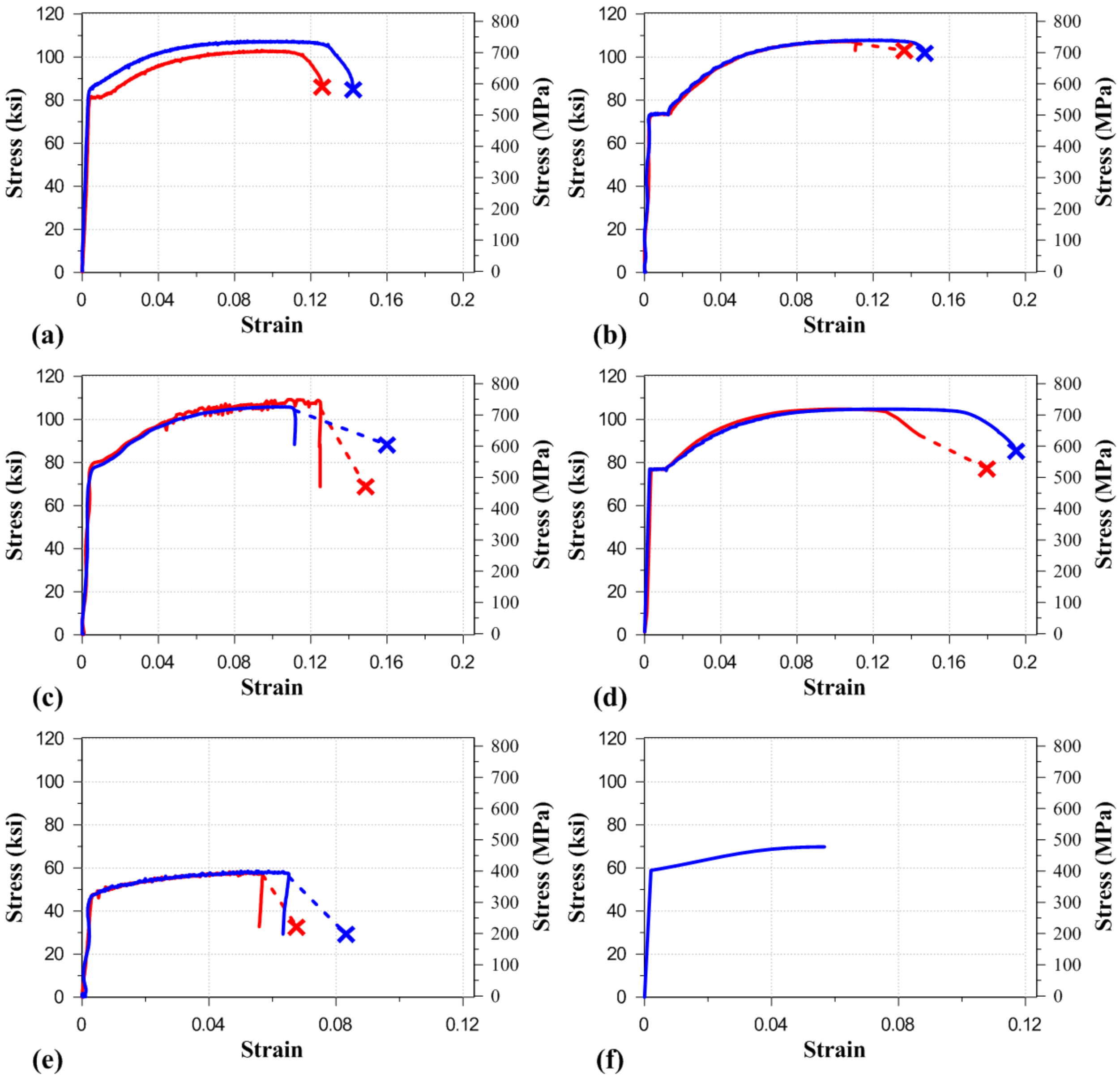

Figure 4-7: Steel reinforcement tensile stress-strain relationship for specimens WP1-WP4 – (a) No. 3 bars, (b) No. 4 bars (c) No. 5 bars, (d) No. 6 bars, (e) 1/4" wire, and (f), 5/16" wire

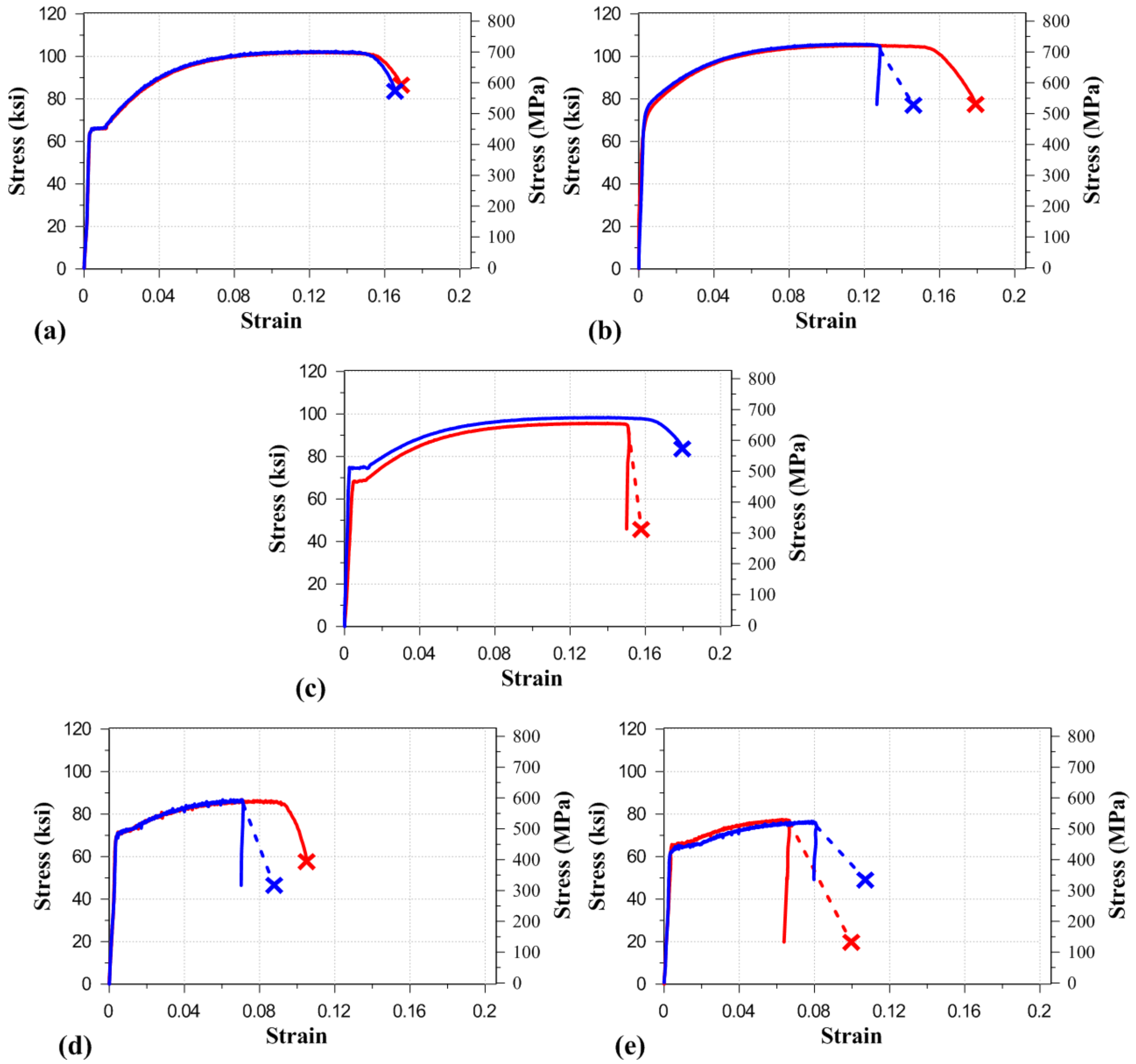

Figure 4-8: Steel reinforcement tensile stress-strain relationship for specimens WP5-WP7 – (a) No. 3 bars, (b) No. 4 bars (c) No. 5 bars, (d) 1/4" wire, and (e), 5/16" wire

4.2 Test Setup

The loading pattern applied to the test specimens was determined based on the Equivalent Lateral Force (ELF) Procedure of ASCE 7-10 Chapter 12 (ASCE/SEI, 2010). Figure 4-9a shows the distribution of code prescribed vertical story forces (P_i) and lateral story seismic forces ($F_{x,i}$) on an eight-story cantilever wall. The resulting shear force, overturning moment, and axial force diagrams for the code prescribed loading are also shown.

For a slender wall designed to yield in flexure, a single critical section is expected to occur near the base of the wall for the loading shown in Figure 4-9a. Inelastic deformations are expected to concentrate within the lower portion of the wall (plastic hinge region), making it possible to capture inelastic response using a wall panel specimen representative of the plastic hinge region of the wall (Figure 4-9b). Figure 4-9b depicts the boundary conditions that need to be applied to a wall panel specimen to achieve the loading conditions at the base of the cantilever tall. At the top of the wall panel specimen, a vertical load is applied to produce the axial load demand expected at the base of the wall, and a moment is applied to capture the overturning demand due to the lateral story forces. A lateral force is applied at the top of the specimen to capture the shear demand resulting from the story forces and to obtain a moment gradient over the height of the panel specimen.

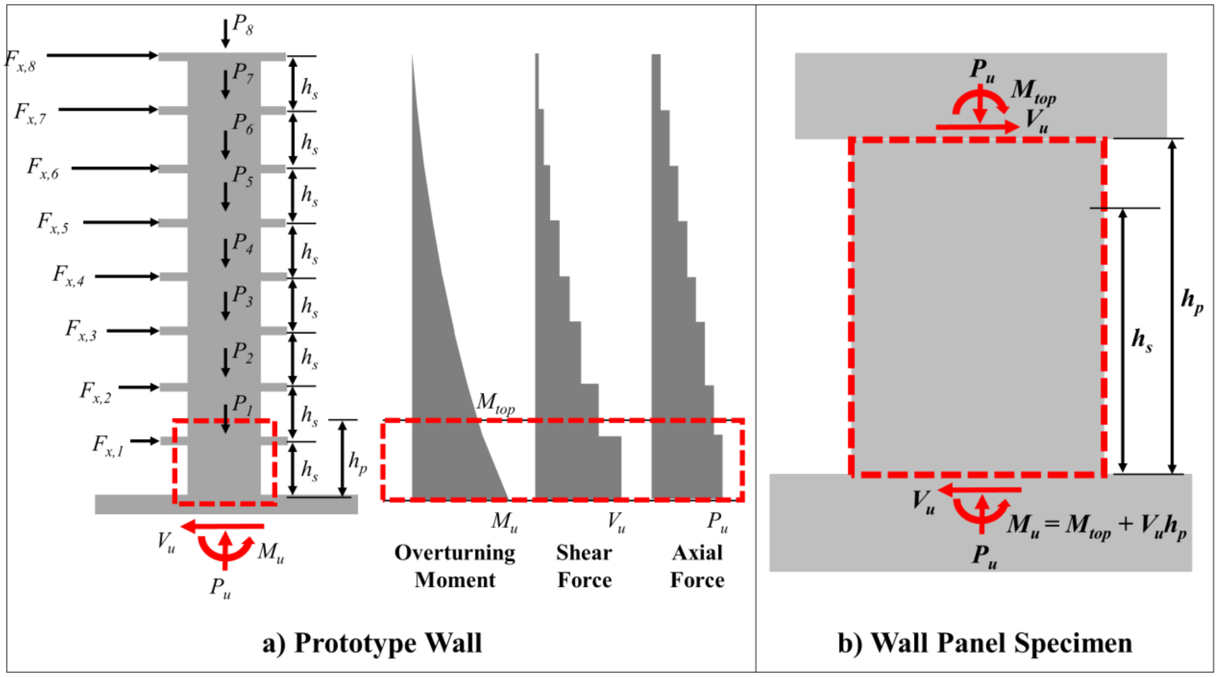

Figure 4-9: a) Code force distribution on prototype wall, and b) Applied loading pattern for wall panel specimen

A schematic diagram of the experimental test setup used to achieve the boundary conditions of Figure 4-9b is shown in Figure 4-10, and photos of the test setup for a typical specimen are shown in Figure 4-11 and Figure 4-12. Specimen footings were secured to the laboratory strong floor using 1.25 in. (32 mm) diameter high-strength post-tensioning rods spaced 24 in. (610 mm) apart. Loading was applied using two vertically-aligned 400 kip (1779 kN) nominal capacity actuators with +/- 18 in. (457 mm) stroke capacity (designated Actuator 1 and Actuator 2 in Figure 4-10), one horizontally-aligned 300 kip (1335 kN) nominal capacity actuator with +/- 12 in. (305 mm) stroke capacity (designated Actuator 3 in Figure 4-10), and two 220 kip (981 kN) capacity hydraulic jacks with 6 in. (152 mm) stroke capacity. The three actuators applied loads to a steel load transfer beam that was attached to specimen top caps using 1.25 in. (32 mm) diameter high-strength post-tensioning rods. The hydraulic jacks were mounted above a second load transfer beam (designated Axial Load Transfer Beam in Figure 4-10) and were each attached to a 1.25 in.

(32 mm) diameter high-strength post-tensioning rod that was anchored to the laboratory strong floor.

Axial compression was applied to the wall panel specimens using the two hydraulic jacks and the two vertical actuators. The two vertical actuators, spaced 18 ft. (5486 mm) apart, applied opposing vertical forces to apply an overturning moment at the top of the specimens. The horizontal actuator applied a lateral force 114 in. (2642 mm) above the top of specimen footings, imposing lateral shear force and additional overturning moment to achieve the desired moment gradient.

Two vertically-aligned control sensors, mounted at opposite ends of the wall, monitored the average rotation at the base of the wall over an assumed hinge length of one-half the length of the wall ($l_w/2$=45 in. [1143 mm]). Out-of-plane movement of the specimen top caps was prevented by an out-of-plane restraint system (Figure 4-12) that connected to a strong wall parallel to the test specimens.

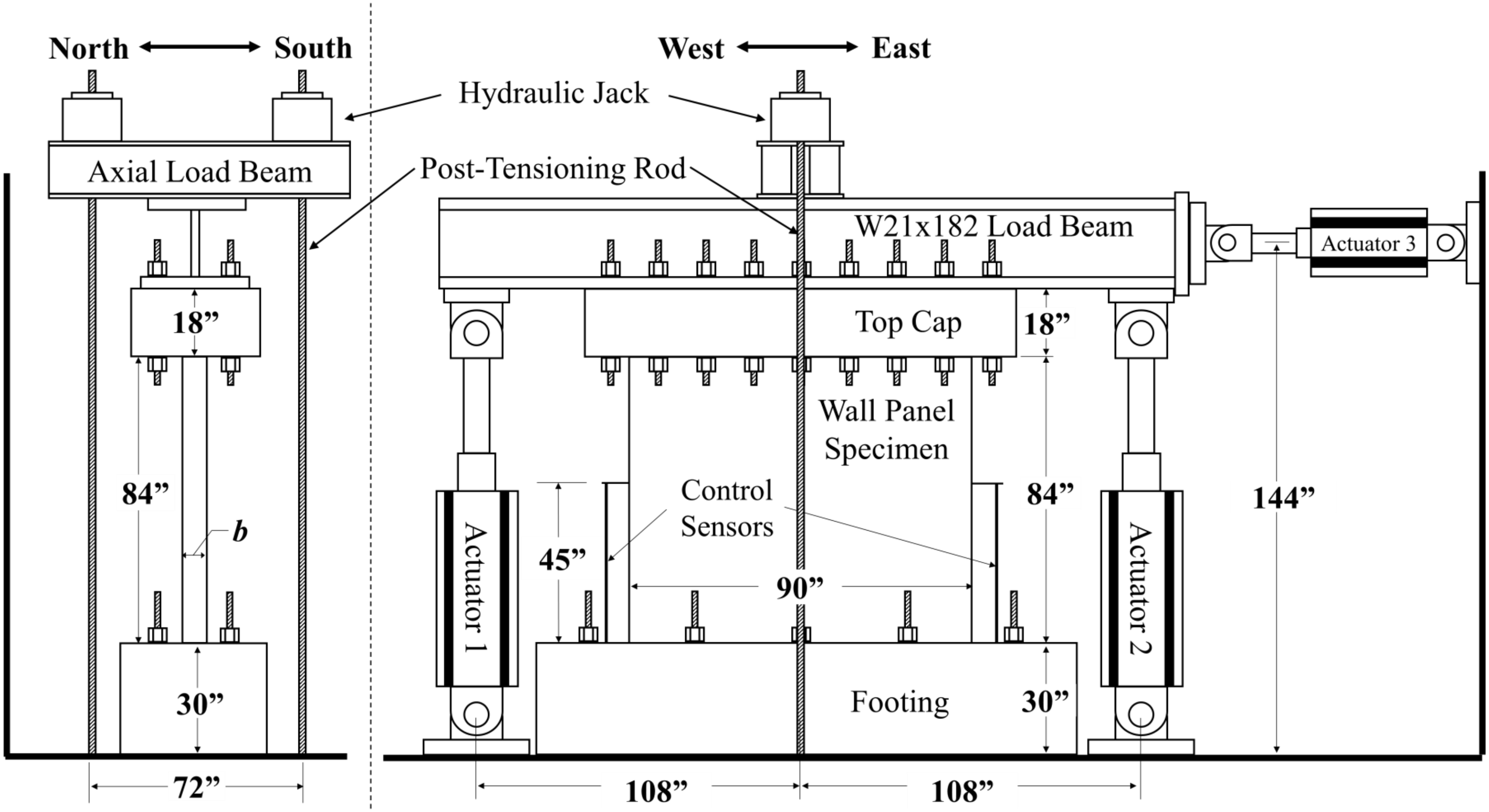

Figure 4-10: Test setup (Conversion: 1”=25.4 mm)

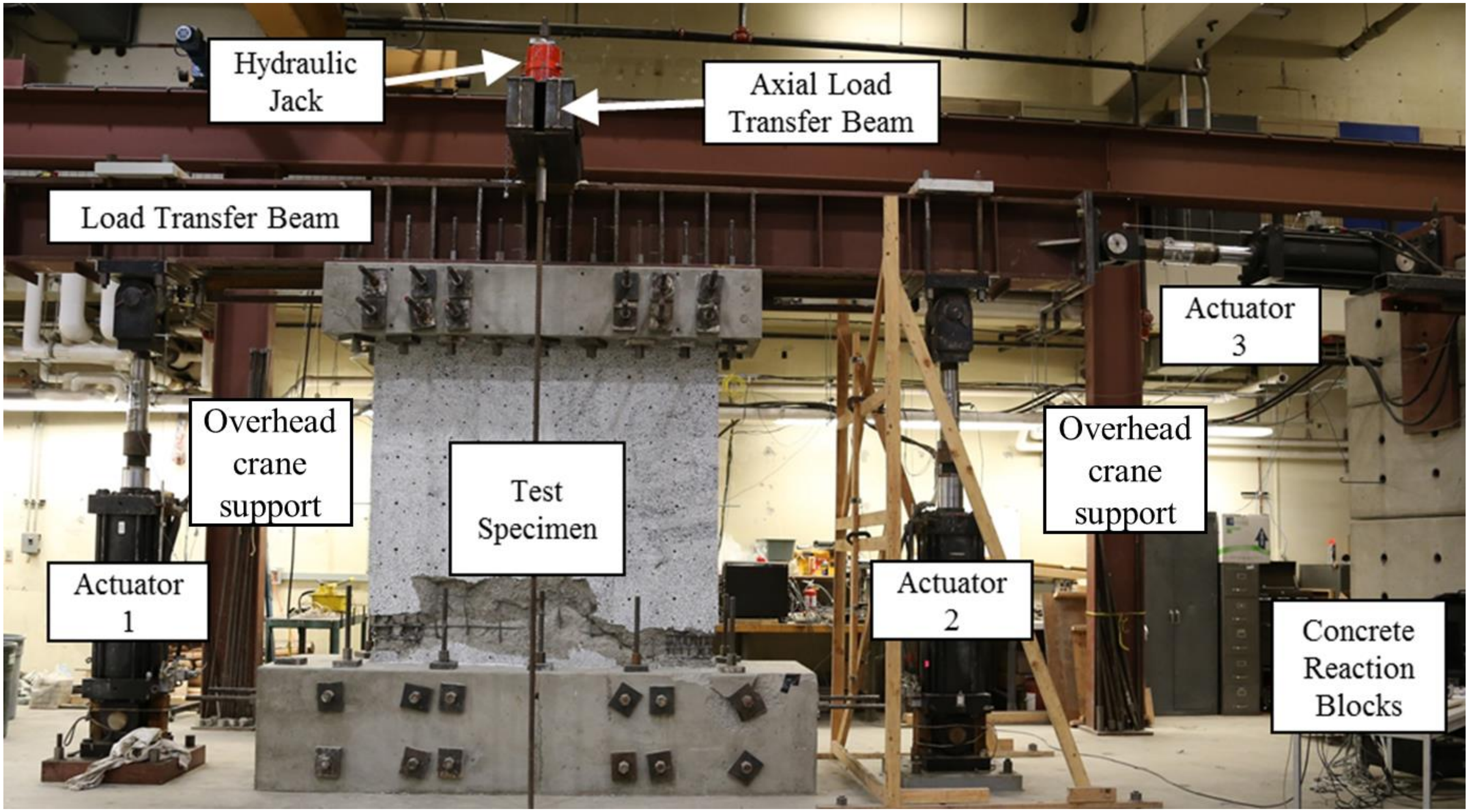

Figure 4-11: Typical test setup

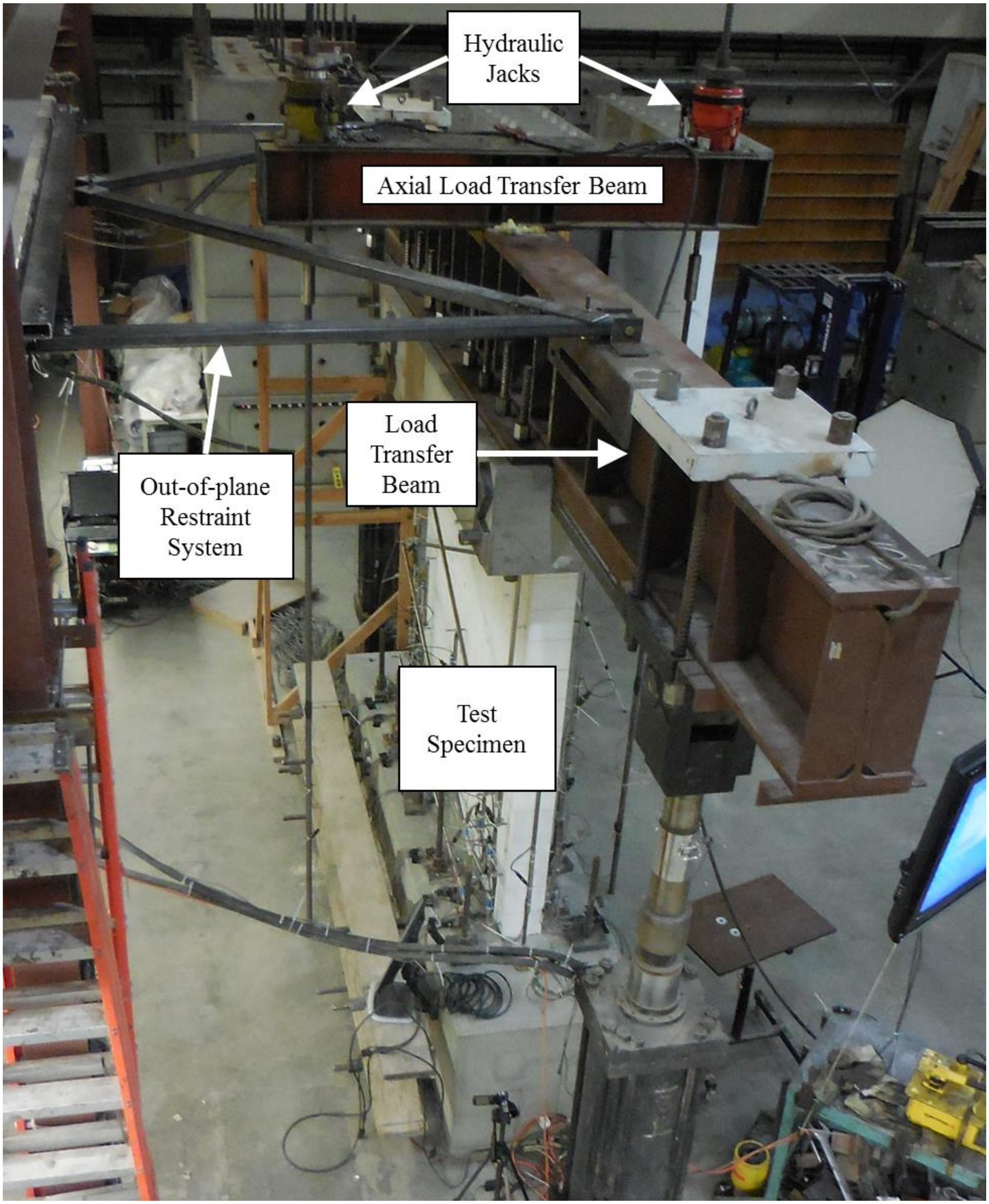

Figure 4-12: Axial load transfer beam and out-of-plane restraint

4.3 Testing Protocol

A free body diagram of the test setup is shown in Figure 4-13. At the beginning of each test, axial load was applied by the hydraulic jacks and by the two vertical actuators. Following application of the axial load, reversed-cyclic moment and shear were applied by the two vertical actuators and the horizontal actuator. Equation 4.1 demonstrates the components of the actuator loads used to apply the loading boundary conditions shown in Figure 4-9b.

$$\begin{aligned} P_u &= P_{jacks} + P_1 + P_2 && (a) \\ V_u &= F_3 && (b) \\ M_{top} &= -\Delta F_1 x_1 + \Delta F_2 x_2 && (c) \end{aligned} \qquad 4.1$$

The lateral forces on the eight-story wall shown in Figure 4-9a are proportional (i.e., $F_{x,i}=\alpha_{i,j}\,F_{x,j}$ where $\alpha_{i,j}$ is a constant). Their magnitude is based on the geometry of the wall (i.e., story heights) and the distribution of story mass. Because they are proportional, the resulting moment-to-shear ratio (M/V) at any particular section along the height of the wall is constant. For an eight-story wall with uniform story height ($h_{s,i} = h_{s,j}$) and story mass ($m_{s,I} = m_{s,j}$), the magnitude of the moment at the top of the first story is approximately 80% of the base moment ($M_1/M_b \approx 0.80$). A relationship between the applied lateral force and the applied moment at the top of the specimens (M_{top}/V_u) was derived to ensure that the ratio M_1/M_b was constant throughout the tests. M_1 and M_b are defined in Equation 4.2.

$$\begin{aligned} M_1 &= -\Delta F_1 x_1 + \Delta F_2 x_2 + F_3\left(x_3 - h_s\right) && (a) \\ M_b &= -\Delta F_1 x_1 + \Delta F_2 x_2 + F_3 x_3 && (b) \end{aligned} \qquad 4.2$$

For a constant M_1/M_b, denoted ζ, M_{top}/V_u is defined by Equation 4.3 based on the definitions of Equations 4.1 and 4.2.

$$\frac{M_1}{M_b}=\frac{-\Delta F_1 x_1+\Delta F_2 x_2+F_3\left(x_3-h_s\right)}{-\Delta F_1 x_1+\Delta F_2 x_2+F_3 x_3}=\frac{M_{top}+V_u\left(x_3-h_s\right)}{M_{top}+V_u x_3}=\zeta \quad (a)$$

$$\frac{M_{top}}{V_u}=\frac{x_3\left(1-\zeta\right)-h_s}{\left(\zeta-1\right)} \quad \text{(b)} \qquad 4.3$$

Equation 4.3 is used to derive a relationship between the moment at the base of the wall and the applied lateral force (M_b/V_u).

$$\frac{M_b}{V_u}=\frac{-\Delta F_1 x_1+\Delta F_2 x_2+F_3 x_3}{F_3} \quad \text{(a)}$$

$$\frac{M_b}{V_u}=\frac{M_{top}}{V_u}+x_3=\frac{x_3\left(1-\zeta\right)-h_s}{\left(\zeta-1\right)}+x_3 \quad (b) \qquad 4.4$$

Table 4-4 summarizes the loading pattern for each test. M_b/V_u was held constant at the value reported in Table 4-4 for the duration of each test. Two values are reported for specimen WP5 because a different axial load was applied in the two loading directions.

Table 4-4: Wall panel loading protocol

ID	P_u	M_n	$V_u @ M_n$	$\frac{V_u}{b l_w \sqrt{f'_c}}$	M_b / V_u	$M_b / V_u \ l_w$
	kip (kN)	**k-ft (kN-m)**	**kip (kN)**	f'_c **in psi (MPa)**	**ft. (m)**	**---**
(1)	**(2)**	**(3)**	**(4)**	**(5)**	**(6)**	**(7)**
WP1	270 (1201)	2198 (2981)	78.2 (348)	2.05 (0.17)	28.1 (8.56)	3.75
WP2	270 (1201)	2198 (2981)	78.2 (348)	2.05 (0.17)	28.1 (8.56)	3.75
WP3	270 (1201)	2198 (2981)	78.2 (348)	2.05 (0.17)	28.1 (8.56)	3.75
WP4	270 (1201)	3392 (4599)	77.1 (343)	2.02 (0.17)	44.0 (13.4)	5.87
WP5	337.5 (1501)	2559 (3470)	95.5 (425)	2.00 (0.17)	26.8 (8.17)	3.57
	270 (1201)	2338 (3170)	87.2 (388)	2.28 (0.19)	26.8 (8.17)	3.57
WP6	337.5 (1501)	2559 (3469)	95.5 (425)	2.00 (0.17)	26.8 (8.17)	3.57
WP7	405 (1802)	3018 (4092)	115 (512)	2.00 (0.17)	26.3 (8.03)	3.50

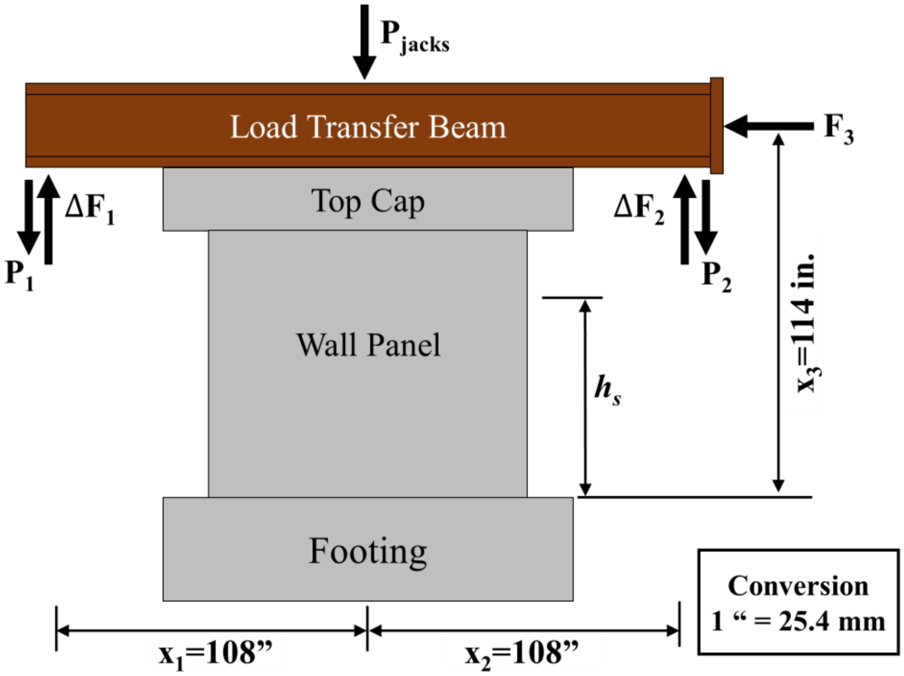

Figure 4-13: Testing protocol free-body diagram

The testing protocol consisted of force-controlled cycles followed by increasing displacement-controlled cycles until failure was observed (Figure 4-14). Force-controlled cycles were conducted such that the moment at the base of the wall (M_b) reached 1/8, 1/4, 1/2, and 3/4 of the expected yield moment (M_y) for three cycles at each target load level. Displacement-controlled cycles were based on wall hinge rotation, determined as the average rotation between two control sensors at opposite ends of the wall (Figure 4-13). Hinge rotation was measured over an assumed hinge length of one-half the length of the wall. Displacement-controlled cycles targeted 0.25%, 0.375%, 0.50%, 0.75%, 1%, 1.5%, 2%, and 3% hinge rotation. Three cycles were performed at each target rotation level up to 1.5% rotation. For cycles exceeding 1.5% rotation, two cycles were performed at each increment level. Positive loading corresponds to loading causing compression at the west boundary of the walls.

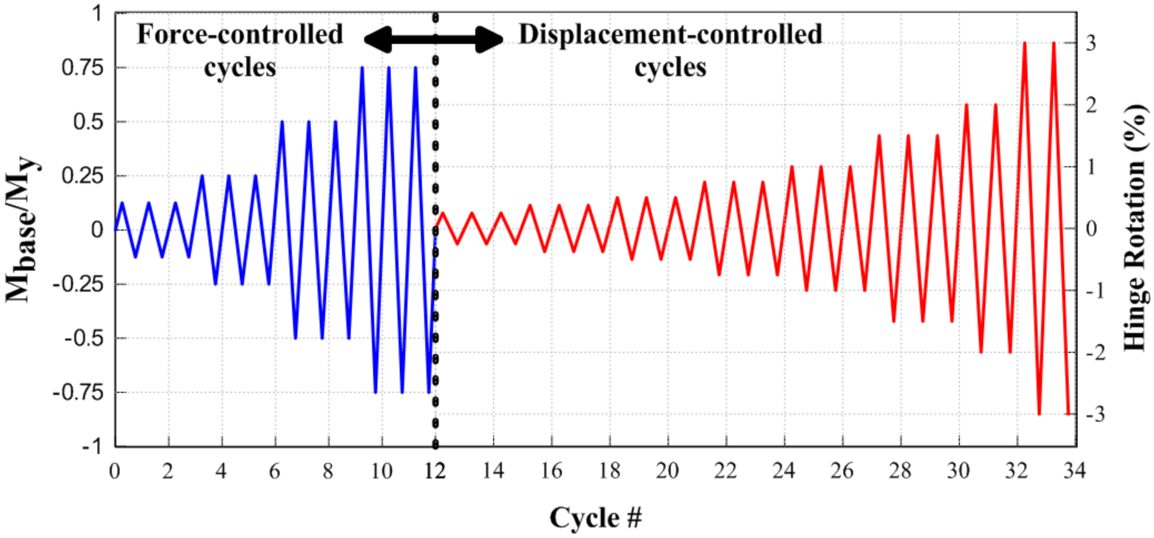

Figure 4-14: Loading protocol

4.4 Experimental Control and Data Acquisition

The loads applied by the horizontal actuator and the two vertical actuators were measured by load cells attached to the actuator extension rods. Actuator displacements were measured by linear variable differential transducers (LVDT) mounted to the outside of the actuators. All three actuators were connected to a single hydraulic pump by two hydraulic lines each – one line supplied hydraulic oil from the pump to the actuator cylinder and the other returned oil from the actuator cylinder to the pump. Flow of oil into and out of actuator cylinders was regulated by the actuator's servo-valve which connected to the oil supply line on one side of the valve and to the return line on the other side of the valve. The servo-valves were commanded by a MTS FlexTest GT controller that operates a proportional-integral-derivative (PID) control feedback loop based on feedback signals from actuator load cells and LVDTs.

The hydraulic jacks were connected to a manually-operated hydraulic hand pump. Two strain gages were mounted on opposite sides of the post-tensioning bars to which the jacks were attached. The axial load applied to wall specimens by the hydraulic jacks was monitored throughout the tests based on calibrated strain gage measurements. Prior to testing specimen WP5, a digital pressure gauge was installed on the hydraulic line of the hand pump. For specimens WP5-WP7, the axial load applied by the jacks was monitored both by strain gage data and digital pressure gauge data.

The three actuators were controlled on a set of equations to satisfy the following conditions (based on the protocol discussed in Section 4.3):

1. The total axial load applied by the two vertical actuators and the hydraulic jacks was constant throughout the test ($P_{jacks}+P_1+P_2 = P_u$). The value of the target axial force (P_u) for each test is given in Table 4-4.

2. The ratio of base moment to base shear (M_b/V_u) was constant throughout the test. The value of M_b/V_u for each test is given in Table 4-4.

For specimens WP1-WP4, Actuator 1 was run in displacement-control and the forces in Actuators 2 and 3 were slaved to Actuator 1. The control equations were as follows:

1. Actuator 1 displacement (δ_1) commanded manually, base moment and rotation between control sensors at opposite ends of wall (hinge rotation) monitored until target force (base moment) or displacement (hinge rotation) value reached

   Control equation 1: δ_1 = manual command

2. The sum of Actuator 1 force, Actuator 2 force, and the force applied by hydraulic jacks commanded to target axial load (P_u) given in Table 4-4: $P_{jacks}+F_1+F_2 = P_u$

   Because the axial load jacks were manually-controlled (i.e., they were not connected to the MTS FlexTest GT), P_{jacks} is considered a constant and the control equation included only the forces applied by Actuators 1 and 2: $F_1+F_2 = P_u - P_{jacks}$. It should be pointed out that $F_1=P_1+\Delta F_1$ and $F_2=P_2+\Delta F_2$ as designated in Figure 4-13.

   Control equation 2: F_1+F_2 = control constant

3. Actuator 3 force commanded proportional to Actuator 1 force ($F_3=\alpha F_1$ where α is a constant), α input as control constant to satisfy M_b/V_u target value from Section 4.3

   Control equation 3: $F_3=\alpha F_1$

The control equations were modified following testing of the first four specimens (WP1-WP4) because some shortcomings of the control technique were identified. The shortcomings identified were:

1. A hinge rotation was not directly commanded. When damage and strength loss occurred, it was not always possible to hold a given rotation level.

2. The forces in Actuators 2 and 3 were directly commanded based on the force in Actuator 1: $F_3 = \alpha F_1$ and $F_2 = P_u - P_{jacks} - F_1$, where $P_u - P_{jacks}$ is a constant. The possibility of an unstable loading condition existed when crushing initiated at the east boundary of the wall.

For specimens WP5-WP7, a rotation was directly commanded in the control equations and the method of achieving a constant M_b/V_u was changed. The modified control equations were as follows:

1. Rotation between Actuator 1 and Actuator 2 commanded manually, rotation calculated as $\frac{\delta_2 - \delta_1}{x_1 + x_2}$ where $x_1 + x_2$ is the horizontal distance between Actuators 1 and 2.

   Base moment and rotation between control sensors at opposite ends of wall (hinge rotation) monitored until target force (base moment) or displacement (hinge rotation) value reached

   Control equation 1: $\frac{\delta_2 - \delta_1}{x_1 + x_2}$ = manual command

2. The sum of Actuator 1 force, Actuator 2 force, and the force applied by hydraulic jacks commanded to target axial load (P_u) given in Table 4-4: $F_1 + F_2 + P_{jacks} = P_u$

   Control equation 2: $F_1 + F_2$ = control constant

3. M_b/V_u commanded as target value from Section 4.3, M_b/V_u calculated from a static analysis (Figure 4-13): $\frac{M_b}{V_u} = \frac{-\Delta F_1 x_1 + \Delta F_2 x_2 + F_3 x_3}{F_3}$

   Control equation 3: $\frac{-\Delta F_1 x_1 + \Delta F_2 x_2 + F_3 x_3}{F_3} =$ control constant

4.5 Instrumentation

Figure 4-15 through Figure 4-24 provide details of the location and type of sensors used to measured wall deformations. Test specimens were carefully instrumented to measure flexural deformations, shear deformations, and reinforcing bar strains throughout the tests. Three horizontally-aligned linear variable differential transducers (LVDTs) were attached to a rigid reference frame and measured wall lateral deformations at different heights. A fourth LVDT was attached to the reference frame and measured horizontal sliding of specimen footings. Two vertically-aligned LVDTs measured uplift of specimen footings from the laboratory strong floor. Out-of-plane movement of specimen top caps was measured using LVDTs that attached to a strong wall parallel to the test specimens.

Columns of vertically-mounted LVDTs were attached to the front (south) and rear (north) faces of specimens, as well as the face of the flange of specimen WP4, to measure wall axial (flexural) deformations at various locations along the length of the walls. Slip-extension was measured at the interface of the wall and footing and at the interface of the wall and top cap. Wall shear deformations were measured using three pairs of LVDTs arranged in X-configurations, and shear sliding deformation was measured at the base of the wall using a horizontally-mounted LVDT.

For each test, approximately forty strain gages were used at various locations to measure strains in boundary and web longitudinal reinforcement, boundary transverse hoops and cross-ties, and web transverse reinforcement. Strain gages on vertical bars were used to track first yield and full yield of primary flexural reinforcement.

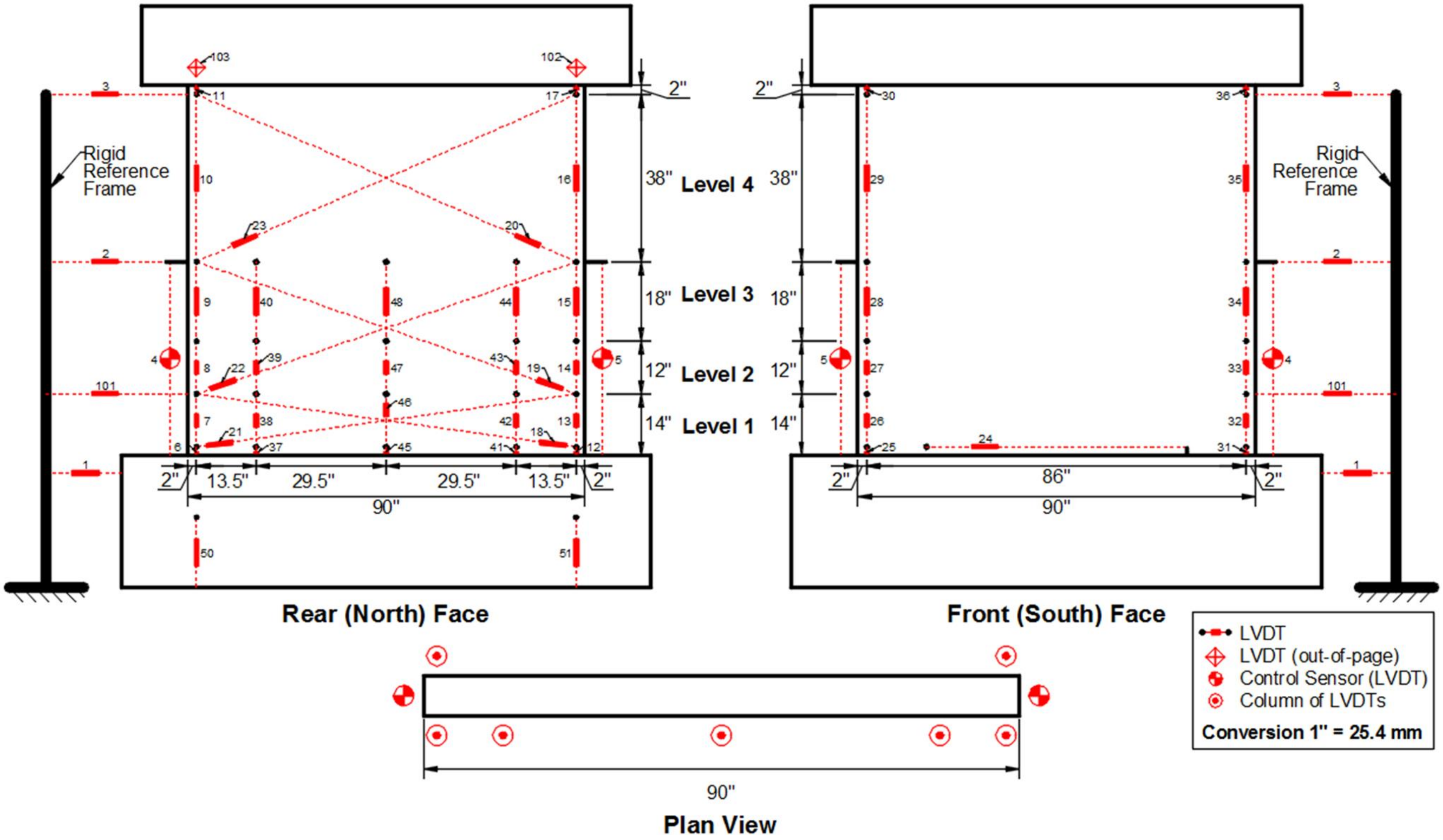

Figure 4-15: LVDT layout for specimen WP1

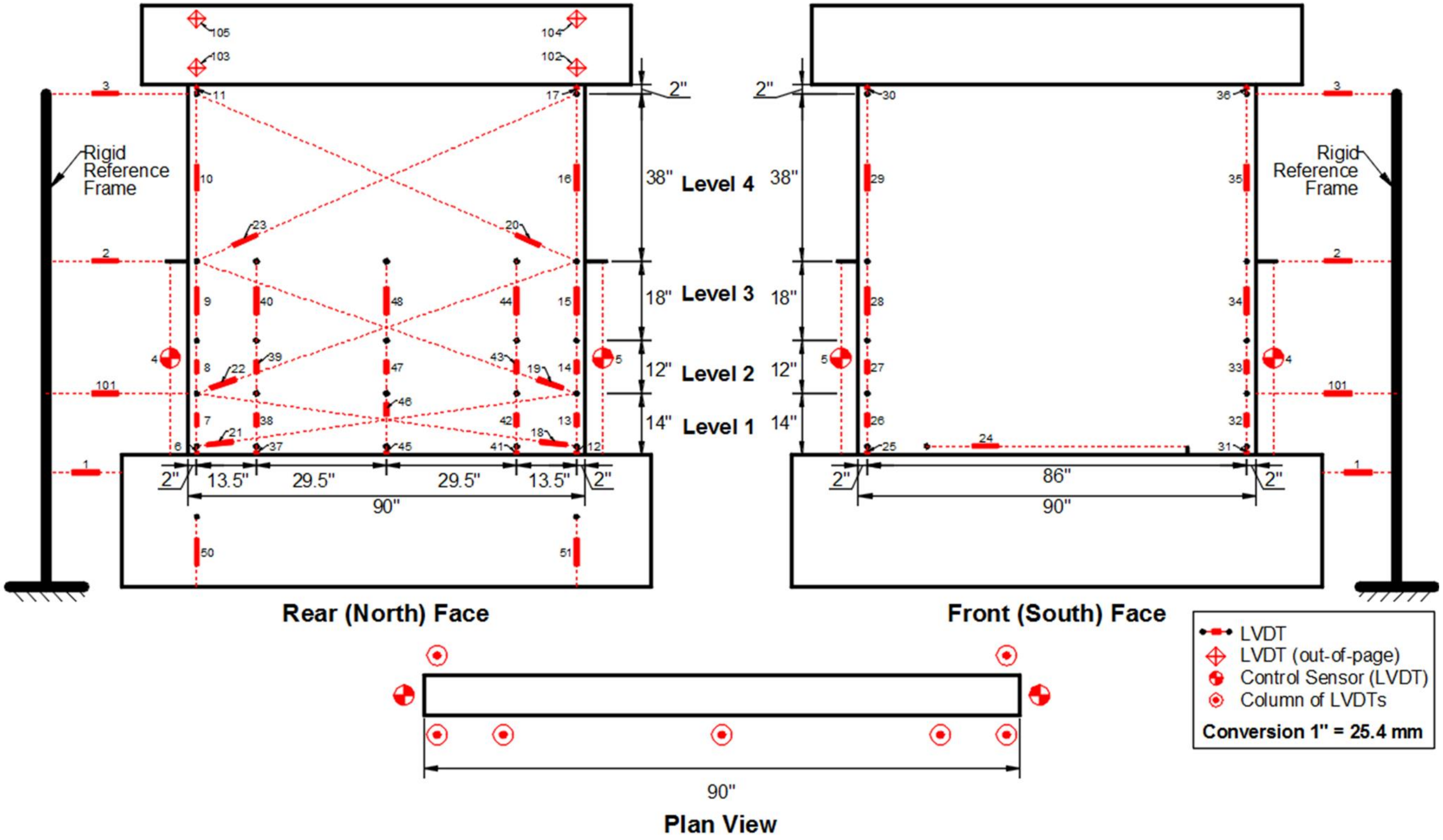

Figure 4-16: LVDT layout for specimens WP2 and WP3

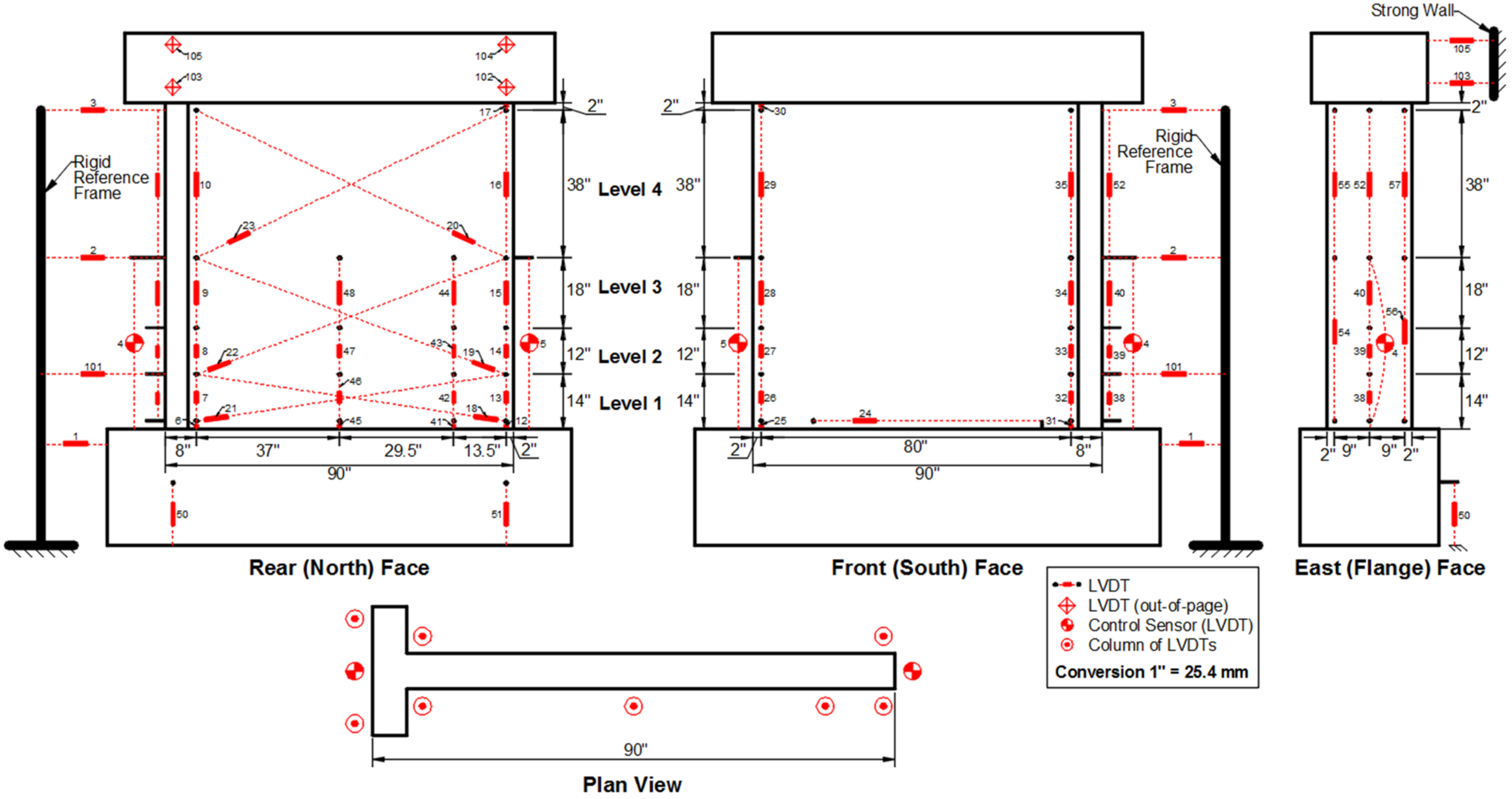

Figure 4-17: LVDT layout for specimen WP4

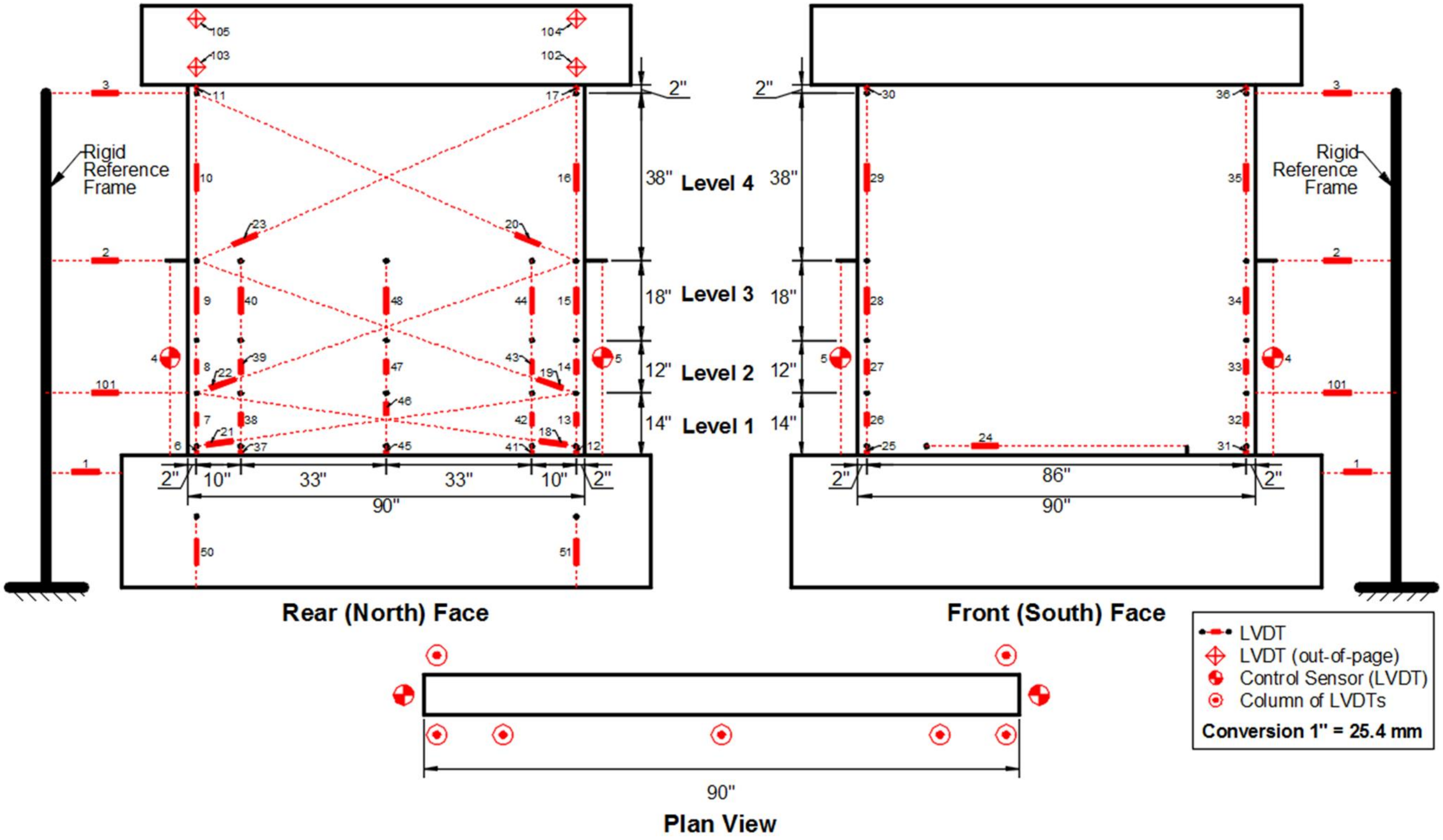

Figure 4-18: LVDT layout for specimens WP5, WP6, and WP7

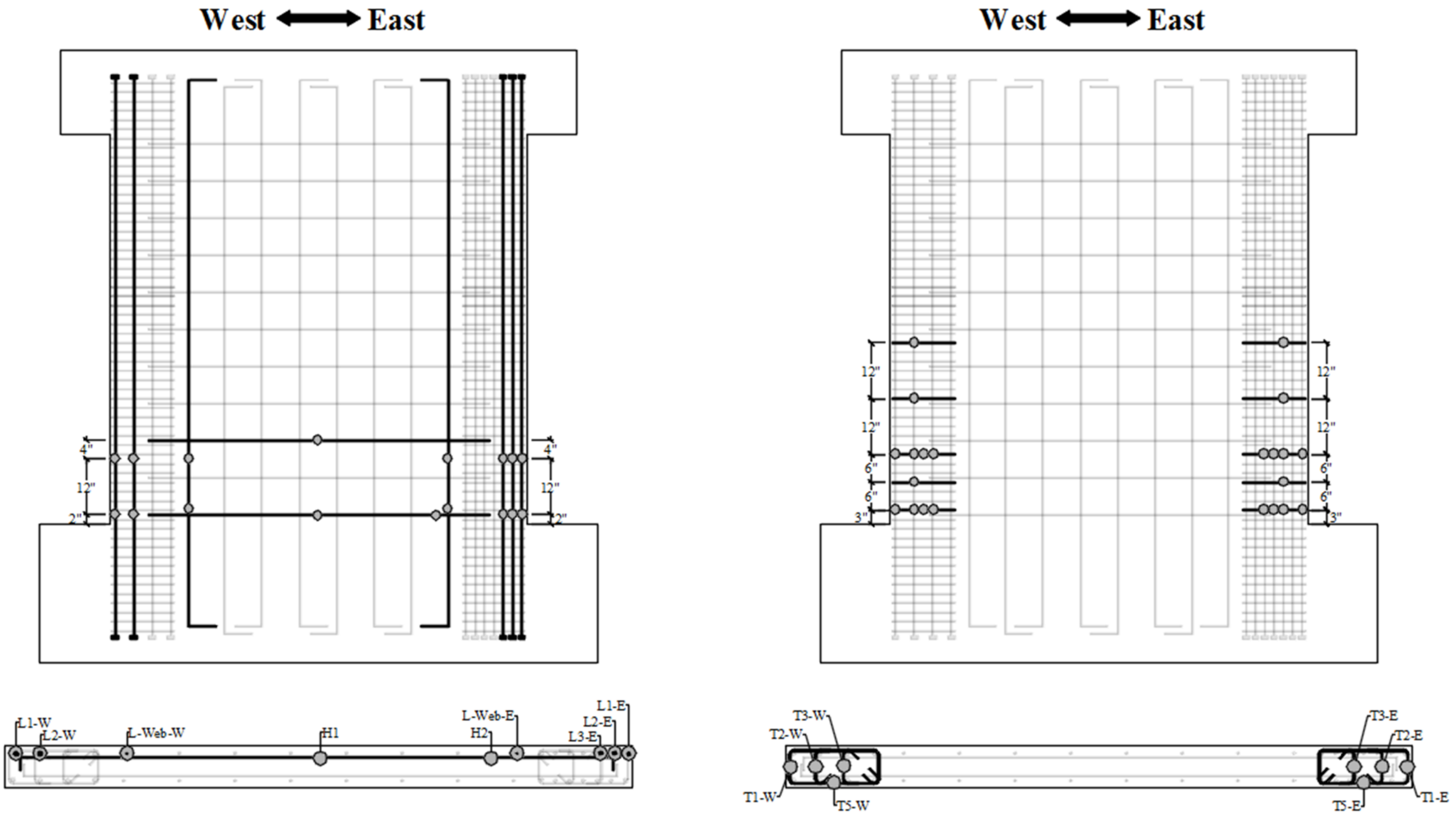

Figure 4-19: Strain gage layout for specimens WP1 and WP2

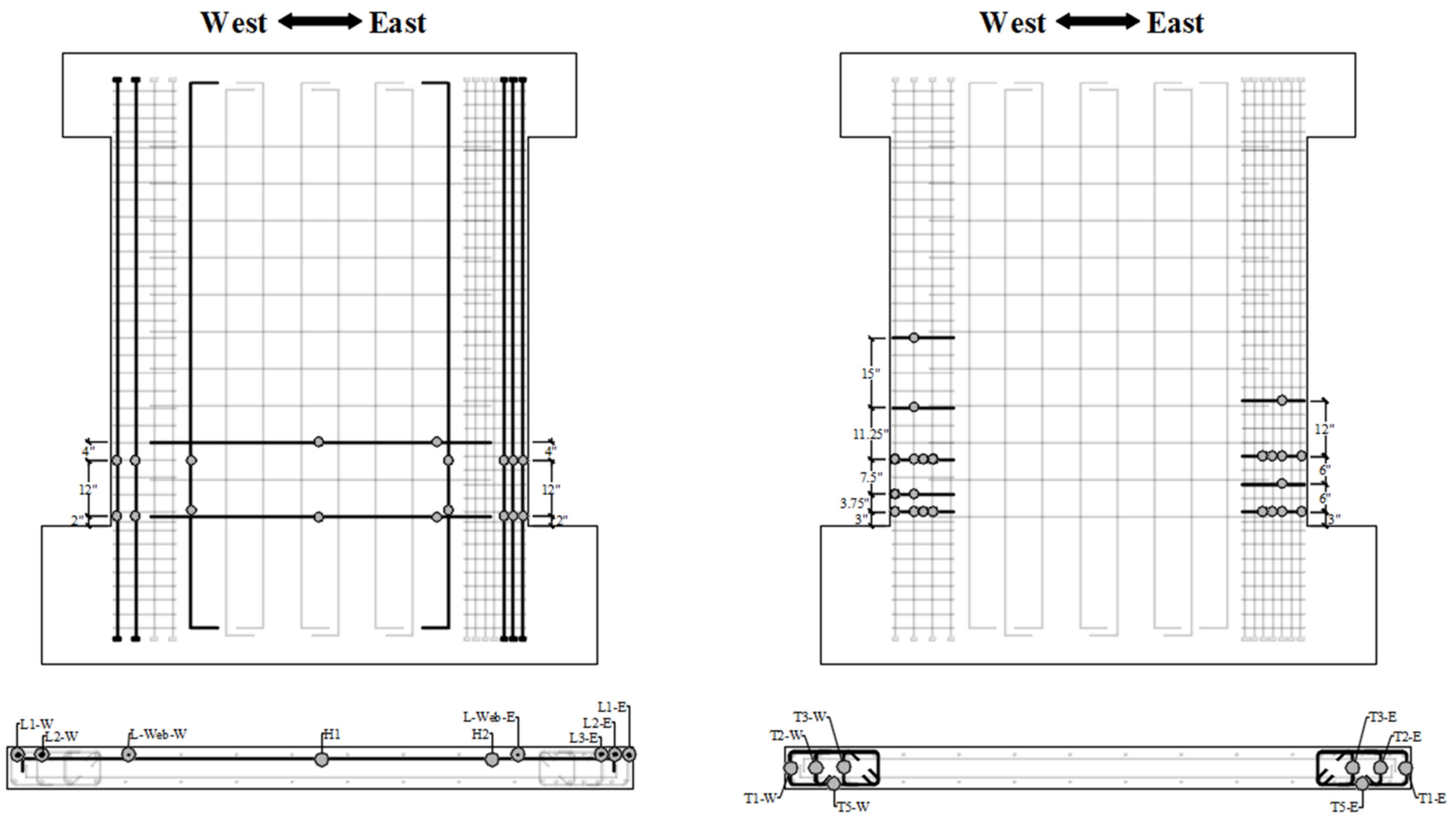

Figure 4-20: Strain gage layout for specimen WP3

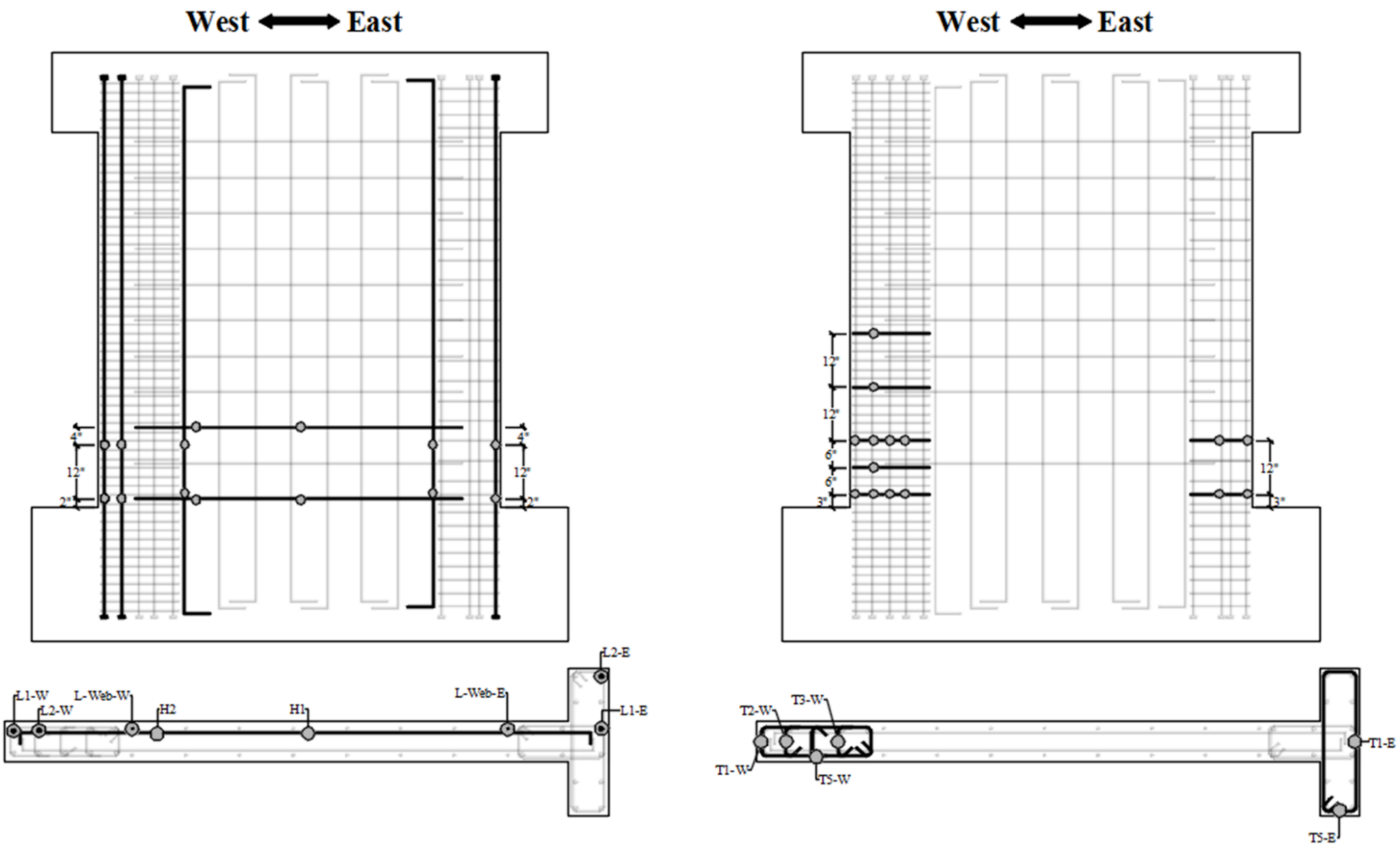

Figure 4-21: Strain gage layout for specimen WP4

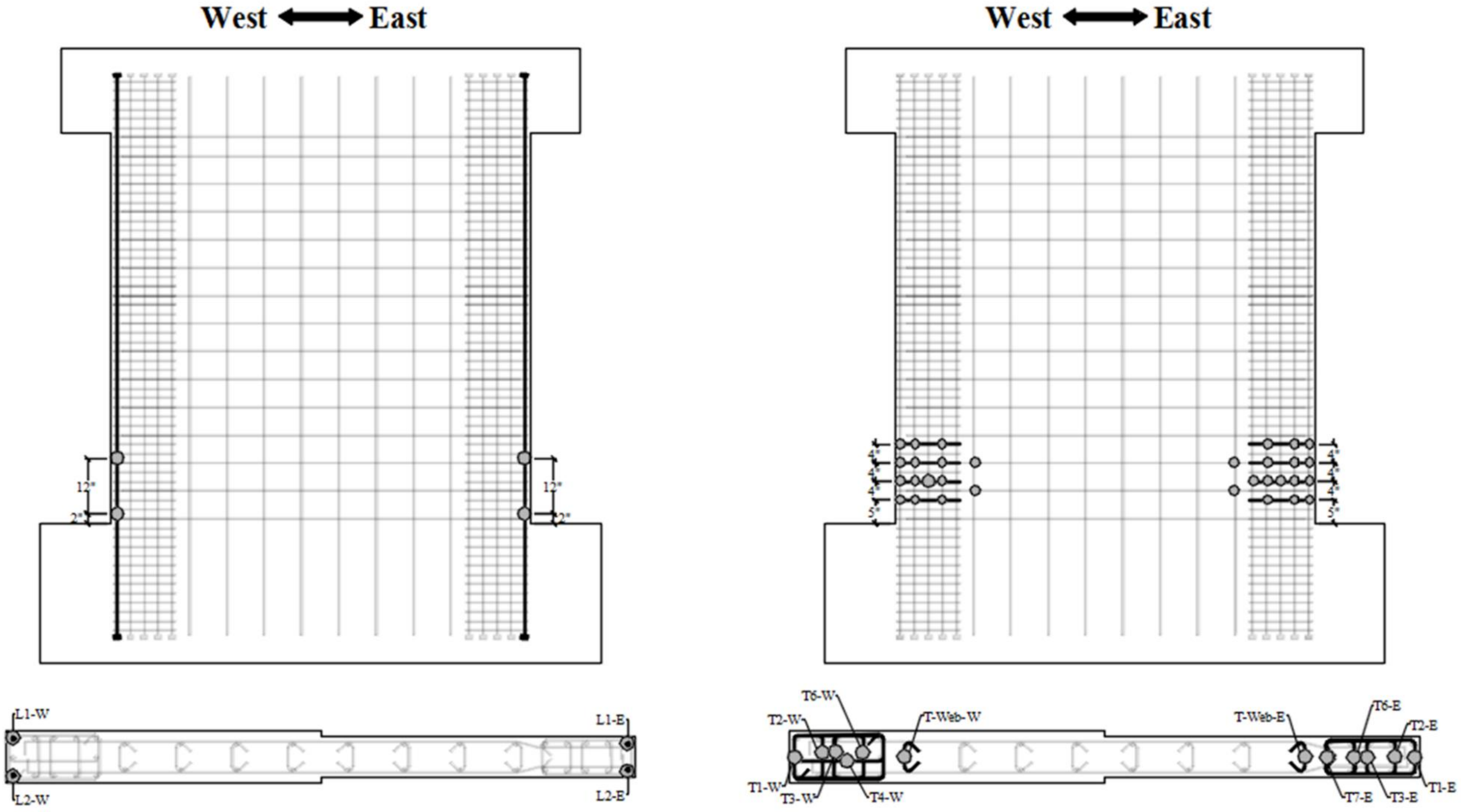

Figure 4-22: Strain gage layout for specimen WP5

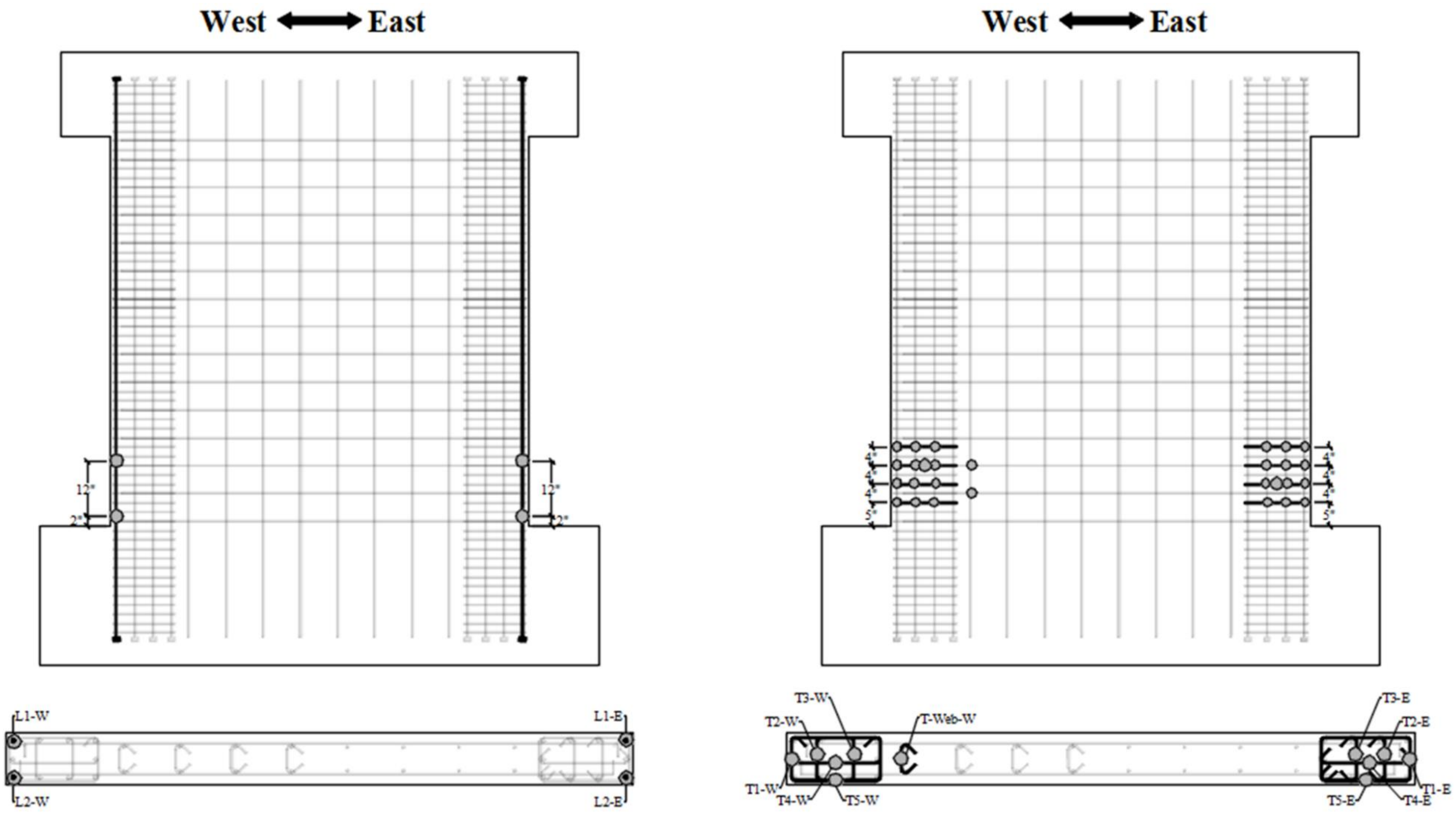

Figure 4-23: Strain gage layout for specimen WP6

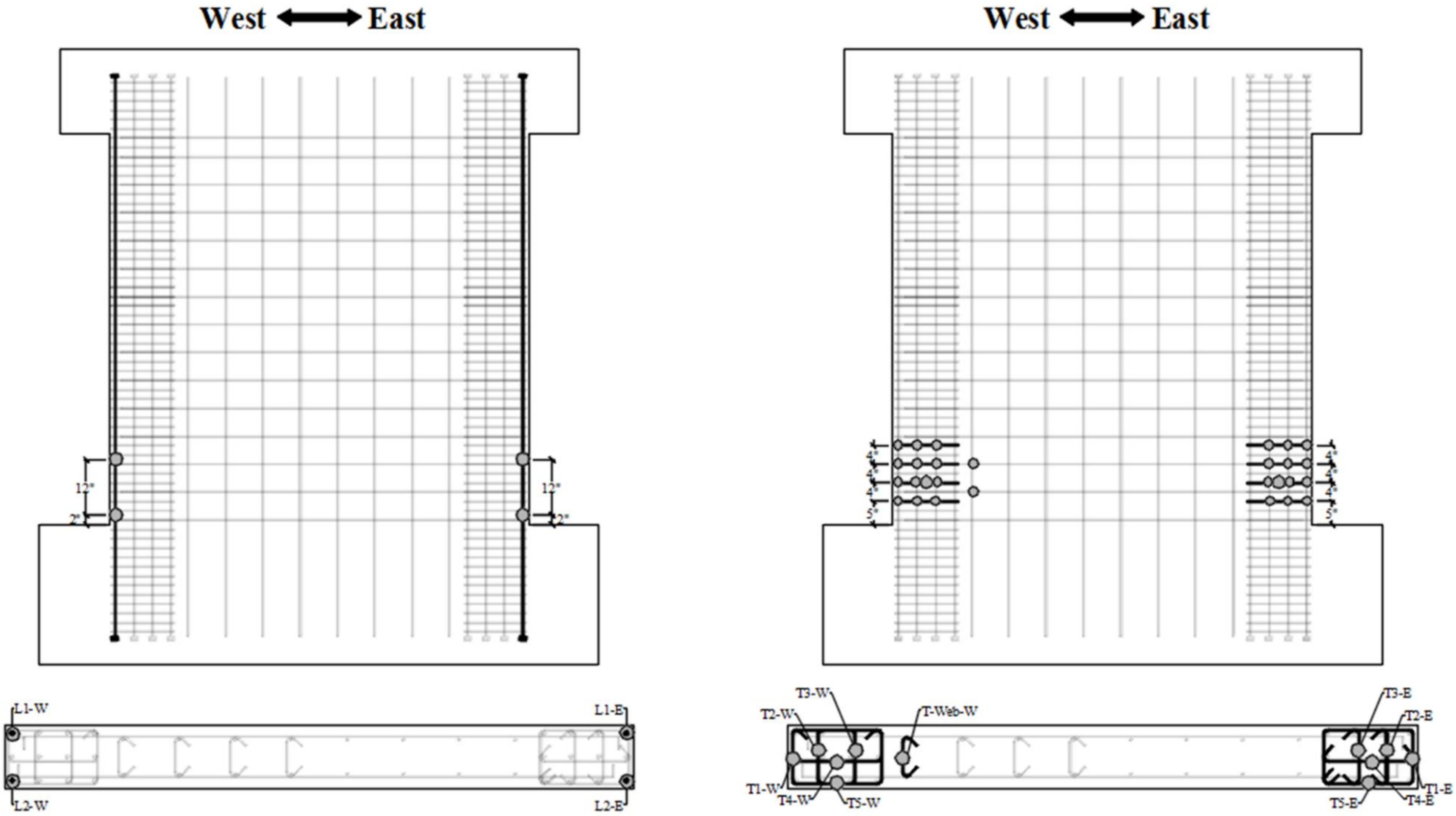

Figure 4-24: Strain gage layout for specimen WP7

A non-contact measurement system was used to measure surface strains on the front face of specimens. The equipment and instrumentation setup are shown in Figure 4-25. The system utilized two digital single-lens reflex (DSLR) cameras, two strobe flashes, and a digital image correlation (DIC) software package (Barthes, 2015). The surface of test specimens was prepared with a light coat of white paint that served as a contrast for a random speckle pattern applied to the front face of specimens using black paint (Figure 4-26). Each black speckle was approximately 5 to 20 pixels in width and height. Approximately thirty-two high resolution images were taken from each camera during each cycle, and the images were processed using the DIC software.

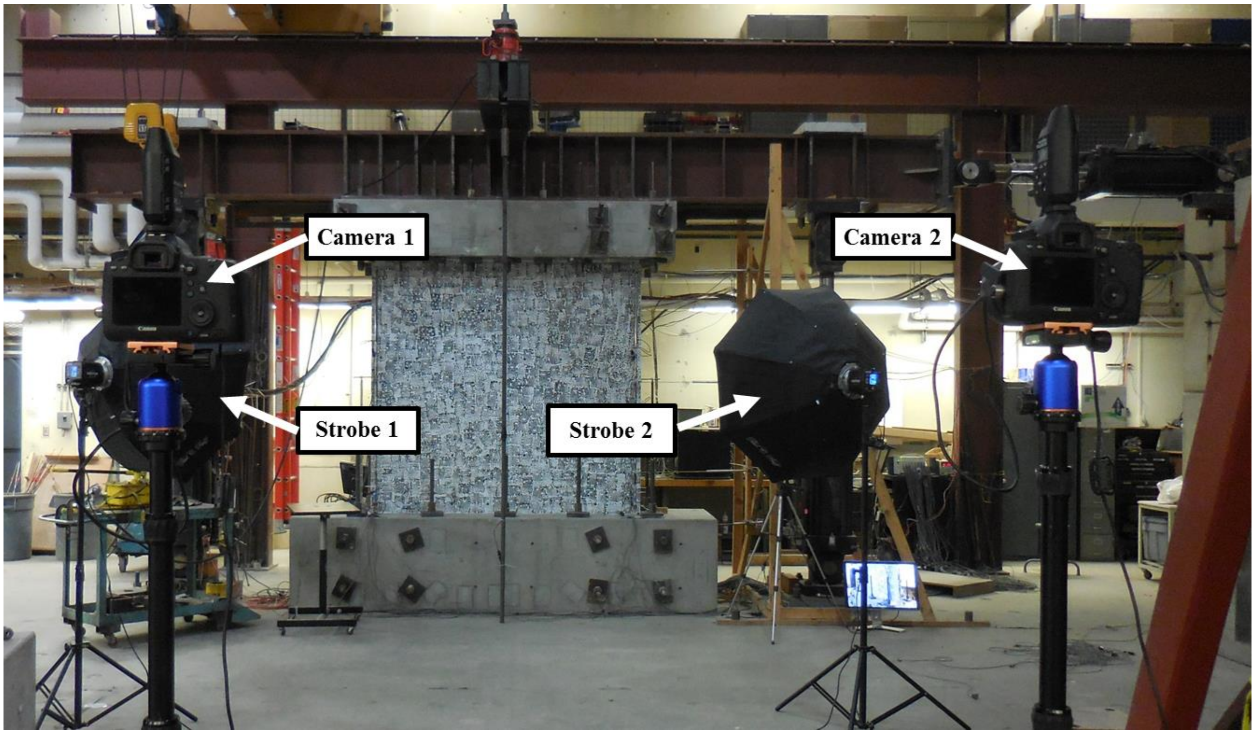

Figure 4-25: Digital image correlation equipment and setup

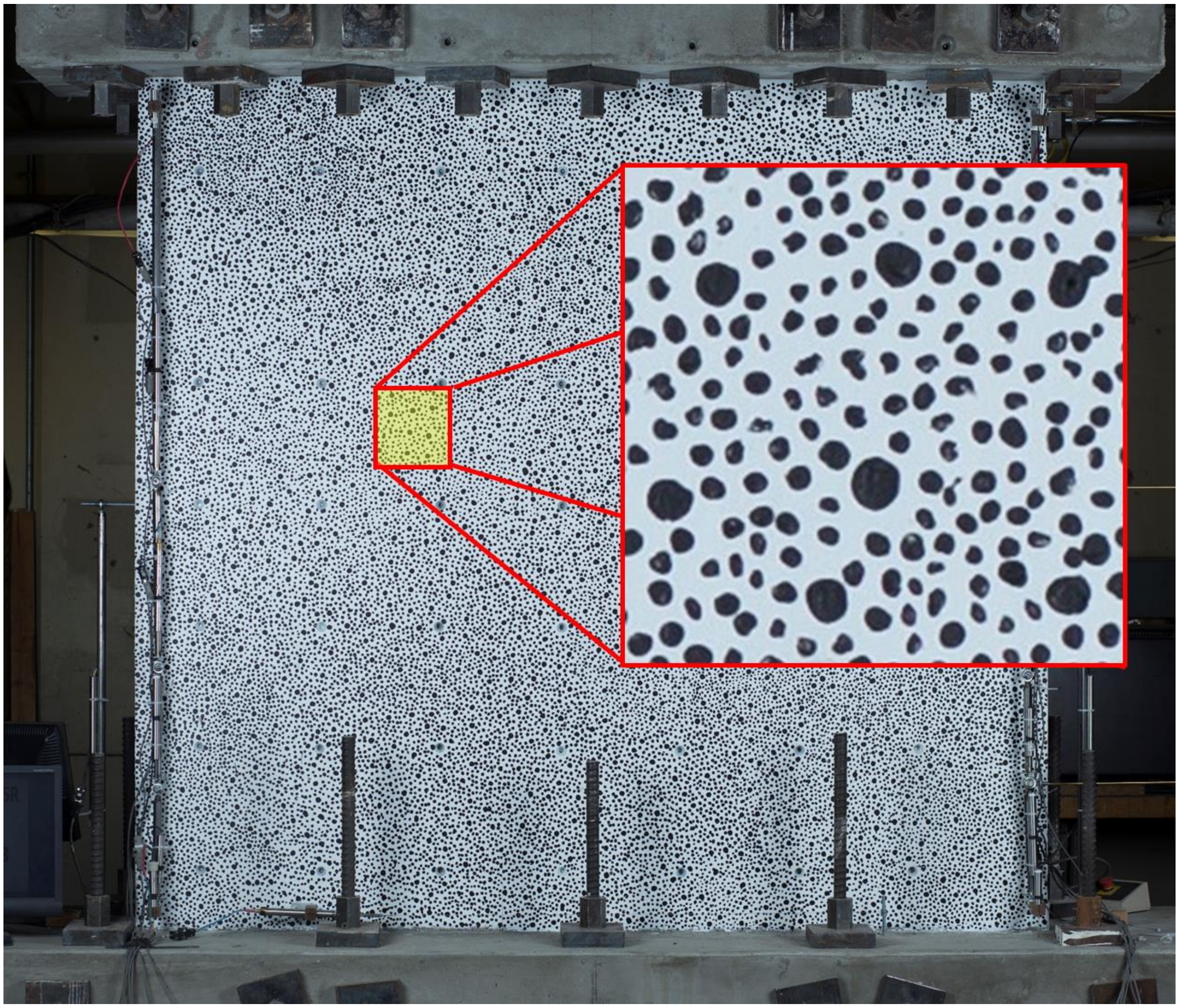

Figure 4-26: Speckle pattern on front face of wall panel specimen

4.6 Construction

Test specimens were constructed in the UCLA Structural/Earthquake Engineering Laboratory in two phases. Construction for specimens WP1-WP4 was completed in August, 2014, and construction for specimens WP5-WP7 was completed in October, 2015. Formwork and concrete placement were handled by Webcor Builders, and steel reinforcement was supplied and fabricated by Gerdau Reinforcing Steel.

Construction photos are shown in Figure 4-27 through Figure 4-38. All specimens were cast in an upright position. Each specimen was constructed in two concrete pours, resulting in a construction joint at the wall-footing interface (Figure 4-32). Strain gages were applied to reinforcing bars at various locations within the wall panel test region (Figure 4-27). The strain gages were installed at UCLA upon delivery of reinforcement to the UCLA laboratory. The construction sequence for a typical specimen was as follows:

1. Reinforcement cut and bent at Gerdau's shop and delivered to UCLA laboratory
2. Strain gages installed on reinforcing bars (Figure 4-27)
3. Formwork assembled for footings (Figure 4-32)
4. Footing and boundary region reinforcing cages assembled (Figure 4-28 - Figure 4-30)
5. Footing reinforcement placed in formwork (Figure 4-32)
6. Boundary reinforcing cages and wall web reinforcement placed (Figure 4-32)
7. Concrete poured to top of footing (Figure 4-32)
8. Formwork and shoring assembled for wall panel specimen and top cap (Figure 4-37)
9. Top cap reinforcing cage assembled and placed in formwork
10. Concrete poured to top of specimen top cap (Figure 4-38)

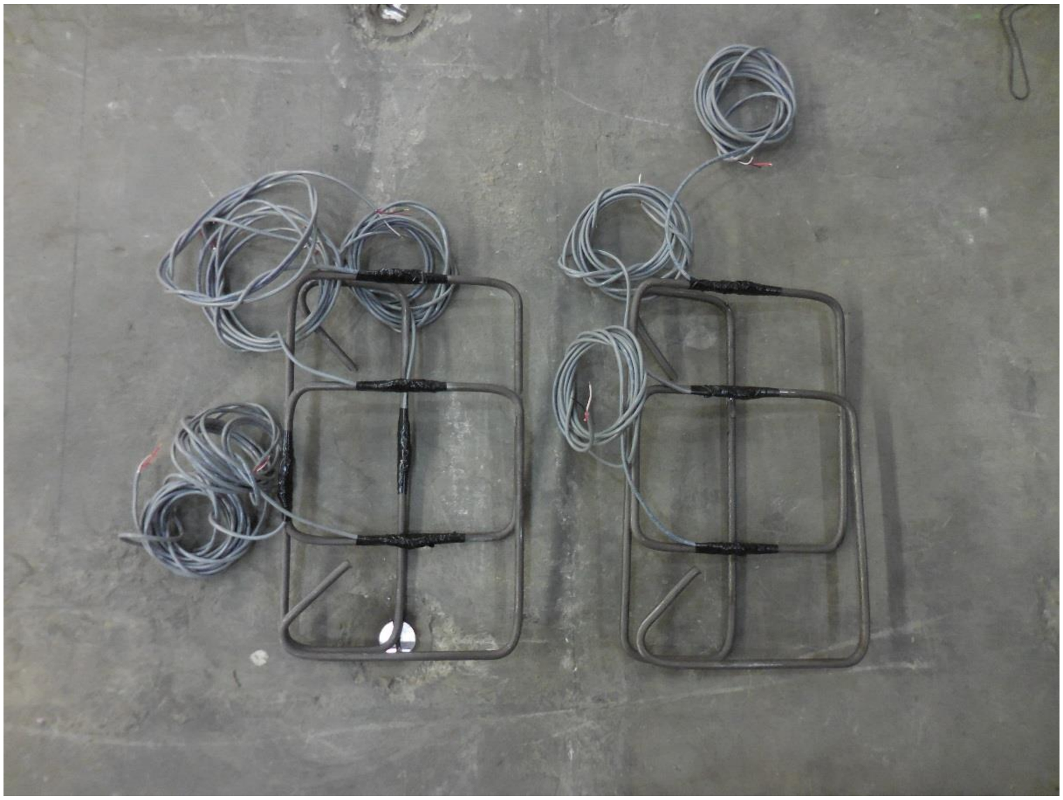

Figure 4-27: Reinforcement with strain gages installed and lead wires attached

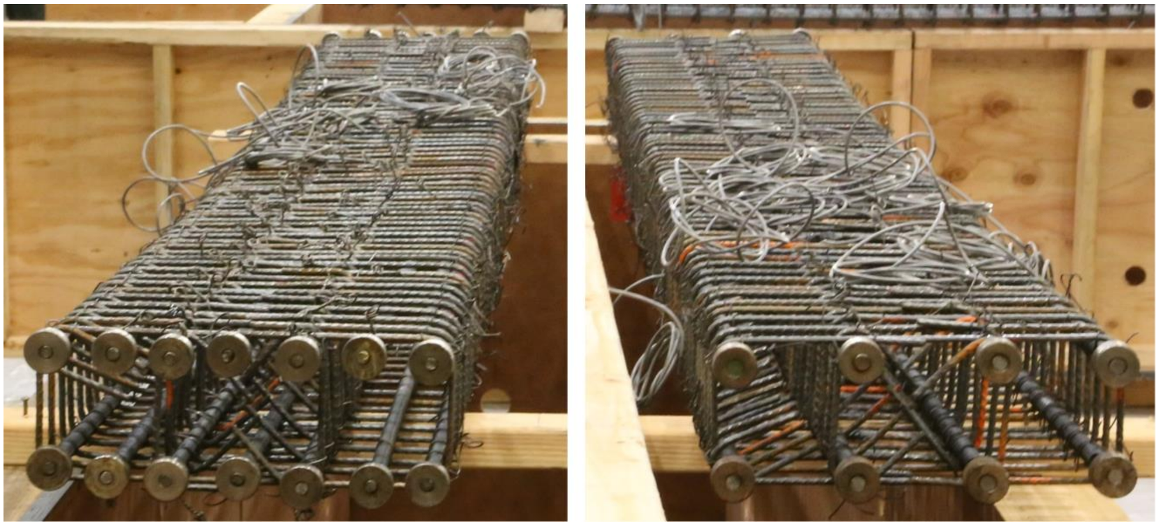

Figure 4-28: Boundary region reinforcing cages – specimen WP1

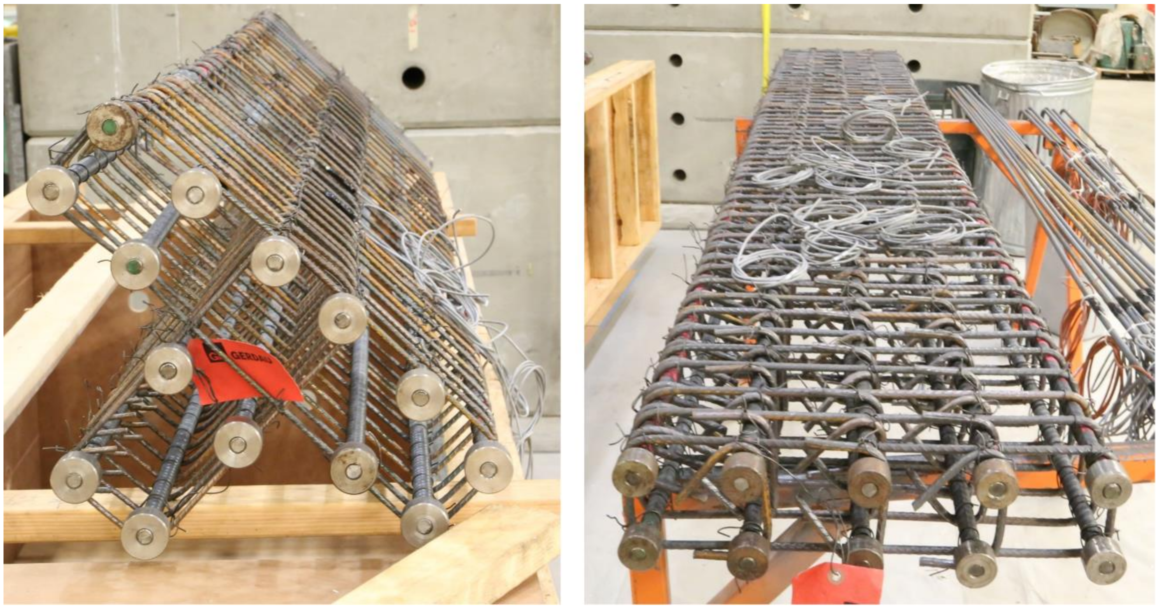

Figure 4-29: Boundary region reinforcing cages – specimen WP4

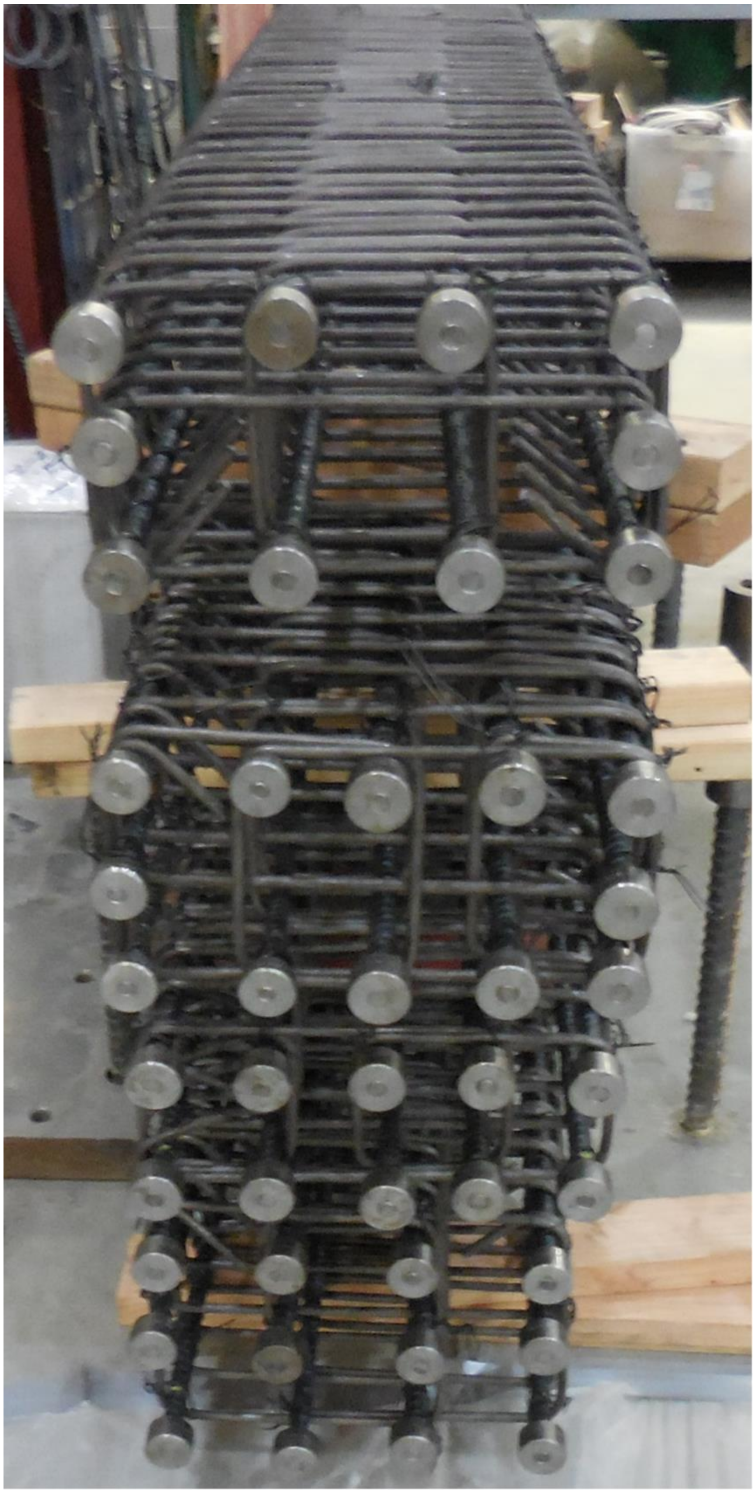

Figure 4-30: Boundary region reinforcing cages – specimens WP6 and WP7

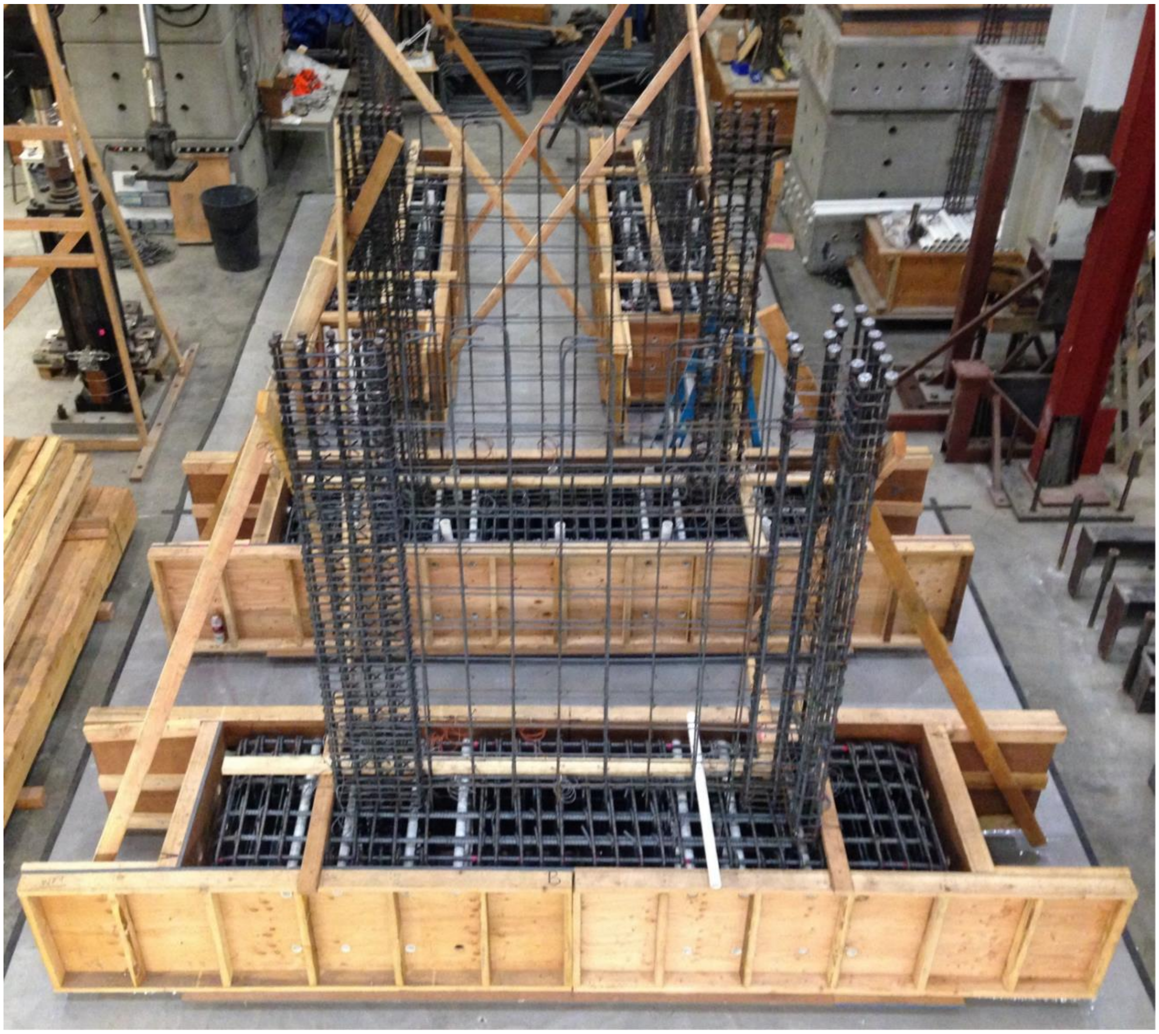

Figure 4-31: Footing formwork with footing and wall reinforcement

Figure 4-32: Concrete footing with wall reinforcement

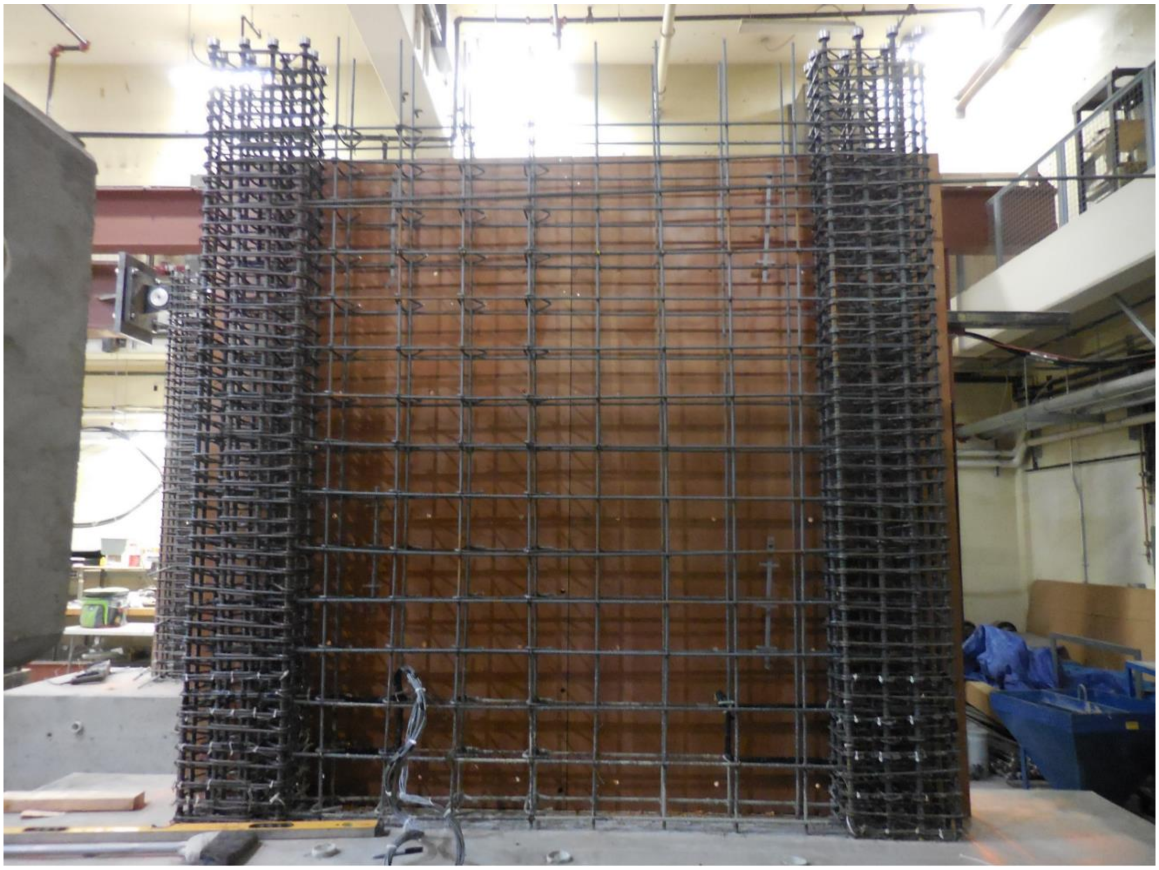

Figure 4-33: Typical wall reinforcement layout

Figure 4-34: Boundary reinforcement cage extension into specimen top cap

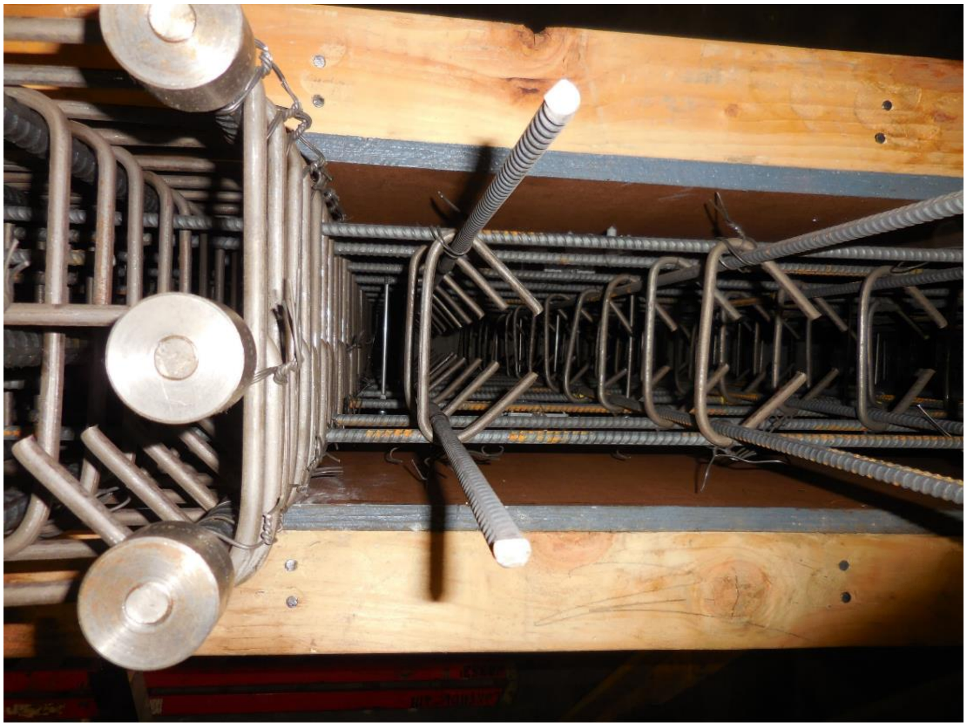

Figure 4-35: View of wall reinforcement from above

Figure 4-36: Wall web reinforcement – cross-ties supporting longitudinal bars on one side only

Figure 4-37: Typical wall and top cap formwork and shoring

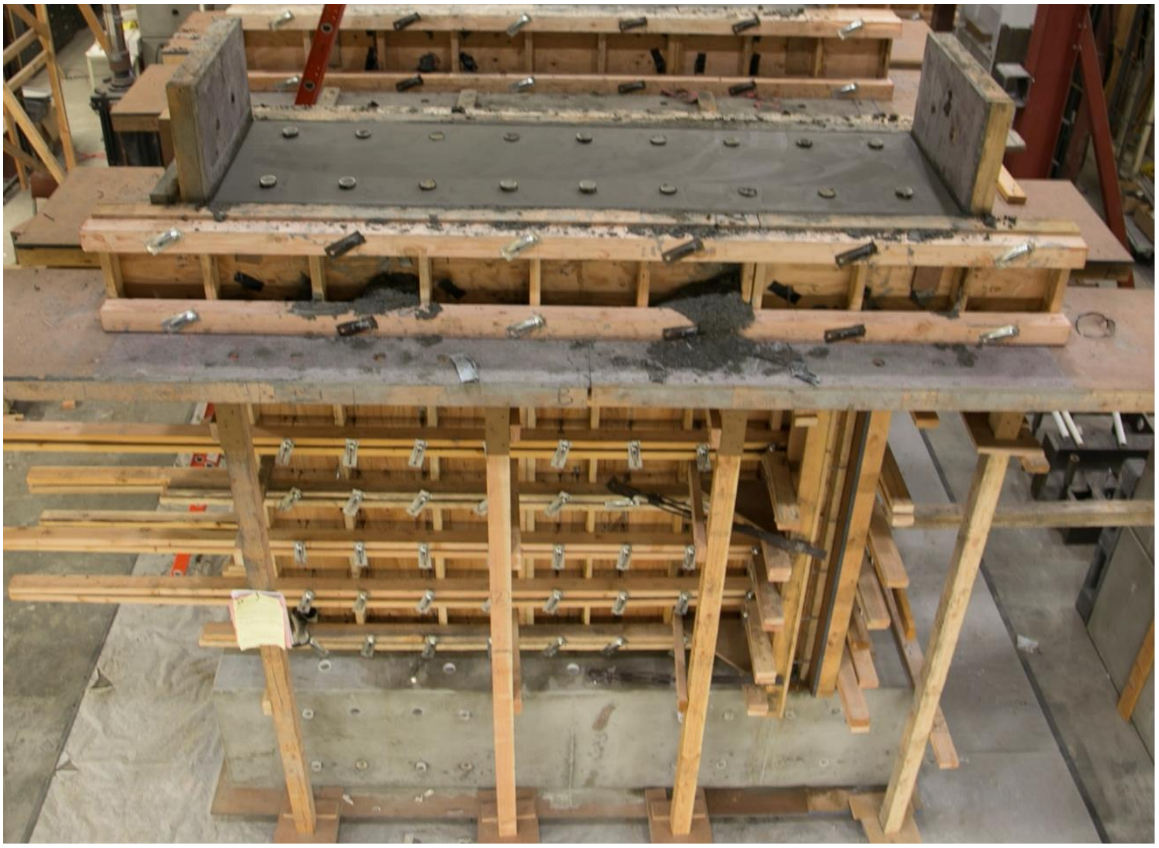

Figure 4-38: Specimen concrete curing

Chapter 5 Summary of Experimental Results

In this chapter, a summary of experimental results for the seven test specimens is provided, along with a detailed description of test day observations for each wall. For reference, cross-sectional geometry and reinforcement details are presented for all seven specimens in Figure 5-1. The testing matrix is presented in Table 5-1, indicating the primary test variable, wall thickness, applied axial load, compression depth, confinement detail (i.e., outer hoop and cross-ties or continuous transverse reinforcement), and ratio of provided-to-required boundary transverse reinforcement. An overview of the test variables and more detailed drawings are provided in Sections 3.1 and 3.2, respectively. The compression depth and the required quantity of boundary transverse reinforcement reported in Table 5-1 were calculated using design material properties (i.e., f_y and f'_c) as well as test day material properties (i.e., $f_{y,test}$ and $f'_{c,test}$).

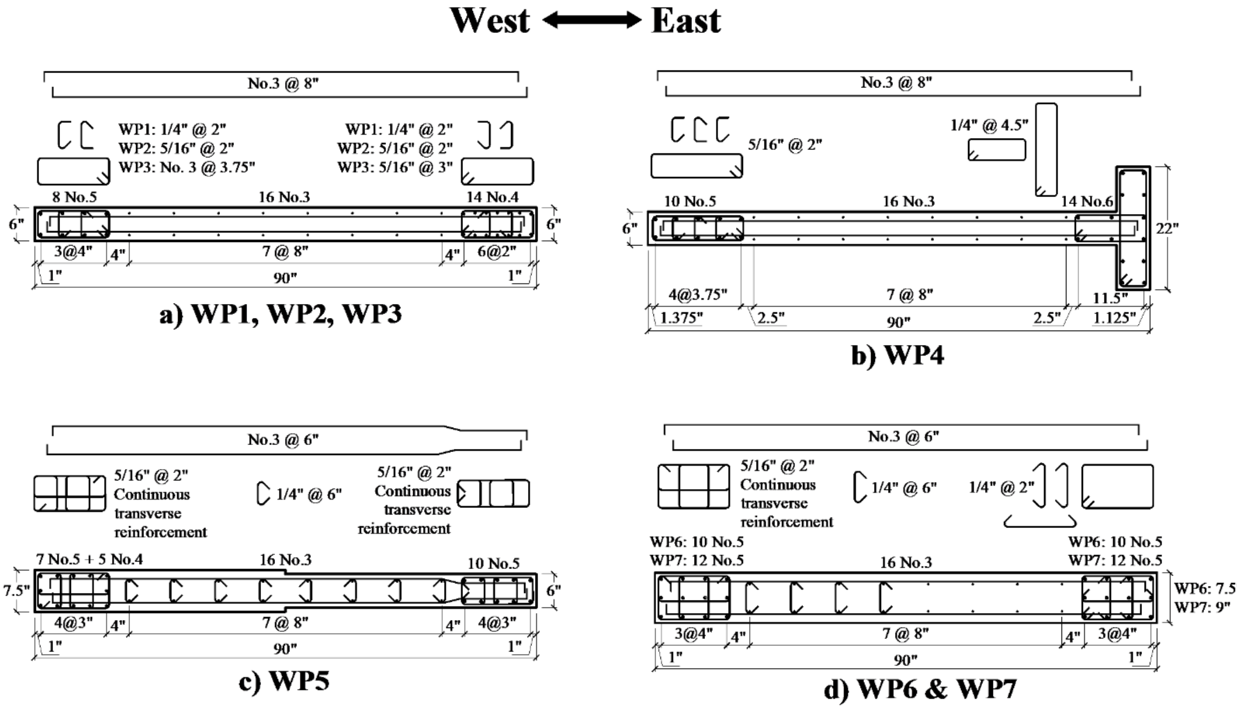

Figure 5-1: Cross-sectional geometry and reinforcement details

Table 5-1: Test Matrix (conversion: 1 in.=25.4 mm, 1 kip=4.448 kN)

Specimen/ Boundary		Primary Test Variable	b	Axial Load	Confinement Detail	A_{sh1}/A_{ACI} *	A_{sh1}/A_{ACI} **	s/d_b	$c/l_w{}^*$	$c/l_w{}^{**}$
			in.	kip						
WP1	West	Reference Specimen	6.0	270	HCT 90°-135°	1.02	0.80	3.2	0.21	0.23
	East							4.0	0.20	0.22
WP2	West	$\boldsymbol{A_{sh}}$	6.0	270	HCT 90°-135°	**1.24**	**1.00**	3.2	0.21	0.22
	East							4.0	0.20	0.21
WP3	West	$\boldsymbol{s/d_b}$	6.0	270	HCT 90°-135°	1.21	1.38	**6.0**	0.21	0.21
	East					1.09	0.87		0.20	0.20
WP4	West	$\boldsymbol{c/l_w}$	6.0	270	HCT 90°-135°	1.23	0.91	3.2	**0.30**	**0.30**
	East				---	---	---	---	**0.06**	**0.07**
WP5	West	Boundary Detail	7.5	337.5	**CTR**	2.05	1.57	3.2	0.20	0.17
	East		6.0	270					0.21	0.19
WP6	West	$\boldsymbol{b}$	**7.5**	337.5	CTR	1.64	1.30	3.2	0.20	0.18
	East				HCT 135°-135°	1.02	0.90			
WP7	West	$\boldsymbol{b}$	**9.0**	405	CTR	1.64	1.24	3.2	0.20	0.18
	East				HCT 135°-135°	1.02	0.85			

$\boldsymbol{A_{sh1}}$: area of transverse reinforcement in direction perpendicular to wall length; $\boldsymbol{A_{ACI}}$: area of transverse reinforcement required by ACI 318-14

HCT: single outer hoop and cross-ties (90° or 135° cross-tie hook indicated); **CTR**: continuous transverse reinforcement

* Determined using nominal material properties; ** Determined using test day material properties

5.1 Measured Base Moment and Shear vs. Hinge Rotation

Experimentally measured base moment and shear versus hinge rotation responses for each specimen are presented in Figure 5-2. The moment and shear reported in Figure 5-2 have been corrected to account for the deformed configuration of the actuators at each loading step. Hinge rotation was measured over an assumed plastic hinge length of one-half the length of the wall ($l_p = l_w/2$). Positive loading corresponds to loading causing compression at the west boundary of the walls (east and west boundaries indicated in Figure 5-1). For each specimen, the ASCE 41 moment versus hinge rotation backbone (ASCE/SEI, 2010) is included for comparison. The slope of the elastic branch of the ASCE 41 backbone was determined using an effective cracked stiffness of $0.5E_cI_g$, and the nominal flexural capacity was calculated according to ACI 318-14 using test day material properties.

Table 5-2 provides a summary of the measured hinge rotation and base overturning moment for loading in both directions at four points: 1) horizontal flexural cracking of concrete at wall boundaries; 2) first yield of boundary longitudinal reinforcement (determined from strain gage data); 3) peak strength; and 4) strength loss (determined at the largest rotation for which lateral strength exceeded 80% of peak strength). The applied axial force (P_u) and nominal flexural strength (M_n) are provided in Table 5-2 for reference. The reported M_n values were calculated using test day material properties. In Section 6.3, the total lateral displacement measured at the top of the specimens, at a height of 82 in. (2083 mm) above the footing of the walls, is reported for each specimen. The contribution of flexural and shear deformations to the total lateral displacement at the top of the specimens is reported in Sections 6.3.1 and 6.3.2. The lateral displacement and drift ratio at the effective height of the walls is approximated in Section 6.5, and summarized in Table 6-1 for the four loading points indicated in Table 5-2.

For the phase 1 tests (WP1-WP4), measured hinge rotation at strength loss ranged between 1.31% (WP4) and 1.59% (WP1). For comparison, ASCE 41 assumes 75% of the peak lateral strength can be maintained at approximately 2.2% rotation for specimens WP1-WP3 and approximately 2.0% rotation for specimen WP4, which are both approximately 1.5 times the measured rotation capacities of the four specimens. On the other hand, the phase 2 specimens (WP5-WP7) demonstrated rotation capacities in excess of 2.0%, reaching as high as 3.0% for the thickest specimen (WP7).

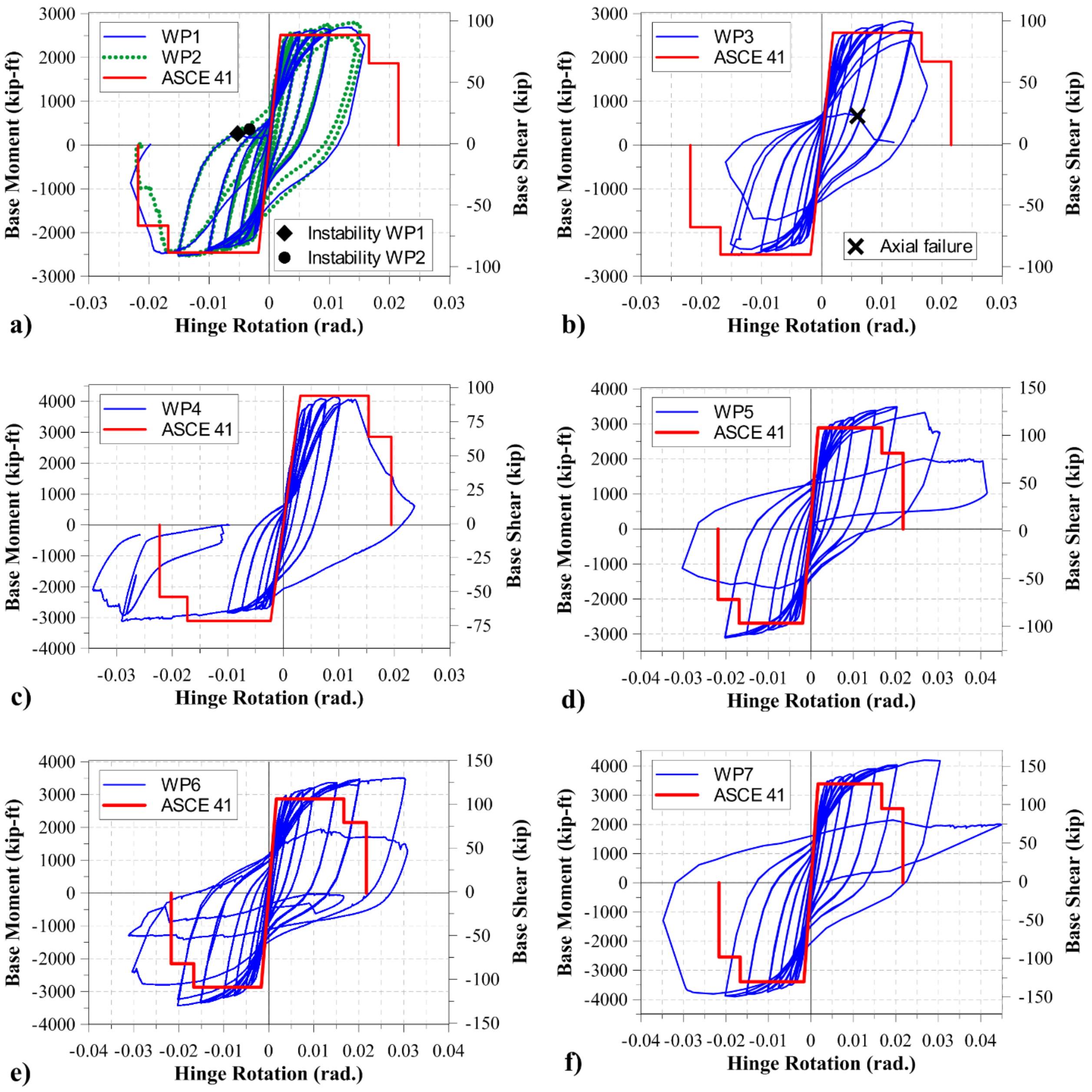

Figure 5-2: Base moment/shear vs. hinge rotation (conversion: 1 kip=4.448 kN, 1 kip-ft=1.356 kN-m)

Table 5-2: Experimental Results Summary (conversion: 1 kip=4.448 kN, 1 kip-ft=1.356 kN-m)

ID	Loading Direction	Axial Force	Flexural Strength	Cracking			Yielding			Peak Load			Strength Loss		
		P_u	M_n	θ_{cr}	M_{cr}	M/M_n	θ_y	M_y	M/M_n	θ_{peak}	M_{peak}	M/M_n	θ_u	M_u	M/M_n
		kip	k-ft	rad.	k-ft	---	rad.	k-ft	---	rad.	k-ft	---	rad.	k-ft	---
WP1	Positive	270	2515	0.050%	1023	0.41	0.21%	2162	0.86	1.26%	2687	1.07	1.59%	2273	0.90
	Negative		-2455	-0.057%	-1009	0.41	-0.20%	-1955	0.80	-1.46%	-2531	1.03	-1.97%	-2107	0.86
WP2	Positive	270	2560	0.049%	1122	0.44	0.22%	2301	0.90	1.35%	2800	1.09	1.52%	2677	1.05
	Negative		-2497	-0.053%	-993	0.40	-0.20%	-1921	0.77	-1.41%	-2528	1.01	-1.79%	-2124	0.85
WP3	Positive	270	2566	0.048%	906	0.35	0.19%	1984	0.77	1.38%	2833	1.10	1.51%	2280	0.89
	Negative		-2502	-0.050%	-896	0.36	-0.19%	-1882	0.75	-1.38%	-2518	1.01	-1.52%	-2260	0.90
WP4	Positive	270	4183	0.054%	1190	0.28	0.21%	2857	0.68	0.91%	4151	0.99	1.31%	4011	0.96
	Negative		-3104	-0.060%	-1249	0.40	-0.21%	-2501	0.81	-2.90%	-3118	1.00	-3.07%	-2626	0.85
WP5	Positive	270	2888	0.058%	974	0.34	0.22%	2196	0.76	2.02%	3489	1.21	2.81%	2906	1.01
	Negative	338	-2690	-0.049%	-742	0.28	-0.22%	-2118	0.79	-2.02%	-3109	1.16	-2.03%	-3077	1.14
WP6	Positive	338	2867	0.047%	952	0.33	0.25%	2601	0.91	2.99%	3507	1.22	3.02%	3483	1.21
	Negative		-2867	-0.037%	-767	0.27	-0.22%	-2242	0.78	-2.03%	-3431	1.20	-2.69%	-2779	0.97
WP7	Positive	405	3389	0.051%	996	0.29	0.23%	2791	0.82	2.67%	4203	1.24	3.04%	4183	1.23
	Negative		-3389	-0.044%	-950	0.28	-0.22%	-2785	0.82	-1.79%	-3899	1.15	-2.98%	-3474	1.03

5.2 Observed Behavior and Damage Progression

5.2.1 Specimen WP1

Specimen WP1 was the reference specimen for the test program. WP1 was 6 in. (152 mm) thick and was constructed with eight No. 5 longitudinal reinforcing bars at the west boundary and fourteen No. 4 longitudinal reinforcing bars at the east boundary. Throughout the test, a constant axial load of 270 kip (1201 kN) was applied. Typical damage observed at the west boundary and east boundary is shown in Figure 5-3 and Figure 5-4, respectively.

Horizontal flexural cracking of concrete was first observed at the east boundary of the wall at +0.05% rotation and at the west boundary at -0.057% rotation. Initial cracking was observed over the full height of the specimen, and a denser distribution of cracks was observed over the full height of the specimen in the proceeding cycles. The measured base overturning moment at the time flexural cracks were first observed (M_{cr}) was 41% of the nominal flexural strength in both loading directions. Tension strains in excess of the yield strain reported in Table 4-3 were indicated by strain gages attached to longitudinal reinforcement at wall edges at +0.21% and -0.20% rotation at the east and west boundaries, respectively. Vertical splitting of cover concrete was first observed at the west edge of the wall at approximately +0.5% rotation (Figure 5-3a) and at the east edge of the walls at approximately -1.0% rotation (Figure 5-4a). In both loading directions, average extreme fiber compression strain, measured over a gage length of $l_w/2$, was approximately 0.003 at the time vertical cracks and spalling were first observed.

Specimen WP1 completed three cycles to ±1.0% rotation without strength loss. Minor crushing of cover concrete along the front and rear faces of the wall, extending horizontally from the west edge of the wall approximately 12 in. ($0.13l_w$; 305 mm), was observed during loading cycles to ±1.0% rotation (Figure 5-3b). The peak lateral strength in the positive loading direction was measured at

+1.26% during the first 1.5% rotation cycle. At peak strength, the measured base overturning moment was 1.07 times the calculated nominal flexural strength. A 15% reduction in strength was evident when loading was stopped at +1.5% (cycle 1), at which time crushing and spalling of cover concrete had occurred over nearly the full length of the confined region (approximately $0.16l_w$) on the front and rear faces of the wall, revealing slight buckling of the two No. 5 longitudinal reinforcing bars at the northwest and southwest corners of the wall (Figure 5-3c). Buckling of the two No. 5 bars occurred at different heights: the bar at the southwest corner of the wall was buckled between hoops at 3 in. (76 mm) and 5 in. (127 mm) above the footing while the bar at northwest corner was buckled between hoops at 5 in. (127 mm) and 7 in. (178 mm) above the footing. It is noted that opening of a 90^o cross-tie hook was observed in the region where cover spalling occurred. The buckled bars straightened in tension while loading in the opposite direction to -1.5% rotation. While attempting to reload to +1.5% rotation (cycle 2), out-of-plane instability of the west boundary occurred at a small positive load with control sensors still measuring negative rotation (Figure 5-3d). The out-of-plane rotation occurred primarily over two or three hoop spacings at the location where buckling of the two corner bars was observed in the previous cycle. A maximum out-of-plane displacement of 2 in. (50.8 mm) was measured approximately 9 in. (22.9 cm) above the footing. Because very little residual strength remained, loading in the positive direction was terminated.

Following the out-of-plane failure at the west boundary, monotonic loading was applied in the negative direction. At -1.87% rotation, cover concrete on the front (south) face of the specimen, at the east boundary, visibly bulged outward between approximately 3 in. (7.6 cm) and 12 in. (30.5 cm) above the specimen footing. At -1.97% rotation, abrupt crushing of the east boundary occurred and all fourteen No. 4 longitudinal bars, and some No. 3 web longitudinal bars, was observed

(Figure 5-4b). The failure caused a nearly instantaneous drop in capacity between approximately 85% and 10% of peak capacity, and axial load immediately dropped from $0.10A_{cv}f'_c$ (265 kip [1178 kN]) to $0.042A_{cv}f'_c$ (115 kip [510 kN]). Damage was concentrated within the bottom 14 in. (356 mm) of the wall, or approximately one-sixth of the wall panel height (h/6), and extended approximately one-third the length of the wall from the east edge (Figure 5-5). A photo of the east boundary of WP1 following removal of loose concrete is shown in Figure 5-4c. Buckling of the No. 4 boundary longitudinal reinforcement generally occurred over multiple hoop spacings except for bars located at the corner of a hoop which typically buckled between hoops. Figure 5-4d shows a photo of hoops and cross-ties removed from the east boundary following the test. In the photo, it can be seen that all three of the hoops fractured; however, fracture of only one of the six cross-ties occurred. Instead, failure of cross-ties generally appeared to occur due to opening of 90^o hooks and some 135^o hooks. Photos of the front and rear faces of the specimen, taken at the end of the test, are shown in Figure 5-5. Damage at both boundaries occurred over a short height at the base of the wall and extended horizontally from the east and west edges about one-third of the length of the wall (l_w/3).

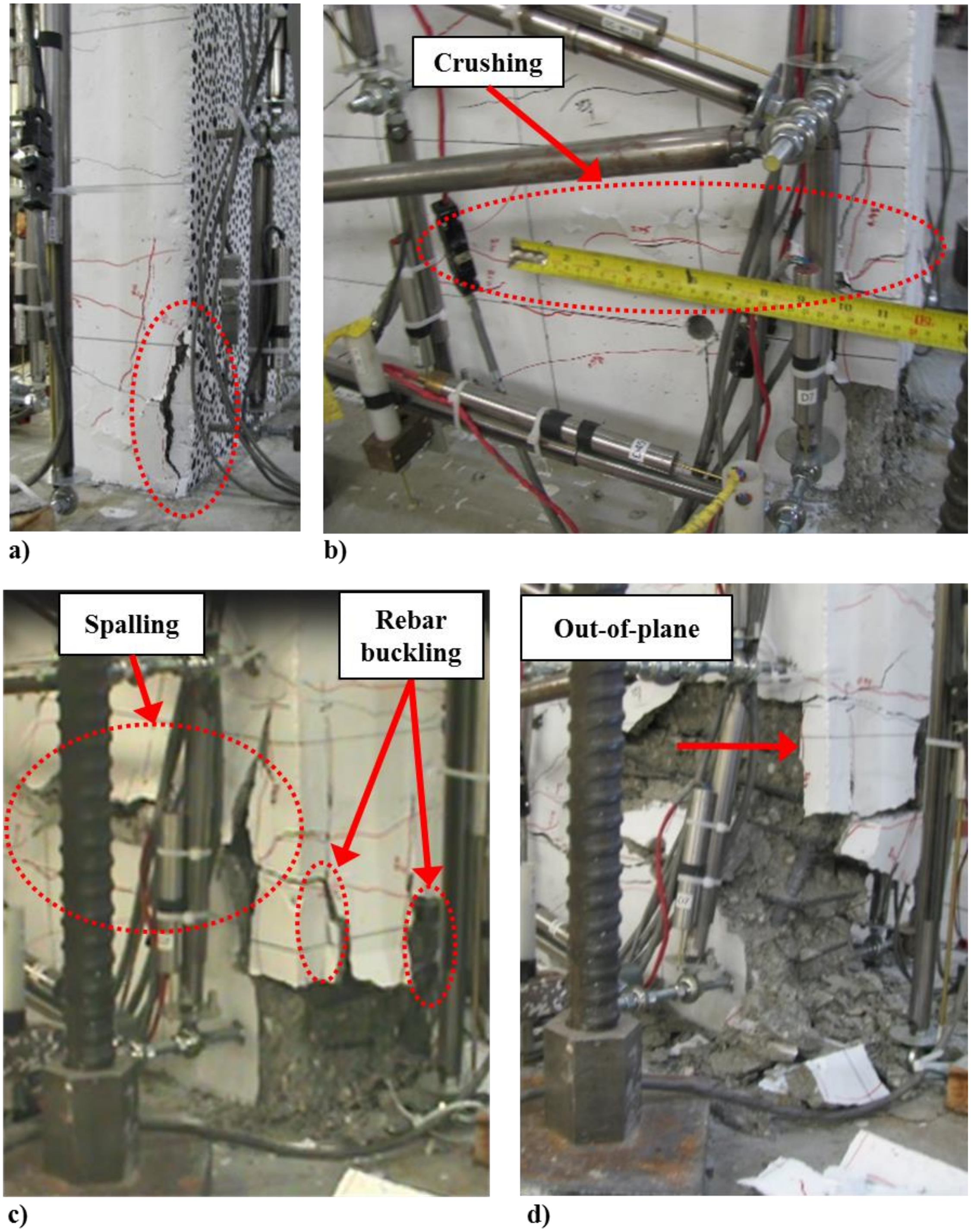

Figure 5-3: Specimen WP1 west boundary damage – a) Vertical splitting and spalling of cover concrete (+0.50% rotation, cycle 3); b) Cover concrete crushing on rear (north) face (+1.0% rotation, cycle 1); c) Cover concrete spalling and buckling of longitudinal reinforcement (+1.5% rotation, cycle 1); and d) Out-of-plane instability

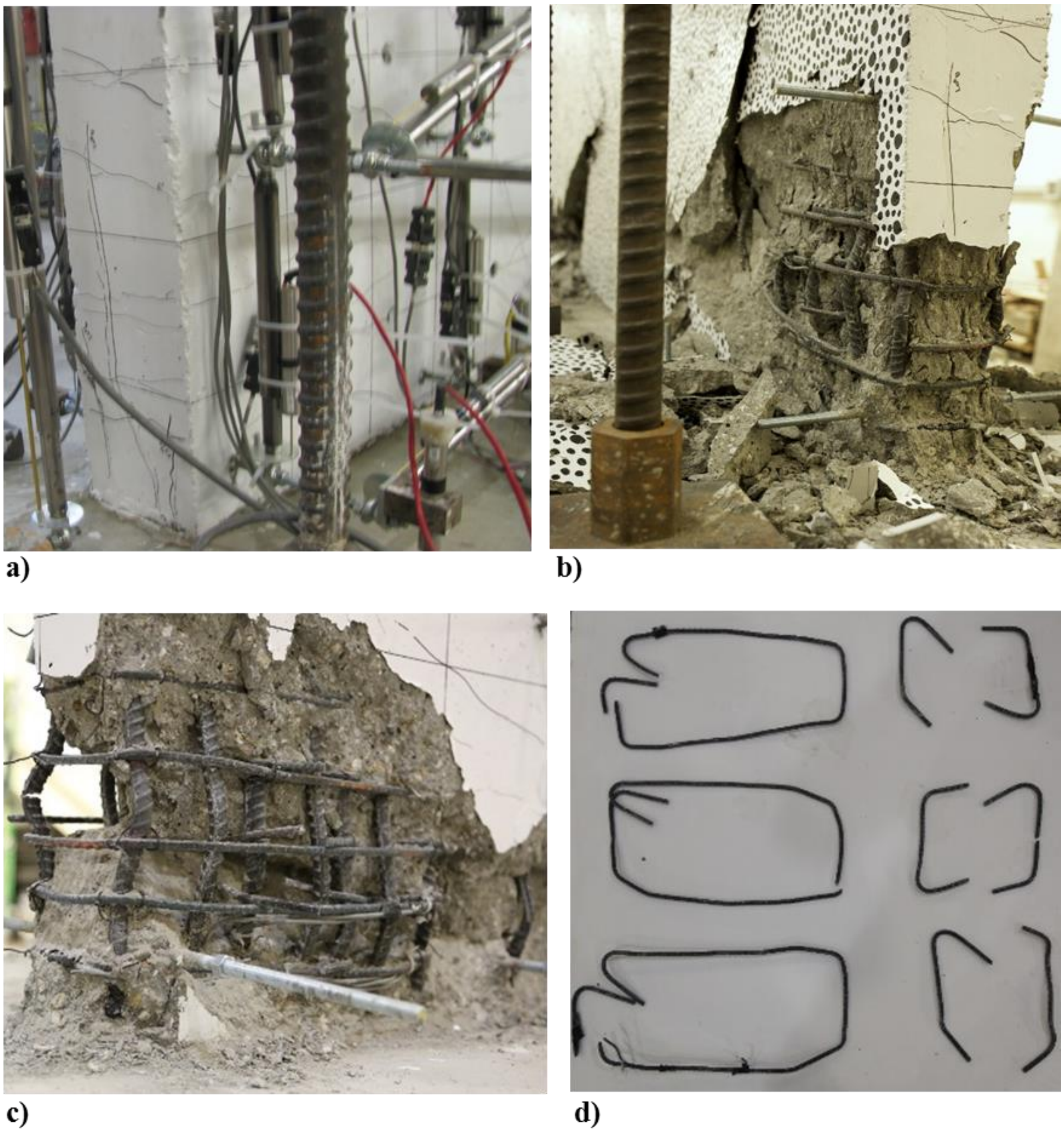

Figure 5-4: Specimen WP1 east boundary damage progression – a) Vertical splitting of concrete (-1.0% rotation, cycle 1); b) Crushed concrete and buckled longitudinal reinforcement immediately after failure (-1.97% rotation); c) After removal of loose concrete; and d) Damaged hoops and cross-ties removed after test

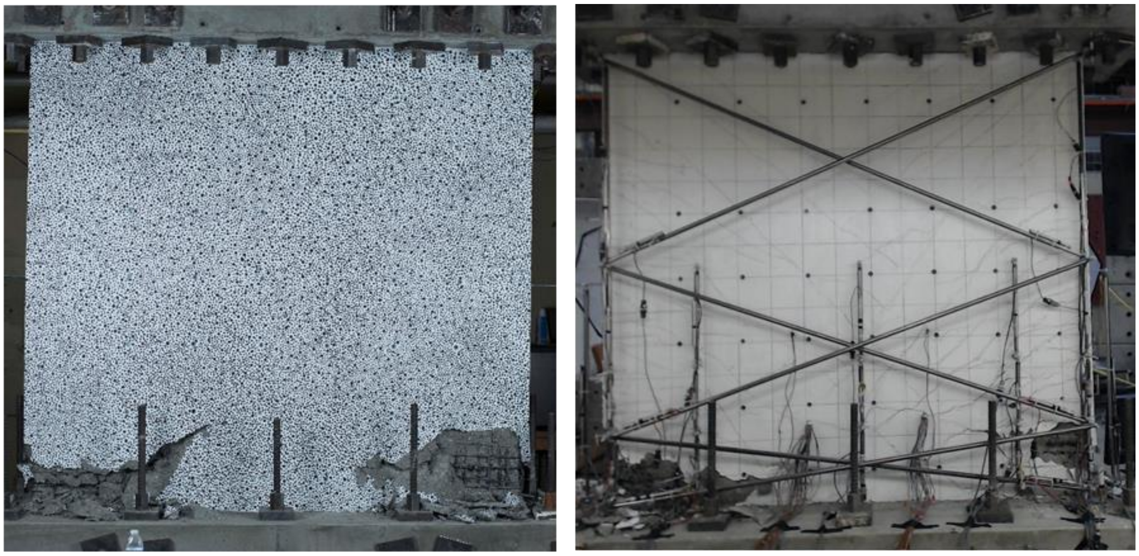

a) b)

Figure 5-5: Specimen WP1 – a) Photo of front (south) face of specimen after test; and b) Photo of rear (north) face of specimen after test

5.2.2 Specimen WP2

Specimen WP2 differed from the reference specimen (WP1) primarily by the quantity of transverse reinforcement provided at the boundaries of the wall. Like specimen WP1, WP2 as 6 in. (152 mm) thick and was constructed with eight No. 5 longitudinal reinforcing bars at the west boundary and fourteen No. 4 longitudinal reinforcing bars at the east boundary. It is noted that cover concrete for WP2 was also slightly thicker (c_c=0.75 in.; 19.2 mm) than specimen WP1 (c_c=0.5 in.; 12.7 mm). The observed behavior for WP2 was similar to WP1 except that an additional cycle was completed at 1.5% rotation. Horizontal flexural cracking of concrete was first observed at the west and east boundaries of the wall at +0.049% rotation and -0.053% rotation, respectively. Tension strains in excess of the yield strain reported in Table 4-3 were indicated by strain gages attached to longitudinal reinforcement at wall edges at +0.22% and -0.20% rotation at the east and west boundaries, respectively. The maximum lateral strength in the positive loading direction was measured at +1.35% (+/- 1.5% rotation cycle 1), at which time the lateral strength was 1.09 times the calculated nominal flexural strength (M_n). Peak lateral strength in the negative loading direction was ($1.01M_n$,) was measured at -1.41% rotation during the same loading cycle (+/- 1.5% rotation cycle 1).

Crushing of concrete at the west boundary was observed just prior to reaching +1.5% rotation during the first loading cycle (Figure 5-6a). In the following loading cycle to +1.5% rotation, crushing of the confined region and a portion of the wall web occurred prior to reaching +1.5% rotation, and nearly a 20% reduction in strength from peak capacity was observed (Figure 5-6b). Damage was concentrated over a short height of approximately 14 in. (h/6; 356 mm) at the base of the wall and extended horizontally from the west edge of the wall approximately 30 in. (l_w/2; 762 mm). While loading to +1.5% rotation a third time, lateral (out-of-plane) instability and crushing of the boundary and web occurred at a small positive load with control sensors still measuring negative rotation (Figure 5-6c). Positive loading was terminated and monotonic loading in the negative direction was applied. While loading monotonically in the negative direction (compression at the east boundary) simultaneous crushing of the confined region and a portion of the wall web occurred at -1.78% rotation (Figure 5-6d) and lateral load-carrying capacity immediately dropped to approximately 40% of the peak strength measured in previous cycles.

Similar to specimen WP2, opening of several cross-ties was observed when loose concrete was removed following the test, and fracture of cross-ties was only observed in a few cases. Photos of the front and rear faces of the wall, following the test, are shown in Figure 5-7. Damage occurred primarily over a short height at the base of the wall, like WP1, and extended almost one-half the length of the wall from the west and east edges.

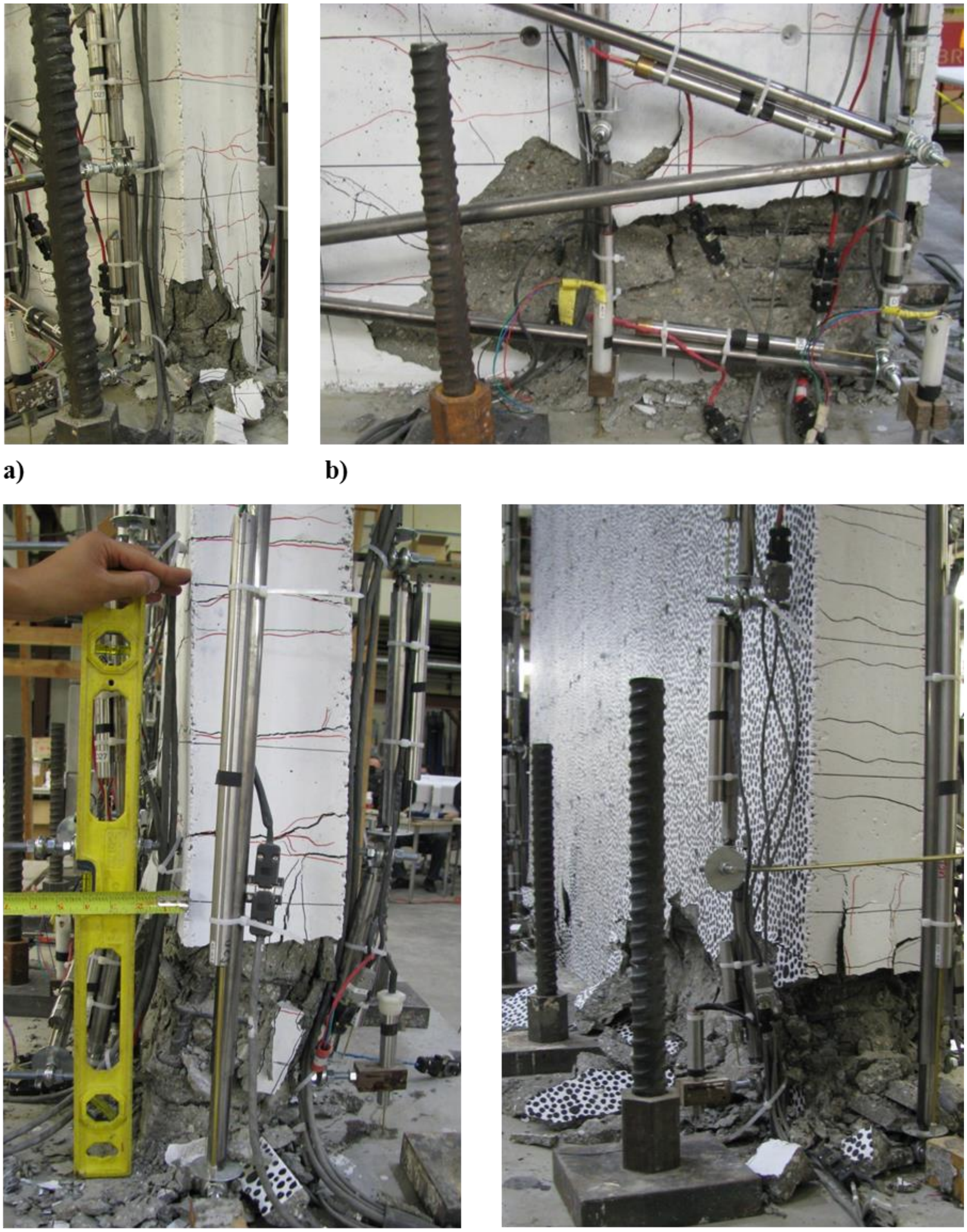

a) b)

c) d)

Figure 5-6: Specimen WP2 damage progression – a) Crushing/spalling of cover concrete at west boundary (+1.5% rotation, cycle 1); b) Spalling of concrete along the rear (north) face of the wall at west boundary (+1.5% rotation, cycle 2); c) Lateral instability of the west boundary (+1.5% rotation, cycle 3); and d) East boundary after the test

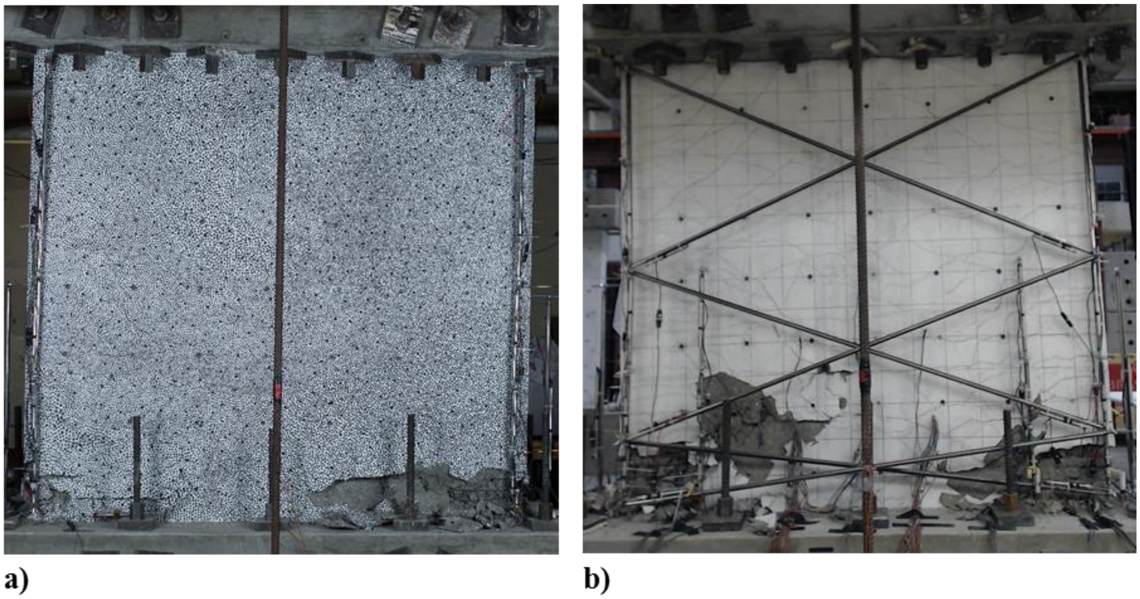
a) b)

Figure 5-7: Specimen WP2 – a) Photo of front (south) face of specimen after test; and b) Photo of rear (north) face of specimen after test

5.2.3 Specimen WP3

Similar to specimen WP1, WP3 was 6 in. (152 mm) thick and was constructed with eight No. 5 longitudinal reinforcing bars at the west boundary and fourteen No. 4 longitudinal reinforcing bars at the east boundary. For specimen WP3, the spacing of boundary transverse reinforcement (s/d_b=6) was larger than WP1, for which s/d_b was 3.2 at west boundary (No. 5 longitudinal reinforcement; d_b=0.625 in. [15.9 mm]) and 4.0 at the east boundary (No. 4 longitudinal reinforcement; d_b=0.5 in. [12.7 mm]). The observed behavior for WP3 was similar to WP1 and WP2 during loading cycles up to, and including, +/-1.0% rotation. Horizontal flexural cracking of concrete was first observed at the west and east boundaries of the wall at +0.048% rotation and -0.050% rotation, respectively. Tension strains in excess of the yield strain reported in Table 4-3 were indicated by strain gages attached to longitudinal reinforcement +0.19% and -0.19% rotation at the east and west boundaries, respectively. The maximum measured lateral strength in the positive and negative loading directions were $1.1M_n$ and $1.01M_n$, respectively, and occurred at +1.38% and -1.38% rotation, respectively.

At the west boundary of WP3, minor crushing of the boundary region and buckling of the two No. 5 longitudinal bars closest to the west edge of the wall were observed at +1.5% rotation during the second loading cycle (Figure 5-8a). During the same loading cycle, at -1.5% rotation, buckling of the four No. 4 longitudinal bars closest to the east edge of the wall was observed. During the third cycle to +1.5% rotation, crushing of the confined region and a portion of the wall web occurred at the west boundary just prior to reaching +1.5% rotation. All eight No. 5 longitudinal bars and four web vertical bars buckled (Figure 5-8b and Figure 5-8c). While loading to -1.5% rotation a third time, three of the eight buckled No. 5 bars at the west boundary fractured in tension prior to reaching -1.5% rotation. As loading continued in the negative direction, an abrupt compression failure occurred at -1.22% rotation, and buckling of all fourteen No. 4 boundary longitudinal bars and four web vertical bars was observed. The lateral strength just prior to the abrupt failure was approximately 68% of the peak strength measured in previous cycles. An additional cycle was attempted in the positive loading direction. At approximately +0.6% rotation, crushing occurred along the full length of the wall and buckling of all boundary and web longitudinal reinforcement occurred (Figure 5-9). Lateral residual capacity immediately dropped to nearly zero, and the axial capacity instantaneously dropped by approximately 60% from $0.10A_{cv}f'_c$ to $0.04A_{cv}f'_c$. A photo of the specimen following the axial failure is shown in Figure 5-9a. Web longitudinal reinforcement was buckled over a height of approximately 12-15 in. (305-356 mm), or about $32d_b$-$40d_b$ (Figure 5-9b). As shown in Figure 5-9c, web longitudinal reinforcement was placed outside of transverse reinforcement (i.e., detail WEB-1), a detail that provided no lateral restraint to suppress buckling once concrete crushing/spalling occurred. Photos of the front and rear faces of the wall, at the end of the test, are shown in Figure 5-10.

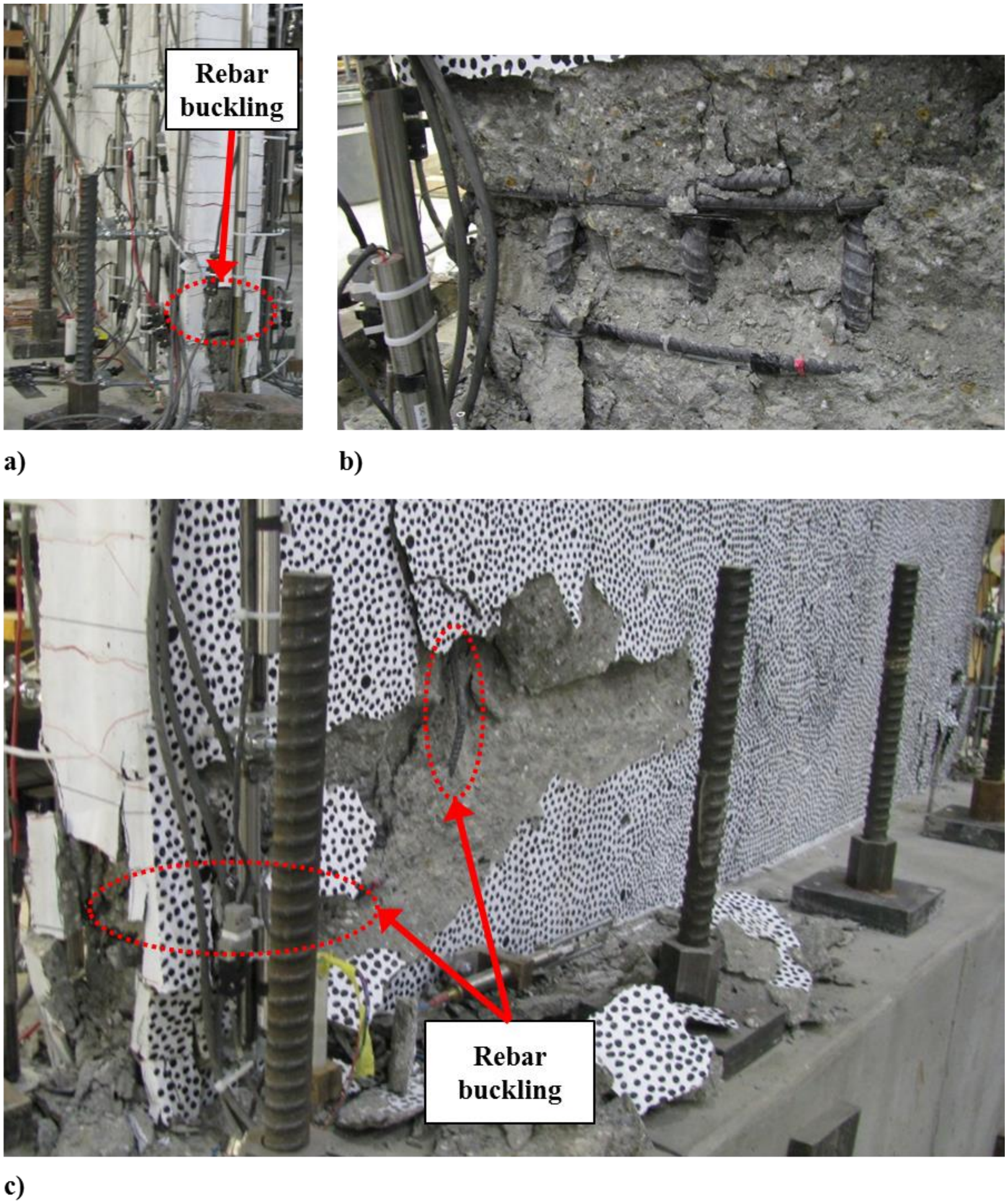

Figure 5-8: Specimen WP3 damage progression at west boundary – a) Concrete crushing/spalling and slight buckling of reinforcement at west edge of wall (+1.5% rotation, cycle 2); b) Buckling of No. 5 longitudinal reinforcement at west boundary (+1.5% rotation, cycle 3); and c) Boundary and web crushing and longitudinal reinforcement buckling (+1.5% rotation, cycle 3)

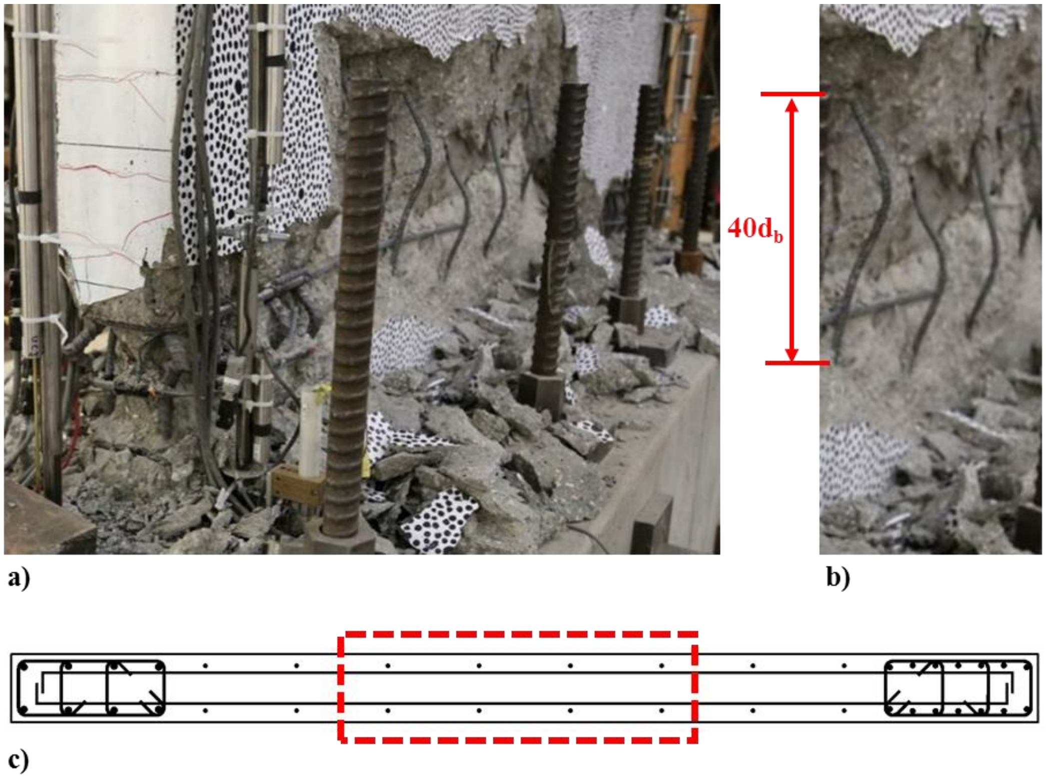

Figure 5-9: Specimen WP3 web damage – a) Crushing of concrete and buckling of longitudinal reinforcement (after test); b) Close up of web longitudinal reinforcement buckling; and c) WP3 web detail (WEB-1) with longitudinal reinforcement placed outside of transverse reinforcement

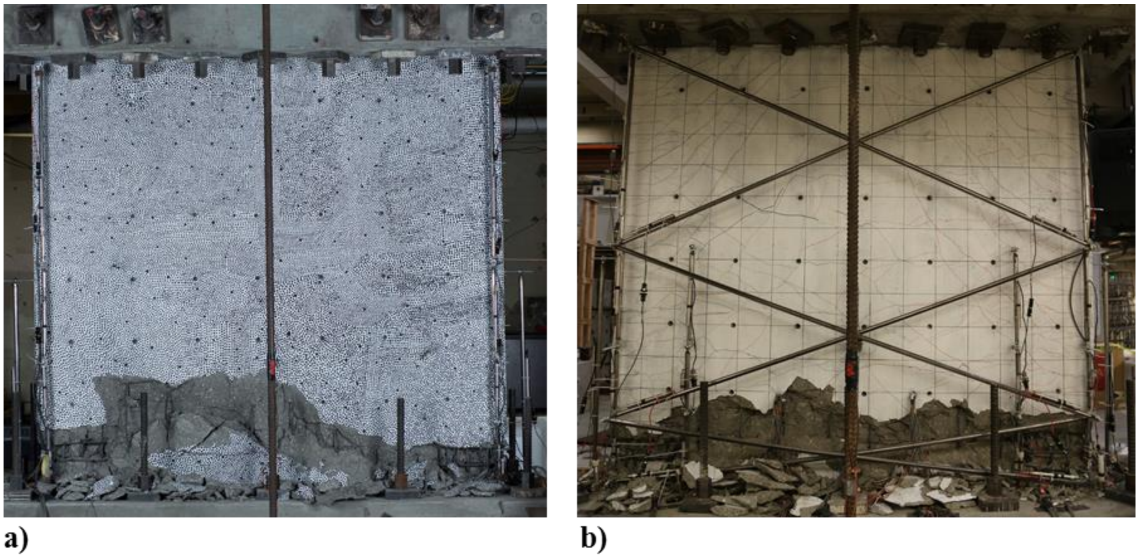

Figure 5-10: Specimen WP3 – a) Photo of front (south) face of specimen after test; and b) Photo of rear (north) face of specimen after test

5.2.4 Specimen WP4

Specimen WP4 was designed for a compression depth, determined for an extreme fiber compression strain of 0.003 and an axial load of $0.10A_{cv}f'_c$, of approximately 30% of the length of the wall (i.e., c/l_w=0.3), which is about 1.5 times the compression depth for the rectangular specimens. To do so, WP4 was constructed with an enlarged boundary at the east end of the wall and a larger quantity of longitudinal reinforcement at the east boundary than at the boundaries of specimens WP1, WP2, and WP3. The web of the wall and the west boundary were 6 in. (152 mm) thick, and the east (flange) boundary was 22 in. (559 mm) thick. Due to the asymmetric cross-section and longitudinal reinforcement, different behavior was observed for loading in the positive loading direction (flange in tension) and negative loading direction (flange in compression). Horizontal flexural cracking of concrete was first observed at the west and east boundaries of the wall at +0.054% rotation and -0.060% rotation, respectively. Tension strains in excess of the yield strain reported in Table 4-3 were indicated by strain gages attached to longitudinal reinforcement +0.21% and -0.21% rotation at the east and west boundaries, respectively. The maximum measured lateral strength in the positive and negative loading directions were $0.99M_n$, measured at +0.91% rotation, and $1.0M_n$, measured at -2.9% rotation.

During the first loading cycle to +1.5% rotation, at a rotation of +1.32%, an abrupt compression failure (concrete crushing and reinforcement buckling) was observed at the west (web) boundary, and the lateral load-carrying capacity dropped to approximately 15% of the peak lateral strength. Damage extended horizontally from the west edge of the wall nearly two-thirds the length of the wall (58 in. [147 cm]). When loose concrete was removed, it was observed that several No. 3 web longitudinal bars buckled over a height of approximately 15 in. (381 mm), or about $40d_b$ (Figure 5-11a). Prior to the failure, no visible signs of lateral (out-of-plane) deformation were evident;

however, as crushing occurred, the compression zone deformed out-of-plane (Figure 5-11b). A maximum out-of-plane displacement of 2.25 in. (57.2 mm) was measured approximately 8 in. (20.3 cm) above the wall footing.

While loading monotonically in the negative direction, minor crushing of cover concrete at the east edge of the wall was observed at approximately -2.5% rotation, and fracture of at least one longitudinal bar at the west (web) boundary occurred. The wall was unloaded after reaching -2.9% rotation with no signs of further damage at the east (flange) boundary. An additional cycle was conducted in the negative direction, during which several web and west boundary longitudinal bars fractured in tension. At -3% rotation, the measured lateral strength was approximately 80% of the peak capacity measured in previous cycles. When the test was stopped, damage at the east boundary consisted only of minor crushing of cover concrete along the east edge of the wall (Figure 5-11c and Figure 5-11d). Photos of the front and rear faces of the wall, taken after the test, are shown in Figure 5-12. Buckling of unsupported web longitudinal reinforcement is evident in Figure 5-12a over the full height over which crushing of concrete occurred.

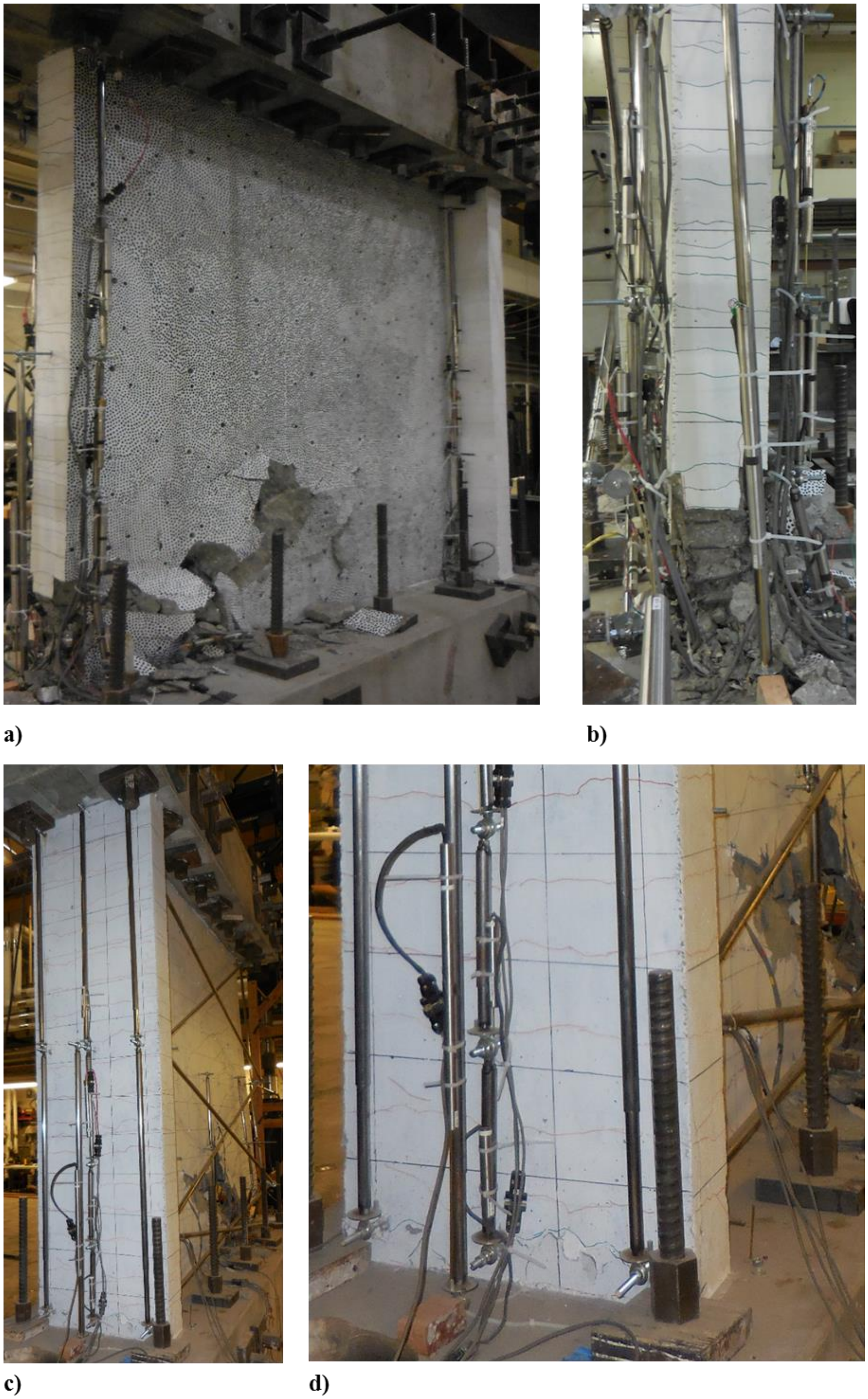

Figure 5-11: Specimen WP4 damage – a) Boundary/web crushing, b) Out-of-plane displacement of web boundary, c) Flange after the test; and d) Minor crushing of cover concrete at flange boundary

a) b)

Figure 5-12: Specimen WP4 – a) Photo of front (south) face of specimen after test; and b) Photo of rear (north) face of specimen after test

5.2.5 Specimen WP5

Specimen WP5 was constructed with a 6 in. (192 mm) thick web along the east half of the wall, and a thicker web (7.5 in. [191 mm]) along the west half of the wall. Continuous transverse reinforcement was used for confinement at both boundaries, and all web longitudinal reinforcement was supported by a cross-tie and placed inside of transverse bars. Additionally, the quantity of boundary transverse reinforcement provided at both boundaries was approximately twice as much as required by ACI 318-14, whereas boundary transverse reinforcement for specimens WP1-WP4 was close to the minimum allowed. To achieve a compression depth of approximately 20% of the length of the wall (c/l_w=0.2), the applied axial load was different in the two loading directions. For loading in the positive direction, causing compression at the 7.5 in. (191 mm) thick boundary, the applied axial load was 337.5 kip (1501 kN). In the opposite loading direction, causing compression at the 6 in. (152 mm) thick boundary, the applied axial load was the same as specimens WP1-WP4 (270 kip; 1201 kN).

Horizontal flexural cracking of concrete was first observed at the boundaries of the wall at +0.058% rotation and -0.049% rotation. Strain gages attached to longitudinal reinforcement indicated that tension strains in excess of the yield strain reported in Table 4-3 were reached at +0.22% and -0.22% rotation at the east and west boundaries, respectively.

Two complete cycles to +/-2% rotation were completed without strength loss. The maximum lateral strength measured in the positive loading direction (1.21M_n) and negative loading direction (1.16M_n) occurred at +2% rotation and -2% rotation, respectively. Crushing and spalling of cover concrete at both wall boundaries was observed during +/-2% rotation cycles, but no damage to the confined core was evident at either boundary. At -2% rotation (cycle 2), slight buckling of longitudinal bars at the east boundary was observed at the base of the wall (Figure 5-13a and Figure 5-13b), although no sign of strength loss was evident. In the following half loading cycle to +3% rotation (cycle 1), three of the previously buckled longitudinal bars at the east boundary ruptured in tension, causing an 18% drop from peak strength at the time loading was stopped at +3% rotation. The first fracture occurred at approximately +1% rotation, and two additional bars fractured prior to reaching +3% rotation (Figure 5-13c). A photo of the front face of the specimen at +3% rotation (cycle 1) is shown in Figure 5-13d. Up to this point, the wall was stable in compression, and crushing/spalling of concrete was limited to the boundary of the wall; that is, damage in the unconfined web region was not observed up to this point.

While loading in the negative direction to -3% rotation (cycle 1), the east boundary (compression zone) began to slide out-of-plane, apparently due to the eccentricity caused by rupture of longitudinal reinforcement and asymmetric crushing/spalling of concrete. The out-of-plane movement concentrated at the base of the wall where longitudinal bars had fractured in tension while loading to +3% rotation (Figure 5-14a and Figure 5-14b). Figure 5-14b shows the lateral displacement between two pieces of a fractured longitudinal bar on the southeast corner of the wall. A lateral displacement of approximately 2.75 in. (70 mm) was measured when loading was terminated at -3% rotation. As compressive stresses began acting on the east edge of the wall, crushing of concrete in the wall web and buckling of web longitudinal reinforcement were observed (Figure 5-14c). Web longitudinal bars buckled between transverse reinforcement, and cross-ties, which provided lateral support at a spacing of $16d_b$ (Figure 5-14d). When loading in the negative direction was terminated at -3% rotation, residual capacity was approximately 36% of the peak capacity.

Following failure at the east boundary, loading in the positive direction was conducted until +4% rotation. While loading to +4% rotation, all longitudinal bars at the east boundary, as well as several web longitudinal bars, fractured. Because so many vertical bars had fractured, very little overturning demand was available to impose compressive stresses at the west boundary. In an attempt to impose additional compression demands, an additional 70 kip (311 kN) of axial load was applied. The test was stopped at +4% rotation with the wall still resisting approximately 52% of its peak strength. Slight buckling of the two outermost longitudinal bars at the west edge of the wall was observed, although very little additional damage was observed (Figure 5-15).

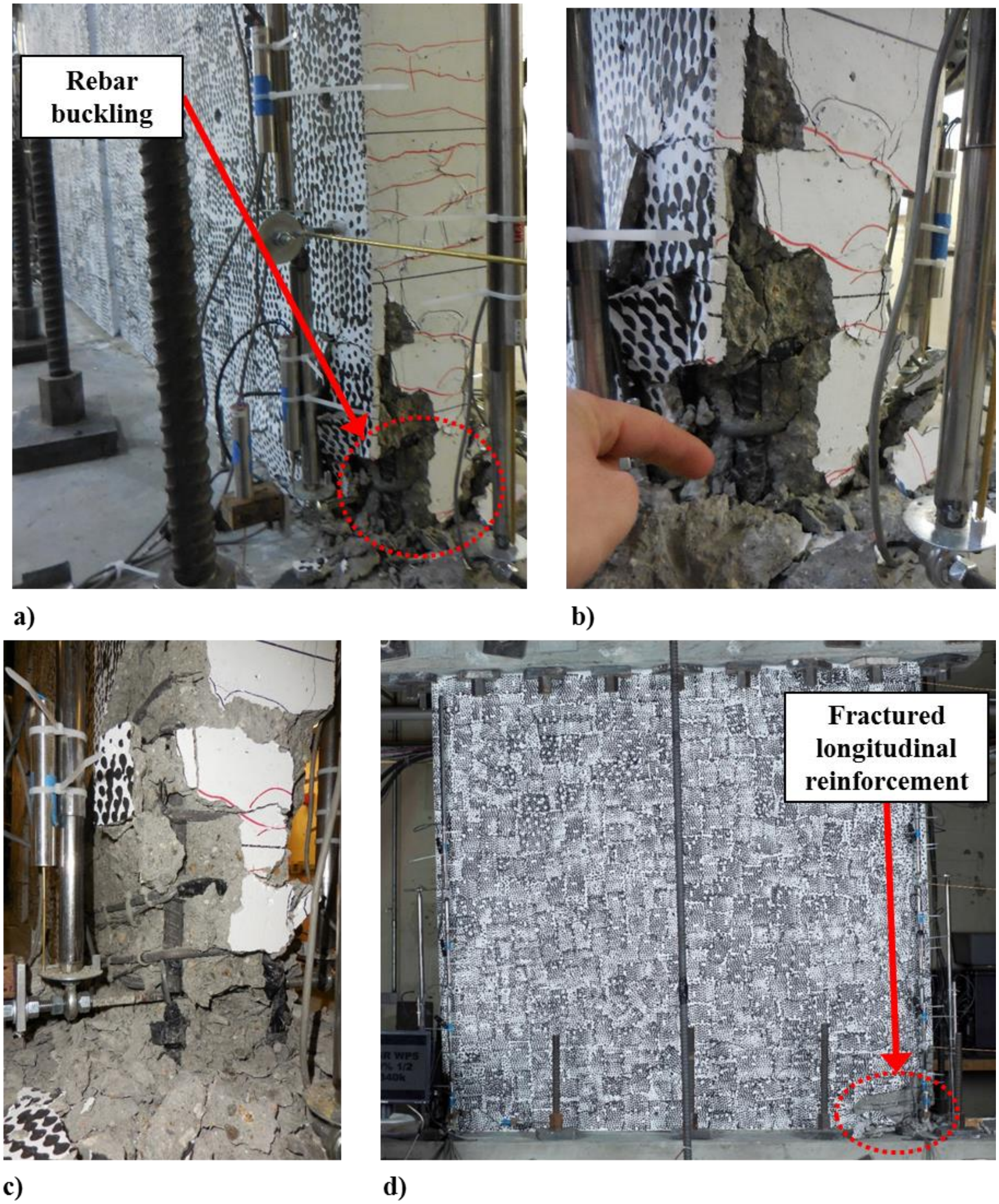

Figure 5-13: Specimen WP5 damage progression at east boundary – a) Buckling of longitudinal reinforcement (-2% rotation, cycle 2); b) Close up of slightly buckled longitudinal bars (-2% rotation, cycle 2); c) Fracture of previously buckled longitudinal reinforcement (+3% rotation, cycle 1); and d) Wall damage at +3% rotation (cycle 1)

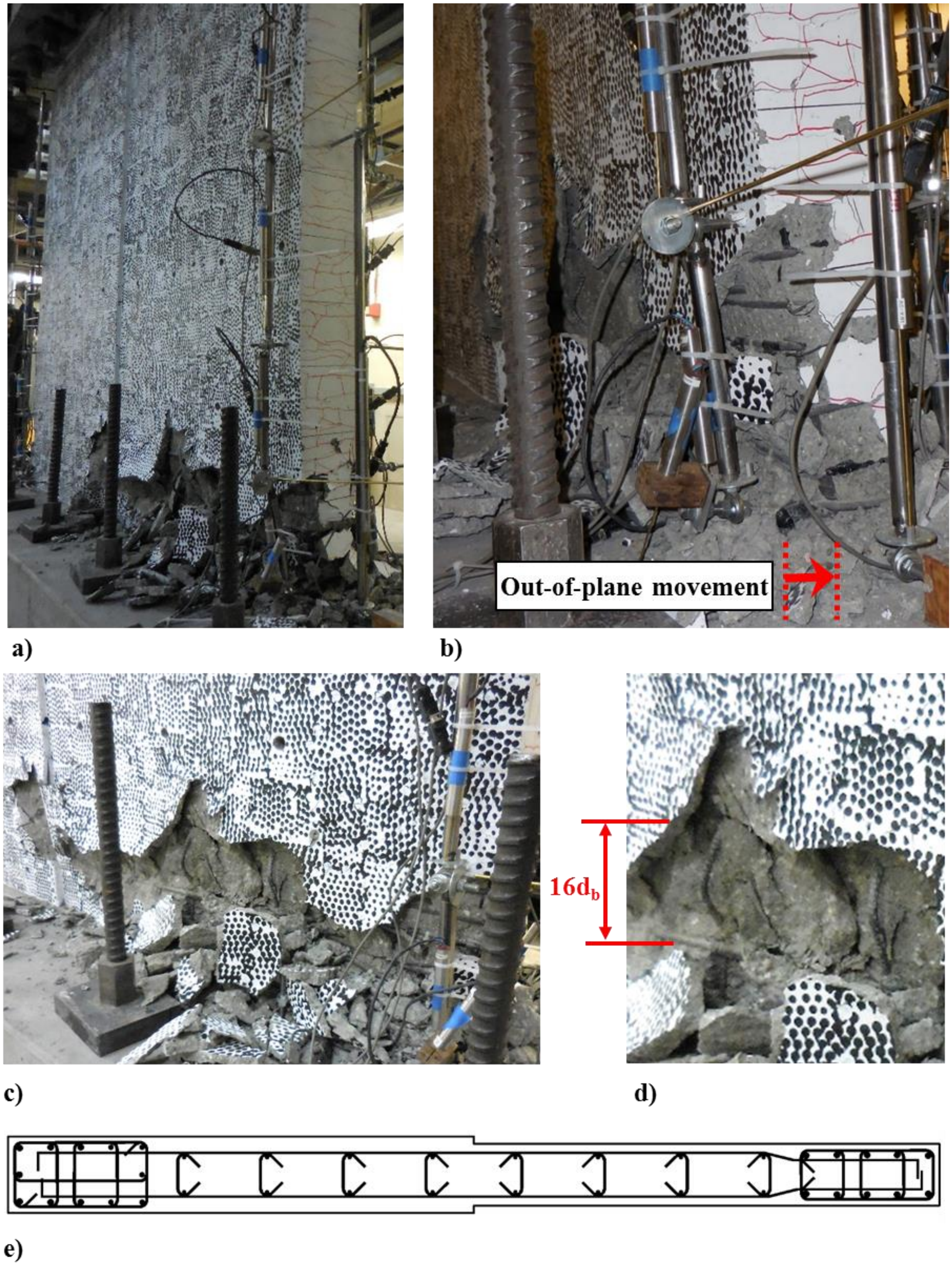

Figure 5-14: Specimen WP5 – a) Web crushing (-3% rotation); b) Out-of-plane movement of east boundary at base of wall (-3% rotation); c) Buckling of longitudinal reinforcement in web; d) Close up of buckled web longitudinal reinforcement; and e) WP5 web detail (WEB-3) with longitudinal reinforcement supported laterally by cross-ties at 16d_b

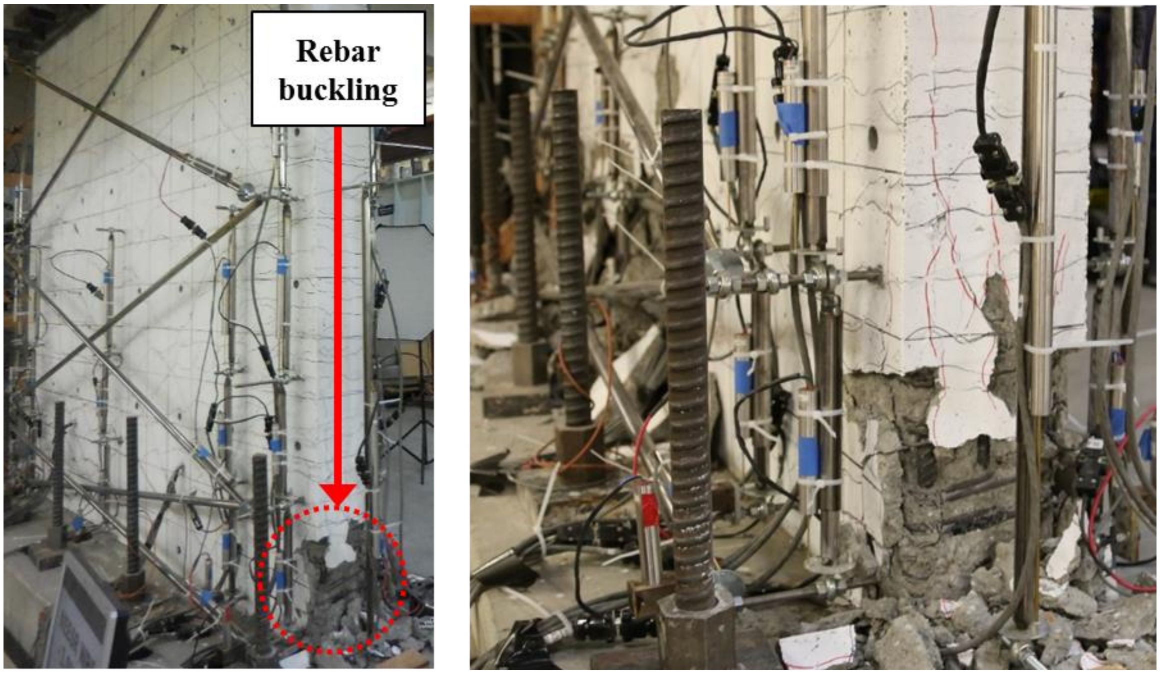

Figure 5-15: Specimen WP5 damage at west boundary – a) Cover crushing/spalling and buckling of longitudinal reinforcement (+3% rotation); and b) Final damage state at +4% rotation

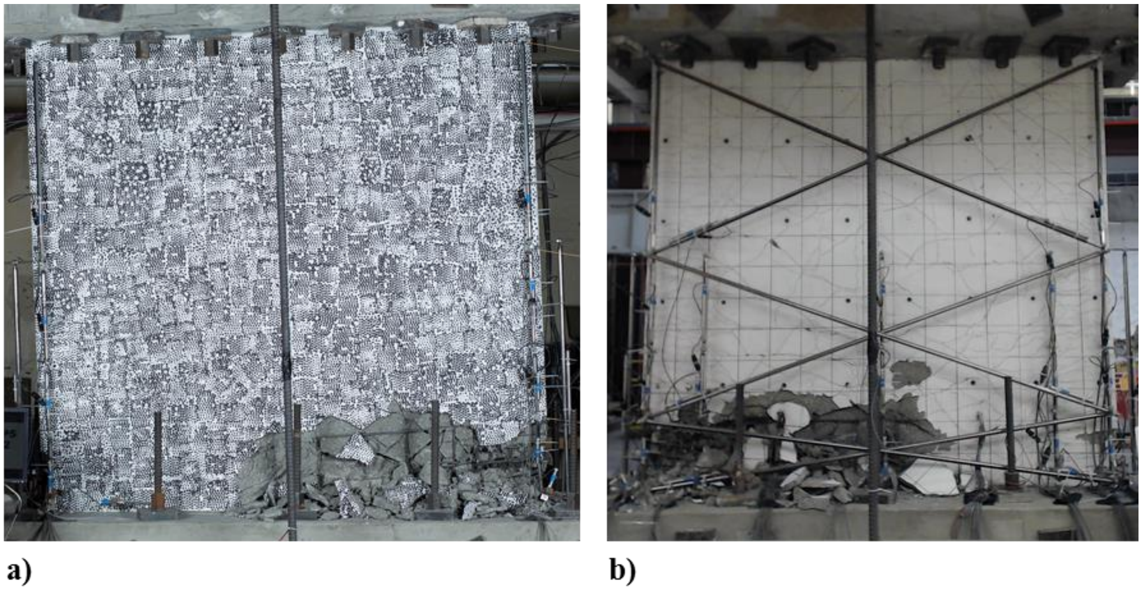

Figure 5-16: Specimen WP5 – a) Photo of front (south) face of specimen after test; and b) Photo of rear (north) face of specimen after test

5.2.6 Specimen WP6

Specimen WP6 was 7.5 in. (191 mm) thick and was constructed with continuous transverse reinforcement at the west boundary and outer hoops and 135°-135° cross-ties at the east boundary. Web longitudinal reinforcement was placed inside of transverse reinforcement, and cross-ties were provided on the west half of the wall. A constant axial load of 337.5 kip (1501 kN) was applied for the duration of the test. Horizontal flexural cracking of concrete was first observed at the boundaries of the wall at +0.047% rotation and -0.037% rotation. Strain gages attached to longitudinal reinforcement indicated that tension strains in excess of the yield strain reported in Table 4-3 were reached at +0.25% and -0.22% rotation at the east and west boundaries, respectively.

Two complete cycles were completed to +/-2% rotation prior to significant strength loss. The peak lateral strength measured in the negative loading direction (1.20M_n) occurred at -2% rotation (cycle 1). A small reduction in strength was observed at +2% rotation (cycle 2), at which time buckling of longitudinal reinforcement at the west edge of the wall was observed between hoops located 3 in. (76 mm) and 5 in. (127 mm) above the footing (Figure 5-17a). While loading to -2% rotation in the following half load cycle, the bar at the southwest corner fractured at approximately -0.25% rotation (Figure 5-17b). At – 2% rotation, the measured load was approximately 95% of the peak strength from previous cycles, and visible damage at the east boundary consisted only of crushing/spalling of cover concrete when loading was reversed at -2% rotation. While unloading from -2% rotation (cycle 2), out-of-plane movement of the west boundary was observed while horizontal flexural cracks were still open. The movement was in the north direction, towards the rear face of the wall, and maximum out-of-plane displacements appeared to occur above a height of approximately 15 in. (381 mm) above the footing. Buckling of the two non-fractured bars at the west edge of the wall was observed at approximately +0.5% rotation, and out-of-plane displacement of the west boundary became more apparent as buckling became more severe. The wall appeared to realign vertically at larger rotations, and the maximum measured lateral strength in the positive loading direction ($1.22M_n$) was measured at +3% rotation. While loading in the negative direction to -3% rotation, several more longitudinal bars fractured in tension (Figure 5-17c). When loading was reversed at -3% rotation, the measured lateral strength was 71% of the peak capacity. While attempting to reload to +3% rotation (cycle 2), out-of-plane movement of the west boundary occurred near the base of the wall. Similar to what was observed for specimen WP5, the out-of-plane movement appeared to occur due to lateral sliding along a flexural crack at the height where longitudinal reinforcement previously fractured in tension. Crushing of the wall web and buckling of web longitudinal bars were observed over more than half the length of the wall (Figure 5-17d).

At the east boundary of WP6, out-of-plane movement of the compression zone was observed while unloading from +3% rotation during the first cycle. The out-of-plane movement occurred while horizontal flexural cracks were open and maximum out-of-plane displacements occurred near midheight of the wall panel, approximately 40 in. (1016 mm) above the footing. As the horizontal cracks closed, out-of-plane movement decreased and was no longer visible. Buckling of longitudinal reinforcement and crushing of the confined boundary occurred just prior to reaching -3% rotation (cycle 1). A small, abrupt drop in strength occurred, and at least four longitudinal bars buckled (Figure 5-18a). While loading to +3% rotation (cycle 2), the three outer bars fractured in tension. During the second cycle to -3% rotation, the remaining longitudinal bars at the east boundary buckled, and crushing of the confined core occurred. Figure 5-18b shows the state of the east boundary following the test, and photos of the front and rear faces of the wall, taken at the end of the test, are shown in Figure 5-19.

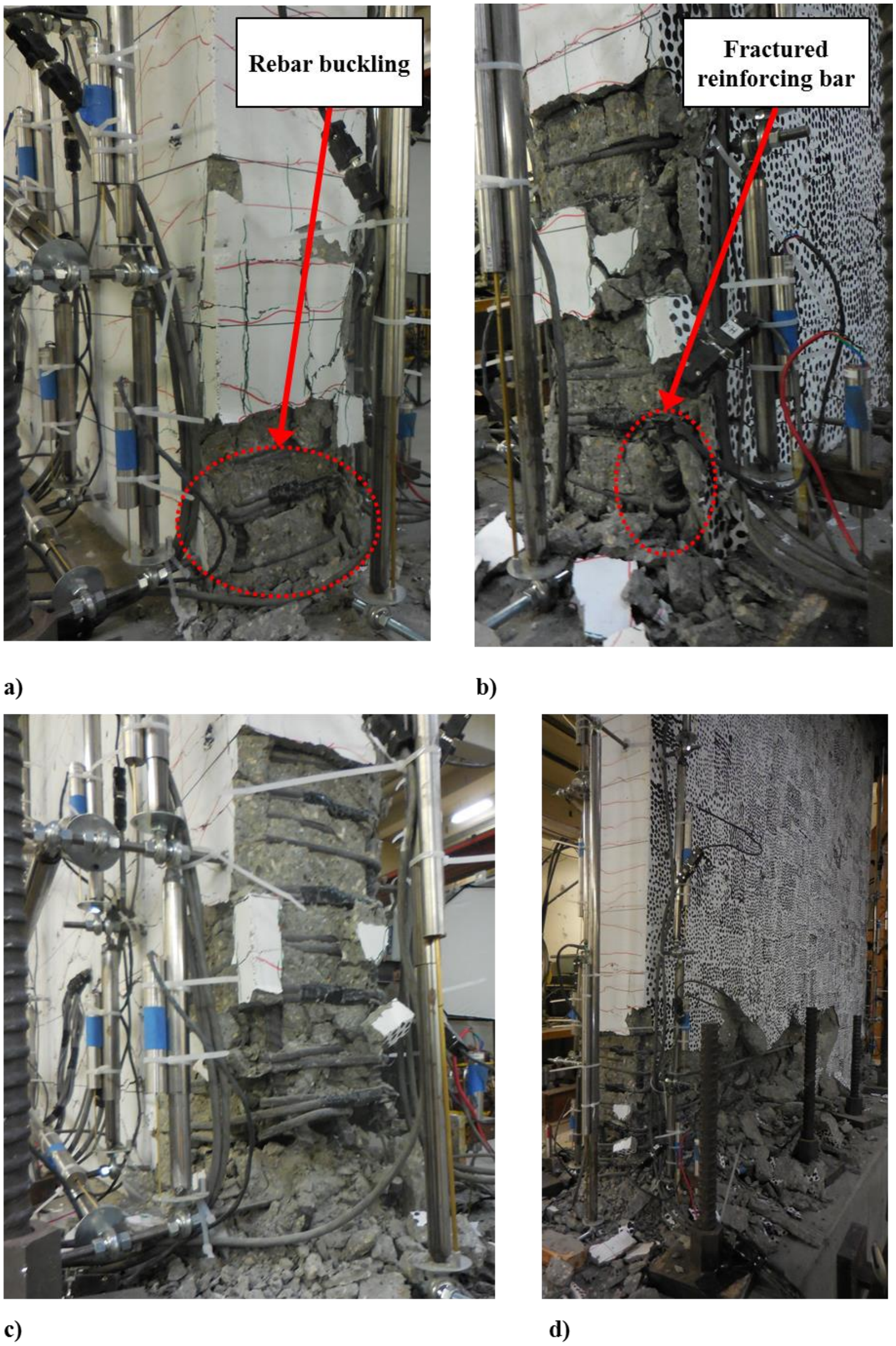

a) b) c) d)

Figure 5-17: Specimen WP6 damage progression at west boundary – a) Buckling of longitudinal reinforcement (+2 % rotation, cycle 2); b) Fracture of longitudinal bar at southwest corner of wall (-2% rotation, cycle 2); c) Fracture of all boundary longitudinal reinforcement (-3% rotation); and d) Out-of-plane sliding of west boundary and web

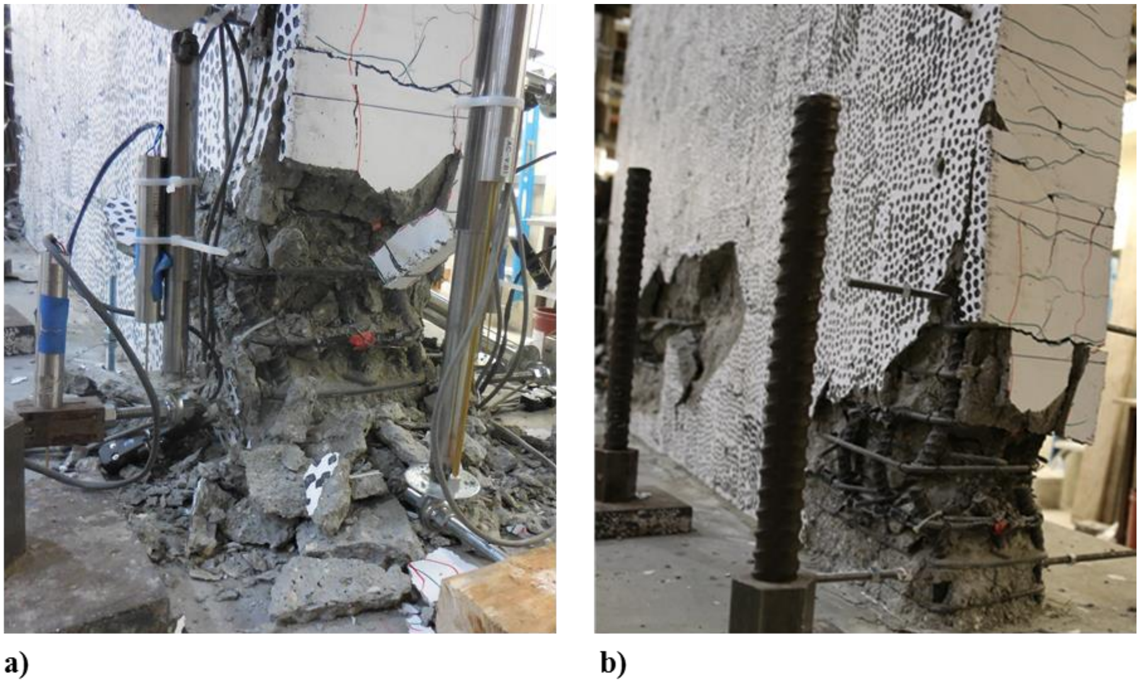

Figure 5-18: Specimen WP6 damage at east boundary – a) Concrete crushing and buckling of longitudinal reinforcement (-3% rotation, cycle 1), b) Damage state at end of test

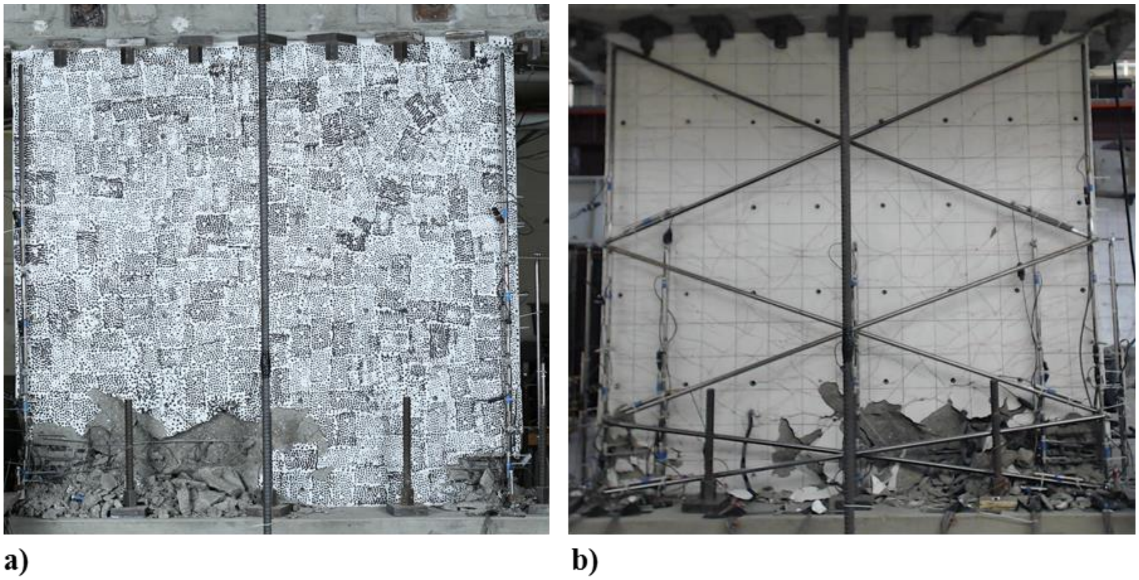

Figure 5-19: Specimen WP6 – a) Photo of front (south) face of specimen after test; and b) Photo of rear (north) face of specimen after test

5.2.7 Specimen WP7

Specimen WP7 was very similar to WP6 except that it was 9 in. (229 mm) thick. A constant axial load of 405 kip (1802 kN) was applied for the duration of the test. Horizontal flexural cracking of concrete was first observed at the boundaries of the wall at +0.051% rotation and -0.044% rotation. Strain gages attached to longitudinal reinforcement indicated that tension strains in excess of the yield strain reported in Table 4-3 were reached at +0.23% and -0.22% rotation at the east and west boundaries, respectively.

Two complete cycles to +/-2% rotation were completed without significant strength loss. In the negative loading direction, peak lateral strength (1.15M_n) was measured at -1.79% rotation. During loading cycles to +/-2% rotation, while unloading from +2% rotation (cycle 2), a small out-of-plane movement of the east boundary of the wall was observed while horizontal flexural cracks were open at the east boundary. The maximum out-of-plane displacement appeared to occur around midheight of the wall panel, approximately 40 in. (1016 mm) above the footing. As the cracks closed, the out-of-plane movement decreased and was no longer visible. Figure 5-20a shows the out-of-plane rotation measured between sensors on the front and rear faces of the specimen at the east edge of the wall. The reported out-of-plane rotation was measured between 14 in. (356 mm) and 44 in. (1118 mm) above the specimen footing, which is the region where the largest out-of-plane displacements were observed. Prior to the 2% rotation cycles, maximum out-of-plane rotations were approximately 0.25%. While unloading from +2% rotation, out-of-plane rotation began to increase as in-plane rotations less than +1.3% were measured. In Figure 5-20b, it can be seen that an in-plane rotation of +1.3% (indicated by a marker on Figure 5-20a and Figure 5-20b) corresponds to the transition point between positive moment and negative moment. At this time, flexural cracks were still open and compressive stresses at the east boundary were resisted primarily by the reinforcing bars. As unloading continued past +1.3%, out-of-plane rotations increased until an in-plane rotation of +0.5% was reached, at which time an out-of-plane rotation of 0.6% was measured. As indicated by the second marker in Figure 5-20b, a change in stiffness is evident at +0.5% rotation, indicating flexural cracks were closing. As the cracks closed, the out-of-plane rotation decreased (Figure 5-20a) and the wall remained stable in compression.

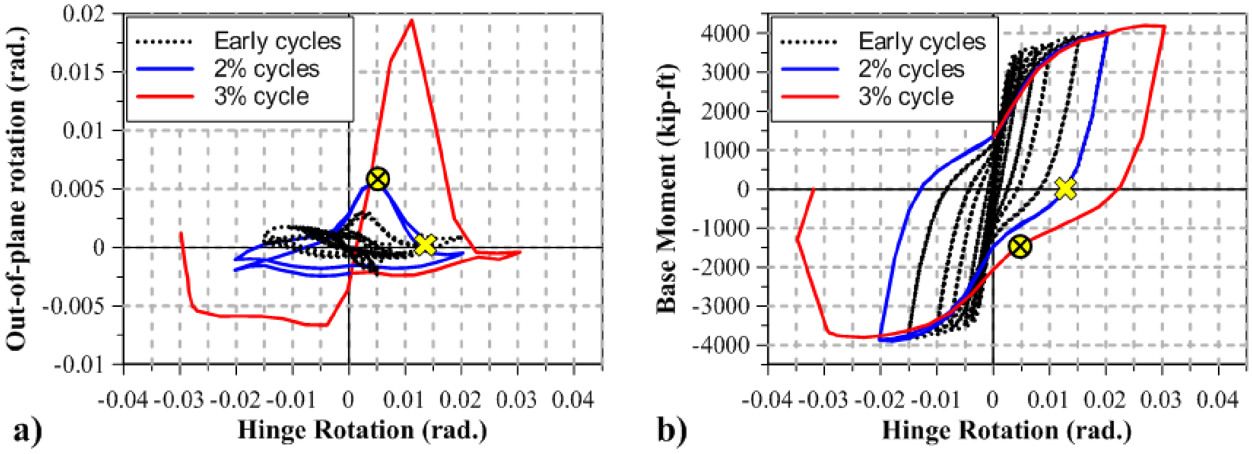

Figure 5-20: East boundary out-of-plane rotation behavior – a) Measured in-plane rotation vs. out-of-plane rotation measured over height of 14”-44” above base, and b) In-plane rotation vs. base moment

At -2% rotation, buckling of the two corner bars at the east edge of the wall was observed between hoops located 5 in. (127 mm) and 7 in. (178 mm) above the footing (Figure 5-21a). During the next loading cycle, an out-of-plane rotation of almost 2% was observed as unloading from +3% rotation occurred. Again, the out-of-plane movement decreased once the horizontal cracks closed. Severe buckling of all three outer longitudinal bars at the east boundary was observed as the applied rotation approached -3%. At -2.98% rotation, abrupt crushing of the east boundary was observed (Figure 5-21b-d). Following the failure, the east boundary had moved out-of-plane in the direction in which out-of-plane movement was observed previously (Figure 5-21d). A displacement of just under 2 in. (51 mm) was measured approximately 24 in. (610 mm) above the footing.. Longitudinal bars at the east boundary buckled and the three confining hoops located between 7 in. (178 mm) and 11 in. (279 mm) above the footing fractured. Several 135° cross-tie hooks were opened at the height where rebar buckling occurred. Two rows of longitudinal web bars were visibly buckled over the height between web transverse reinforcement. Damage extended approximately 36 in. (914 mm; $0.40l_w$) from the east edge of the wall.

The maximum lateral strength measured in the positive loading direction ($1.24M_n$) occurred at +2.67% rotation. Following failure at the east boundary, monotonic loading was conducted to +4.5% rotation. All east boundary longitudinal reinforcement and a few web bars fractured. At +4.5% rotation, residual lateral strength was 44% of the peak strength. Figure 5-22 shows the state of the west boundary at the end of the test. Longitudinal reinforcement at the west edge of the wall buckled; however, the west boundary remained stable in compression and supported residual lateral strength and axial load to +4.5% rotation.

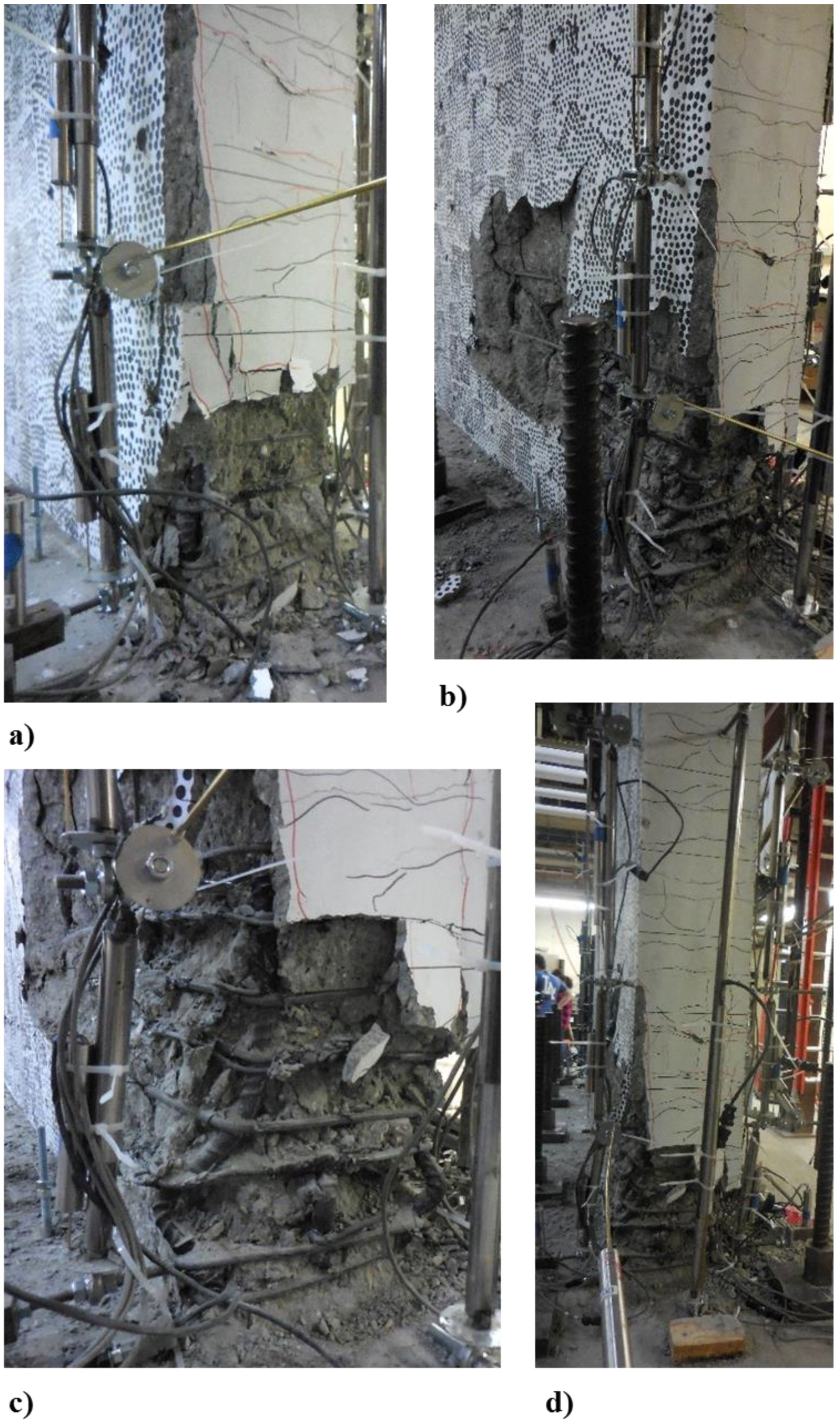

Figure 5-21: Specimen WP7 east boundary damage progression – a) Crushing of concrete and buckling of longitudinal reinforcement (-2% rotation, cycle 2); b) Boundary and web crushing damage (-3% rotation); c) Close up of damaged compression zone; and d) Out-of-plane movement

a) b)

Figure 5-22: Specimen WP7 east boundary at end of test (+4.5% rotation)

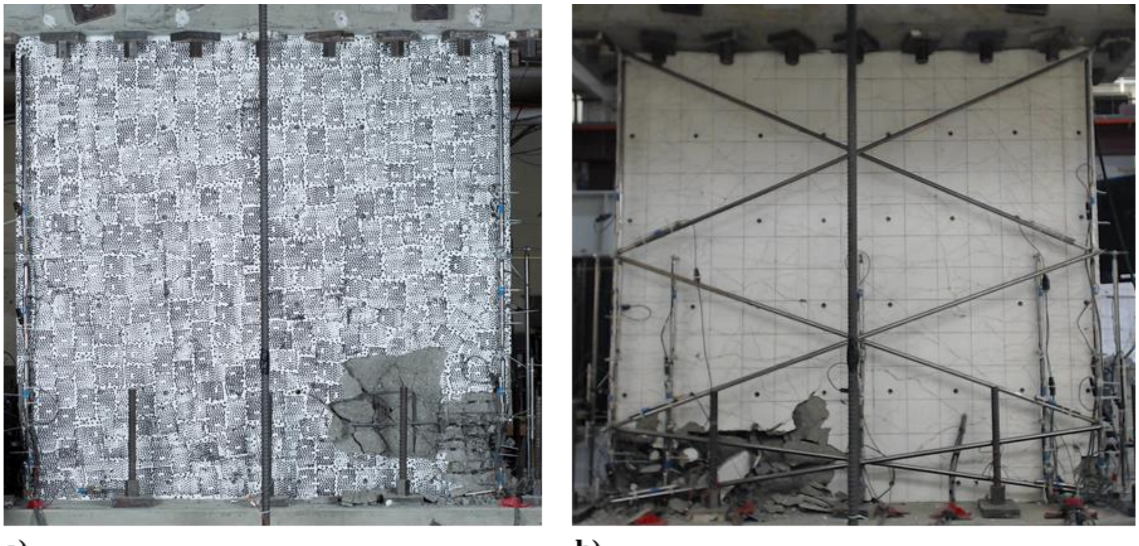

a) b)

Figure 5-23: Specimen WP7 – a) Photo of front (south) face of specimen after test; and b) Photo of rear (north) face of specimen after test

Chapter 6 Analysis of Experimental Data and Discussion of Test Results

A detailed analysis of experimental data is presented in this chapter. To begin, a brief discussion of the observed behavior is provided, followed by an analysis of the observed failure modes. In the following sections, the flexural and shear components of the wall panel lateral deformations are presented. Based on the methods used to determine flexural and shear deformations, effective flexural and shear stiffness values are calculated at various wall rotation levels. Suitable effective stiffness values are then used to estimate elastic deformations above the wall panel region (i.e., plastic hinge) of the wall specimens to enable a direct comparison to tests conducted on cantilever walls.

6.1 Discussion of Observed Behavior

All seven specimens were designed for relatively low shear stress, making it possible to study wall flexural behavior. For specimens WP1-WP4, which were the thinnest walls tested (b=6 in. [152 mm]), brittle flexural-compression failures occurred at plastic rotations ranging between 1.1% and 1.4%. Upon failure, residual lateral strength abruptly fell to near zero and the walls were no longer able to support the design axial load. Specimens WP5-WP7 were able to achieve plastic rotations between 1.8% (WP5) and 2.8% (WP7) prior to strength loss, which are about 1.3 and 2.0 times the rotation capacity of WP1. For comparison, ASCE 41 modeling parameters indicate that all of the specimens, except WP4, would maintain 75% of the nominal flexural capacity up to plastic rotations of 2%, which was not the case for any of the 6 in. (152 mm) thick walls, including WP5. The improved deformation and residual capacities for specimens WP5-WP7 is attributed to better detailing of boundary transverse reinforcement (specimen WP5), wall thickness (WP6 and WP7), and better detailing in wall webs. Unlike WP1-WP4, specimens WP5-WP7 generally demonstrated the ability to support lateral residual loads after strength loss was observed, especially when improved boundary and web detailing was used (e.g., specimen WP5 and loading in negative direction for WP6 and WP7). For specimens WP6 and WP7, stable buckling of longitudinal reinforcement was observed at wall boundaries. In contrast, rapid loss of strength was observed following initial bar instability for the 6 in. (152 mm) thick walls, including WP5 (east boundary). For WP1-WP4, slight buckling of longitudinal reinforcement was accompanied by abrupt crushing of the confined boundary or out-of-plane instability. The enhanced confinement detail for WP5 (i.e., continuous transverse reinforcement) prevented compression failure, and the slightly buckled bars ruptured in tension in the following half load cycle. Test results for WP5 demonstrated moderately improved deformation capacity; however, it is noted that the quantity of boundary transverse reinforcement (A_{sh}) was twice the amount required by ACI 318-14, and continuous boundary reinforcement (similar to overlapping hoops) was used. Thus, although it may be possible to improve the deformation capacity of thin walls, the quantity of the boundary transverse reinforcement required may not be practical or economical. On the other hand, even greater improvement in deformation capacity was achieved by increasing wall thickness (WP6 and WP7) without increasing A_{sh} or using continuous transverse reinforcement

6.2 Analysis of Observed Failure Modes

For all seven specimens, strength loss was associated with flexural-compression behavior (i.e., concrete crushing and longitudinal reinforcement buckling) and/or flexure-tension behavior (i.e., rupture of longitudinal reinforcement), indicating axial (flexural) compression and tension strain limits were reached. In Figure 6-1, strain profiles are presented at various hinge rotation levels for the walls. The results for specimens WP1 and WP2 were nearly identical, so strain profiles are shown for WP1 only. The reported strains were measured by vertical sensors at five locations along the length of the walls (Figure 4-15 through Figure 4-18), over a gage length of approximately one-half the length of the wall (44 in.; 1118 mm). The 44 in. (1118 mm) gage length corresponds to sensor Levels 1 through 3 in Figure 4-15 through Figure 4-18. Figure 6-1 indicates compression depths were approximately 15-19 in. ($0.17l_w$-$0.21l_w$; 381-483 mm), except for specimen WP4 ($c/l_w \approx 0.3$). Thus, for a given rotation/curvature demand, strains were similar. Because the rotation capacities of WP5-WP7 were considerably larger than those of WP1-WP4, extreme fiber strains were generally larger for WP5-WP7, as compared to WP1-WP4, prior to strength loss.

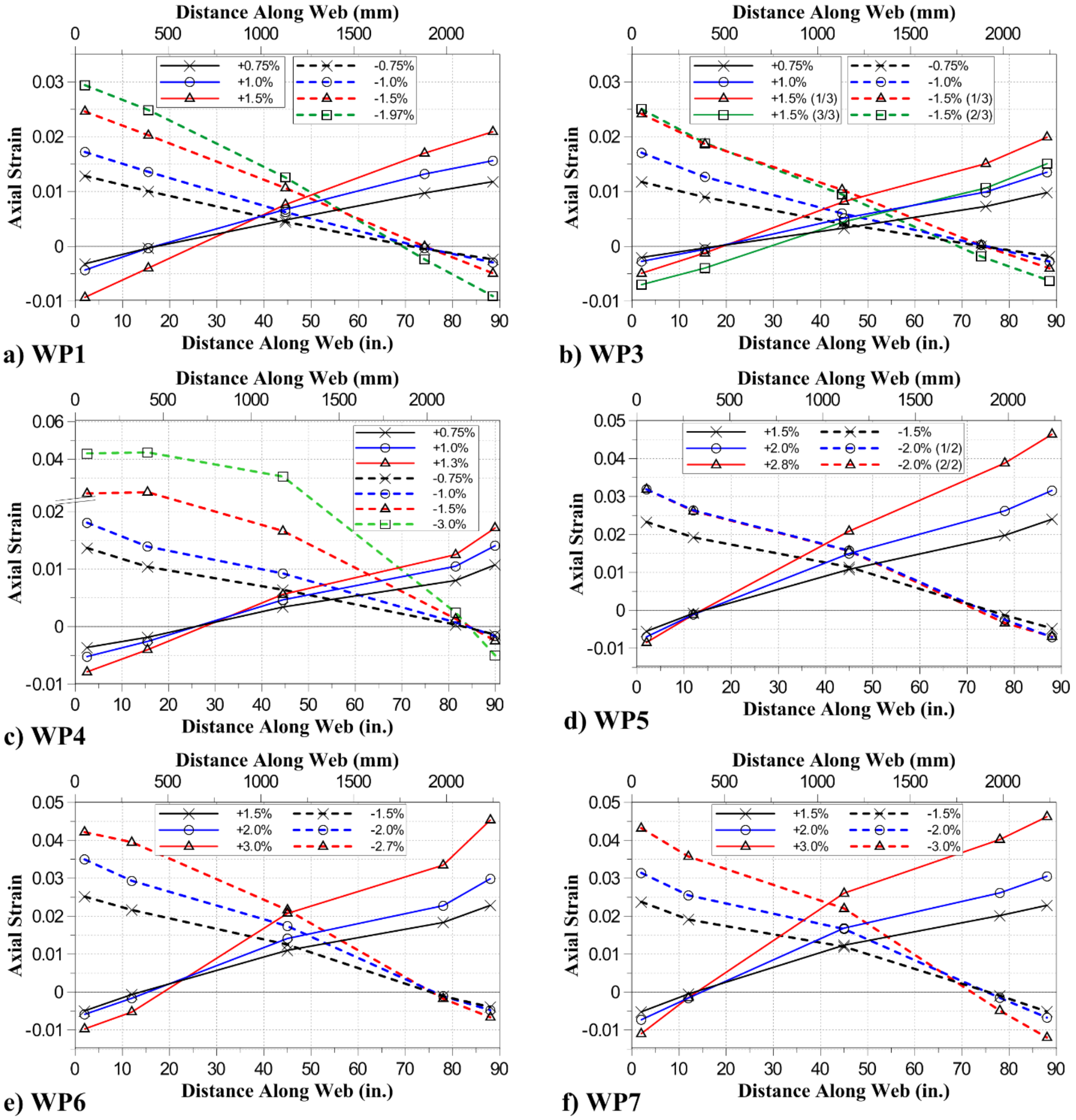

Figure 6-1: Axial strain profiles at various hinge rotation levels (strains measured over gage length equal to $l_w/2$ [44 in.; 1118 mm])

At the boundaries of all seven walls, softening in the compression zones occurred, and compression strains concentrated over a short height near the base of the walls. Figure 6-2 demonstrates this behavior at the east boundary of specimen WP1 (Figure 6-2a) and at the east boundary of WP7 (Figure 6-2c), which are representative of the behavior of the seven walls. Average compression strain measurements vs. base overturning moment are shown over two different heights above the specimen footing: Level 1 as indicated in Figure 4-15 (0-14 in.; 0-356 mm), where inelastic compression strains concentrated, and Levels 2 through 3 (14-44 in.; 356-1118 mm). The strains reported in Figure 6-1 and Figure 7-4 are average strains over these two heights (0-44 in.; 0-1118 mm) and are included in Figure 6-2 for comparison. For both walls, initial softening near the base of the wall (0-14 in.) was observed following compression yielding of longitudinal reinforcement at approximately 0.25% rotation, corresponding to an average compression strain of approximately 0.002. At larger rotation demands, all inelastic compression strain developed in the softened region, and strain unloading occurred above the softened region as strength loss occurred. Prior to failure, sensors in the softened region measured compression strains of 0.025 for specimen WP1 and 0.036 for specimen WP7. Compression strains measured by sensors above the softened region did not exceed 0.002 at any point in the test.

Figure 6-2b and Figure 6-2d compare the measured axial compression strains in the softened region (Level 1: 0-14 in.) to transverse strains from a cross-tie located at a height of 9 in. (229 mm) above the footing (designated T2-E in Figure 4-19 and Figure 4-24). A rapid increase in cross-tie strain was observed as axial strains concentrated in the softened region. For WP1, cross-tie strains in excess of 0.03 were measured just before the strain gage broke at 1.87% rotation. For WP7, similar behavior was observed, although transverse (tie) strain demands were lower than those observed for WP1. As discussed in Chapter 5, opening of cross-tie hooks was observed following crushing/spalling of cover concrete, and fracture of cross-ties was only observed in a few cases. As shown in Figure 6-2, significant cross-tie strains were measured in the damaged region of the wall prior to pullout of the cross-ties, indicating the cross-ties were relatively effective prior to failure. However, once cover concrete spalled, cross-tie hooks were vulnerable to opening, even for cross-ties with 135^o-135^o hooks.

In Figure 6-3, measured transverse cross-tie strains and extreme fiber axial compression strains are shown for specimens WP1 (b=6 in.), WP6 (b=7.5 in.), and WP7 (b=9 in.) at various loading levels. For specimens WP6 and WP7, the reported values are for the negative loading direction, causing compression at the east boundary which was constructed with a single outer hoop and cross-ties for confinement. Axial strains were measured over Level 1 (0-14 in.; 0-356 mm), as indicated in Figure 4-15, where compression damage was concentrated. The reported transverse strains are for the most heavily strained cross-tie which was gage T2-E at a height of 9 in. (229 mm) above the footing for all three specimens (Figure 4-19 through Figure 4-24). Figure 6-3 indicates that as wall thickness increases, transverse strains decrease for a given axial strain. The trend shown in Figure 6-3 may be attributed to the relative quantity of unconfined cover concrete for the specimens. Concrete cover was the same for all three specimens (c_c=0.5 in. [13 mm]). As such, the post-spalled thickness ($b-2c_c$) accounted for a greater percentage of the gross thickness (b) in the thinner specimens. Thus, it is anticipated that the effect of cover crushing/spalling in the thinner sections may have imposed larger axial demands on longitudinal bars, making them more vulnerable to instability and, therefore, imposing larger transverse strain demands on cross-ties.

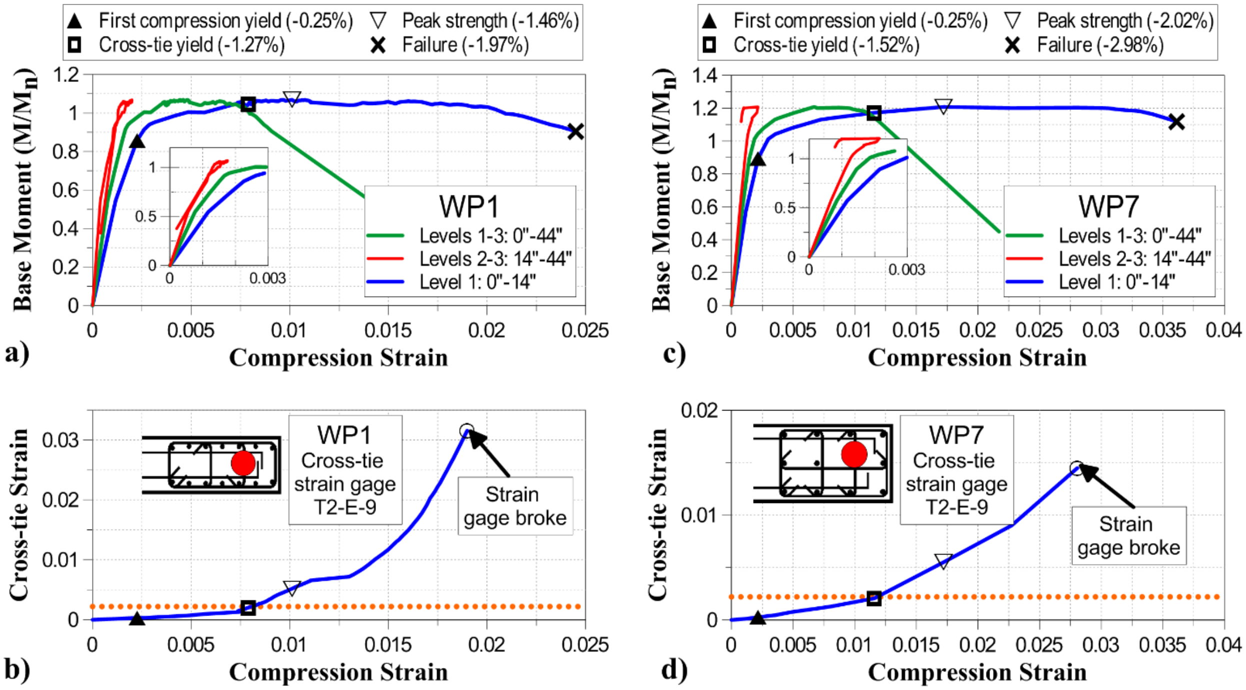

Figure 6-2: Softening behavior at wall boundaries – a) WP1 moment vs. compression strain measured at different levels; b) WP1 cross-tie strain vs. compression strain in Level 1; c) WP7 moment vs. compression strain measured at different levels; and d) WP7 cross-tie strain vs. compression strain in Level 1

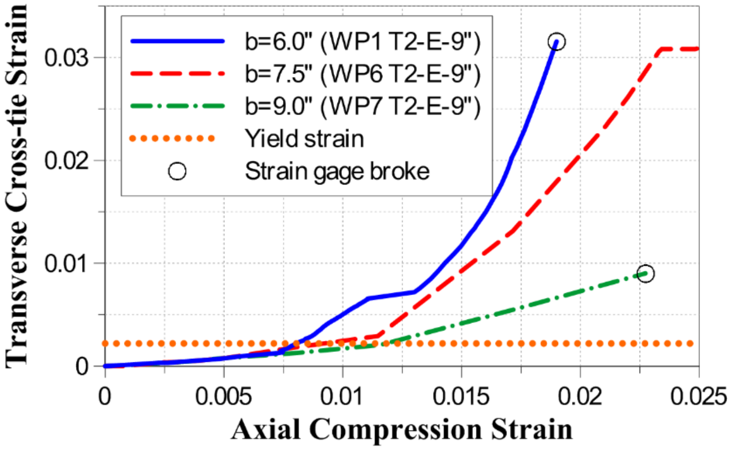

Figure 6-3: Influence of wall thickness on axial compression strain and transverse cross-tie strain

Figure 6-4 compares strain measurements for transverse reinforcement at the east and west boundaries of specimen WP7 at various rotation levels. The reported strains in Figure 6-4 were measured on transverse reinforcement located at a height of 9 in. (229 mm) above the footing (Figure 4-24), the height at which transverse strains were largest. In the negative loading direction, causing compression at the east boundary (hoop and cross-tie [Detail BE-3]), strain gage T1-E-9 (hoop strain at the east boundary height of 9 in. above footing) reached yield strain at approximately 1.2% rotation, and strain gage T2-E-9 (cross-tie) reached yield at approximately 1.7% rotation. Beyond 2% rotation, a rapid increase in cross-tie strains (gages T2-E-9, T3-E-9, and T4-E-9) occurred, which may be attributed to bar instability which was first observed at 2% rotation. In the positive loading direction, causing compression at the west boundary (continuous transverse reinforcement [Detail BE-4]), transverse strains were smaller for a given rotation level, even though axial compression strains were nearly identical in the two loading directions (Figure 6-1). Based on Figure 6-4, it appears transverse strains became disproportionately large at the locations of cross-ties at the boundary with the hoop and cross-tie detail, whereas the continuous transverse reinforcement detail appears to provide more uniformly distributed transverse strains. As a result, the boundary with continuous transverse reinforcement remained stable in compression, even after bar buckling occurred. In contrast, abrupt crushing of the east boundary (hoop and cross-ties) was observed.

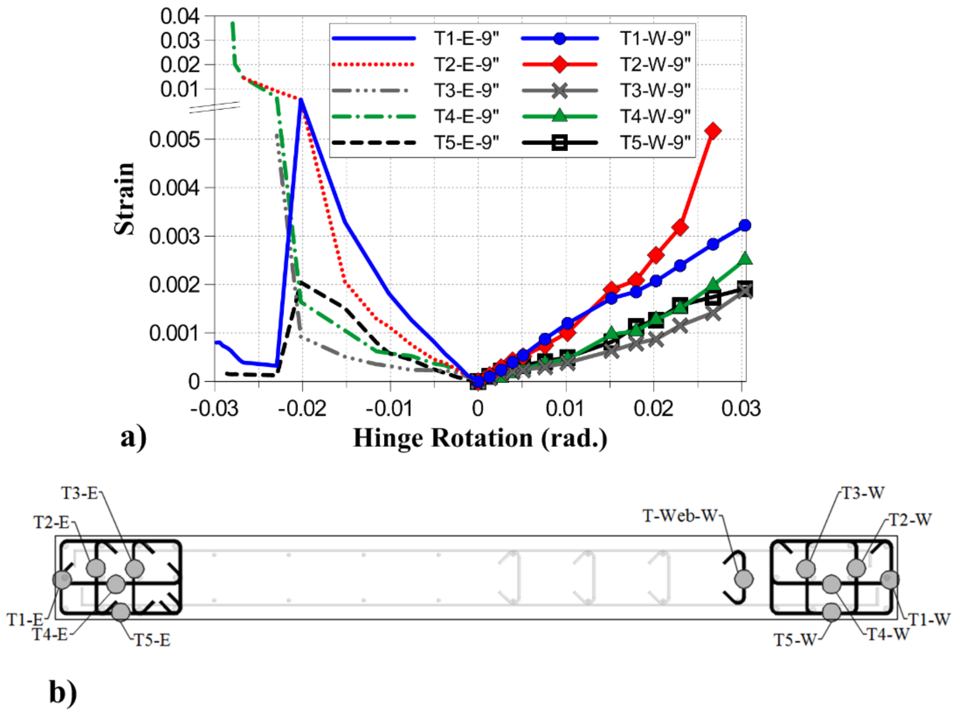

Figure 6-4: Specimen WP7 boundary transverse reinforcement strain measurements – a) Behavior of cross-ties vs. continuous transverse reinforcement; b) Strain gage layout

For specimens WP1 and WP2, failures associated with out-of-plane instability of the compression zone were observed. In Figure 6-5, the axial strain history at the west boundary of WP1 is shown over the bottom 44 in. (i.e., Levels 1-3; 0-1118 mm) of the wall on the front (north) and rear (south) faces of the specimen. Throughout the test, average axial strains were nearly identical on the front and rear faces of the wall (Figure 6-5a). However, as shown in Figure 6-5b, in the region where concrete crushing and rebar buckling was observed (Level 1: 0-14 in. [0-356 mm]), axial compression strains were significantly different on the two sides of the wall. As a result, out-of-plane rotation occurred over the short height of the damaged region of the wall (Figure 6-5c). Photos of significant damage states are shown in Figure 6-5d and indicated in Figure 6-5c. The first sign of substantial out-of-plane rotation coincided with vertical cracking and spalling of concrete on the southwest corner of the wall at +0.5% rotation. In the following cycles, an increase in out-of-plane rotation was evident at peak compression points (indicated by markers in Figure

6-5c) because damage was primarily concentrated on the south face of the wall. At +1.5% rotation, crushed concrete on the north face spalled off and slight buckling of the two longitudinal bars at the west face of the wall was observed. The out-of-plane failure was observed in the following cycle, with out-of-plane rotation occurring primarily over two or three hoop spacings at the location where buckling of longitudinal reinforcement initiated in the previous cycle. Previous studies on lateral instability of thin walls (Paulay, et al., 1993; Chai, et al., 1999) have explored a "global buckling" mode by which out-of-plane deformations occur over a significant height (i.e., plastic hinge length), influenced by slenderness (h_u/b) and inelastic tension strain demand (ε_{tu}). It is noted that the east boundary of specimen WP5, which was the same thickness and height as WP1 and WP2 ($h_u/b=14$), remained stable even though the tension strain demand for WP5 ($\varepsilon_{tu}=0.045$) was nearly double that of WP1 and WP2 ($\varepsilon_{tu}<0.03$). Thus, instabilities for WP1 and WP2 were likely influenced primarily by asymmetric crushing/spalling of concrete and buckling of longitudinal reinforcement. Detailed studies conducted following the 2010 earthquake in Chile indicate that this instability mode, initiated by concrete crushing, was likely the cause for instability in many walls in Chile (NIST, 2014). It is noted that a minimum wall thickness requirement ($b \geq h_u/16$) was added to ACI 318-14 (and was previously in UBC-97), which all seven test specimens satisfied. Based on the performance of WP1 and WP2, it may be necessary to modify the wall thickness requirement to account for additional variables such as drift demand.

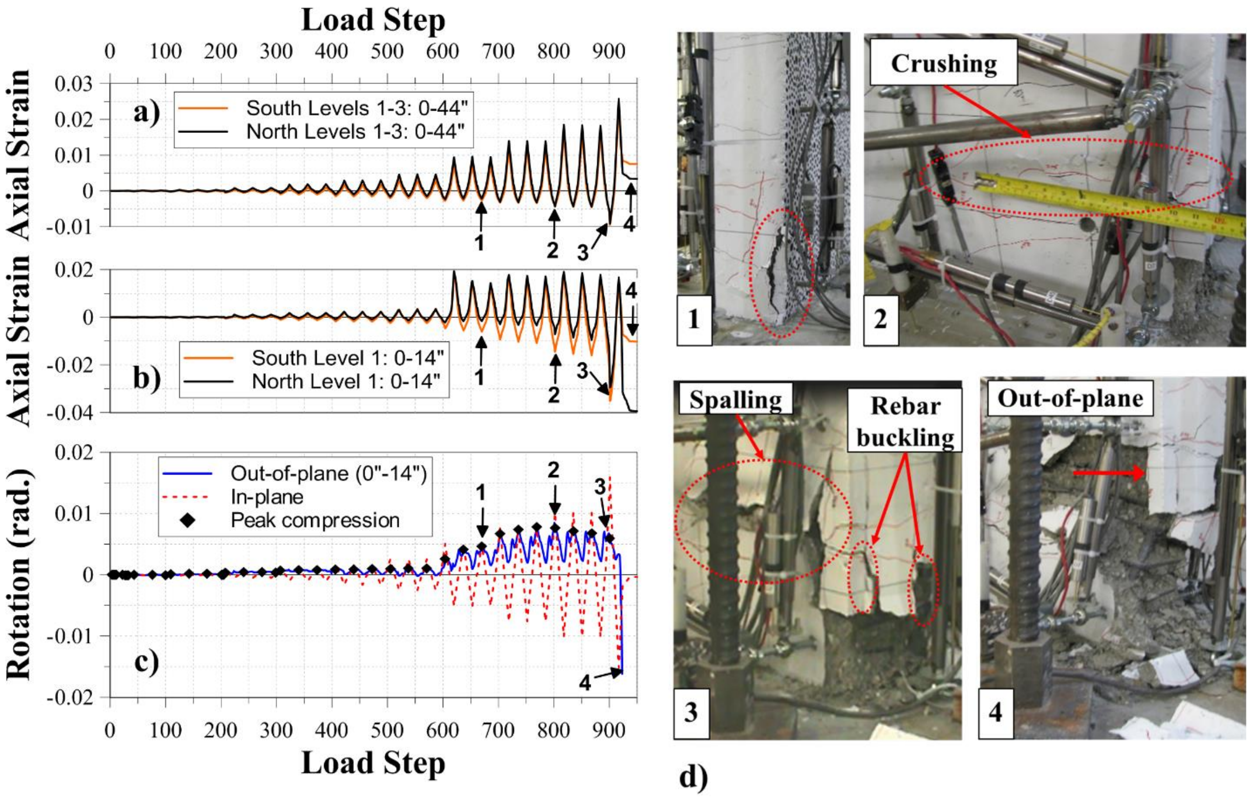

Figure 6-5: Out-of-plane behavior at west boundary of specimen WP1 – a) Average axial strain over Levels 1-3 (0-44 in.); b) Axial strain in Level 1 (0-14 in.); c) Out-of-plane rotation in Level 1; and d) Damage states: (1) Vertical cracking and spalling on southwest corner (+0.5% rotation), (2) Minor cover crushing on north face (+1% rotation), (3) Cover spalling and rebar buckling (+1.5% rotation, cycle 1), and (4) Out-of-plane instability

6.3 Components of Lateral Deformation

In this section, the total measured lateral displacement at the top of the wall panels is presented, and the contributions of flexural and shear deformations to total wall lateral deformations are described. The lateral displacement at the top of the wall panel specimens can be expressed as the sum of flexural deformations (δ_f) and shear deformation (δ_s). Flexural deformations include rotation/curvature along the height of the wall ($\delta_{f,wall}$), as well as slip/extension (strain penetration) of longitudinal reinforcement at the wall-footing interface ($\delta_{f,base}$). Shear deformations include pure translation (shear distortion) along the height of the wall ($\delta_{s,wall}$) and shear sliding along the wall-footing interface ($\delta_{s,slide}$).

$$\delta_{tot} = \delta_{f,wall} + \delta_{f,\mathrm{base}} + \delta_{s,wall} + \delta_{s,slide} \qquad 6.1$$

Experimentally measured base moment/shear versus total top lateral displacement (δ_{tot}) and drift ratio responses are presented in Figure 6-6 for all seven specimens. The reported displacements were measured 82 in. (2083 mm) above the base of the walls, which is approximately the middle of the second story in the full-height prototype wall. As such, the drift ratios are essentially first story interstory drift ratios. Brittle compression failures were observed for specimens WP1-WP4, which were all 6 in. (152 mm) thick, prior to reaching interstory drift ratios expected for Design Earthquake (DE) and Maximum Considered Earthquake (MCE) demands, which could approach 2% and 3%, respectively. Compression failures were also observed for specimens WP6 and WP7, which were 25% and 50% thicker than WP1-WP4; although, interstory drift ratios of at least 3% were measured prior to failure.

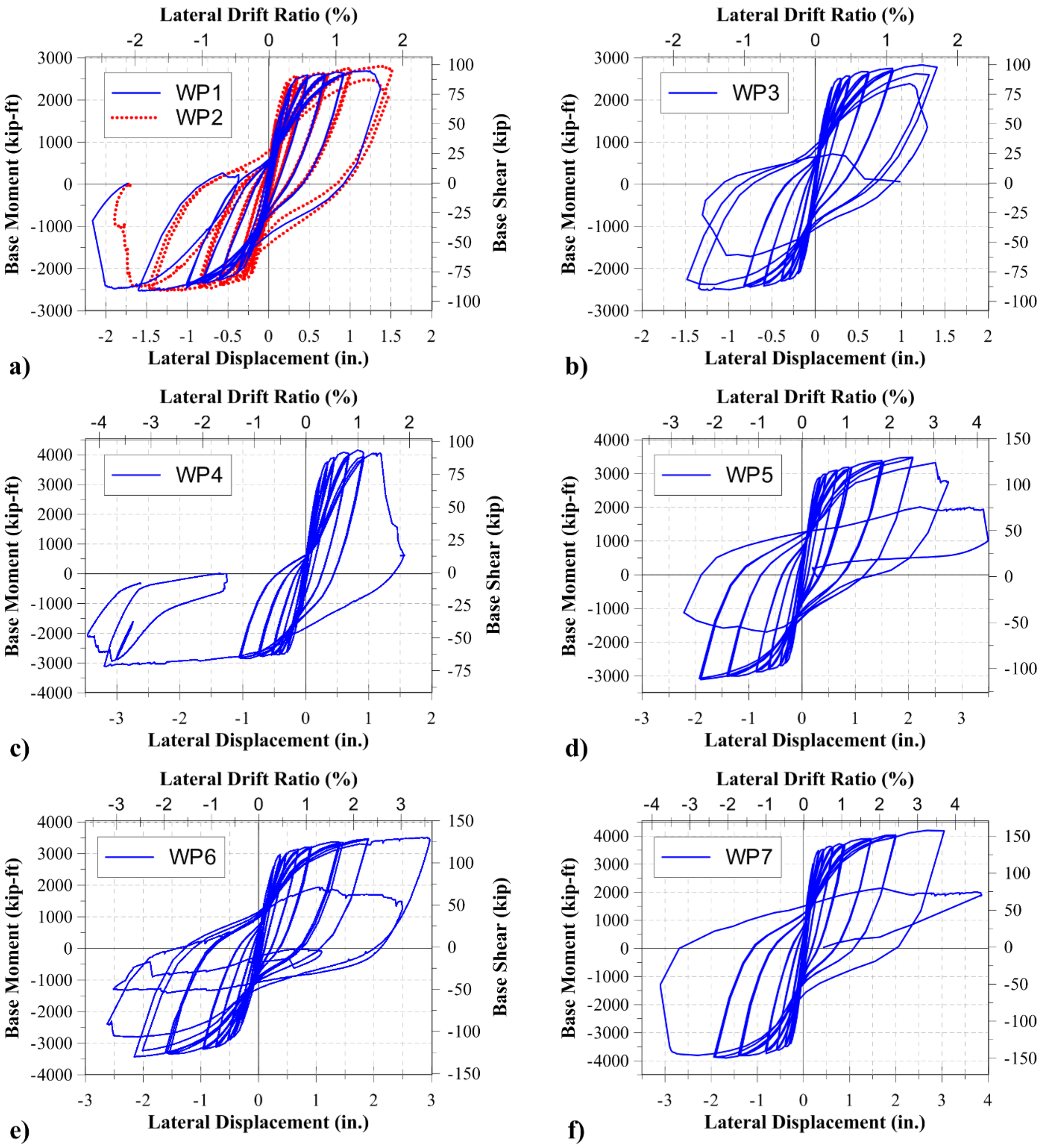

Figure 6-6: Base moment/shear vs. top lateral displacement measured 82 in. (2083 mm) above wall footing (conversion: 1 in. = 25.4 mm, 1 kip=4.448 kN, 1 kip-ft=1.356 kN-m)

6.3.1 Flexural Deformations

The flexural contribution to the total lateral displacement at the top of the specimens may be determined as the sum of the contributions from rotation measurements at individual sections (θ_i) along the height of the specimen (Eqn. 6.2). Individual section rotations are assumed to occur about the centroid of the curvature distribution for the particular section $\left(\bar{x}_i\right)$.

$$\delta_{f,wall} = \sum_{i=1}^{n} \theta_i (h - \bar{x}_i) \qquad 6.2$$

As shown in Figure 6-7, the average rotation over an individual section height (Eqn. 6.3) is determined as the difference in axial displacement, measured by sensors at the two ends of the wall (V_1-V_2), divided by the horizontal distance between the sensors (l_{1-2}), which is approximately equal to the length of the wall.

$$\theta_i = \frac{V_1 - V_2}{l_{1-2}} \qquad 6.3$$

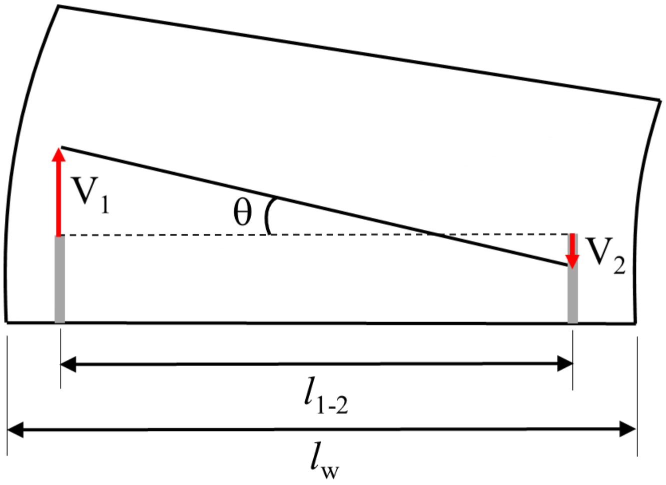

Figure 6-7: Average rotation over individual section/sensor height

At sections where the response is essentially linear elastic, the flexural stiffness may be assumed as constant over the section height ($EI(y) = EI$), in which case curvature is directly proportional to moment (i.e., $\phi_u(y) = M(y)/EI$). Thus, $\overline{x}_i$ is easily determined based on the known moment distribution. At yielding sections, the curvature distribution is nonlinear (i.e., inelastic curvature), and the centroid must either be estimated or determined experimentally using an adequate number of sensors to capture the inelastic response. The layout of sensors used to measure wall rotations and lateral drift at the top of the specimens is shown in Figure 6-8, which is an abridged version of the LVDT layouts shown in Figure 4-15 through Figure 4-18. Based on the suggestion of Massone and Wallace (2004), four pairs of sensors were used in the assumed plastic hinge region (l_p=l_w/2), designated Section A, to adequately capture the distribution of inelastic curvature. A single pair of sensors was used in Section B because inelastic curvature was expected to be relatively small above Section A. The lateral displacement/drift at the top of the specimen, reported in Figure 6-6, was measured by the horizontal sensor shown in Figure 6-8.

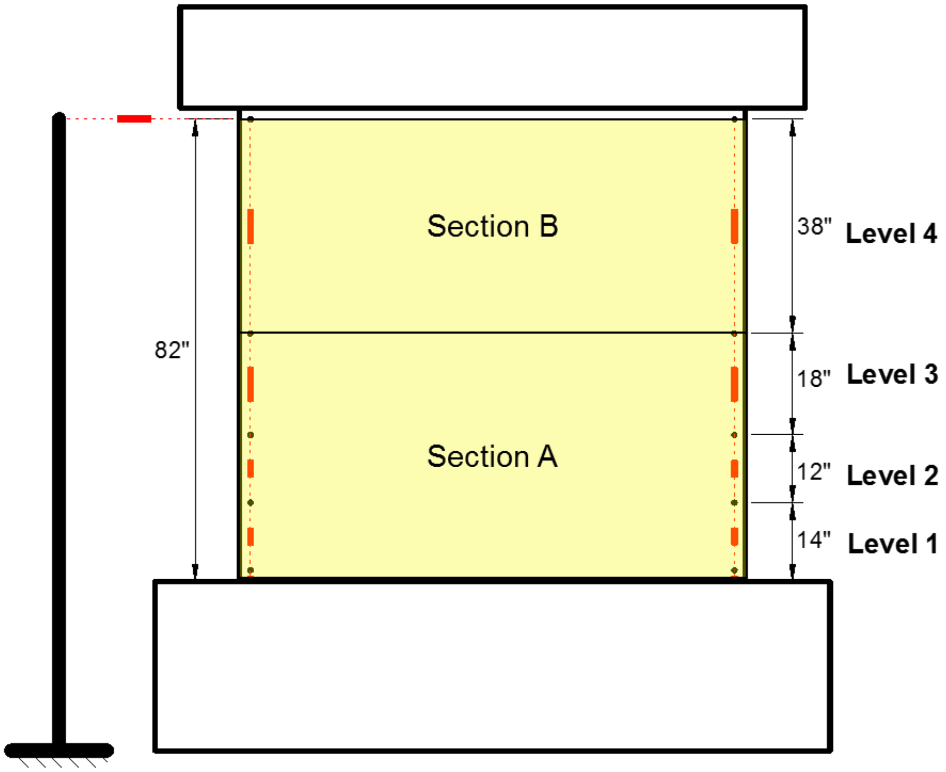

Figure 6-8: Section heights and sensors used to measure section rotations

Curvature profiles are shown in Figure 6-9 at various rotation levels for each test specimen. Average curvature at each sensor height (Levels 1 through 4 in Figure 6-8) was determined as the average rotation (θ_i) divided by the gage length of the sensor (shown in Figure 6-8). For specimens WP1-WP4, average curvature measurements above the assumed plastic hinge region (Section B) reached no more than about two to three times the yield curvature; thus, for those specimens, it is reasonable to approximate the centroid of Section B based on the moment distribution (i.e., assuming constant stiffness over Section B). The moment distribution over Section B is trapezoidal, and the moment at the bottom of the section is approximately 1.15 times the moment at the top of the section. Based on the trapezoidal moment distribution, the elastic centroid of the section is located at a height $\bar{x}_B = 44'' + 0.48(38'') = 62.6''$ above the wall footing. This is essentially midheight of Section B, which is at 63 in. (1575 mm) above the wall footing; thus, for simplicity, $\bar{x}_B = 63''$ was assumed. For specimens WP5-WP7, average curvature measurements in Section B reached up to approximately eight times the yield curvature, which was much larger than those measured for WP1-WP4. Because significant inelastic curvature was measured in Section B, it appears that more sensors should have been used to better capture the inelastic curvature profile in Section B. Because only one pair of sensors was used in Section B, it is not possible to capture the distribution; however, because curvature measurements were substantially larger in Section A, than in Section B, the computation of flexural deformations is not very sensitive to the selected location of the centroid of Section B. Therefore, to determine flexural deformations, the centroid in Section B was assumed as the centroid of the moment distribution (i.e., constant EI assumed for Section B), as was done for WP1-WP4.

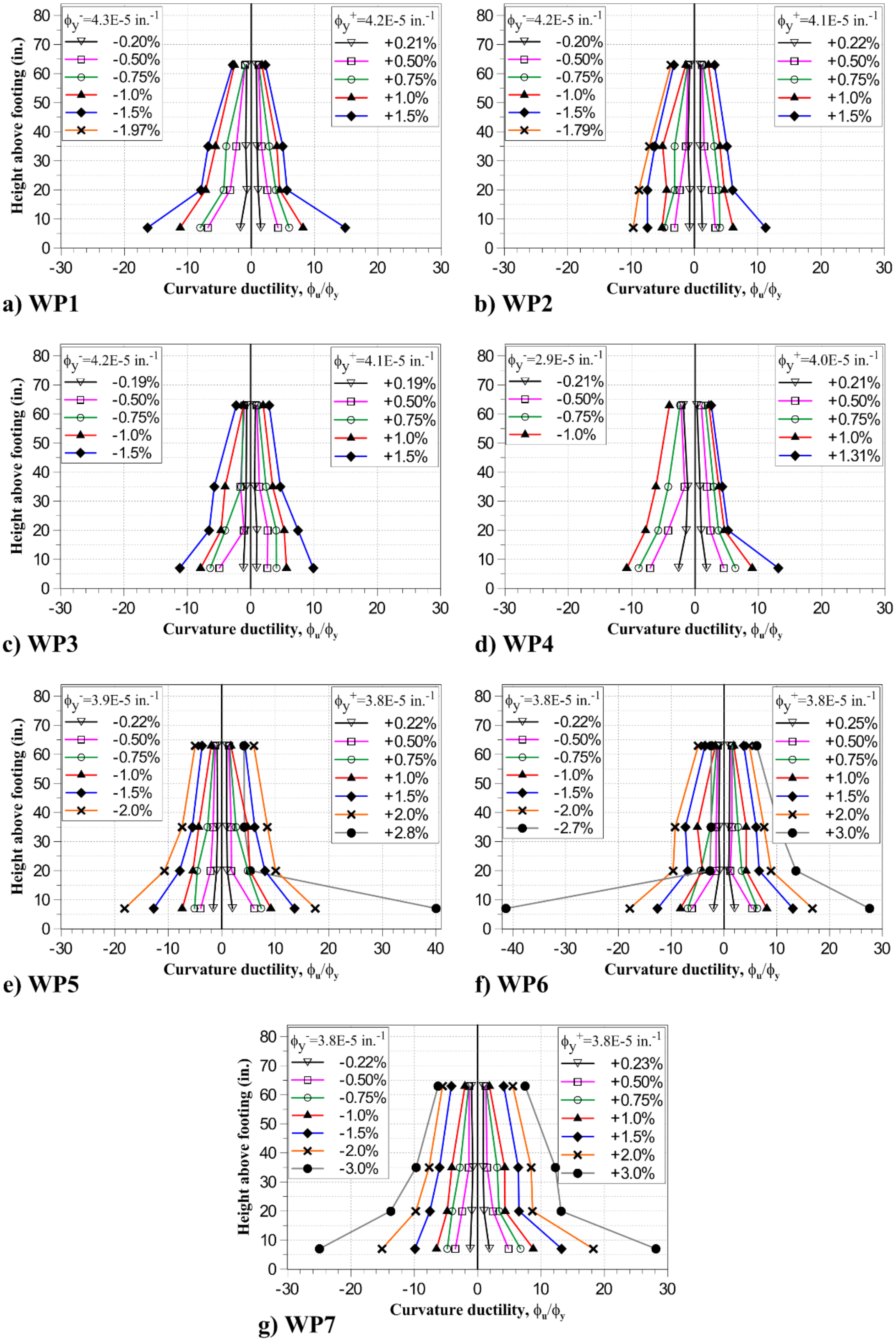

a) WP1

b) WP2

c) WP3

d) WP4

e) WP5

f) WP6

g) WP7

Figure 6-9: Curvature profiles at various rotation levels

Base slip/extension at the wall-footing interface ($\delta_{f,base}$) was determined using sensors located at the base of the walls (designated sensor numbers 6, 12, 25, and 31 in Figure 4-15 through Figure 4-18). The base slip sensors had a 2 in. (50.8 mm) gage length. As such, in addition to measuring base slip/extension, the sensors also captured some wall rotation/curvature over the 2 in. (50.8) gage length. The contribution attributed only to base slip/extension was approximated (Eqn. 6.4) by assuming that curvature is constant over Level 1 (0-14 in.; 0-356 mm), which includes the 2 in. (50.8 mm) gage length of the base slip sensors and the 12 in. (305 mm) gage length of the first set of wall rotation/curvature sensors (designated sensor numbers 7, 13, 26, and 32 in Figure 4-15 through Figure 4-18). Because slip/extension is concentrated at the base of the wall, $\delta_{f,base}$ was calculate as base slip rotation (θ_{slip}) times the height (*h*) at which $\delta_{f,base}$ is measured (Eqn. 6.4).

$$\delta_{f,\text{base}} = \theta_{slip} h = \frac{h}{l_{1-2}} \left(V_{slip,1} - V_1 \left(\frac{2"}{12"} \right) \right) - \left(V_{slip,2} - V_2 \left(\frac{2"}{12"} \right) \right) \qquad 6.4$$

The flexural component of the lateral deformation at the top of the specimens is presented in Figure 6-10. The displacements/drifts in Figure 6-10 include the contribution of base slip/extension, calculated according to Eqn. 6.4, as well as flexural deformations within Sections A and B, which were calculated according to Eqn. 6.2. At each loading step, the centroid of the inelastic curvature distribution in Section A was calculated from the four pairs of vertical sensors at the ends of the walls, and the centroid in Section B was assumed at midheight of Section B. For all seven walls, the response was dominated by flexure which comprised about 70% of the total deformations reported in Figure 6-6. The contribution of each component to the total lateral deformation is discussed in more detail in Section 6.3.3.

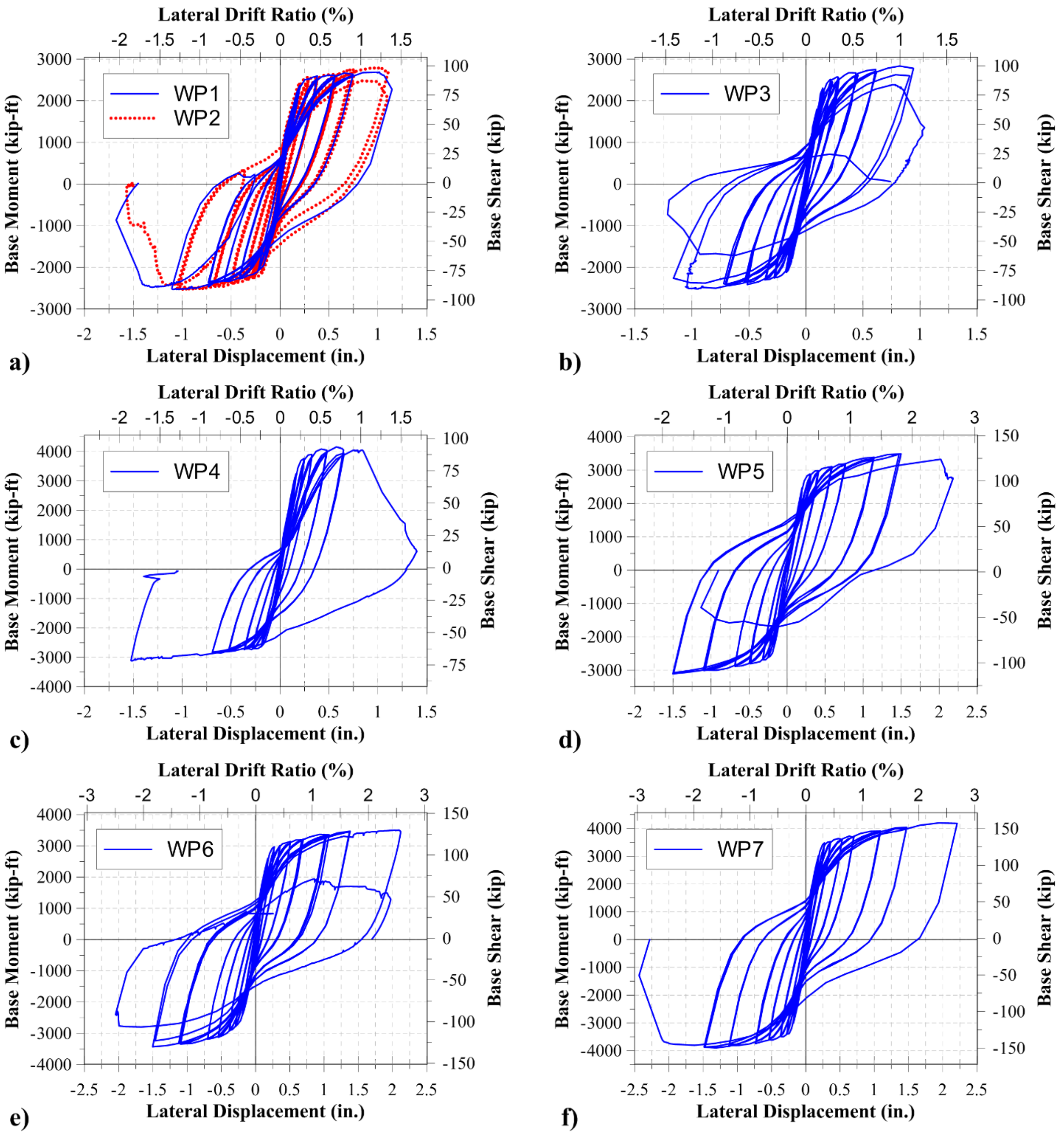

Figure 6-10: Flexural contribution to lateral displacement at top of specimen

6.3.2 Shear Deformations

For simplicity, the shear contribution of lateral deformations was estimated using the relationship in Eqn. 6.5, which attributes any deformations not associated with flexure or shear sliding to shear distortion of the wall panel.

$$\delta_s = \delta_{tot} - \delta_{f,wall} - \delta_{f,\mathrm{base}} - \delta_{s,slide} \qquad 6.5$$

Shear sliding deformations ($\delta_{\mathrm{s,slide}}$) were measured directly using sensor number 24 in Figure 4-15 through Figure 4-18. It is noted that, because of the low shear stress demands on the walls, the contribution of shear sliding was negligible (less than 2% of total response). The shear contribution to the lateral deformation at the top of the specimens is presented Figure 6-11. Shear deformations comprised approximately 30% of the total lateral response of the wall panel specimens, which is discussed in more detail in Section 6.3.3.

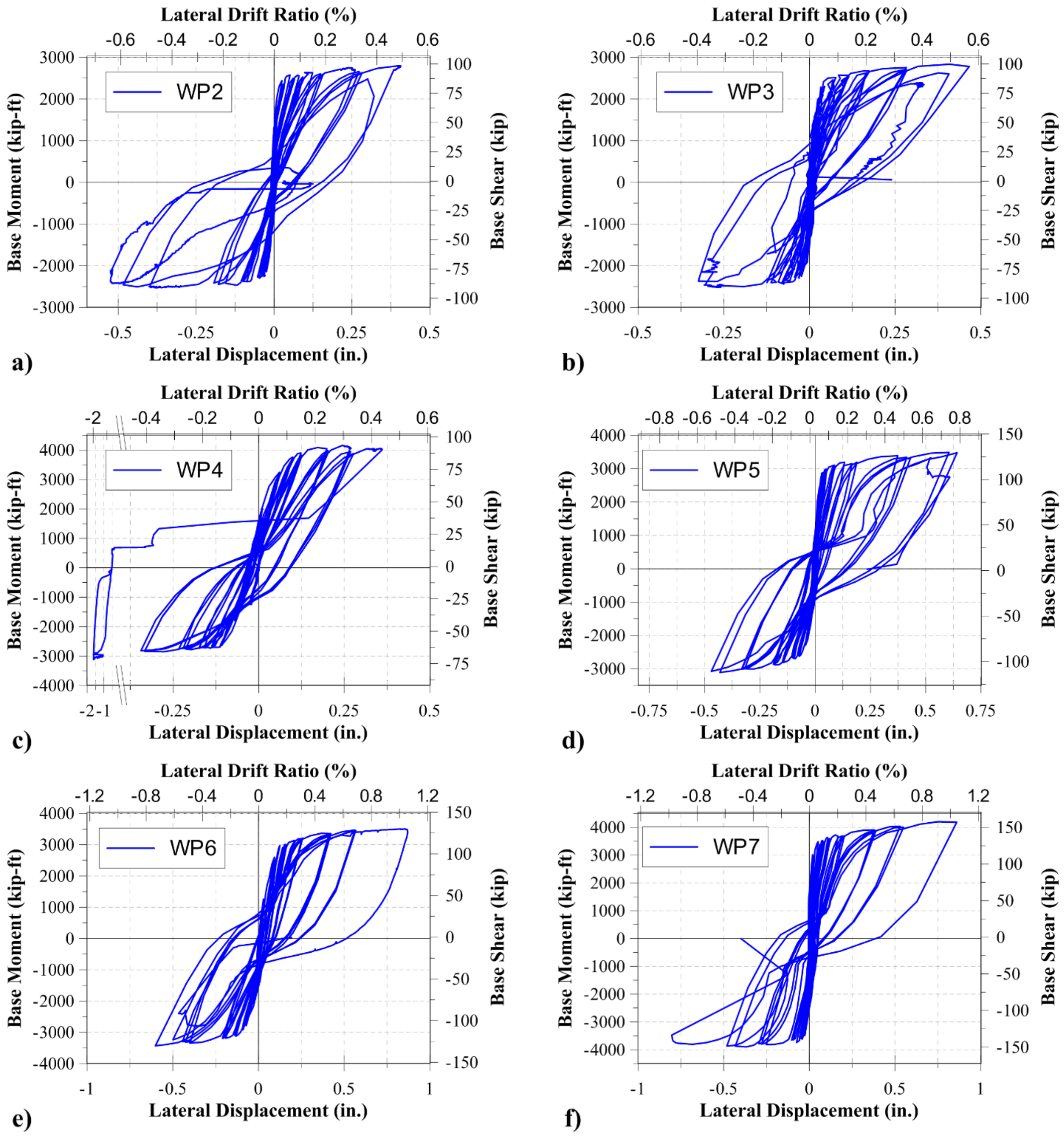

Figure 6-11: Shear contribution to lateral displacement at top of specimen

6.3.3 Percent Contribution of Lateral Deformation Components

The relative contributions of wall flexural deformations ($\delta_{f,wall}$), base slip/extension ($\delta_{f,base}$), and shear (δ_s) are summarized at various hinge rotation levels, for loading in both directions, in Figure 6-12. The reported contribution of shear deformations includes sliding shear ($\delta_{s,slide}$), which comprised less than 2% of the total lateral displacement at the top of the specimens. Beyond approximately 1% hinge rotation, flexural deformations comprised about 60% of the total response, on average, and base rotation comprised about 10% of the total response, on average. Shear deformations made up approximately 30% of the total response. It is important to point out that the wall panel specimens represented approximately the bottom 1.5 stories (i.e., plastic hinge region) of an eight story cantilever wall. For a cantilever wall, inelastic flexural drift ratio is relatively constant up the height of the wall due to plastic rotation within the plastic hinge region (i.e., $\delta_{f,p}/h_w \approx \theta_p$). In contrast, inelastic shear deformations result in pure translation, so shear drift ratio decreases up the height of the wall. Thus, the contribution of shear to the drift at the effective height, or at the top of the wall, in the full-height prototype wall is expected to be considerably smaller than the values shown in Figure 6-12. Total lateral deformations at the effective height of the walls are approximated in Section 6.5.

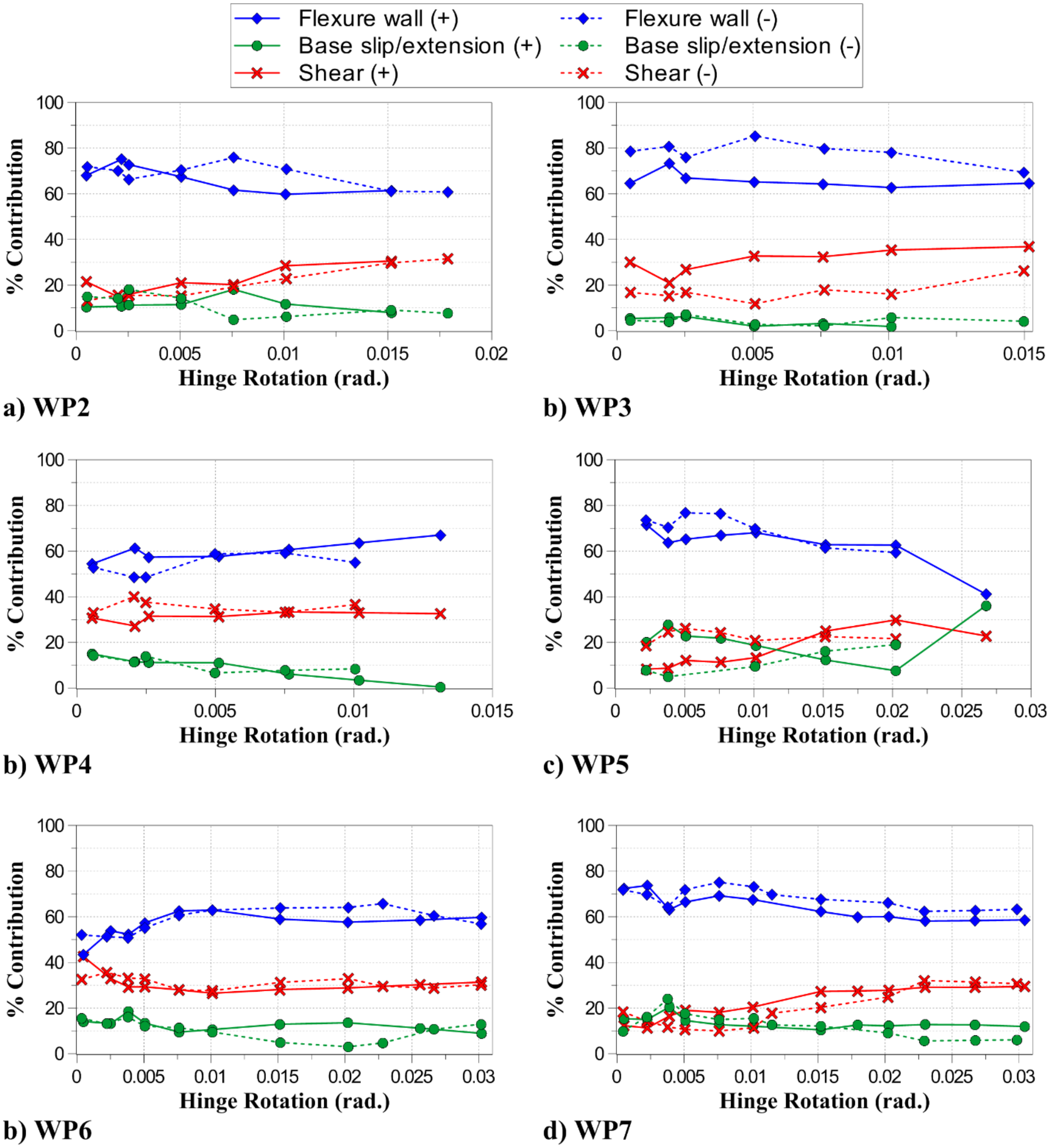

a) WP2 b) WP3

b) WP4 c) WP5

b) WP6 d) WP7

Figure 6-12: Contributions of flexural and shear deformations to the lateral displacement at the top of specimens

6.4 Effective Stiffness

Effective flexural and shear stiffness values were calculated for all seven walls in order to determine suitable values to estimate elastic deformations above the wall panel height. Stiffness values were determined using the measured flexural deformation (i.e., rotation, θ) within the assumed plastic hinge region (l_p=l_w/2) – that is, within Section A, as indicated in Figure 6-8. The measured rotations correspond to the hinge rotations reported in Figure 5-2, except that rotation due to slip/extension at the wall-footing interface was not included in the stiffness calculations. A relationship was derived (Eqns. 6.6 and 6.7), based on the free body diagram shown in Figure 6-13, that relates the applied moment (M_{top}), the applied lateral force (F_{top}), and the rotation at the top of the plastic hinge (at height l_p), to the effective flexural stiffness (EI_{eff}).

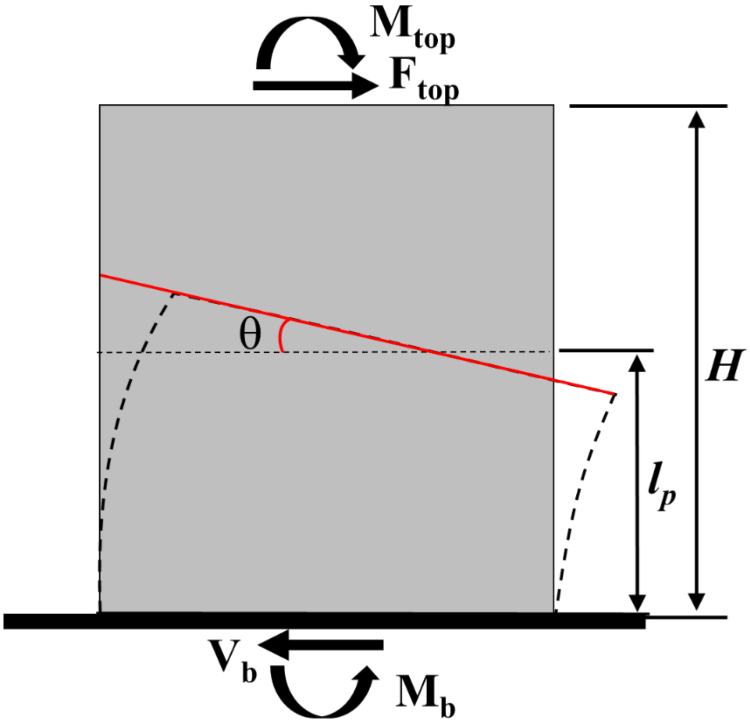

Figure 6-13: Free body diagram of wall panel specimens

$$EI_{eff} = \frac{M_{top} l_p + F_{top} l_p H - \frac{1}{2} F_{top} l_p^{\ 2}}{\theta} \tag{6.6}$$

$$EI_{eff} = \frac{M_b l_p - \frac{1}{2} V_b l_p^{\ 2}}{\theta} \tag{6.7}$$

Figure 6-14 shows flexural stiffness measurements, normalized to the concrete modulus of elasticity (E_c) times the gross section moment of inertia (I_g), at various rotation levels for all seven wall panel specimens. E_c was approximated as $57,000\sqrt{f'_c\,[psi]}$ based on the recommendations of ACI 318-14. Markers in Figure 6-14 indicate the effective stiffness values associated with initial horizontal flexural cracking of concrete ($M_{base}=M_{cr}$) and first yield of boundary longitudinal reinforcement ($M_{base}=M_y$). Figure 6-15 describes these two effective stiffness measurements based on an idealized moment (M) vs. curvature (ϕ) relationship. The uncracked stiffness ($EI_{uncracked}$), calculated herein at the point when flexural cracking is first observed ($M_{base}=M_{cr}$), is the slope between the origin and the moment-curvature at flexural cracking (M_{cr}, ϕ_{cr}). The cracked stiffness ($EI_{cracked}$) is the slope between the origin and the yield point (M_y, ϕ_y). Based on the measured EI_{eff} values (Figure 6-14) at flexural cracking ($M_{base}=M_{cr}$) and first yield ($M_{base}=M_y$), an uncracked flexural stiffness of $0.7E_cI_g$ and a cracked flexural stiffness of $0.4E_cI_g$ appear reasonable to approximate elastic flexural deformations. For comparison, ASCE 41-06 recommends uncracked and cracked flexural stiffness values of $0.8E_cI_g$ and $0.5E_cI_g$, respectively (ASCE/SEI, 2007). It is noted that the 2013 version of ASCE 41 no longer provides a recommendation for uncracked flexural stiffness (ASCE/SEI, 2014).

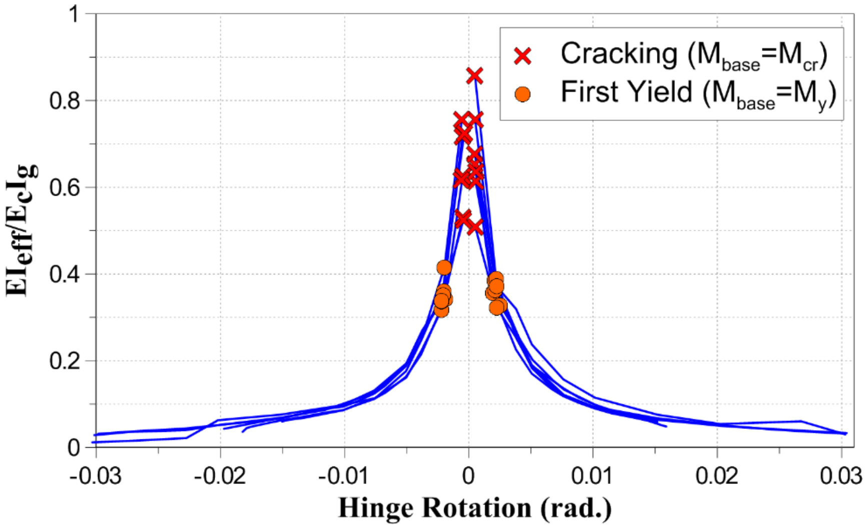

Figure 6-14: Measured effective flexural stiffness (EI_{eff}), normalized to E_cI_g, at various rotation levels

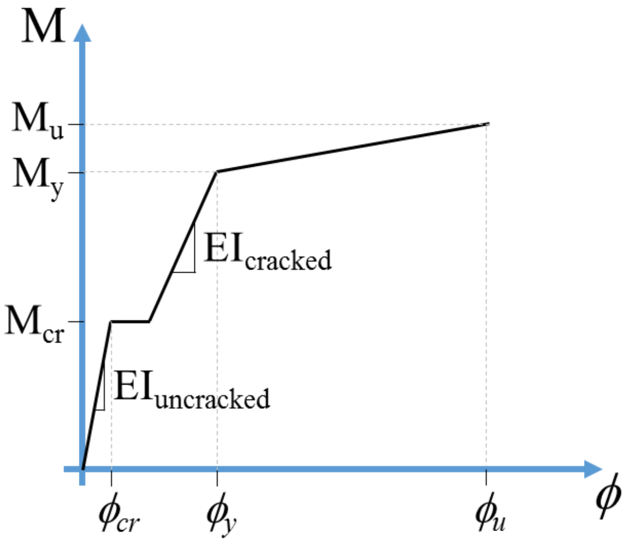

Figure 6-15: Effective uncracked and cracked flexural stiffness

Effective shear stiffness (GA_{eff}) was determined based on the relationship in Eqn. 6.8, which relates GA_{eff} to the applied lateral (shear) force and the measured shear deformation (δ_s). Shear deformation was measured over the height of the assumed plastic hinge region (l_p=l_w/2; Section A in Figure 6-8), which explains the term "l_p" in Eqn. 6.8. Shear deformations within Section A

(Figure 6-8) were calculated based on the methods described in Section 6.3.2. Shear sliding deformations at the wall-footing interface were not included in the stiffness calculations.

$$GA_{eff} = \frac{V_u l_p}{\delta_s} \tag{6.8}$$

Figure 6-16 presents measured effective shear stiffness values, normalized to E_c times the web area of the wall ($A_{cv}=b \cdot l_w$), at various rotation levels for all seven specimens. Like Figure 6-14, markers indicate the values associated with flexural cracking ($M_{base}=M_{cr}$) and first yield of longitudinal reinforcement ($M_{base}=M_y$). The effective shear stiffness measurements demonstrate more dispersion than the measured effective stiffness responses (Figure 6-14). The dispersion is attributed to the fact that shear deformations were quite small; therefore, stiffness measurements are sensitive to small differences in measured shear deformations. Figure 6-16 suggests that effective shear stiffness values less than $0.2E_cA_{cv}$ may be suitable. For comparison, ASCE 41-06 suggests an effective cracked and uncracked shear stiffness of $0.4E_cA_{cv}$, which is larger than measured stiffness values for WP1-WP7 (ASCE/SEI, 2007). It is noted that the 2013 version of ASCE 41 no longer provides a recommendation for uncracked shear stiffness (ASCE/SEI, 2014).

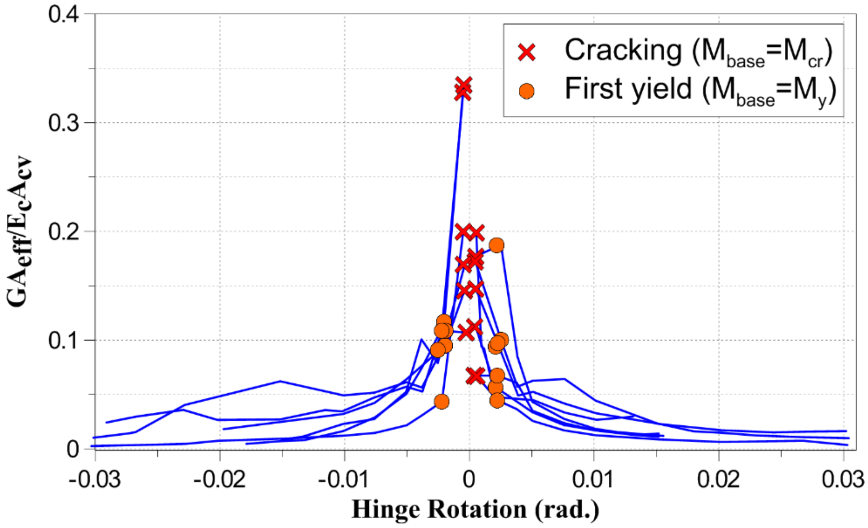

Figure 6-16: Measured effective shear stiffness (GA_{eff}), normalized to E_cA_{cv}, at various rotation levels

6.5 Lateral Drift at the Effective Height

The majority of slender wall tests have been conducted on cantilever specimens, which capture the response of the plastic hinge region, as well as additional elastic or essentially elastic response above the plastic hinge region. Specimens WP1-WP7 were so-called "wall panel" specimens representing approximately the bottom 1.5 stories (essentially about twice the plastic hinge region) of an eight story cantilever wall. To enable a direct comparison of the wall panel experimental results to cantilever wall tests, lateral deformations were approximated at the effective height of the walls. The effective height is defined herein as the ratio of the base overturning moment-to-shear ($h_{eff}=M_b/V_b$), which is consistent with wall height (h_w) for a cantilever wall test. The lateral deformations at the effective height were calculated using the plastic hinge formulation in Eqn. 6.9, which expresses the total lateral displacement ($\delta_u@h_{eff}$) as the sum of the elastic drift at the effective height ($\delta_e@h_{eff}$) and inelastic drift due to plastic rotation (θ_p), centered about the centroid ($\bar{x}$) of the inelastic curvature distribution.

$$\delta_u @ h_{eff} = \delta_e @ h_{eff} + \theta_p (h_{eff} - \bar{x}) \qquad 6.9$$

Plastic rotation and curvature distributions (Figure 6-9) were directly measured within the height of the wall panel specimens, and it is assumed that only elastic deformations occur above the panel specimen height. As shown in Figure 6-17, the elastic displacement at h_{eff} ($\delta_e@h_{eff}$) consists of elastic drift within the wall panel region ($\delta_{e,exp}$) and elastic drift above the wall panel ($\delta_{e,upper}$). The elastic displacement and rotation at the top of the "wall panel" region ($\delta_{e,exp}$ and $\theta_{e,exp}$) were measured in the laboratory; therefore, only $\delta_{e,upper}$ needs to be estimated. The height of the wall panel region (h_p in Figure 6-17) was 82 in. (2083 mm) for all seven specimens, which is the height at which the lateral displacements and drift ratios reported in Figure 6-6 were measured. The lateral loading pattern shown in Figure 4-9 (ASCE 7 Equivalent Lateral Force pattern) was assumed to calculate the story shear forces ($V_{s,i}$) and moment distribution over each story. The lateral displacement ($\delta_{s,i}$) and rotation ($\theta_{s,i}$) at the top of each story were calculated according to Eqns. 6.10 and 6.11, where $M_{s,i}$ is the moment at the bottom of the story and h_s is the story height, which was assumed as constant at all stories. The elastic displacement at the effective height ($\delta_e@h_{eff}$) was determined within the story coinciding with h_{eff}.

$$\delta_{s,i} = \delta_{s,i-1} + \theta_{s,i-1} h_s + \frac{M_{s,i} h_s^2}{2EI_{eff}} - \frac{V_{s,i} h_s^3}{6EI_{eff}} + \frac{V_{s,i} h_s}{GA_{eff}} \qquad 6.10$$

$$\theta_{s,i} = \sum_{k=1}^{i} \theta_{s,k} + \frac{M_{s,i} h_s}{EI_{eff}} - \frac{V_{s,i} h_s^2}{2EI_{eff}} \qquad 6.11$$

The displacement at the top of the second story, which is needed to determine the story displacements in the upper stories, is calculated according to Eqn. 6.12, and includes all deformations within the wall panel region.

$$\delta_{s,2} = \delta_{e,\exp} + \theta_{e,\exp}(2h_s - 82") + \frac{M_{s,i}(2h_s - 82")^2}{2EI_{cracked}} - \frac{V_{s,i}(2h_s - 82")^3}{6EI_{cracked}} + \frac{V_{s,2}(2h_s - 82")}{GA_{cracked}} \qquad 6.12$$

The effective stiffness within each story was chosen based on whether the applied loading produced flexural cracking (i.e., moment greater than the cracking moment; $M_u>M_{cr}$) or an uncracked section ($M_u<M_{cr}$). Within the expected cracked region ($h \le h_{cr}$), cracked effective stiffness values ($EI_{cracked}$ and $GA_{cracked}$) were used to determine elastic deformations, and above the expected cracked region ($h>h_{cr}$), uncracked stiffness values ($EI_{uncracked}$ and $GA_{uncracked}$) were used. At each loading step, the height over which cracking was expected (h_{cr} in Figure 6-17) was determined based on the moment distribution up the height of the wall; that is, h_{cr} represents the height at which $M_u=M_{cr}$. In Section 6.4, average uncracked and cracked flexural stiffness values were shown to be approximately $EI_{uncracked}=0.7E_cI_g$ and $EI_{cracked}=0.4E_cI_g$, respectively, which are fairly consistent with ASCE 41 recommendations ($EI_{uncracked}=0.8E_cI_g$, $EI_{cracked}=0.5E_cI_g$). Average effective shear stiffness measurements at flexural cracking and first yield were approximately $GA_{uncracked}=0.15E_cA_{cv}$ and $GA_{cracked}=0.1E_cA_{cv}$, respectively, which are considerably less than the values recommended in ASCE 41 ($GA_{cracked}=GA_{uncracked}=0.4E_cA_{cv}$).

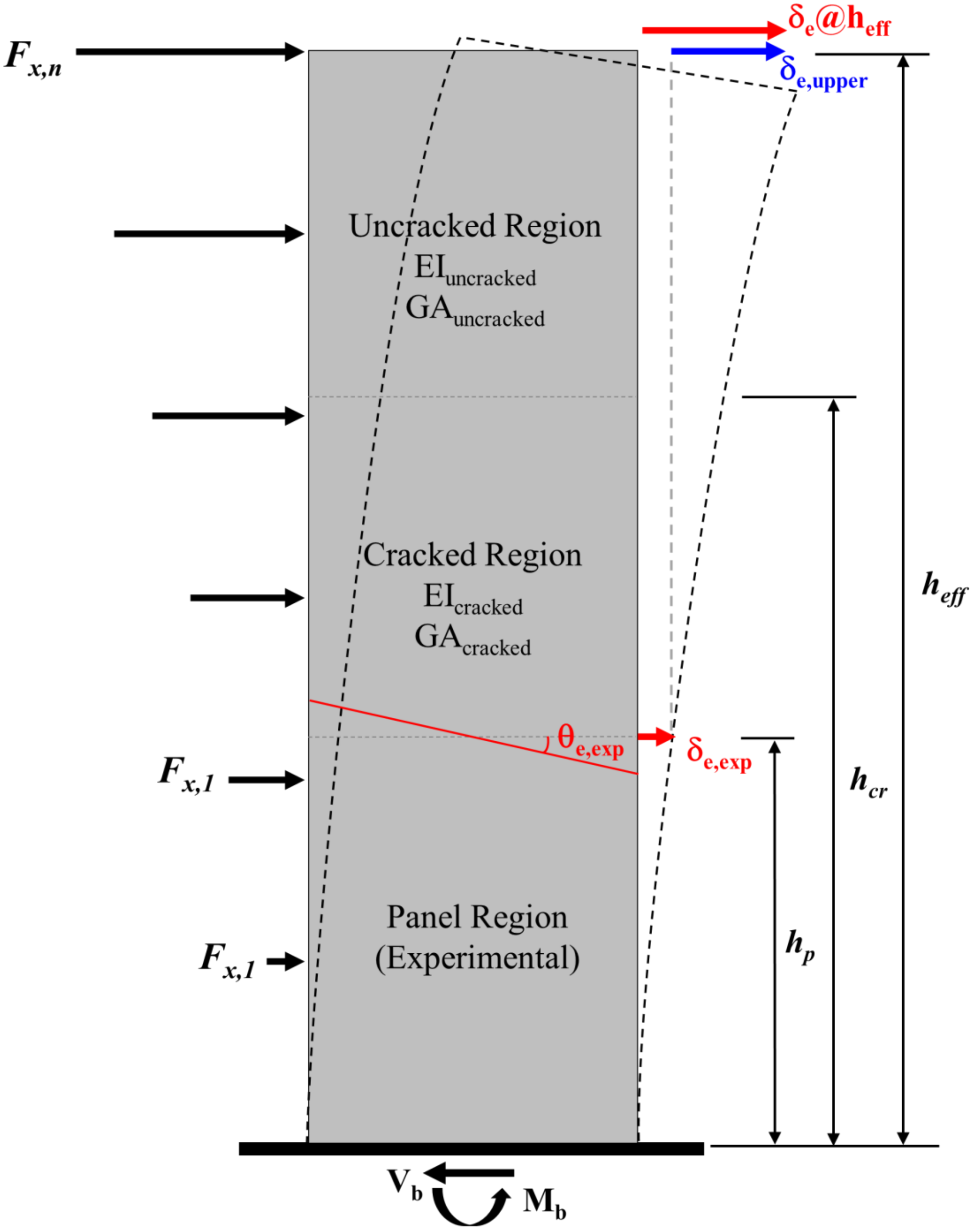

Figure 6-17: Elastic deformations in the full-height prototype wall

In Table 6-1, estimated lateral displacements and drift ratios at h_{eff} are reported at 1) horizontal flexural cracking of concrete at wall boundaries; 2) first yield of boundary longitudinal reinforcement; 3) peak strength; and 4) strength loss (determined at the largest lateral displacement for which lateral strength exceeded 80% of peak strength). The values reported in Table 6-1 were calculated assuming the following effective cracked and uncracked stiffness values: $EI_{uncracked}=0.7E_cI_g$, $EI_{cracked}=0.4E_cI_g$, and $GA_{uncracked}=GA_{cracked}=0.2E_cA_{cv}$. It is noted that using an effective shear stiffness of $0.2E_cA_{cv}$, which is larger than the experimentally measured values, had almost no impact on the drift estimates because elastic shear deformations are very low. Displacements/drift ratios were also calculated using the values recommended by ASCE 41 ($EI_{uncracked}=0.8E_cI_g$, $EI_{cracked}=0.5E_cI_g$, and $GA_{cracked}=GA_{uncracked}=0.4E_cA_{cv}$), which resulted in drift estimates that ranged between 93% and 98% (96% on average) of the values reported in Table 6-1. Thus, using either the experimentally measured values or the values recommended by ASCE 41 is reasonable as both will produce similar lateral drift approximations.

The effective height for each of the walls is reported in Table 6-1. The effective height was varied in order to subject the walls to approximately the same peak shear stress demands $\left(v_u\ @\ M_n \approx 2.5\sqrt{f'c[psi]}\ \left(0.2\sqrt{f'c[\text{MPa}]}\ \right)\right)$. For the rectangular specimens, h_{eff} ranged between 320 in. (WP5-WP7) and 336 in. (WP1-WP3). Because of the reinforcement layout and thin web of WP4, the ratio of moment to shear was larger (h_{eff} =528 in.; 13.4 m) in order to subject the wall to similar shear stress demands as the rectangular walls. Based on the ASCE 7 Equivalent Lateral Force loading pattern (Figure 4-9) the effective height is approximately 72% of the full height prototype wall. For the one-half scale specimens, 60 in. (1524 mm) story heights were assumed; thus, the lateral deformations in Table 6-1 were calculated (Eqn. 6.10) at about midheight of the fifth story for the rectangular walls (h_{eff}≈330 in.), and near the top of the eight story for specimen WP4 (h_{eff}=528 in.).

Table 6-2 reports the contribution of flexure to the total lateral deformations at the effective height. Flexure contributed between 91% and 96% of the total lateral drifts at h_{eff}, which is a much larger contribution than was measured within the wall panel specimen (Figure 6-12). This is due to the fact that inelastic flexural drift ratio is relatively constant up the height of the wall, unlike inelastic shear drift ratio, and elastic shear deformations are very small in comparison to elastic flexural deformations. For all seven walls, elastic flexural drift ratio ($\delta_{f,e}/h_{eff}$) estimates are approximately 0.4% at first yield of longitudinal reinforcement, and generally exceed 0.5% prior to strength loss (Table 6-2). For specimen WP4, δ_e@h_{eff} is the largest because the effective height is about 1.5 times the effective height of the rectangular walls, and elastic drift ratio tends to increase with height (e.g., Eqn. 2.3: $\delta_{f,y}/h_w = \gamma \phi_y h_w$). At strength loss, elastic drift made up almost 40% of the flexural response for WP4. Even though the lateral drift capacity for WP4 was comparable to specimens WP1-WP4 (Table 6-1), WP4 demonstrated the smallest plastic rotation capacity (θ_{pu}=1.25%). In contrast, elastic deformations compromised only 16% of the flexural drift for specimen WP7, which demonstrated the largest plastic rotation capacity (θ_{pu}=3.34%). It is noted that plastic rotation measurements in Table 6-2 include inelastic rotation along the full height of the wall panel specimens, unlike Table 5-2 which only includes rotation within the assumed hinge region (l_p=l_w/2).

Table 6-1: Estimated lateral displacement and drift ratio at effective height

ID	Loading Direction	Flexural Strength	Effective Height	Cracking			First Yield			Peak Load			Strength Loss		
		M_n	h_{eff}	δ_u	δ_u/h_{eff}	M/M_n	δ_u	δ_u/h_{eff}	M/M_n	δ_u	δ_u/h_{eff}	M/M_n	δ_u	δ_u/h_{eff}	M/M_n
		k-ft	in.	in.	rad.	---	in.	rad.	---	in.	rad.	---	in.	rad.	---
WP1	Positive	2515	336	0.47	0.14%	0.41	1.59	0.47%	0.86	5.68	1.69%	1.07	6.78	2.02%	0.90
	Negative	-2455	336	-0.50	-0.15%	0.41	-1.53	-0.46%	0.80	-6.83	-2.03%	1.03	-8.59	-2.56%	0.86
WP2	Positive	2560	336	0.57	0.17%	0.44	1.70	0.51%	0.90	6.60	1.97%	1.09	7.24	2.16%	1.05
	Negative	-2497	336	-0.54	-0.16%	0.40	-1.48	-0.44%	0.77	-6.55	-1.95%	1.01	-8.26	-2.46%	0.85
WP3	Positive	2566	336	0.50	0.15%	0.35	1.45	0.43%	0.77	6.55	1.95%	1.10	7.07	2.10%	0.89
	Negative	-2502	336	-0.21	-0.06%	0.36	-0.78	-0.23%	0.75	-5.99	-1.78%	1.01	-6.68	-1.99%	0.90
WP4	Positive	4183	528	0.95	0.18%	0.28	2.72	0.52%	0.68	8.30	1.57%	0.99	10.71	2.03%	0.96
	Negative	-3104	528	-1.10	-0.21%	0.40	-3.05	-0.58%	0.81	-19.85	-3.76%	1.00	-20.47	-3.88%	0.85
WP5	Positive	2888	320	0.54	0.17%	0.34	1.60	0.50%	0.76	9.51	2.97%	1.21	11.21	3.50%	1.01
	Negative	-2690	320	-0.43	-0.14%	0.28	-1.61	-0.50%	0.79	-9.12	-2.85%	1.16	-9.07	-2.83%	1.14
WP6	Positive	2867	320	0.43	0.14%	0.33	1.89	0.59%	0.91	12.29	3.84%	1.22	13.06	4.08%	1.21
	Negative	-2867	320	-0.31	-0.10%	0.27	-1.61	-0.50%	0.78	-9.37	-2.93%	1.20	-10.28	-3.21%	0.97
WP7	Positive	3389	320	0.47	0.15%	0.29	1.60	0.50%	0.82	12.06	3.77%	1.24	13.52	4.23%	1.23
	Negative	-3389	320	-0.41	-0.13%	0.28	-1.62	-0.51%	0.82	-8.29	-2.59%	1.15	-12.77	-3.99%	1.03

Table 6-2: Flexural contribution to lateral deformations at effective height

ID	Loading Direction	Effective Height	Cracking	First Yield	Peak Load			Strength Loss		
		h_{eff}	δ_f/h_{eff}	δ_f/h_{eff}	δ_f/h_{eff}	$\delta_{f,p}/h_{eff}$	θ_p	δ_f/h_{eff}	$\delta_{f,p}/h_{eff}$	θ_{pu}
		in.	rad.	rad.	rad.	rad.	rad.	rad.	rad.	rad.
WP1	Positive	336	0.13%	0.45%	1.61%	1.05%	1.13%	1.94%	1.41%	1.51%
	Negative	336	-0.14%	-0.42%	-1.89%	-1.36%	-1.46%	-2.38%	-1.89%	-2.02%
WP2	Positive	336	0.16%	0.49%	1.83%	1.25%	1.34%	2.00%	1.43%	1.53%
	Negative	336	-0.15%	-0.42%	-1.83%	-1.30%	-1.39%	-2.30%	-1.80%	-1.92%
WP3	Positive	336	0.14%	0.41%	1.81%	1.28%	1.37%	1.94%	1.44%	1.54%
	Negative	336	-0.06%	-0.21%	-1.70%	-1.19%	-1.27%	-1.87%	-1.38%	-1.47%
WP4	Positive	528	0.17%	0.50%	1.51%	0.75%	0.78%	1.94%	1.19%	1.25%
	Negative	528	-0.20%	-0.55%	-3.41%	-2.75%	-2.87%	-3.53%	-2.91%	-3.04%
WP5	Positive	320	0.16%	0.48%	2.76%	2.12%	2.28%	3.32%	2.71%	2.92%
	Negative	320	-0.13%	-0.48%	-2.70%	-2.08%	-2.24%	-2.69%	-2.07%	-2.22%
WP6	Positive	320	0.12%	0.55%	3.59%	2.90%	3.12%	3.78%	3.09%	3.32%
	Negative	320	-0.09%	-0.46%	-2.69%	-2.07%	-2.23%	-2.98%	-2.40%	-2.58%
WP7	Positive	320	0.14%	0.48%	3.51%	2.88%	3.10%	3.93%	3.30%	3.55%
	Negative	320	-0.12%	-0.49%	-2.46%	-1.85%	-1.99%	-3.70%	-3.11%	-3.34%

Chapter 7 Drift Capacity of Slender RC Walls

In this chapter, experimental results for specimens WP1-WP7 are compared to other laboratory tests conducted on cantilever walls and wall panel specimens with well-detailed boundaries. Performance limitations identified for WP1-WP7 are used to formulate a lateral drift capacity prediction formulation, developed using a displacement-based design format.

7.1 Measured Lateral Deformations in Laboratory Tests

To complement the laboratory tests reported herein, a database of tests conducted on thin, well-detailed walls was assembled to study the deformation capacity of walls designed for relatively large compression demands, which, therefore, may experience brittle flexural-compression failure. The walls in the database were selected from the experimental programs discussed in Section 2.4. Test specimens were included in the database because they satisfied the following criteria: 1) the shear span-to-depth ratio (M/Vl_w) was at least 2.0 (slender wall); 2) the wall was designed for moderate/large compression depth (i.e., $c/l_w>0.10$); 3) confinement consisted of either an outer hoop and cross-ties or overlapping hoops; 4) the quantity of boundary transverse reinforcement was at least 50% of that required by ACI 318-14; 5) the spacing of boundary transverse reinforcement was no larger than $8d_b$; and 6) premature anchorage failure was not reported. Table 7-1 contains details for twenty walls that were selected for inclusion in the database including the cross-sectional shape of the walls, wall thickness, M/Vl_w, applied axial load, the quantity, spacing and configuration of boundary transverse reinforcement. The walls tested by Oesterle et al. (1976) were excluded from the database because compression demands were relatively low ($c/l_w<0.10$), and failures were associated with tension behavior as a result. The tests conducted by Dazio et al. (2009) were excluded because the reinforcement properties did not meet ACI 318 provisions

(ASTM A706). Specimen RWS, tested by Johnson (2007), was excluded because a premature anchorage failure was reported.

For the twenty database walls, lateral drift capacities at the effective height (δ_u/h_{eff}) were compared to the values reported in Section 6.5 for specimens WP1-WP7. For three of the eight experimental programs included in the database (Paulay, et al., 1985; Lowes, et al., 2012; Brueggen, 2009), tests were conducted on wall panel specimens, similar to specimens WP1-WP7, to which a unique loading scheme was applied. For the wall panel specimens tested by Lowes et al. (2012), δ_u/h_{eff} was reported by the authors using experimentally measured effective flexural and stiffness values to estimate elastic deformations in the upper stories. For the other wall panel tests, lateral drift capacities at h_{eff} were determined by approximating elastic flexural and shear deformations above the panel test region using the effective stiffness values recommended in ASCE 41 ($EI_{uncracked}=0.8E_cI_g$, $EI_{cracked}=0.5E_cI_g$, and $GA_{eff}=0.4E_cA_{cv}$), which were shown to produce very similar total drift predictions, for WP1-WP7, as the experimentally measured effective stiffness values in Section 6.5.

Lateral drift capacities at h_{eff} (δ_u/h_{eff}) are presented in Figure 7-1 for the twenty database walls and specimens WP1-WP7. It is important to point out that all of the walls included in the study satisfy, or nearly satisfy, ACI 318 Special Structural Wall requirements; however, a large range of experimental results is evident in Figure 7-1, with measured drift capacities varying between 1.2% and 4%. The lowest drift capacities ($\delta_u/h_{eff} \leq 2\%$) were measured for specimens WP1-WP4 and the walls tested by Lowes et al. (2012), which is of concern because these walls were designed according to current ACI 318 standards. The variability in test results shown in Figure 7-1 indicates that it may be necessary to impose a drift limit, minimum wall thickness, or compression strain limit for Special Structural Walls to ensure adequate ductility.

Table 7-1: Slender wall experimental database

Author (Year)	ID	Shape	b (in.)	l_w (in)	$P/A_g f'_{c,test}$	M/Vl_w	$v_u@M_n/f'_c{}^{1/2}$	c/l_w*	$A_{sh}/A_{sh,318\text{-}14}$	s/d_b	Confinement Detail
Shiu et al. (1981)	CI-1	Rectangular	4.0	75.0	0.00	2.9	3.11	0.15	0.98	2.67	Single hoop
Paulay & Goodsir (1985)	Wall 1	Rectangular	3.9	59.1	0.27	3.0	4.32	0.39	1.04	3.33	Overlapping hoops
Paulay & Goodsir (1985)	Wall 2	Rectangular	3.9	59.1	0.16	2.6	4.34	0.27	0.78	6.00	Overlapping hoops
Paulay & Goodsir (1985)	Wall 3	T-shape	3.9	51.2	0.17	3.3	3.52	0.34	0.99	4.00	Overlapping hoops
Paulay & Goodsir (1985)	Wall 4	Rectangular	3.9	59.1	0.15	2.8	3.34	0.26	0.82	3.33	Overlapping hoops
Thomsen & Wallace (1995)	RW1	Rectangular	4.0	48.0	0.09	3.0	2.34	0.20	0.85	8.00	Hoop + crossties
Thomsen & Wallace (1995)	RW2	Rectangular	4.0	48.0	0.06	3.0	2.05	0.17	0.46	5.33	Single hoop
Thomsen & Wallace (1995)	TW1	T-shape	4.0	48.0	0.08	3.0	5.18	0.45	0.79	8.00	Hoop + crossties
Thomsen & Wallace (1995)	TW2	T-shape	4.0	48.0	0.07	3.0	4.76	0.42	0.76	3.33	Overlapping hoops
Johnson (2007)	RWN	Rectangular	6.0	90.0	0.00	2.7	3.89	0.19	0.83	4.00	Hoop + crossties
Johnson (2007)	RWC	Rectangular	6.0	90.0	0.00	2.7	3.97	0.20	0.87	4.00	Hoop + crossties
Brueggen (2009)	NTW1	T-shape	6.0	90.0	0.04	3.5	3.97	0.28	0.89	3.20	Overlapping hoops
Brueggen (2009)	NTW2	T-shape	6.0	90.0	0.06	3.5	4.21	0.30	1.28	3.20	Overlapping hoops
Lowes et al. (2012)	PW1	Rectangular	6.0	120.0	0.10	2.8	3.31	0.22	1.45	4.00	Hoop + crossties
Lowes et al. (2012)	PW2	Rectangular	6.0	120.0	0.13	2.1	4.63	0.26	1.30	4.00	Hoop + crossties
Lowes et al. (2012)	PW3	Rectangular	6.0	120.0	0.10	2.0	3.96	0.25	1.51	4.00	Hoop + crossties
Lowes et al. (2012)	PW4	Rectangular	6.0	120.0	0.12	2.0	4.31	0.22	1.76	4.00	Hoop + crossties
Tran (2012)	A20-S38	Rectangular	6.0	48.0	0.07	2.0	3.52	0.18	0.84	4.00	Hoop + crossties
Tran (2012)	A20-S63	Rectangular	6.0	48.0	0.07	2.0	6.03	0.22	1.08	2.67	Hoop + crossties
Matsubara et al. (2013)	N(M/Qd3.1)	Rectangular	4.7	68.5	0.07	3.1	2.97	0.25	1.09	3.50	Hoop + crossties

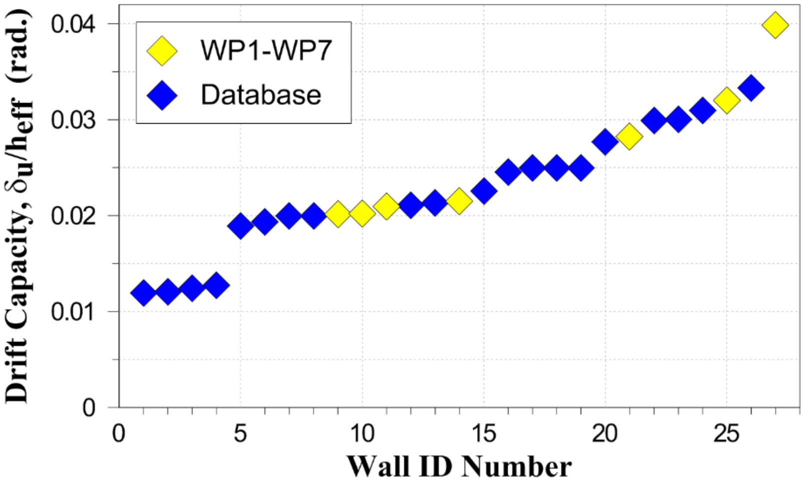

Figure 7-1: Drift capacity at effective height for all walls included in study

As discussed in Section 2.3, a compression strain limit of 0.008, with a corresponding gage length equal to one-half the length of the wall (i.e., l_p=l_w/2), has been enforced in the Chilean reinforced concrete standard, DS No. 60 (MINVU, 2011). It was shown in Section 2.3 that the compression strain (ε_{cu}) demand at the extreme compression fiber within the plastic hinge region of a cantilever wall may be related to the inelastic flexural drift demand at the top of the wall ($\delta_{f,pu}/h_w$) by the formulation given in Eqn. 7.1. A simplified form of Eqn. 7.1 is given in Eqn. 7.2, which estimates $\delta_{f,pu}/h_w$ as plastic rotation demand (θ_{pu}) and neglects elastic curvature (ϕ_y).

$$\frac{\delta_{f,pu}}{h_w} = \frac{1}{h_w}\left(\frac{\varepsilon_{cu}}{c} - \phi_y\right) l_p (h_w - l_p/2) \qquad 7.1$$

$$\frac{\delta_{f,pu}}{h_w} \approx \theta_{pu} \approx \frac{\varepsilon_{cu} l_p}{c} \qquad 7.2$$

A drift or strain limit may be formulated based on Eqn. 7.1 or 7.2, which has been done in DS No. 60, assuming ε_{cu}=0.008 and l_p=l_w/2 (DS No. 60 Eqns. 21-7a and 21-7b). The compression strain limit in the Chilean code is intended for walls in stiff buildings with detailing similar to that required in ACI 318-14 for walls with ordinary boundary elements (OBEs), which is less stringent than ACI 318-14special boundary element (SBE) detailing. It was shown in Section 2.1 that a drift/strain limit (ε_{cu}=0.003, $l_p=l_w/2$) has already been implemented in ACI 318-14 for walls with OBEs; however, no such limit is placed on walls with SBEs.

To evaluate the validity of a drift/strain limit for Special Structural Walls with SBEs, based on the plastic hinge formulation of Eqns. 7.1 and 7.2, the contribution of flexural deformations to the drift capacities reported in Figure 7-1 were determined for each of the walls included in the study. Total flexural drift capacities ($\delta_{f,u}/h_{eff}$), plastic flexural drift capacities ($\delta_{f,pu}/h_{eff}$), and plastic rotation capacities (θ_{pu}) for specimens WP1-WP7 are reported in Table 6-2.

Contributions of flexural and shear deformations were measured by the authors in a variety of ways. Massone and Wallace (2004) conducted a study on shear deformation measurements in slender walls, demonstrating that shear deformations are likely to be largely overestimated in a variety of reported tests because typical methods used to determine the contribution of shear (i.e., X-configuration of sensors) did not include a correction to adjust for the centroid of the curvature distribution in the plastic hinge region. Therefore, flexural deformations were carefully estimated using the information available in the experimental reports. For some of the more recent tests (Johnson, 2007; Brueggen, 2009; Tran, 2012; Matsubara, et al., 2013), reported flexural and shear deformations are dependable because the researchers addressed the issues reported by Massone and Wallace (2004). For the walls tested by Lowes et al. (2012), flexural and shear deformations were reported over the wall panel specimen height, which represented the bottom three stories of a ten story wall. Total lateral deformations at the effective height were reported, and Birely (2011) indicated that an effective shear stiffness of $0.2E_cA_{cv}$ was assumed for the drift approximation at h_{eff}, thus, making it possible to estimate flexural and shear deformations based on the applied loading.

For specimen CI-1, tested by Shiu et al. (1981), it is anticipated that shear deformations were overestimate by the authors. However, total lateral deformations were reported for the first and second stories, where nonlinear shear deformations occur, as well as at the top of the wall. Rotations were also reported for the base (i.e., slip/extension) and over the first and second stories (i.e., plastic hinge region), making it possible to estimate flexural deformations. The contribution of flexural deformations to total deformations within the bottom two stories was estimated by assuming that the centroid of the inelastic curvature distribution was located at a height of one-third of the first story height, which is in agreement with methods used by Massone and Wallace (2004) for cases in which inadequate information was available to estimate the centroid height. Elastic shear deformations in the upper stories were estimated using an effective shear stiffness of $0.4E_cA_{cv}$ (ASCE/SEI, 2014) for the applied loading, and the remainder was attributed to flexure.

For the walls tested by Paulay and Goodsir (1985), flexural deformations were reported in the first story, and total deformations at the top of the wall were reported (Goodsir, 1985). Using this information, and the applied loading, the contribution of shear to the top displacement was determined using an effective shear stiffness of $0.4E_cA_{cv}$ (ASCE/SEI, 2014). It is noted that an eccentric axial load was applied to the walls, resulting in an effective height (h_{eff}=M/V) above the top of the wall for loading in one direction, and below the top of the wall in the reverse loading direction. Flexural and shear deformations were adjusted to h_{eff} for loading in the direction with the larger effective height, which is the direction in which failures occurred. For the adjustment to h_{eff}, an effective flexural stiffness of $0.8E_cI_g$ (uncracked) was assumed since flexural cracking would not be expected in the region above the test specimen.

Thomsen and Wallace (1995) reported total lateral deformations and flexural deformations over the first story, making it possible to estimate nonlinear shear deformations in the first level. Shear distortions in the second story were also reported, from which elastic shear deformations were approximated in the second story. Shear deformations in the upper stories were estimated using an effective shear stiffness of $0.4E_cA_{cv}$ and the applied loading. Flexural deformations were then calculated by subtracting the estimated shear deformations from the total reported top displacement.

Figure 7-2 reports the flexural drift capacity ($\delta_{f,u}/h_{eff}$) and plastic flexural drift capacity ($\delta_{f,pu}/h_{eff}$) for each of the database walls and WP1-WP7. Total measured drift capacities (δ_u/h_{eff}) are also shown for comparison. The percent contribution of $\delta_{f,u}$ and $\delta_{f,pu}$ to the total drift capacity is indicated on the figure for each wall. On average, plastic flexural drift comprised 70% of the total response, and elastic flexural drift accounted for 17% of the total response. The remainder is attributed to shear which tends to be relatively small (approximately 13% on average for the walls in the database) for slender walls. Similar to the total drift capacity measurements, a large range of experimental results is evident in the flexural drift capacities of the walls. For comparison to the drift ratios in Figure 7-2, ASCE 7 allows between 2% and 2.5% interstory drift for shear wall buildings classified as Seismic Risk Category I or II. The contribution of elastic deformation over a single story height is expected to be relatively small, and shear deformations are typically small for slender walls, as shown in Figure 7-2. Therefore, the plastic flexural drift ratios reported in Figure 7-2 may be appropriate for comparison to ASCE 7 drift limits. It can be seen in Figure 7-2 that plastic flexural drift capacity is less than 1.5% for thirteen of the twenty seven walls included in the study, and less than 2% for eighteen of the walls. It is important to point out that lateral drift demands are typically determined for the Design Earthquake (DE) spectra which are defined in ASCE 7 as two-thirds of the Maximum Considered Earthquake (MCE) spectra. Thus, in order to meet the performance objective of ASCE 7 of a low probability of collapse for MCE demands, it may be reasonable to require code-compliant walls to demonstrate interstory drift capacities of about 1.5 times the interstory drift ratio allowed by code. As such, code-compliant walls in buildings classified as Seismic Risk Category I or II may be expected to possess interstory drift capacities on the order of 3%, which would very likely result in plastic rotation demands greater than 2%. In Figure 7-2 it is clear that not all code-compliant walls possess the plastic drift/rotation capacity to meet ASCE 7 allowable drifts. An alternative to a single drift limit, in which drift capacity is approximated based on wall thickness, compression depth, confinement detailing, and/or other variables is discussed in the following section.

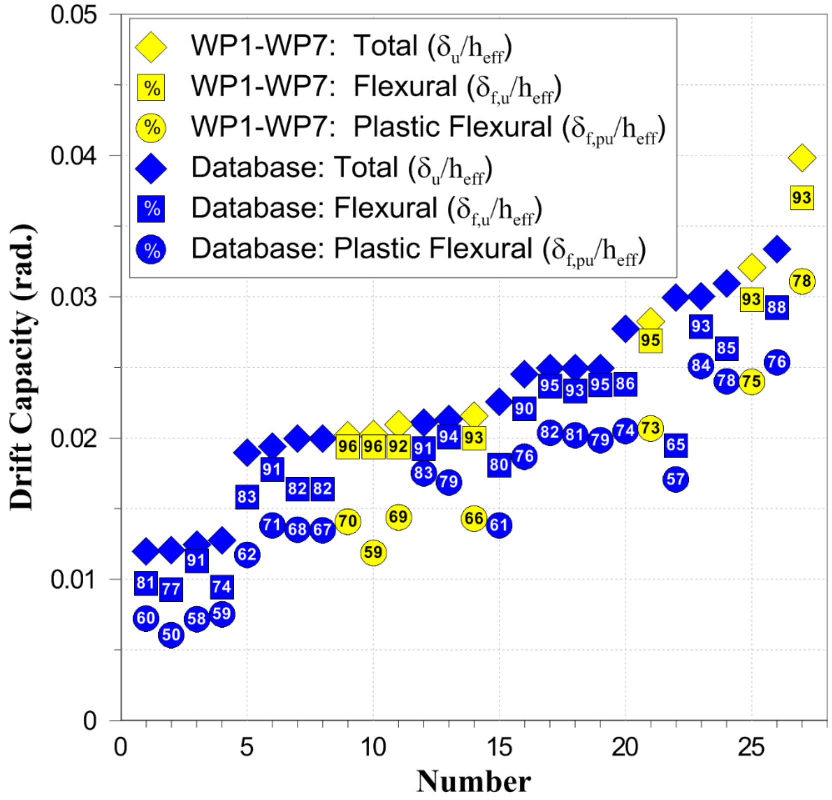

Figure 7-2: Flexural drift capacity at effective height for all walls included in study

7.2 Lateral Drift Limits of Well-Detailed Slender Walls

As indicated by Eqns. 7.1 and 7.2, it may be possible to express the drift capacity of a wall that is expected to fail in compression in terms of a compression strain limit (ε_{cu}) and the compression depth (c). Compression depth may be computed by a section analysis using the design axial load, and is typically assumed to be relatively constant for extreme fiber compression strains greater than 0.003. Compression strain limit(s) must be inferred from experimental data. Figure 7-3 presents axial strain profiles for specimens WP2, WP4, and WP7, which differed from one another in terms of wall thickness (b=6 in. [152 mm] for WP2 and WP4 and b=9 in. [229 mm] for WP7) and compression depth ($c/l_w \approx 0.2$ for WP2 and WP7; $c/l_w \approx 0.3$ for WP4). WP2, WP4, and WP7 represent the range of experimental measurements observed for specimens WP1-WP7. Specimen WP4 demonstrated the smallest plastic rotation capacity of the seven walls, which is attributed to WP4 being one of the thinnest walls tested and having the largest compression depth. On the other hand, WP7 was the thickest wall tested, and demonstrated the largest plastic rotation capacity of the seven specimens. The strains reported in Figure 7-3 were measured over a gage length of approximately $l_w/2$ (44 in.; 1118 mm). The maximum measured extreme fiber compression strain for WP2 (ε_{cu}=0.0092), WP4 (ε_{cu}=0.0079) and WP7 (ε_{cu}=0.012) each exceeded or closely matched the 0.008 Chilean strain limit. In Figure 7-4, the maximum extreme fiber compression strain (ε_{cu}) and tension strain (ε_{tu}) measured prior to strength loss are compared. Markers indicate whether strength loss occurred due to **compression** (abrupt boundary/web crushing) or **tension** rupture of longitudinal reinforcement. The confinement detail used at the boundary of the wall is indicated on the horizontal axes of Figure 7-4a and Figure 7-4b, and each confinement detail is shown in Figure 7-4c for reference. Compression failures were observed at all boundaries utilizing cross-ties, regardless of whether the cross-ties had 90°-135° hooks (Details BE-1 and BE-2) or 135°-135° (Detail BE-3). Prior to failure, ε_{cu} was between 0.0063 (WP3) and 0.012 (WP7). It is noted in that specimen WP3, for which the smallest ε_{cu} value was measured, violated the requirement of ACI 318-14 that limits boundary transverse reinforcement spacing to one-third of the compression zone thickness (s≤b/3). With the exception of WP3, extreme fiber compression strains were greater than or equal to 0.008 prior to strength loss.

Wall boundaries confined by continuous transverse reinforcement (Detail BE-4) remained stable in compression, and strength loss was attributed to tension rupture of longitudinal reinforcement, preceded by buckling of longitudinal reinforcement in all cases. As shown in Figure 7-4b, tension strains in excess of 0.04 were measured prior to strength loss in cases when tension failures were observed. For specimens WP1-WP4, which failed in compression, extreme fiber tension strains did not exceed 0.03 at any time during the tests.

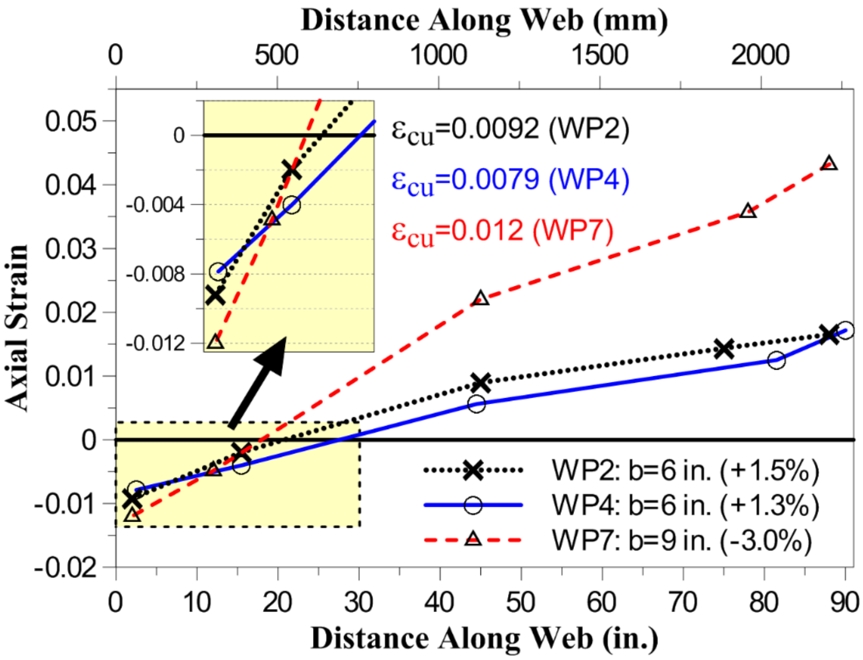

Figure 7-3: Axial strain profiles prior to strength loss for specimens WP2 (b=6 in.; $c/l_w=0.2$), WP4 (b=6 in.; $c/l_w=0.3$), and WP7 (b=9 in.; $c/l_w=0.2$)

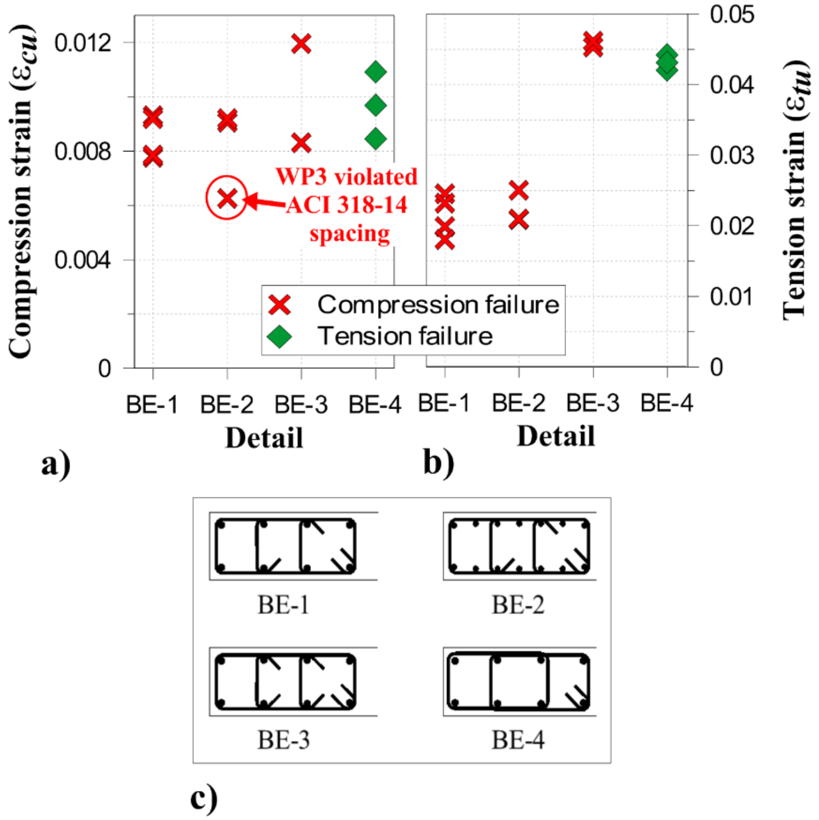

Figure 7-4: Maximum extreme fiber strains prior to strength loss – a) Compression strain; b) Tension strains; and c) Boundary details

For nineteen of walls included in the study, including six of the seven walls reported herein, confinement consisted of a single outer hoop with or without cross-ties, which is a detail allowed by ACI 318-14 for transverse reinforcement at wall boundaries. For these specimens, the plastic drift capacities reported Figure 7-2 were compared to predicted drift capacities determined according to Eqns. 7.1 and 7.2 using the range of compression strain limits identified for WP1-WP7 (Figure 7-4: ε_{cu}=0.008-0.012). The compression strain limits in Figure 7-4 correspond to a gage length of $l_w/2$; therefore, a plastic hinge length of $l_p=l_w/2$was assumed, making it possible to approximate plastic drift or rotation capacity as a function of c/l_w (Eqns. 7.3 and 7.4).

$$\frac{\delta_{f,\mathrm{pu}}}{h_w} = \frac{1}{h_w}\left(\frac{\varepsilon_{cu}}{c} - \phi_y\right)\frac{l_w}{2}\left(h_w - \frac{l_w}{2}\right) \tag{7.3}$$

$$\theta_{pu} \approx \frac{\varepsilon_{cu}}{c}\frac{l_w}{2} \qquad 7.4$$

Plastic rotation capacities for the nineteen walls utilizing hoops and cross-ties for confinement at wall boundaries are shown in Figure 7-5. Predictions of the plastic rotation capacity, determined according to Eqn. 7.4, are also plotted for compression strain limits of ε_{cu}=0.008 and ε_{cu}=0.012. The results plotted in Figure 7-5 demonstrate that rotation capacity generally decreases as c/l_w increases. This trend is to be expected because larger compression depths will result in larger extreme fiber compression strains for a given curvature/rotation demand. However, as shown in Figure 7-5, rotation capacity is significantly overestimated for about one-third of the walls in the study even though the range of predicted plastic rotation capacity, using ε_{cu}=0.008 and 0.012, is relatively large for a given c/l_w.

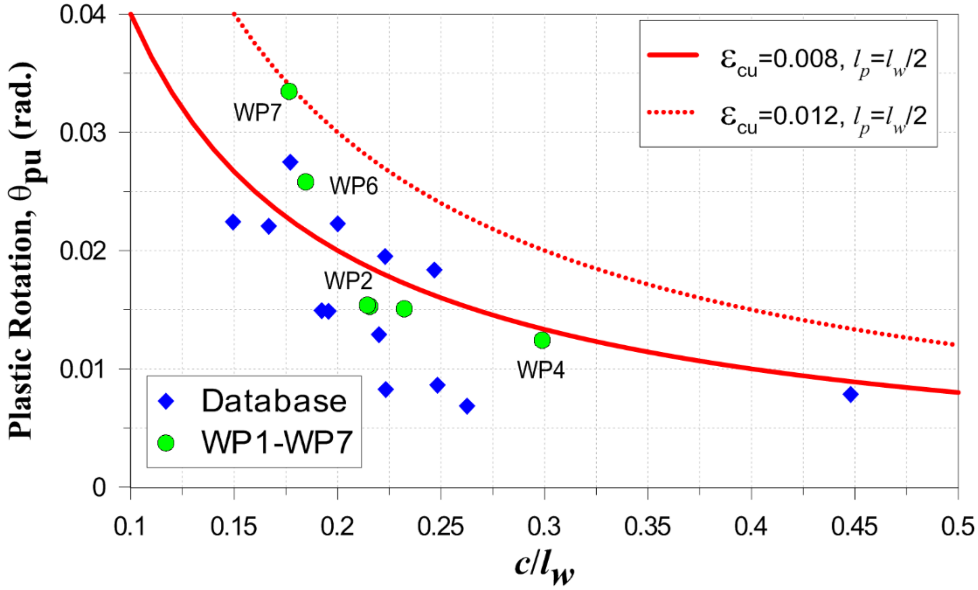

Figure 7-5: Plastic rotation capacity vs. c/l_w

In Figure 7-6, the ratio of measured-to-predicted plastic drift capacity ($\delta_{f,pu}/\delta_{f,p\_predicted}$) is presented for each of the walls. The predicted drift capacities in Figure 7-6 were determined according to Eqn. 7.3, which is the more complex form of Eqn. 7.4 (i.e., Figure 7-5). The ratio of wall length-to-thickness (l_w/b) is indicated on the horizontal axis. It is observed that the best plastic drift predictions ($\delta_{f,pu}/\delta_{f,p\_predicted} \approx 1$) are made for the walls with $l_w/b = 15$, which is understandable since l_w/b was 15 for five of the seven tests used to define the strain limits used for the prediction. However, drift capacity is overestimated (($\delta_{f,pu}/\delta_{f,p\_predicted} < 1$) for the walls with the largest length-to-thickness ratio (e.g., $l_w/b \geq 15$) and underestimated for walls such that $l_w/b \leq 10$. It is important to point out that it was assumed that plastic hinge length is related to wall length ($l_p = l_w/2$) for the results plotted in Figure 7-5 and Figure 7-6. Based on this assumption, two walls of the same length ($l_{w,1} = l_{w,2}$), designed for the same compression depth ($c_1 = c_2$), and with **different** wall thickness ($b_1 > b_2$), are predicted to have the same drift or rotation capacities (Eqns. 7.3 and 7.4) because c/l_w is the same for the two walls. This contradicts experimental observations specimens WP1-WP7 which indicate wall thickness influences plastic drift/rotation capacity. It is noted that specimens WP2 (b=6 in.; 152 mm), WP6 (b=7.5 in.; 191 mm), and WP7 (b=9 in.; 229 mm) exhibited a wide range of plastic rotation capacities (Figure 7-5), between 1.5% and 3.4%, even though c/l_w was comparable for the three walls ($c/l_w = 0.18\text{-}0.22$). On the other hand, plastic rotation capacities for specimens WP2 ($\theta_{pu} = 1.5\%$) and WP4 ($\theta_{pu} = 1.2\%$), which were both 6 in. (152 mm) thick, were similar over a wider range of c/l_w ($c/l_w = 0.22\text{-}0.30$). Both of these observations indicate that using $l_p = l_w/2$ to approximate the plastic rotations in Figure 7-5 is not suitable.

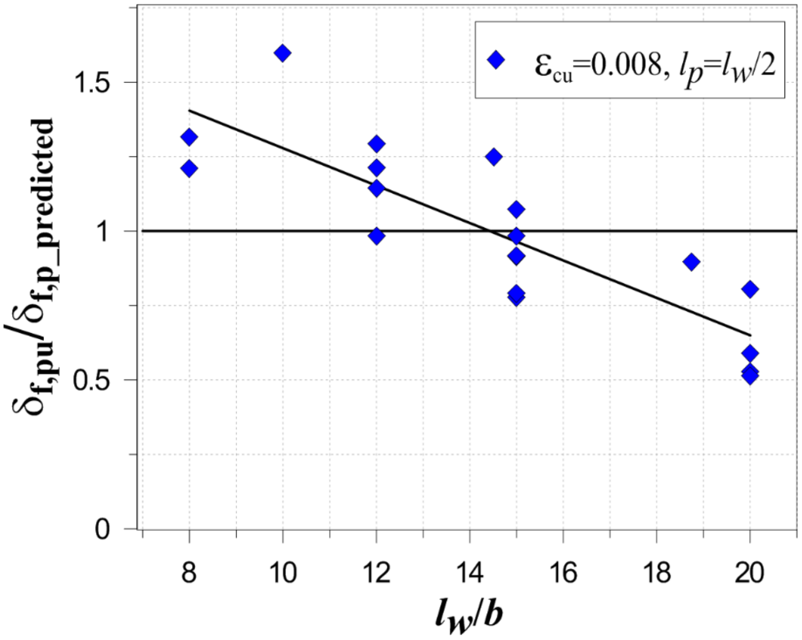

Figure 7-6: Comparison of measured and predicted plastic drift capacities vs. wall length-to-thickness ratio (l_w/b)

Researchers have indicated that inelastic compression behavior (i.e., crushing/spalling of concrete and buckling of longitudinal reinforcement) occurs over a short height in thin wall sections, and it has been suggested that a plastic hinge length related to wall thickness (i.e. $l_p = \alpha b$, where α is a constant) may be better suited to estimate the plastic curvature capacity of thin walls (Wallace, 2012; Wallace, et al., 2012; Takahashi, et al., 2013; Arteta, 2015). In this case, plastic drift/rotation may be expressed directly in terms of wall thickness and compression depth (Eqn. 7.5).

$$\frac{\delta_{f,p}}{h_w} \approx \theta_{pu} \approx \frac{\alpha \varepsilon_c}{c/b} \qquad 7.5$$

Field and laboratory observations suggest α-values ranging between approximately 1.0 and 3.0. Figure 7-7 presents the full axial strain field, determined from digital image correlation analysis (Barthes, 2015), for specimen WP4 at the loading step just prior to strength loss (+1.31% rotation). Inelastic tension strains (approximately $\varepsilon \geq 0.002$), which are shown as dark red regions in Figure

7-7, were well distributed up the height of the wall. However, softening occurred in the compression zone following crushing/spalling of cover concrete, and inelastic compression strains ($\varepsilon \leq -0.002$), which are shown as dark blue regions in Figure 7-7, concentrated over a short height at the base of the wall. Similar behavior was observed for all seven tests specimens (WP1-WP7) with compression strains concentrating within the bottom 14 in. (356 mm) of the walls, corresponding to α-values between 1.6 (b=9 in.; 229 mm) and 2.3 (b=6 in.; 152mm).

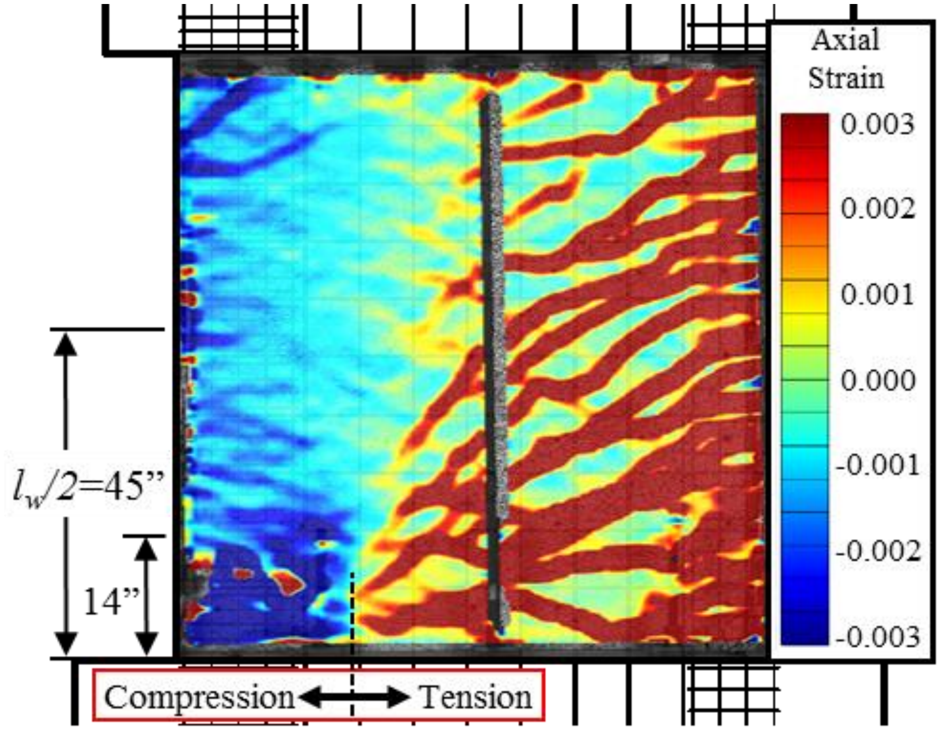

Figure 7-7: Full axial strain field prior to strength loss for specimen WP4 (+1.31% rotation); Analysis conducted with Opecal (Barthes, 2015)

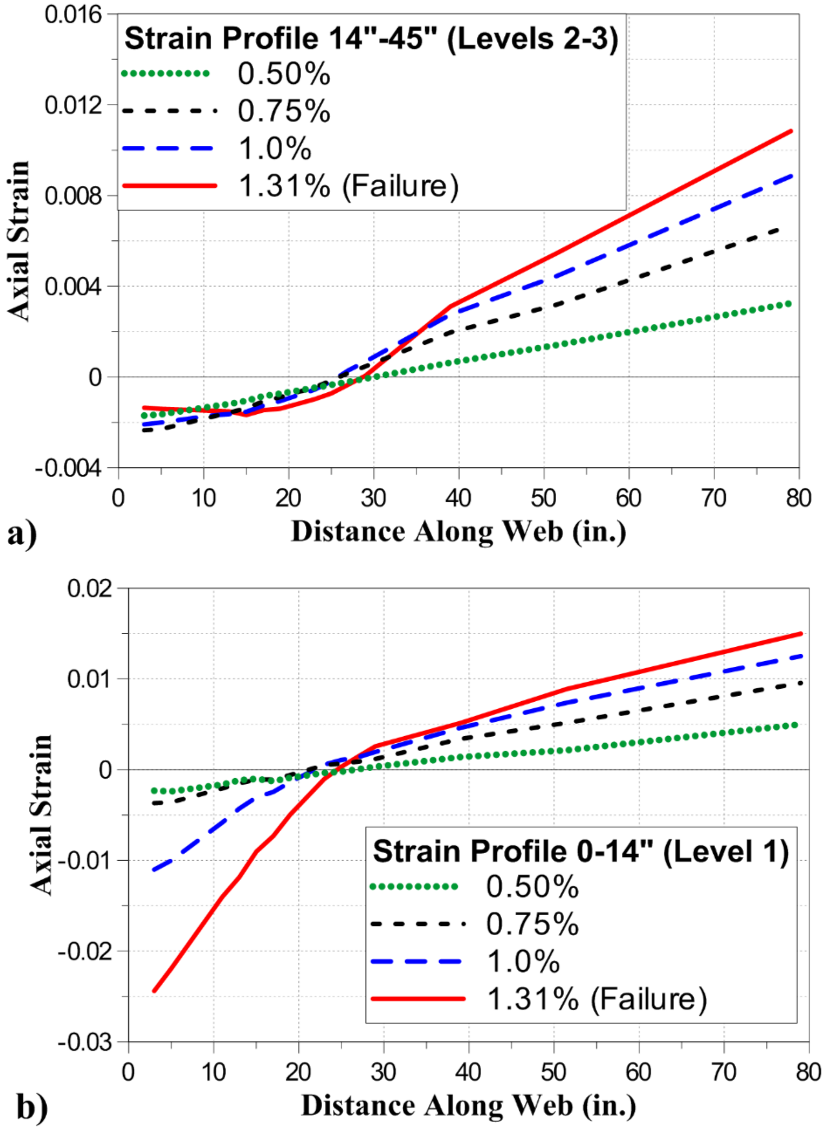

Figure 7-8: Axial strain profiles for specimen WP4 measured from digital image correlation analysis at various hinge rotation levels – a) Average axial strains in Levels 2 through 3 (14-45 in. above specimen footing); and b) Average axial strains in Level 1 (0-14 in. above specimen footing); Analysis conducted with Opecal (Barthes, 2015)

The maximum compression strains measured within the bottom 14 in. (356 mm) of the wall are presented for specimens WP1-WP7 in Figure 7-9a. Maximum compression strains, measured over the 14 in. (356 mm) gage length, ranged between 0.022 and 0.036 at boundaries where compression failure was observed. Average compression strains measured by sensors above the 14 in. (356 mm) height did not exceed 0.002 at any time during the test. As such, axial deformations due to the compression strains limits ($\Delta_{axial}=\varepsilon_{cu}l_p$) shown in Figure 7-4a and Figure 7-9a are nearly identical because all inelastic behavior was captured within the bottom 14 in. (356 mm) of the wall; that is, the strains reported in Figure 7-9a (l_p=14 in. [356 mm]) are essentially regularized measurements of the strains in Figure 7-4a (l_p=44 in. [1118 mm]). The horizontal axis of Figure 7-9a indicates the wall thickness of the specimens for which compression strain measurements are reported. The trend in Figure 7-9a suggests that, as wall thickness increases, compressive strain capacity increases for a constant gage length (l_p=14 in. [356 mm]). The strains reported in Figure 7-9a are regularized to wall thickness in Figure 7-9b such that the values reported in Figure 7-9b represent the term $\alpha\varepsilon_c$ in Eqn. 7.5. At all of the boundaries where compression failures were observed, $\alpha\varepsilon_{cu}$ exceeded 0.05.

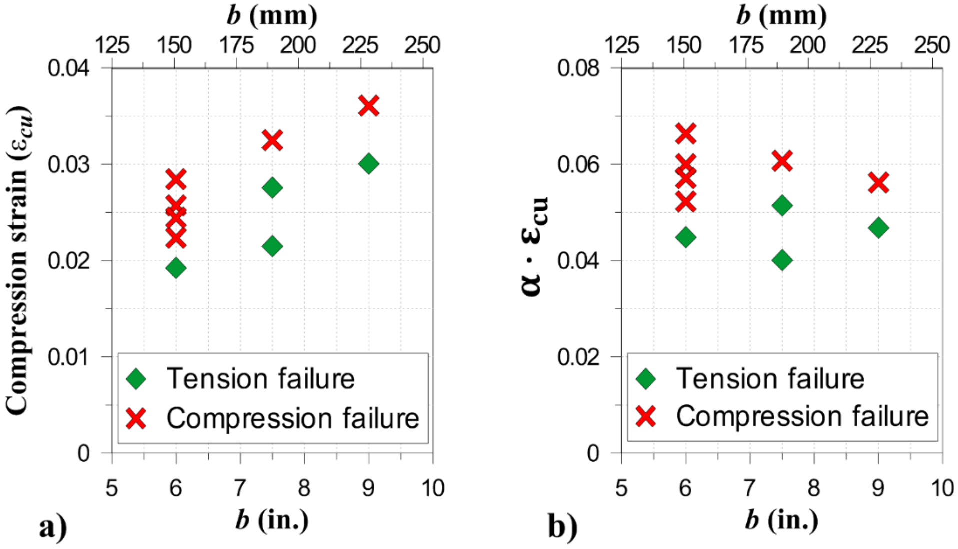

Figure 7-9: Maximum measured extreme fiber compression strain– a) Measured over bottom 14 in. (356 mm) of wall; and b) Compression strain limit regularized to wall thickness

The predicted plastic rotation capacity according to Eqn. 7.5, using $\alpha\varepsilon_{cu}l_p$=0.05$b$, is plotted in Figure 7-10 along with measured plastic rotations for the walls included in the study. The data in Fig. 11 demonstrate significantly less dispersion than Figure 7-5 (l_p= l_w/2), and predicted rotation capacities (Eqn. 7.5) closely match test data using a single compression strain limit. The test data and predictive equation indicate flexural drift capacities greater than 2% may be expected for *c/b*<2.5, and drifts less than 1% may be expected for *c/b*>5.

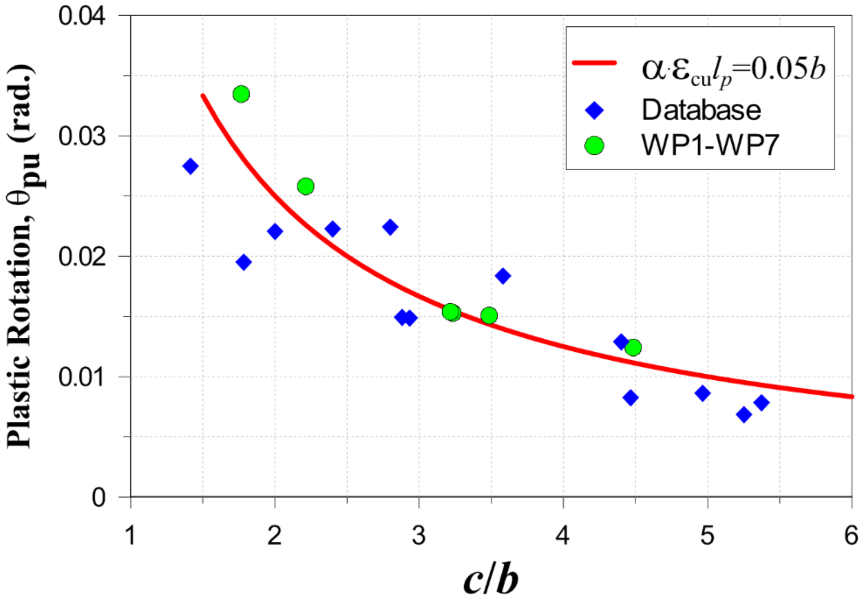

Figure 7-10: Plastic rotation capacity vs. c/b

While the test results in Figure 7-10 appear to agree reasonably well with the prediction, rotation capacities are overestimated for a few of the walls. In Figure 7-11, the ratio of measured-to-predicted plastic drift capacity is compared to the shear span-to-depth ratio (M/Vl_w), an indicator of the relative flexural and shear demands. It can be seen that $\delta_{f,p}$ is over predicted for walls with M/Vl_w<3.0 (i.e., relatively high shear demand), which might suggest that the compression strain capacity of the walls with M/Vl_w<3.0 is smaller than that of the relatively slender walls (M/Vl_w≥3.0). However, walls with M/Vl_w<3.0 typically exhibit more notable interaction between the flexural and shear responses than relatively slender walls (Massone, et al., 2004; Tran, et al., 2015; Kolozvari, et al., 2015). As a result, degradation of the shear resisting mechanism may occur as wide flexural cracks open in the plastic hinge region, leading to significant nonlinear shear deformations and larger stain demands along diagonal compression struts. As shown in Figure 7-12a and Figure 7-12b, shear deformations (δ_s) comprised 15-35% of the total response for walls with $M/Vl_w<3.0$ and design shear stress ($v_u=V_u/A_{cv}$) greater than $3\sqrt{f'c\,[\text{psi}]}$, while shear comprised less than 10% of the total deformation for the relatively slender walls ($M/Vl_w\geq3.0$) which all had low shear stress demands $\left(v_u \leq 3\sqrt{f'c\,[\text{psi}]}\right)$.

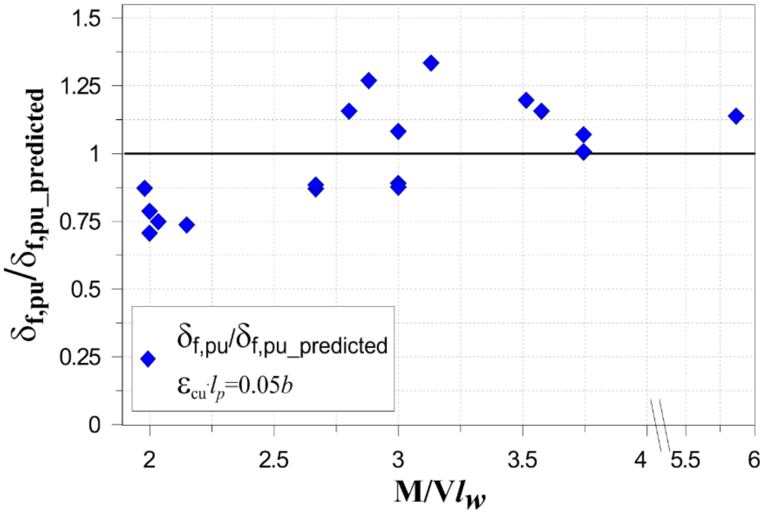

Figure 7-11: Ratio of measured-to-predicted plastic flexural drift capacity vs M/Vl_w

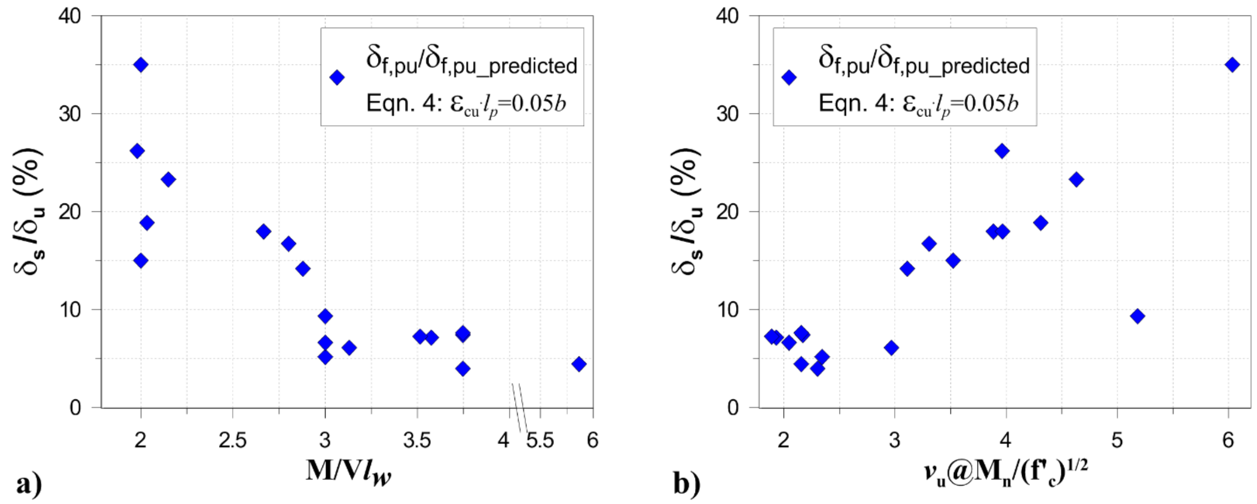

Figure 7-12: a) Contribution of shear deformation to total lateral deformation capacity (δ_s/δ_u) vs. M/Vl_w; and b) δ_s/δ_u vs. design shear stress demand

In Figure 7-13, total measured plastic deformations, including shear (i.e., $\delta_{pu}=\delta_{f,p}+\delta_{s,p}$), are compared to the predicted inelastic drift capacity. Inelastic shear deformations ($\delta_{s,p}$) were determined by subtracting an assumed elastic contribution, estimated using the effective cracked shear stiffness values recommended in ASCE 41 ($GA_{eff}=0.4E_cA_{cv}$). When inelastic shear is included, the predicted plastic drift capacity is reliable for all measured values of M/Vl_w and shear stress demand (v_u). On average, the measured plastic drift capacity (δ_{pu}) is 1.19 times the predicted value, indicating that the walls with M/Vl_w<3.0 likely possess the compression strain capacity assumed in Figure 7-10 and Figure 7-11, with a larger portion of the compression strain demand attributed to inelastic shear (i.e., compression strut) than is observed for walls with M/Vl_w≥3.0.

As shown in Figure 7-13b, the maximum design shear stress demand for the walls included in the study was approximately $6\sqrt{f'c\text{ [psi]}}$, and the majority of the walls were designed for shear stress demands less than $6\sqrt{f'c\text{ [psi]}}$. ACI 318-14 permits shear stress demands up to $10\sqrt{f'c\text{ [psi]}}$ for slender walls. Further research may be necessary to quantify the impact of shear demand on the compression strain demand at wall boundaries, and to determine whether the trend shown in Figure 7-13 ($\delta_{pu}>\delta_{f,pu\_predicted}$) applies for walls with shear stress demands close to the maximum allowed by ACI 318.

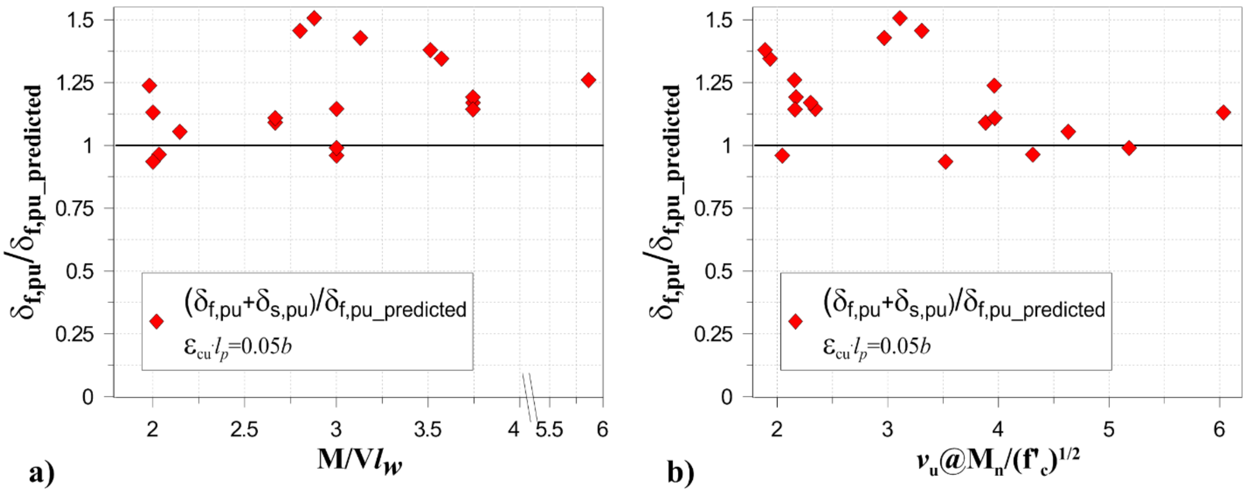

Figure 7-13: a) Ratio of total measured plastic drift capacity ($\delta_{f,pu}+\delta_{s,pu}$) to predicted drift capacity vs. M/Vl$_w$; and b) Ratio of total measured plastic drift capacity ($\delta_{f,pu}+\delta_{s,pu}$) to predicted drift capacity vs. design shear stress demand

Figure 7-10 primarily reports the drift capacities at which compression failure occurred; however, for a few of the walls, drift capacity was limited by tension rupture of longitudinal reinforcement, preceded by initial buckling of longitudinal reinforcement in all cases. At the limit state of tension rupture, plastic drift/rotation may be expressed directly in terms of wall thickness and compression depth (Eqn. 7.6).

$$\frac{\delta_{f,p}}{h_w} \approx \theta_{pu} \approx \left(\frac{\varepsilon_{tu}}{l_w - c}\right) l_p \tag{7.6}$$

The tension strain limits reported in Figure 7-4b were measured over gage length of $l_p=l_w/2$. As shown in Figure 7-7, inelastic tension strains were able to spread over the full height of the approximately 1.5 story panel specimens, which is approximately equal to the length of the wall (l_w). Thus, assuming a plastic hinge length of at least one-half the length of the wall ($l_p=l_w/2$) is reasonable for the limit state of tension strain rupture. It is noted that using $l_p=l_w/2$, with the tension strain limits in Figure 7-4b ($\varepsilon_{tu}\approx0.04$), will likely produce a lower bound estimate of the plastic drift capacity at the limit state of tension rupture because plastic curvature is neglected above $l_w/2$. If axial tension deformations above $l_w/2$ are considered for the specimens that reached $\varepsilon_{tu}>0.04$, ε_{tu} is at least 0.05 when strains are regularized to $l_p=l_w/2$, which is expected to provide a more accurate estimate of the plastic drift capacity of a wall at the flexure-tension limit state.

7.3 Drift Capacity Limit for Well-Detailed Slender Walls

Based on the lateral drift limit prediction formulations in Eqn. 7.5 (compression strain limit) and Eqn. 7.6 (tension strain limit), a recommended drift limit (δ_{max}/h_w) equation is summarized in Eqn. 7.7. The drift limit is intended for ACI 318-14 compliant Special Structural Walls with Special Boundary Element detailing. The drift limit uses compression and tension strain limits identified in Figure 7-9b and Figure 7-4b, respectively, and is expressed in terms of compression depth (*c*), wall thickness (*b*), wall length (l_w), and elastic deformations (δ_y/h_w).

$$\frac{\delta_{\max}}{h_w}=\left(\frac{\delta_y}{h_w}+\frac{0.05}{c/b}\right)\le\left(\frac{\delta_y}{h_w}+\frac{0.025}{1-c/l_w}\right) \qquad 7.7$$

The elastic drift in Eqn. 7.7 can be estimated for a given load pattern (e.g., ASCE 7 Equivalent Lateral Force or Response Spectrum Analysis) using appropriate effective stiffness values (e.g., ASCE 41-13). For preliminary design, elastic drift may be estimated as $\delta_y/h_w=\frac{11}{40}\phi_y h_w$, where $\phi_y=\frac{0.0025}{l_w}$ may be assumed based on the recommendations of Wallace and Moehle (1992). For simplicity, the elastic contribution may be neglected, as is done in ACI 318 for determining the need for SBE detailing at wall boundaries. For the case in which elastic deformations are neglected, the drift limit of Eqn. 7.7 is shown in Figure 7-14 for several compression depth demands

(c/l_w=0.05-0.38). The drift capacity associated with the tension strain limit is shown as a horizontal line, for each c/l_w value, which places an upper limit on the allowable drift for lower wall length-to-thickness (l_w/b) ratios at which the compression strain limit will not govern the drift capacity of the wall. The trends in Figure 7-14 demonstrate that drift capacity is expected to decrease as the wall length-to-thickness ratio (l_w/b) increases, and as the compression depth increases (c/l_w).

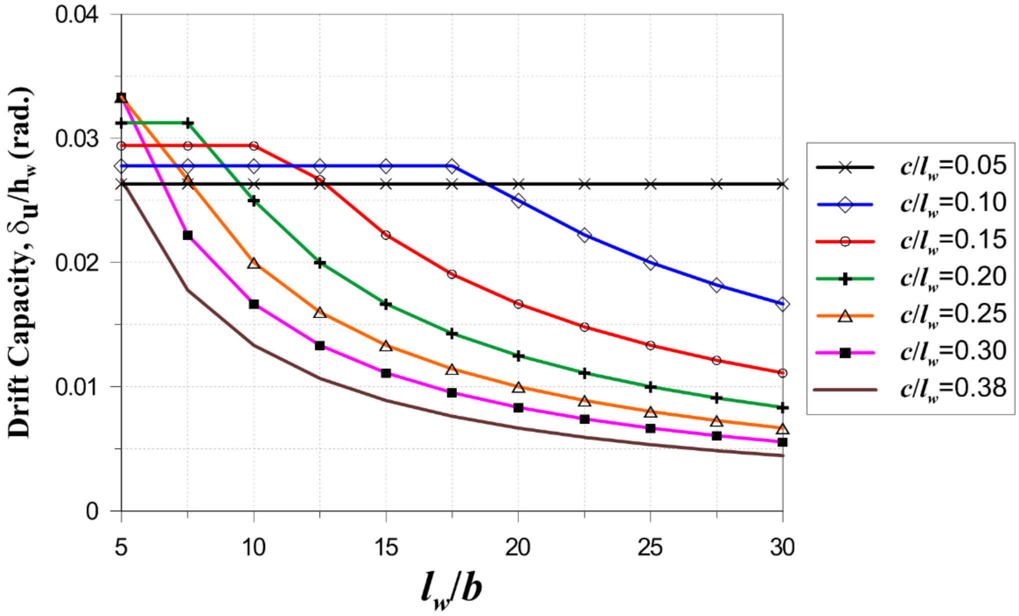

Figure 7-14: Recommended drift capacity limit for well-detailed slender walls

The drift limits in Eqn. 7.7 and Figure 7-14 are intended for comparison to roof drift ratio demands (δ_u/h_w). For the walls included in the study, lateral drift ratios were measured at h_{eff}, which is less than the roof height (h_w). It is noted that plastic drift ratio is essentially constant up the height of the building ($\delta_{f,p}/h_w \approx \theta_p$; Figure 2-2); therefore, the trends in Figure 7-10, which do not include elastic deformations, are valid at the roof level. However, elastic drift ratio, which comprised approximately 10-30% of the total drift capacity at h_{eff} for the database walls (Figure 7-2), increases with height according to Eqn. 2.3 (i.e., $\delta_{f,y}/h=\gamma\phi_y h$). Based on the ASCE 7 Equivalent Lateral Force load distribution, h_w is about 1.3 to 1.4 times h_{eff} for a shear wall building between three and ten stories in height, and even higher for taller buildings. In Figure 7-15, the drift limit of Eqn. 7.7 is compared to the lateral roof drift capacities ($\delta_u@h_w$) for the database walls. Data points are included in Figure 7-15 for the case when elastic drift is included in the drift prediction, and when elastic drift is neglected. Drifts at h_w were determined by amplifying elastic drifts assuming h_w=1.3h_{eff}. Because shear deformations are small, they were neglected above h_{eff}. Due to the difference in height between h_{eff} and h_w, δ_u/h_w is only 6% higher than δ_u/h_{eff}, on average, for the walls in the study. It is noted that, because of the small differences between drift ratios at h_w and h_{eff}, amplification of elastic drifts was not very sensitive to the choice of h_w/h_{eff}. As shown in Figure 7-15, measured drift capacities at h_w are generally greater than or equal to 1.25 times the drift limit when elastic drift is neglected, except for a few walls with δ_u/h_{eff}>3% (δ_u/h_{eff} indicated on horizontal axis), which is acceptable given the large observed deformation capacity. When elastic deformations are included, δ_u/δ_{max} is close to 1.0 for most of the walls.

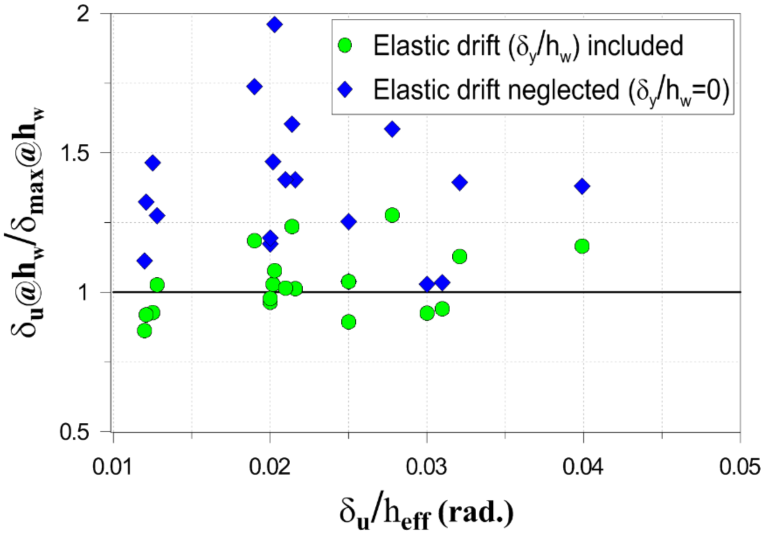

Figure 7-15: Comparison of recommended drift limit to measured drift capacities

For new building design (ASCE 7, ACI 318), the design drift ratio (δ_u/h_w) is based on Design Earthquake (DE) demands which are assumed to be two-thirds of MCE demands. Eqn. 7.7 is a limit state formulation intended for collapse prevention, which makes it more suitable for comparison to MCE demands. In this case, the design drift ratio (δ_u/h_w) and drift limit (δ_{max}/h_w) should be compared in accordance with Eqn. 7.8.

$$\frac{1.5\delta_{\mathrm{u}}}{h_w} \le \frac{\delta_{\mathrm{max}}}{h_w} \qquad 7.8$$

Based on the limited results presented in Figure 7-15– that is, δ_u/δ_{max} generally greater than or equal to 1.0, Eqn. 7.8 is expected to provide a low probability of collapse for a shear wall building subjected to MCE demands, consistent with the building code intent. A detailed reliability study, using a larger database of experimental tests, may help to further explore the level of reliability associated with the use of Eqn. 7.8 for DE and MCE demands.

In Figure 7-16, plastic rotation capacities for walls with overlapping hoop configurations, which are not included in Figure 7-10, are compared to those with hoop and cross-tie configurations. In general, the walls with overlapping hoops demonstrate larger plastic rotation capacity for a given *c/b*. Linear trend lines suggest walls with overlapping hoops possess approximately 1% more drift capacity, on average, for a given value of *c/b*. According to Figure 7-16, it may be reasonable to allow drifts larger than those recommended in Figure 7-14 if transverse reinforcement is provided by overlapping hoops. A detailed survey of monotonic and cyclic tests on code compliant boundary element specimens may help to quantify the compression and tension strain limits for boundary transverse reinforcement in excess of that required by ACI 318-14. It is noted that the drift capacity for walls designed with enhanced detailing may be governed by tension rupture of longitudinal reinforcement except for walls with moderate or large compression depths (i.e., $c/b \ge 4$).

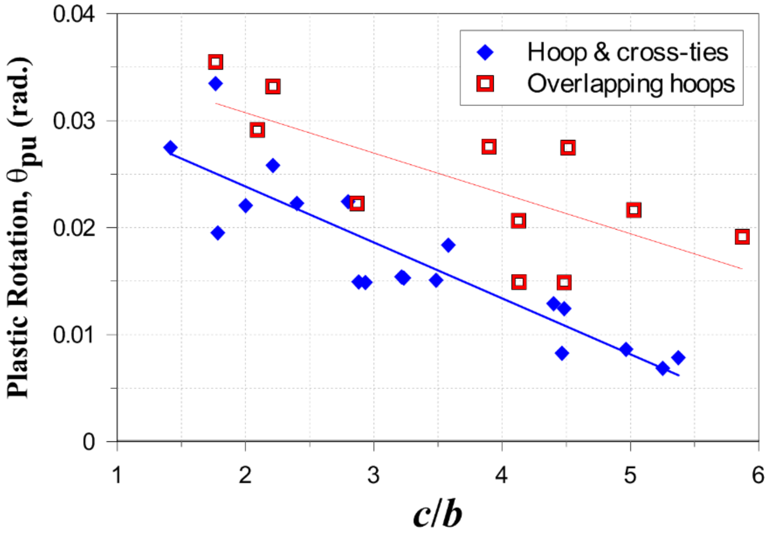

Figure 7-16: Plastic rotation capacity vs. c/b for walls with hoop and cross-tie confinement detail and walls with overlapping hoops

Chapter 8 Summary and Conclusions

Based on poor performance observed for slender reinforced concrete structural walls in recent earthquakes and laboratory tests, an experimental program was undertaken to identify critical deign limitations for slender walls, to assess the deformation capacity of well-detailed walls satisfying current ACI 318 provisions, and to make recommendations for future code releases. The experimental study consisted of large-scale reversed cyclic testing of seven reinforced concrete structural wall panel specimens, designated WP1-WP7, which represented approximately the bottom 1.5 stories of an eight story cantilever wall. The walls were designed according to ACI 318-14 Special Structural Walls. For all seven walls, a constant axial load of $0.10A_{cv}f'_c$ was applied for the duration of the test, and peak shear stresses demands were less than $3\sqrt{f'_c\ [psi]}$. The test variables for the study included: the arrangement of boundary longitudinal reinforcement, the quantity and spacing of boundary transverse reinforcement, the compression depth (influenced by longitudinal reinforcement, axial load, and wall geometry), wall thickness, the confinement detail used at the boundaries of the wall, and the arrangement of web longitudinal reinforcement.

Experimental data for WP1-WP7 were used to formulate a predictive equation to estimate the lateral drift capacity at which a slender wall will fail due to flexural-compression (i.e., concrete crushing and buckling of longitudinal reinforcement) or flexure-tension (i.e., tension rupture of longitudinal reinforcement). To complement the experiments reported herein, a database of twenty wall tests performed on well-detailed walls designed for moderate-to-large compression was assembled and used to validate the drift limit formulation. Based on the study, the following observations and conclusions are made:

1. Experimental results for test specimens representing full-scale, 12 in. [305 mm] thick walls indicate thin walls may fail in compression prior to achieving the lateral drift or rotation

capacities assumed by ASCE 7 and ASCE 41, respectively, even though the walls satisfy ACI 318-14 provisions. Plastic rotation capacities as low as 1.1% were measured for the thinnest walls tested (b=6 in.; 152 mm), followed immediately by a drop in lateral load capacity to near zero. Walls that were 25% and 50% thicker (7.5 in. [191 mm] and 9 in. [229 mm]) were able to achieve plastic rotations greater than 2.5% prior to strength loss. Based on test observations, it is apparent that equivalent performance is not expected for all walls that satisfy ACI 318-14 Special Structural Wall requirements. Further study is required to determine how to address drift capacity limitations for thin walls in future building codes and specifications.

2. Abrupt compression failure was observed for walls utilizing a single outer hoop and cross-ties for boundary confinement. Strain gage data indicated cross-tie strains become disproportionately large in comparison to hoop strains once crushing/spalling of cover concrete occurs, leading to rapid degradation of the compression resisting mechanism. In contrast, compression failure was not observed at boundaries of walls confined by continuous transverse reinforcement, which is similar to overlapping hoops. Continuous transverse reinforcement, and presumably overlapping hoops, enable more uniform distribution of transverse strains, providing more stable confinement than a single hoop with cross-ties.
3. For two of the walls presented (WP1 and WP2), premature strength loss occurred due to out-of-plane instability of the compression zone following concrete crushing/spalling and initial buckling of longitudinal reinforcement, even though the slenderness ratio (h/b=14) for these walls was less than the maximum allowed by ACI 31-14 ($h/b \leq 16$). Thicker walls (WP6 and WP7) demonstrated greater stability in compression at similar or larger

compression strain demands, indicating that it may be necessary to modify the requirements for minimum wall thickness in ACI 318-14 to include additional variables, such as drift demand. The data presented for the approximately one-half scale walls suggests that walls designed for moderate compression demands (c/l_w=0.2-0.3) may necessitate at least a 15-18 in. (381-457 mm) thick compression zone. A review of a larger database of laboratory tests may help to better define a minimum wall thickness and to further study the impact of compression depth and confinement detail on lateral stability.

4. Fracture of cross-ties was only observed in a few cases for the tests reported in this paper. Instead, following crushing and spalling of cover concrete, 90^o cross-tie hooks opened, making them less effective in providing confinement and resisting longitudinal bar buckling. Very little, if any, performance enhancement was observed for cross-ties with 135^o hooks on each end. It is suggested to avoid the use of a boundary element with a single hoop and cross-ties, and to use overlapping hoops or continuous transverse reinforcement for boundary transverse reinforcement.
5. ACI 318-14 allows web longitudinal reinforcement to be placed outside of transverse reinforcement with no requirement for lateral restraint by cross-ties. For walls designed with this detail (WP1-WP4), buckling of web longitudinal reinforcement was observed over heights up to approximately $40d_b$ and the walls were unable to maintain lateral residual strength and axial load following compression failure at approximately 1.5% rotation. For walls in which longitudinal bars were laterally restrained at $16d_b$ (WP5-WP7), residual lateral strength greater than approximately 40% of peak capacity was maintained to at least 3% rotation. Lateral restraint for longitudinal web reinforcement using cross-ties

is recommended in the plastic hinge region to maintain residual strength and protect against axial failure.

6. Experimental data indicate that drift capacity increases as wall thickness (*b*) increases for a given compression depth (*c*). A lateral drift limit equation was formulated in a displacement-based design (DBD) format based on experimentally measured compression strain and tension strain limits, and good agreement of the drift limit with experimental data was observed for relatively slender walls ($M/Vl_w \geq 3.0$). The predictive equation and test data indicate drift capacities greater than 2% may be expected for code compliant walls designed such that the compression depth is less than 2.5 times the wall thickness ($c/b<2.5$), while drift capacities less than 1% are expected for walls with $c/b>5$. Additional research is suggested to quantify the impact of shear span-to-depth ratio (M/Vl_w) and shear stress on the compression strain demands at wall boundaries.
7. For DBD, it is common to assume a plastic hinge length of one-half the length of the wall in order to capture inelastic curvature. It was shown that drift predictions using a DBD format may be unconservative for relatively long walls (i.e., $l_w/b \geq 15$), and overly conservative for shorter walls (i.e., $l_w/b \leq 10$), when compression strain capacity is assumed to be constant (e.g., $\varepsilon_{cu}=0.008$) and plastic hinge length is assumed to be related to wall length (e.g., $l_w/2$). This is because drift capacity is assumed to be directly related to the ratio of compression depth to wall length (c/l_w). By this definition, two walls with the same c/l_w and different wall thickness are expected to possess similar drift capacity, although it has been shown that thinner walls tend to be less ductile.
8. For thick walls and/or walls designed for relatively low compression (e.g., $c/b<3$), drift capacity may be limited by the low-cycle fatigue capacity of longitudinal reinforcement.

A tension strain limit of 0.05, with an associated plastic hinge length of $l_p = l_w/2$, is suggested based on a review of limited test data.

9. Based on the information presented, equivalent performance is not expected for all walls that satisfy ACI 318-14 provisions. Walls with lower c/b and/or overlapping hoop confinement are more stable in compression, making it possible to achieve larger inelastic deformations. An approach that involves comparing drift demands to drift capacities for individual walls is presented that would enable a designer to make informed decisions about the impact of building (wall) layout and wall proportioning and detailing on expected building performance. Another approach might be to suggest a minimum wall thickness and/or minimum detailing requirements to achieve a given drift demand. A detailed survey of monotonic and cyclic tests on code compliant boundary element specimens is suggested to quantify the compression and tension strain limits of confinement details exceeding ACI 318-14 requirements.

REFERENCES

Aaleti, S., Brueggen, B. L., Johnson, B., French, C. E., and Sritharan, S. (2013). Cyclic Response of Reinforced Concrete Walls with Different Anchorage Details: Experimental Investigation. *Journal of Structural Engineering*, 139, 1181-1191.

ACI Committee 318 (1983). Building Code Requirements for Structural Concrete (ACI 318-83). Farmington Hills, MI: American Concrete Institute.

ACI Committee 318 (2014). Building Code Requirements for Structural Concrete (ACI 318-14) and Commentary. Farmington Hills, MI: American Concrete Institute.

Arteta, C. A. (2015). Seismic Response Assessment of Thin Boundary Elements of Special Concrete Shear Walls. *PhD Dissertation*. University of California, Berkeley.

ASCE/SEI (2007). Seismic Rehabilitation of Existing Buildings (ASCE/SEI 41-06). Reston, VA: American Society of Civil Engineers.

ASCE/SEI (2010). Minimum Design Loads for Buildings and Other Structures (ASCE/SEI 7-10). Reston, VA: American Society of Civil Engineers.

ASCE/SEI (2014). Seismic Rehabilitation and Upgrade of Existing Buildings (ASCE/SEI 41-13). Reston, VA: American Society of Civil Engineers.

ASTM A615/A615M-16 (2016). Standard Specification for Deformed and Plain Carbon-Steel Bars for Concrete Reinforcement. West Conshohocken, PA: ASTM International.

ASTM A706/A706M-16 (2016). Standard Specification for Low-Alloy Steel Deformed and Plain Bars for Concrete Reinforcement. West Conshohocken, PA: ASTM International.

Barda, F., Hanson, J. M., and Corley, W. G. (1977). Shear Strength of Low-Rise Walls with Boundary Elements. *ACI Special Publication*, 53(8), 149-202.

Barthes, C. B. (2015). Optecal [Computer software]. Available at www.optecal.com.

Birely, A. C. (2011). Seismic Performance of Slender Reinforced Concrete Structural Walls. *PhD Proposal*. University of Washington.

Brueggen, B. L. (2009). Performance of T-shaped Reinforced Concrete Structural Walls under Multi-Directional Loading. *PhD Dissertation*. University of Minnesota.

Cardenas, A. E., and Magura, D. D. (1973). Strength of High-Rise Shear Walls - Rectangular Cross Section. *ACI Special Publication*, 36(7), 119-150.

Cardenas, A. E., Hanson, J. M., Corley, W. G., and Hognestad, E. (1973). Design Provisions for Shear Walls. *ACI Journal*, 70(3), 221-230.

Cardenas, A. E., Russell, H. G., and Corley, W. G. (1980). Strength of Low-Rise Structural Walls. *ACI Special Publication*, 63(10), 221-242.

Chai, Y. H., and Elayer, D. T. (1999). Lateral Stability of Reinforced Concrete Columns Under Axial Reversed Cyclic Tension and Compression. *ACI Structural Journal*, 96(5), 780-789.

Corley, W. G., Fiorato, A. E., and Oesterle, R. G. (1981). Structural Walls. *ACI Special Publication*, 72(4), 77-132.

Dazio, A., Beyer, K., and Bachmann, H. (2009, July). Quasi-Static Cyclic Tests and Plastic Hinge Analysis of RC Structural Walls. *Engineering Structures*, 31(7), 1556-1571.

EERI (1986). The Chile Earthquake of March 3, 1985. *Earthquake Spectra*, 2(2).

EERI (2010). The Mw 8.8 Chile Earthquake of February 27, 2010. *EERI Special Earthquake Report*.

EERI (2011, May). The M 6.3 Christchurch, New Zealand, Earthquake of February 22, 2011. *EERI Special Earthquake Report*.

Elwood, K. J. (2013). Performance of Concrete Buildings in the 22 February 2011 Christchurch Earthquake and Implications for Canadian Codes. *Canadian Journal of Civil Engineering*, 40, 759-776.

Goodsir, W. J. (1985). The Design of Coupled Frame-Wall Structures for Seismic Actions. *PhD Dissertation*. University of Canterbury.

Instituto Nacional de Normalización (INN) (1996). NCh433.Of96: Earthquake Resistant Design of Buildings. Santiago, Chile [in Spanish].

International Conference of Building Officials (ICBO) (1997). Uniform Building Code (UBC-97). Whittier, CA.

Johnson, B. M. (2007). Anchorage Detailing Effects on Lateral Deformation Components of RC Shear Walls. *Master's Thesis*. University of Minnesota.

Kam, W. Y., Pampanin, S., and Elwood, K. (2011). Seismic Performance of Reinforced Concrete Buildings in the 22 February Christchurch (Lyttleton) Earthquake. *Bulleting of the New Zealand Society for Earthquake Engineering*, 44(4), 239-278.

Kolozvari, K., Orakcal, K., and Wallace, J. W. (2015). Modeling of Cyclic Shear-Flexure Interaction in Reinforced Concrete Structural Walls - Part I: Theory. *Journal of Structural Engineering*, 143(7).

Lehman, D., Welt, T., and LaFave, J. (2015). Recommendations for Confinement in Boundary Elements of Special Structural Walls. *Proceedings of the 2015 SEAOC Convention*.

Lowes, L. N., Lehman, D. E., Birely, A. C., Kuchma, D. A., and Marley, K. P. (2012). Earthquake Response of Slender Planar Concrete Walls with Modern Detailing. *Engineering Structures*, 43, 31-47.

Mander, J. B., Priestley, M., and Park, R. (1988). Observed Stress-Strain Behavior of Confined Concrete. *Journal of Structural Engineering*, 114(8), 1827-1849.

Massone, L. M., and Wallace, J. W. (2004). Load-Deformation Responses of Slender Reinforced Concrete Walls. *ACI Structural Journal*, 101(1).

Massone, L. M., Bonelli, P., Lagos, R., Lüders, C., Moehle, J., and Wallace, J. W. (2012). Seismic Design and Construction Practices in RC Structural Wall Buildings. *Earthquake Spectra*, 28(S1), S245-S256.

Matsubara, S., Sanada, Y., Tani, M., Takahashi, S., Ichinose, T., and Fukuyama, H. (2013). Structural Parameters of Confined Area Affect Flexural Deformation Capacity of Shear Walls that Fail in Bending with Concrete Crushing. *Journal of Structural and Construction Engineering*, 78(691), 1593-1602 [in Japanese].

MINVU (2011). Reinforced Concrete Design Code (DS No. 60). Ministry of Housing and Urbanism. Santiago, Chile [in Spanish].

Moehle, J. P., and Cavanagh, T. (1985). Confinement Effectiveness of Crossties in RC. *Journal of Structural Engineering*, 111(10), 2105-2120.

Nagae, T., Tahara, K., Fukuyama, K., Matsumori, T., Siohara, H., Kabeyasawa, T., Ghannoum, W. (2012). Test Results of Four-Story Reinforced Concrete and Post-Tensioned Concrete Buildings: The 2010 E-Defense Shaking Table Test. *Proceedings of the 15th World Conference on Earthquake Engineering*. Lisbon, Portugal.

NIST (2014). Recommendations for Seismic Design of Reinforced Concrete Wall Buildings Based on Studies of the 2010 Maule, Chile Earthquake. NEHRP Consultants Joint Venture, National Institute of Standards and Technology. Gaithersburg, MD.

Oesterle, R. G., Arisizabal-Ochoa, J. D., Shiu, K. N., and Corley, W. G. (1984). Web Crushing of Reinforced Concrete Structural Walls. *ACI Journal*, 81(3), 231-241.

Oesterle, R. G., Aristixabal-Ochoa, J. D., Fiorato, A. E., Russell, H. G., and Corley, W. G. (1979). Earthquake Resistant Structural Walls - Tests of Isolated Walls - Phase II. Construction Technology Laboratories. Portland Cement Association. Skokie, IL.

Oesterle, R. G., Fiorato, A. E., Johal, L. S., Carpenter, J. E., Russell, H. G., and Corley, W. G. (1976). Earthquake Resistant Structural Walls - Tests of Isolated Walls. Construction Technology Laboratories. Portland Cement Association. Skokie, IL.

Paulay, T., and Goodsir, J. (1985). The Ductility of Structural Walls. *Bulletin of the New Zealand National Society for Earthquake Engineering*, 18(3), 250-269.

Paulay, T., and Priestley, M. J. (1993). Stability of Ductile Structural Walls. *ACI Structural Journal*, 90(4), 385-392.

Shiu, K. N., Daniel, J. I., Aristizabal-Ochoa, J. D., Fiorato, A. E., and Corley, W. G. (1981). Earthquake Resistant Structural Walls - Tests of Walls With and Without Openings. Construction Technology Laboratories. Portland Cement Association. Skokie, IL.

Takahashi, S., Yoshida, K., Ichinose, T., Sanada, Y., Matsumoto, K., Fukuyama, H., and Suwada, H. (2013). Flexural Drift Capacity of Reinforced Concrete Wall with Limited Confinement. *ACI Structural Journal*, 110(1).

Thomsen, J. H., and Wallace, J. W. (1995). Displacement-Based Design of RC Structural Walls: An Experimental Investigation of Walls with Rectangular and T-Shaped Cross-Sections. Clarkson University.

Thomsen, J. H., and Wallace, J. W. (2004). Displacement-Based Design of Slender Reinforced Concrete Structural Walls - Experimental Verification. *Journal of Structural Engineering*, 130(4), 618-630.

Tran, T. A. (2012). Experimental and Analytical Studies of Moderate Aspect Ratio Reinforced Concrete Structural Walls. University of California, Los Angeles.

Tran, T. A., and Wallace, J. W. (2015). Cyclic Testing of Moderate-Aspect-Ratio Reinforced Concrete Structural Walls. *ACI Structural Journal*, 112(6), 653-666.

Wallace, J. W. (1994). New Methodology for Seismic Design of RC Shear Walls. *Journal of Structural Engineering*, 120(3), 863-884.

Wallace, J. W. (2012). Behavior, Design, and Modeling of Structural Walls and Coupling Beams - Lessons from Recent Laboratory Tests and Earthquakes. *International Journal of Concrete Structures and Materials*, 6(1), 3-18.

Wallace, J. W., and Moehle, J. P. (1992). Ductility and Detailing Requirements of Bearing Wall Buildings. *Journal of Structural Engineering*, 118(6), 1625-1644.

Wallace, J. W., and Orakcal, K. (2002). ACI 318-99 Provisions for the Seismic Design of Structural Walls. *ACI Structural Journal*, 99(4), 499-508.

Wallace, J. W., Massone, L. M., Bonelli, P., Dragovich, J., Lagos, R., Lüders, C., and Moehle, J. (2012). Damage and Implications for Seismic Design of RC Structural Wall Buildings. *Earthquake Spectra*, 28(S1), S281-S299.

Welt, T. S. (2015). Detailing for Compression in Reinforced Concrete Wall Boundary Elements: Experiments, Simulations, and Design Recommendations. *PhD Dissertation*. University of Illinois at Urbana-Champaign.

Wood, S. L., and Sittipunt, C. (1996). Cyclic Response of Reinforced Concrete Structural Walls. *ACI Special Publication*, 162(16), 399-429.

Wood, S. L., Wight, J. K., and Moehle, J. P. (1987). The 1985 Chile Earthquake, Observations on Earthquake Resistant Construction in Viña del Mar. University of Illinois Urbana-Champaign.